

**Synthesis, characterization and luminescent mechanism of
ZnS:Mn²⁺ nanophosphor**

by

Mart-Mari Biggs

(B.Sc Hons)

A thesis submitted in fulfillment of the requirements for the degree

MAGISTER SCIENTIAE

in the

Faculty of Natural and Agricultural Sciences

Department of Physics

at the

University of the Free State

Republic of South Africa

Promoter: Prof H.C. Swart

Co-promoter: Prof O.M. Ntwaeaborwa

November 2009

*This thesis is dedicated to my husband Giel,
father, mother and brother.*

Acknowledgements

- To my heavenly Father who gave me the strength to pursue my goals.
- Prof H.C. for being the best promoter ever and for giving me the freedom to do new things.
- Prof O.M. Ntwaeaborwa for being my co-promoter and assisting me with all the chemistry involved in my project.
- Liza Coetzee for introducing me to the wonderful world of phosphors and helping me to understand the characterization techniques.
- Dr. V. Kumar for his discussions on absorptions techniques.
- Charl Jafta, Ebrahiem Botha and Jacques Maritz for being true friends and for their support during my research.
- Dawie van Jaarsveld who always helped me to make physics easier by turning the page upside down.
- Personnel at the Physics Department for discussions and encouragements.
- Beanelri Jannecke of the Centre for Microscopy UFS for her assistance in doing SEM and EDS measurements.
- Huibré Pretorius and Annegret Lombard at the Geology Department for their assistance in doing XRD measurements.
- Prof J.R. Botha of NMMU for his assistance with PL measurements.
- To my parents, John-William and Serah, for all their love, support and encouragement throughout my studies, without you none of this would have been possible.
- My brother, Stanley-John, for all his science related questions and his interest in my research.
- Last but not least, my husband, Giel – you are the love of my life.

Abstract

ZnS:Mn²⁺ is commercially used in field emission displays (FEDs) and biological imaging of brain tumors. This study was done to determine the luminescent mechanism of both bulk and nano sized ZnS:Mn²⁺.

Luminescent zinc sulphate doped with manganese (ZnS:Mn²⁺) nanoparticles were synthesized via a chemical precipitation method. These nanoparticles were embedded in an amorphous silica (SiO₂) matrix by a sol-gel process. The prepared nanocomposite materials were then crushed into powders, sieved and annealed at 600 °C in air. The morphology of the samples was determined by scanning electron microscopy (SEM) and the chemical composition was analyzed by energy dispersive x-ray spectroscopy (EDS). The crystal structure, morphology and particle sizes of ZnS:Mn²⁺ and SiO₂-ZnS:Mn²⁺ nanoparticles were determined with x-ray diffraction (XRD) and transmission electron spectroscopy (TEM). Both the cubic zincblende crystal structure for ZnS and the hexagonal wurtzite crystal structure for ZnO were found. The particle sizes for the unannealed samples estimated from the XRD peaks and the TEM images were 2 – 4 nm in diameter.

Absorption measurements were performed on the ZnS:Mn²⁺ samples. All the samples were absorbing in the UV range between 280 - 340 nm. The band gap of the samples was obtained from the absorption data and it was found to be 4.1 ± 0.2 eV. It is blue-shifted from that of bulk particles by 0.4 eV. This blue-shift can be attributed to quantum confinement effects in the crystal. The mean particle radius was also obtained from the absorption data and it was found to be 1.5 ± 0.1 nm. This corresponds well to the values obtained from XRD and TEM.

The ZnS:Mn²⁺ and SiO₂-ZnS:Mn²⁺ powders were irradiated with a 325 nm (He-Cd) laser and a 15W Xenon flash lamp for photoluminescence (PL) measurements. Two emission peaks at 450 nm (blue) and 600 nm (orange) were observed. The excitation peak was blue shifted from 340 nm to ~ 300 nm. This blue-shift can be attributed to the increase in the band gap of the nanoparticles caused by quantum confinement effects. A proposed luminescent mechanism for ZnS, ZnS:Mn²⁺ and ZnO is discussed. The blue emission (450 nm) associated with ZnS can be attributed to the hole trapping and recombination with electrons by defect states (zinc or sulphur vacancies) in ZnS. The orange emission at 600 nm for nano particles can be attributed to the

${}^4T_1 \rightarrow {}^6A_1$ transitions of Mn^{2+} ions. These transitions are explained in terms of the Tanabe-Sugano diagrams for the d^5 level, the Russell Saunders coupling scheme and the Ligand field theory. 6A_1 is the ground state of Mn^{2+} , while 4T_1 is one of the excited states. For the annealed samples a broad peak with a maximum at 550 nm (green) was observed. In the case of ZnO the emission is due to hole capturing and recombination with electrons by defect states.

Commercial $ZnS:Mn^{2+}$ powder were subjected to 2keV electron beam irradiation in a vacuum chamber at a pressure of 1×10^{-8} Torr for 24 hours. The cathodoluminescence (CL) intensity was measured with a S200/PC2000/USB2000/HR2000 spectrometer and it showed an emission peak at ~ 600 nm. This emission is attributed to the 4T_1 - 6A_1 transitions of Mn^{2+} ions. Changes in the chemical composition of the surface together with the corresponding changes in the CL intensity were investigated using Auger electron spectroscopy (AES), the CL spectrometer and a residual gas analyzer. The data showed a decrease in sulphur and carbon on the surface of the sample, while there was an increase in oxygen. The CL intensity decreased simultaneously with the decrease of the sulphur Auger peak-to-peak height. This may be due to the formation of volatile SO_x and a non-luminescent ZnO or $ZnSO_4$ layer on the surface according to the electron stimulated surface chemical reaction (ESSCR) degradation mechanism.

Keywords

$ZnS:Mn^{2+}$ nanoparticles, Photoluminescence, Absorption, Band gap, Cathodoluminescence, Degradation, Luminescent mechanism

Please note that the references are given at the end of each chapter.

Table of contents

Keywords	4
Chapter 1	11
Introduction.....	11
1. Background.....	11
2. Problem statement.....	14
3. Aim of this study.....	15
4. Layout of the thesis.....	16
References.....	17
Chapter 2	19
Background information and applications of phosphors.....	19
1. History of phosphors.....	19
2. Definition and terminology.....	22
3. Physical processes taking place during luminescence.....	22
3.1 Fluorescence	22
3.2 Phosphorescence	23
3.3 Radiationless transitions	23
4. Types of light emission.....	24
4.1 Incandescence	24
4.2 Luminescence	25
4.2.1 Fluorescence	25
4.2.2 Phosphorescence.....	26
4.2.3 Electroluminescence	27
4.2.4 Bioluminescence.....	28
4.2.5 Chemiluminescence	30
4.2.6 Thermoluminescence	31
4.2.7 Other types of luminescence.....	32
5. Applications of phosphors	33
5.1 Fluorescent lamps	34
5.2 Display devices	35

5.2.1 Cathode ray tubes (CRTs).....	35
5.2.2 Flat panel displays (FPDs).....	36
5.2.3 Field emission displays (FEDs)	38
5.3 X-ray screens and scintillators	39
5.4 Other applications	41
5.4.1 “Glow-in-the-dark” materials	41
5.4.1.1 Luminescent paints.....	41
5.4.1.2 Clothing.....	42
5.4.1.3 Signs and house numbers	43
5.4.1.4 Other applications.	44
5.4.2 Biological labelling.....	45
6. Types of phosphors	49
6.1 Band gap transition phosphors.....	50
6.2 Intra-atomic transition phosphors	51
7. ZnS.....	53
7.1 Sphalerite	54
7.2 Wurtzite.....	55
7.3 Matraite.....	57
References.....	58
Chapter 3	65
Theory of characterization techniques.....	65
1. Scanning electron microscopy (SEM)	65
1.1 Theory	65
2. Energy dispersive x-ray spectroscopy (EDS)	67
2.1 Theory	67
3. Transmission electron microscopy (TEM)	69
3.1 Theory	69
4. X-ray diffraction (XRD)	72
4.1 Crystal structure	72
4.2 Bragg’s Law	74
5. UV-Vis spectroscopy	75

5.1 Theory	75
5.2 Beer's Law	77
5.3 Tauc's relation	77
6. Photoluminescence spectroscopy (PL)	80
6.1 Theory	80
6.1.1 Determination of the band gap.....	81
6.1.2 Detection of impurity levels and defects.	81
6.1.3 Mechanisms of recombination.....	82
7. Cathodoluminescence (CL)	83
7.1 Theory	83
8. Auger electron spectroscopy (AES).....	85
8.1 Theory	85
9. Residual gas analysis (RGA)	87
9.1 Theory	87
References.....	90
Chapter 4	92
Luminescent mechanism of ZnS:Mn²⁺	92
1. Introduction.....	92
2. Orgel (Correlation) diagrams.....	92
3. Tanabe-Sugano diagram for a d5 ion.....	94
4. Russell-Saunders or LS coupling scheme.....	97
4.1 Quantum numbers.....	97
4.1.1 Principle quantum number (n)	97
4.1.2 Azimuthal or Orbital quantum number (<i>l</i>)	97
4.1.3 Magnetic quantum number (<i>m_l</i>).....	98
4.1.4 Spin quantum number (<i>m_s</i>)	99
4.2 Coupling types	100
4.2.1 Spin-spin coupling (S)	100
4.2.2 Orbit-orbit coupling (L)	101
4.2.3 Spin-orbit coupling (J)	103
4.3 Russell-Saunders (LS) coupling	103

4.4 jj coupling	104
4.5 Term symbols.....	105
• S.....	106
• L.....	106
• J.....	107
Term symbol for the ground state.....	107
4.6 Microstates.....	108
5. Ligand field theory.....	112
6. Band theory.....	118
7. Configurational coordinate model	122
References.....	124
Chapter 5	127
Preparation of ZnS:Mn²⁺ and SiO₂-ZnS:Mn²⁺ nano particle phosphors and structural and chemical analysis of these phosphors.	127
1. Introduction.....	127
2. Experimental.....	128
2.1 Preparation of ZnS:Mn ²⁺ nano particles	128
2.2 Preparation of SiO ₂ -ZnS:Mn ²⁺ nano particles	129
3. Results and discussions.....	130
3.1 Scanning electron microscopy (SEM) results.....	130
3.1.1 Commercially available ZnS:Mn ²⁺ phosphor powders.....	131
3.1.2 Synthesized ZnS and ZnS:Mn ²⁺	132
3.1.3 Synthesized SiO ₂ :ZnS.....	133
3.2 EDS results.....	138
3.3 TEM results.....	146
3.4 XRD results.....	149
4. Conclusion	157
References.....	159
Chapter 6	160
Luminescent properties of ZnS:Mn²⁺ and SiO₂-ZnS:Mn²⁺ nanoparticle phosphors.	160
1. Absorption.....	160

1.1 Synthesized ZnS.....	161
1.2 Commercial ZnS:Mn ²⁺	161
1.3 Synthesized ZnS:Mn ²⁺ (un-annealed).....	162
1.4 Synthesized ZnS:Mn ²⁺ (annealed)	163
1.5 Synthesized SiO ₂	164
1.6 Synthesized SiO ₂ :Mn ²⁺	165
1.7 Synthesized SiO ₂ :ZnS.....	166
1.8 Synthesized SiO ₂ -ZnS:Mn ²⁺ (un-annealed).....	167
1.9 Synthesized SiO ₂ -ZnS:Mn ²⁺ (annealed)	168
2. Band gap determination	169
2.1 Determination of the band gap of the commercial and synthesized samples.	169
2.1.1 Commercial ZnS:Mn ²⁺	169
2.1.2 Un-annealed ZnS	170
2.1.3 Annealed ZnS.....	171
2.1.4 Un-annealed ZnS:Mn ²⁺	172
2.1.5 Annealed ZnS:Mn ²⁺	174
3. Particle size	175
4. Photoluminescence	177
4.1 Commercial ZnS:Mn ²⁺	177
4.2 Synthesized ZnS.....	178
4.3 Synthesized ZnS:Mn ²⁺ (un-annealed)	179
4.4 Synthesized ZnS:Mn ²⁺ (annealed 600°C 2h).....	181
4.5 Synthesized SiO ₂	182
4.6 Synthesized SiO ₂ :ZnS.....	183
4.7 Synthesized SiO ₂ -ZnS:Mn ²⁺ (un-annealed).....	184
4.8 Synthesized SiO ₂ -ZnS:Mn ²⁺ (annealed 600°C 2h).....	185
5. Auger electron spectroscopy (AES) and cathodoluminescence (CL).....	186
5.1 Auger spectra	186
5.2 Residual gas analysis (RGA) spectra.....	188
5.3 Degradation of commercial ZnS:Mn ²⁺	191
6. Conclusion	194

References.....	196
Chapter 7	197
Luminescent mechanism of ZnS, ZnS:Mn²⁺ and ZnO.....	197
1. Luminescent mechanism of ZnS and ZnS:Mn ²⁺	197
1.1 Part 1.....	199
1.2 Part 2.....	200
1.3 Part 3.....	201
2. Luminescent mechanism of ZnO.....	204
3. Conclusion.....	205
References.....	206
Chapter 8	207
Conclusion and future work	207
1. Conclusion.....	207
2. Future work:.....	209
Appendix A.....	211
Publications.....	211
Conferences.....	212

Chapter 1

Introduction

1. Background

Nanotechnology is a field where phenomena on the atomic and molecular levels are used to provide structures and materials that can perform tasks that are not possible if the materials are used in their macroscopic form. Nanotechnology can provide a significant improvement in the optical, electrical, chemical, mechanical, etc. properties of materials [1,2]. Research in the different areas of nanotechnology is a rapidly growing field of science where the efforts of physicist, chemists, materials scientists, engineers and biological scientists have merged [3]. This interdisciplinary technology will provide a broad platform for medicine, industry and the overall economy [4]. This technology is expected to become one of the biggest driving forces in the research of material science in the 21st century [3].

Nanotechnology, much like information technologies, is expected to be embodied in many products. Within 10 years half of all new products could be using nanotechnology. Among the anticipated developments are improvements in computing, data storage and communications. It can provide renewable energy sources and water filters that can remove contaminants, salts and viruses. It can be used to treat cancer and other diseases. It can also offer protection to persons in hazardous environments, by monitoring the physiological vital signs of soldiers on the battle field and camouflage that matches the changing lighting conditions and background [4]. Most of the applications that are derived from nanomaterials are still in an early state of development and much work must still be done on this new field in science.

Nanotechnology is formally defined by the USA National Nanotechnology Initiative (USA-NNI) as: “Nanotechnology is the understanding and control of matter at dimensions between approximately 1 and 100 nanometers, where unique phenomena enable novel applications” [5]. A nanometer (nm) is equal to 1/1,000,000,000th or one-billionth of a meter (10^{-9} m). The diameter of a hair (Figure 1(a)) is $40\text{-}50 \times 10^{-6}$ m wide, while a virus is $30\text{-}50 \times 10^{-9}$ m

(Figure 1(b)), carbon nanotubes (~1 nm in diameter) and DNA (2.5 nm). In the nanoscale, common materials are exhibiting unusual properties. Some of these properties include lower melting points, faster chemical reactions and remarkably lower resistance to electricity. Another interesting property of nanomaterials is that their interaction with light differs from that of bulk. When the particle diameter is decreased the band gap (E_g) is blue-shifted due to the quantum confinement effect. CdSe quantum dot nanoparticles are an example of this phenomenon. Their emission color differs depending on their particle size (Figure 2). Nanoparticles also have a very large surface-to-volume ratio (Figure 3). This large fraction of surface atoms also contributes to the different properties displayed by these nanoparticles.

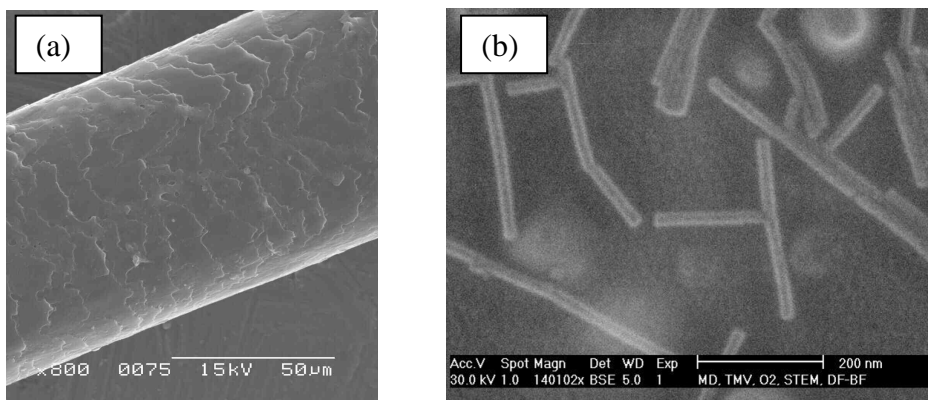


Figure 1: (a) SEM image of a human hair [6] and (b) SEM image of the Tobacco Mosaic Virus (TMV) [7].

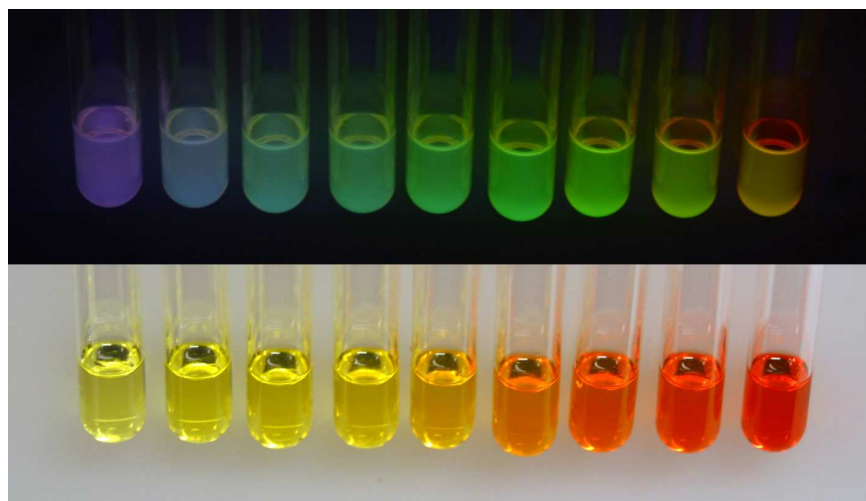


Figure 2: Top: Illumination with long wave UV and bottom: Ambient illumination. Solutions are shown in order of increasing particle size [8].

**Surface area increases while
total volume remains constant.**

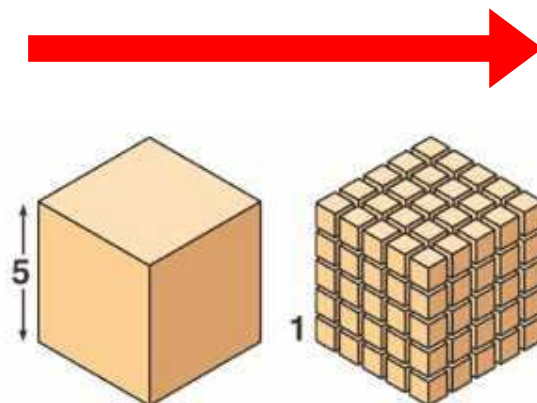


Figure 3: Schematic diagram of large surface-to-volume ratio [9].

The main focus of this study is on phosphors particles that are in the nano-scale. A phosphor can be defined as any material that will emit light when an external excitation source is applied. This source can include photons, electrons, heat etc. These phosphors may either be in the powder or thin film form. The phosphor materials are doped intentionally with certain impurities to get the desired wavelength. These phosphor powders and thin films are critical in the development and also in the improvement of display technologies. Smaller size phosphor particles are needed for high-resolution images. There is therefore a desire for the production and development of phosphor nano particles with stronger emission intensities. Phosphor particles that have submicrometer size, narrow particle distribution and spherical morphology give higher particle packing densities than commercial products (3-5 μm in size) and are therefore effective in the enhancement of luminescence efficiency [10].

ZnS is a wide band gap semiconductor with its band gap at 340 nm (3.66 eV) [11]. ZnS shows emission at 420 nm with excitation at 325 nm. When ZnS is doped with Mn^{2+} two emission peaks at 420 nm and 590 nm are observed. The blue emission peak at 420 nm corresponds to emission from the host, while the yellow-orange peak at 590 nm corresponds to the ${}^4\text{T}_1\text{-}{}^6\text{A}_1$ transition of Mn^{2+} [12]. Doped semiconductor nanocrystals are regarded as new types of luminescent materials. They have a wide range of applications in displays, laser devices, sensors, nonlinear optical devices and electronic devices, etc [12]. ZnS has many applications including

efficient phosphors in flat-panel displays, photovoltaic devices, UV light emitting diodes, etc. Mn^{2+} doped ZnS nanoparticles have potential applications in field emission devices (FED) [13].

Generally, when the mean particle size of phosphors is smaller than 1-2 μm , there is a drop in their luminescence efficiency. This is due to the fact that surface defects become more important with decreasing particle size and an increase in the surface area. This can often lead to the reduction of the emission intensity [10]. However, the emission intensity of the $\text{Y}_2\text{O}_3:\text{Eu}^{3+}$ phosphor was increased by decreasing the particle size from 6 μm to 10 nm [10]. Yang et al [14] also reported that when CdS:Mn is capped with ZnS it results in better photostability of the nanoparticles. Capping of ZnS: Mn^{2+} nanoparticle phosphors with SiO_2 was therefore applied to minimize the surface effects and to improve the luminescent properties of these phosphors.

2. Problem statement

Phosphors with enhanced or new properties are needed for the development of new types of high efficiency and high resolution displays. Monodispersed crystalline fine particles of high efficiency phosphor materials are the keys to the development of these devices. Phosphors must have narrow size distribution, fine size, spherical morphology particles and nonaggregation to display good luminescent characteristics [15]. Yang et al [14] reported that submicron particle sizes are required for high definition displays to maximize screen resolution and luminescence efficiency. The commercial processes that are currently in use to manufacture phosphors are controlling the particle sizes by mechanical milling. This results in particles that are in the order of 2 μm . Nanoparticles, with sizes between 2 and 100 nm, can be synthesized to fulfill the size requirement without mechanical milling of the powders. These nano-sized phosphors are displaying interesting properties such as ultra-fast recombination time, an increase in the band gap due to the decrease in particle size and high quantum efficiency for photoluminescence [16].

ZnS is of considerable interest as a phosphor for luminescent displays [13]. It has a wide band gap of 3.66 eV and a small Bohr radius of 2.5 nm. This makes it a good phosphor for display devices and development of this phosphor can have a huge impact on the technology of the future. Band gap determination of nanoparticle ZnS and photoluminescence (PL) studies will be

performed on the nanoparticle powder phosphors. The luminescent properties are compared for applications in FEDs and other display devices.

Nanoparticles are modified with silica because it plays a significant role in the quantum confinement effect, surface passivation and control over particle size [17]. When nanoparticles are embedded into dielectric materials such as glasses and ceramics, the individual particles are isolated by the dielectric material offering better and stable quantum confinement. The luminescence efficiency will also be increased by the surface modification as it provides capping of undesired sites that are detrimental to luminescence intensity [18]. For appropriate fabrication processes and applications, the importance of chemical stability in ZnS nanoparticles is vital. ZnS is easily converted into ZnO during annealing in air. Even when there are only traces of oxygen present, the surface of the ZnS will be converted into a ZnO layer which will reduce the luminescence intensity significantly. When SiO₂ is applied as a protective layer on the surface of ZnS it could isolate the surface and enhance the chemical stability to avoid the conversion of ZnS into ZnO at high temperatures [17]. SiO₂:ZnS is also reported to be more stable against electron bombardment than uncoated ZnS [19].

3. Aim of this study

1. To synthesize ZnS:Mn²⁺ nanoparticle phosphors using an inorganic method and to embed these phosphors in a SiO₂ matrix using the sol-gel technique.
2. Determining the morphology of the samples with Scanning Electron Microscopy (SEM) and Transmission Electron Microscopy (TEM).
3. To determine the chemical composition of the samples by Energy Dispersive X-Ray analysis (EDS).
4. Determining the crystal structure and particle size with X-Ray Diffraction (XRD) and Transmission Electron Microscopy (TEM).
5. Measuring the absorption and transmittance of the samples and determining the band gap and particle sizes from this data.
6. To study the photoluminescence (PL) properties of ZnS:Mn²⁺ and to evaluate the effects of annealing and the capping with SiO₂ on the PL intensity of the samples.

7. To investigate the cathodoluminescence (CL) degradation of commercial ZnS:Mn²⁺ phosphor powders.
8. To formulate a luminescent mechanism for the emission of ZnS, ZnS:Mn²⁺ and ZnO.

4. Layout of the thesis

Chapter 1 presents the introduction and aim of this study. It is followed by the history and theory of luminescence and phosphors in *chapter 2*. A brief description of the different applications of phosphors is also included. A summary of the different characterization techniques are given in *chapter 3*. This includes a description of the operation of each of the techniques. *Chapter 4* describes the theory that is involved in the luminescent mechanism of ZnS and ZnS:Mn²⁺. It contains the description of the Russell Saunders coupling scheme, the Tanabe-Sugano diagrams for a d⁵ ion and the ligand field theory. The synthesis methods and the structural and chemical analysis of the phosphor samples by SEM, EDS, TEM and XRD are given in *chapter 5*. *Chapter 6* describes the luminescent properties of the samples. This includes the absorption and transmittance data of the different samples as well as their respective band gaps and particle sizes. It shows the PL spectra of the different samples and the effect of annealing and SiO₂ capping on the luminescence intensity. The CL spectrum of commercial ZnS:Mn²⁺ is discussed as well as the degradation of this phosphor and the effect of the electron stimulated surface chemical reaction (ESSCR) mechanism. *Chapter 7* gives the luminescent mechanism of ZnS, ZnS:Mn²⁺ and ZnO. It shows how it corresponds to the PL spectra that were obtained from different samples. In *chapter 8* a summary of the thesis as well as future work are presented.

References

1. A.K. Rana, S.B. Rana, A. Kumari and V. Kiran, *International Journal of Recent Trends in Engineering*, **1** (4) (2009) 46.
2. K.P. Chong, *J. Physics and Chemistry of Solids*, **65** (2004) 1501.
3. A.L. Rogach, A. Eychmuller, S.G. Hickey and S.V. Kershaw, *Reviews; Infrared emission*, www.small-journal.com, **3** (4) (2007) 536.
4. M.C. Roco and W.S. Bainbridge, *Social Implications of Nanoscience and Nanotechnology*, (Springer, Boston) 2001, 1 - 2.
5. What is nanotechnology?, [online]. Available from <http://mrsec.wisc.edu/Edetc/nanotech/index.html> [Accessed 11 September 2009].
6. Biological Images, [online]. Available from <http://www.semguy.com/gallery.html> [Accessed 11 September 2009].
7. Virus, [online]. Available from <http://www.mardre.com/homepage/mic/tem/samples/bio/virus/tmv3.htm> [Accessed 11 September 2009].
8. Quantum Dots & Nanoparticles, [online]. Available from http://mrsec.wisc.edu/Edetc/background/quantum_dots/index.html [Accessed 11 September 2009].
9. Cell Structure and Function: Organelles, [online]. Available from http://fajerpc.magnet.fsu.edu/Education/2010/Lectures/13_Cell_Structure.htm [Accessed 11 September 2009].
10. T. Hirai, Y. Asada and I. Komasaawa, *J. Colloid Interface Sci.* **276** (2004) 339.
11. D.R. Lide, *Handbook of Chemistry and Physics*, 74th ed., CRC Press, Boca Raton, FL, 1994.
12. R. Sarkar, C.S. Tiwary, P. Kumbhakar, S. Basu and A.K. Mitra, *Physica E* **40** (2008) 3115, 3119.
13. B.S. Rema Devi, R. Raveendran and A.V. Vaidyan, *Pramana – J. Phys.* **68** (4) (2007) 679.
14. H. Yang, S. Santra and P.H. Holloway, *J. Chem. Phys.* **121** (2004) 7421.
15. L. Sun, C. Qian, C. Liao, X. Wang and C. Yan, *Solid State Communications* **119** (2001) 393.
16. M.S. Dhlamini, PhD Thesis, University of the Free State, South Africa (2008) p4-5.
17. Z. Li, W. Shen, L. Fang and X. Zu, *J. Alloys Compd.* (2007), doi: 10.1016/j.jallcom.2007.09.075.

18. B. Bhattecharjee, D. Ganguli, S. Chaudhuri and A.K. Pal. *Thin Solid Films*, **422** (2002) 98.
19. Y.R. Do, D.H. Park, H.G. Wang, W. Park, B.K. Wagner, K. Yasuda and C.J. Summers, J. *Electrochem. Soc.* **148** (2001) G548.

Chapter 2

Background information and applications of phosphors.

In this chapter background information about phosphors and their properties is given. The chapter starts with the history of phosphors and also gives the terminology involved in phosphors. A description of cathode ray tubes (CRTs), liquid crystal displays (LCDs) and field emission displays (FEDs) devices is given. The theory of luminescence and the background of the ZnS and ZnS:Mn²⁺ phosphor are discussed. The chapter concludes with the different applications of phosphors.

1. History of phosphors

The word *phosphor* was first invented in the early 17th century and until today its meaning is unchanged. Vincenzo Casciarolo of Bologna, Italy, found a heavy crystalline stone (Figure 1) with a gloss at the foot of the volcano Monte Paderno. Casciarolo was an alchemist interested in the transformation of humbler materials into gold. He thought the stone, that he called “solar”, was most suitable for the production of gold by virtue of its notable weight and content of sulphur. He fired the stone in a charcoal oven (Figure 2) intending to convert it into a noble metal, but no metals were found. Instead he found that the sintered stone was emitting red light in the dark after exposure to sunlight. The stone was called the “Bolognian Stone” or “Litheophosphorus” and it became the first object of scientific study of the luminescent phenomena. From what is now known as the Bolognian Stone appears to have been barite (BaSO₄), with the fired product being BaS, which is a host for phosphor materials. Similar findings were reported from many places in Europe after the first discovery, and these light emitting stones were called *phosphors* [1, 2].



Figure 1: A piece of Bolognian Stone, BaSO_4 (barite), with a maximum diameter of about 12 cm, found on Monte Paderno, Bologna. Part of the private collection of Aldo Roda [2].



Figure 2: An illustration showing the magic-alchemic phenomenon of the emission of light (phosphorescence) achieved by calcination of the Bolognian Stone [2].

The credit for preparing the first phosphor should however go to the Japanese. It is reported that they have prepared phosphorescent paint from seashells. A 10th century Chinese document (Song dynasty) describes this fact. It is concerning a painting of the Emperor Tai Zong (976 - 998). In his book: *A History of Luminescence* [3], Harvey cites a story of an interesting painting that was presented to the second emperor of the Song dynasty. The painting showed a cow that appeared

during the day as eating grass outside a pen, but at night as resting within the pen. When it was shown to the court, none of the officials could offer any interpretation for the phenomenon. The monk Zan Ning, however, said that the ink (or colour) that appeared only at night was mixed with drops from a (special kind of) pearl shell and the ink (or colour) that appeared only during the day was made by grinding a rock that had fallen from a volcano to the seashore. The monk claimed that the information about the ink come from a book by Zhang Xian. Figure 3 shows the record of the cow's painting. Harvey gives comments that the story of the luminous cow should be given little serious consideration because nothing is known of any book left by the explorer Zhang Xian. Also, the author of the book *Xiang-Shan Ye-Lu*, Wen Ying who lived in the 11th century, was not noted for his veracity. It seems however certain that the Japanese and Chinese knew of luminescent paint more than 1000 years ago and that the paint had some relationship with material found from a volcano and seashells. It is well known that sulphur that was obtained from a volcano was one of the representative exports from Japan to China at that time. In 1768 John Canton from Europe prepared a phosphor from oyster shells that had reacted with sulphur [1, 4].

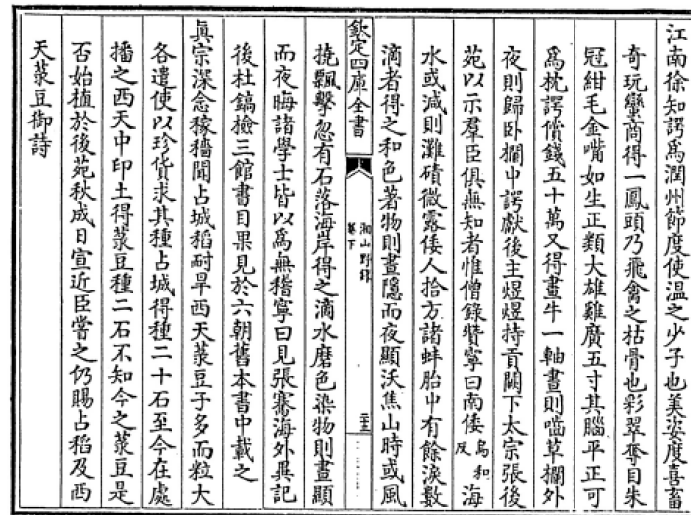


Figure 3: A note concerning a luminous paint in the Chinese book *Xiang-Shan Ye-Lu* [1].

2. Definition and terminology

The word *phosphor* means “light bearer” in Greek and it appears in the Greek myths as the personification of the morning star Venus [1]. A phosphor is any substance capable of absorbing energy and re-emitting it in the form of visible light [5]. The word *phosphorescence*, which means persisting light emission from a substance after the exciting radiation has ceased, was derived from the word *phosphor*. The word *fluorescence* refers to the light emission from a substance during the time when it is exposed to exciting radiation [1].

3. Physical processes taking place during luminescence.

Luminescence is defined as the phenomenon in which the electronic state of a substance is excited by some kind of external energy and the excitation energy is given off in the form of light. The word light not only includes electromagnetic waves in the visible region of 400 to 700 nm, but also those in the neighbouring region on both ends, i.e. the near ultra-violet and the near-infrared regions (Figure 4) [1]. Luminescence is divided into fluorescence and phosphorescence according to the duration time of the after-glow.

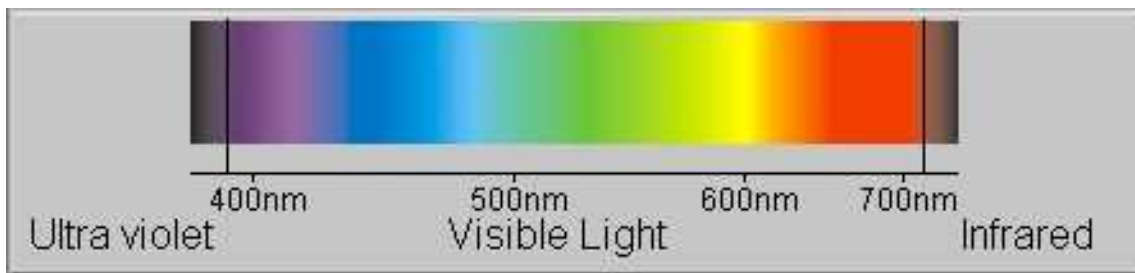


Figure 4: The spectrum of visible light [6].

3.1 Fluorescence

When a molecule absorbs UV radiation it gets excited from a vibrational level in the electronic ground state to one of the many vibrational levels in the electronic excited state. This excited state is usually the first excited singlet state (Figure 5). Once a molecule arrives at the lowest vibrational level of an excited singlet state, it can do a number of things, one of which is to return to the ground state by photon emission. This process is called fluorescence. The lifetime of an

excited singlet state is approximately 10^{-9} to 10^{-7} seconds and therefore the decay time of fluorescence is of the same order of magnitude [7].

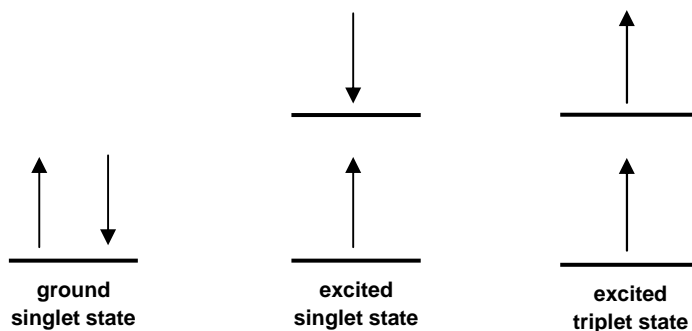


Figure 5: The ground and excited state of a molecule [8].

3.2 Phosphorescence

Phosphorescence results when a molecule gets excited to the triplet state (Figure 5). It loses energy by emission of a photon. A radiative transition between the lowest triplet state and the ground state takes place and this type of emission is called phosphorescence. As phosphorescence originates from the lowest triplet state, it will have a decay time approximately equal to the lifetime of the triplet state. This lifetime is approximately 10^{-4} to 10 seconds. Phosphorescence is therefore often characterized by an afterglow that is not observed for fluorescence.

3.3 Radiationless transitions

A molecule can also undergo some radiationless transitions. These processes are called the radiationless transfer of energy. These processes are explained in Figure 6. There are three processes that can occur, namely vibrational relaxation, intersystem crossing and internal conversion. When a molecule returns to the electronic ground state non-radiatively, the excess energy is converted to vibrational energy (*internal conversion*) and the molecule is placed in an extremely high vibrational level of the electronic ground state. The excess vibrational energy is lost by collision with other molecules (*vibrational relaxation*). The spin of an excited electron can be reversed and this leaves the molecule in an excited triplet state. This is then called *intersystem crossing*. The triplet state is in a lower electronic energy than that of the excited

singlet state. The probability that this will happen is increased if the vibrational levels of these two states overlap.

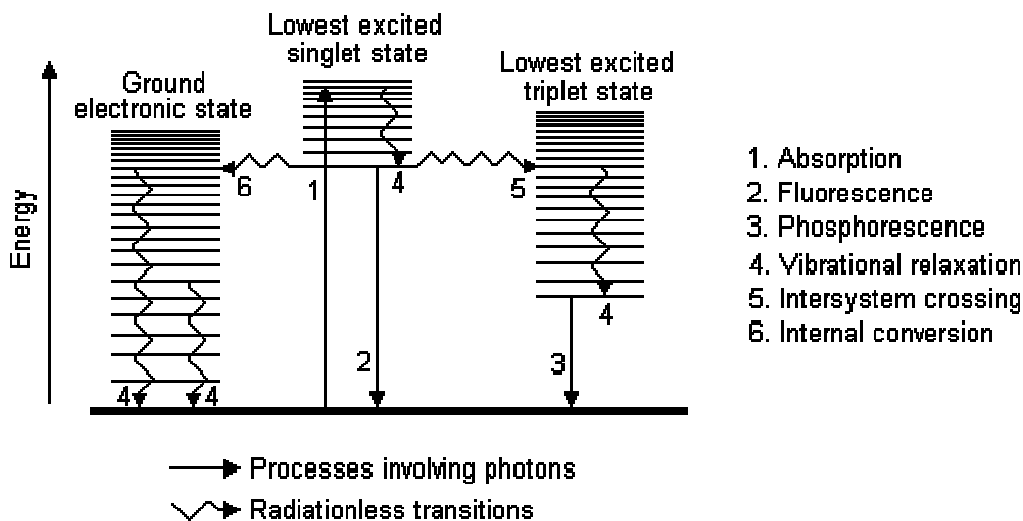


Figure 6: Possible physical processes following the absorption of a photon by a molecule [8].

4. Types of light emission

Light is a form of energy. Another form of energy must be supplied in order to create light. There are two common ways for this to occur, incandescence and luminescence.

4.1 Incandescence

Incandescence is light coming from heat energy. Something will begin to glow when you heat it to a high enough energy. When metal heated in a flame or an electric stoves heater begins to glow “red hot”, that is incandescence. When the tungsten filament of an ordinary incandescence light bulb is heated still hotter, it glows brightly “white hot” by the same means. The sun and stars glow by incandescence [9]. The different types of incandescence are shown in Figure 7.



Figure 7: Different types of incandescence [10, 11, 12].

4.2 Luminescence

Luminescence is the so called “cold light”, light coming from other sources of energy, which can take place at normal and lower temperatures. In luminescence, some energy source kicks an electron of an atom out of its ground or lowest energy state into an excited or higher energy state. The electron then gives back the energy in the form of light so it can fall back to its ground state.

There are several varieties of luminescence, each named according to what the source of energy is, or what the trigger for the luminescence is [9].

4.2.1 Fluorescence

Fluorescence is a luminescence mostly found as an optical phenomenon in cold bodies, in which the molecular absorption of a photon triggers the emission of a photon with a longer (less energetic) wavelength. The energy difference between the absorbed and emitted photons ends up as vibrations, heat or molecular rotations. Sometimes the absorbed photon is in the ultraviolet range and the emitted light is in the visible range [13]. Fluorescence is seen in fluorescent lights, amusement park and movie special effects, and the redness of rubies in sunlight, “day-glo or neon” colours and in emission nebulae seen with telescopes in the night sky. Bleaches enhance their whitening power with the addition of a white fluorescent material. Figure 8 shows different types of fluorescence.

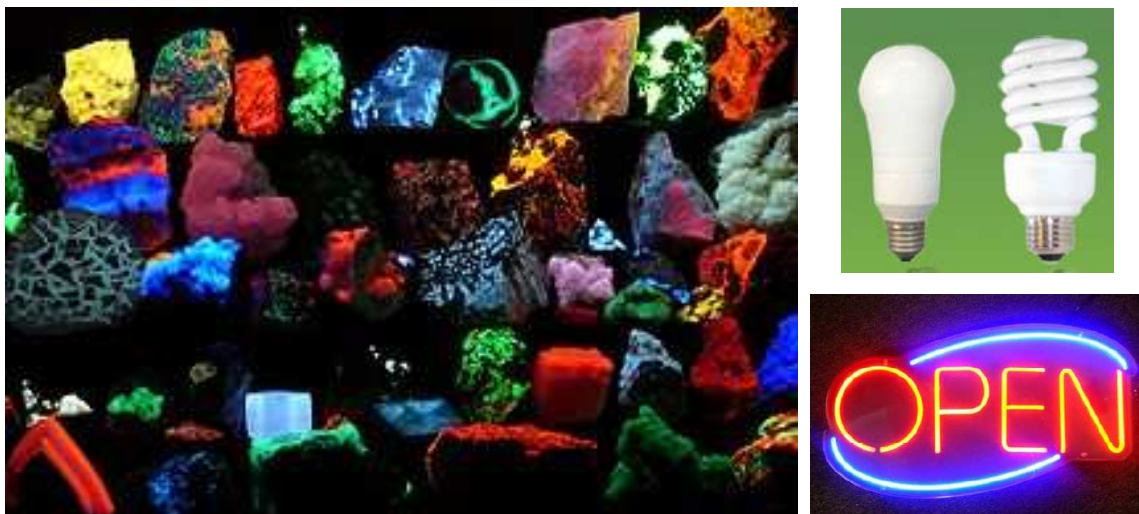


Figure 8: Different fluorescent materials including fluorescent minerals [13], fluorescent bulbs [14] and a neon sign [15].

4.2.2 Phosphorescence

Phosphorescence is a specific type of photoluminescence that is related to fluorescence. Unlike fluorescence, the absorbed radiation is not immediately re-emitted in a phosphorescent material. The slower time scales associated with the re-emission are due to forbidden energy state transitions in quantum mechanics. Because these transitions occur less often in certain materials, absorbed radiation can be re-emitted at a lower intensity for up to several hours. In simple terms, phosphorescence is a process in which energy absorbed by a substance is released slowly in the form of light. In some cases this is the mechanism used for “glow-in-the-dark” materials which are “charged” when exposed to light. The phosphorescent materials that are used for these materials absorb the energy and then “store” it for a longer time as the processes required to re-emit the light occur less often [16]. Figure 9 shows different types of phosphorescent materials.

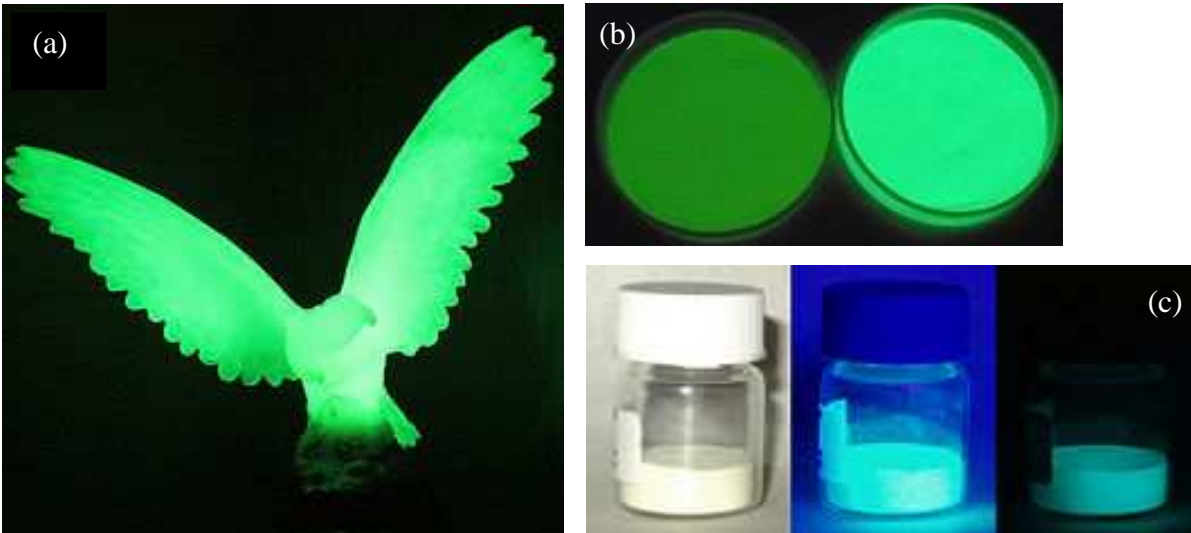


Figure 9: Different types of phosphorescence. (a) A “glow-in-the-dark” statue of an eagle, (b) aluminate phosphorescent pigments in the dark and (c) phosphorescent powder under visible light, ultraviolet light and total darkness [16].

4.2.3 Electroluminescence

Electroluminescence is an electrical and optical phenomenon where a material will emit light in response to a strong electric field, or to an electric current that is passed through it. It is the result of the radiative recombination of electrons and holes in a material (usually a semiconductor). The excited electrons will release their energy as photons (light). Prior to recombination, the holes and electrons are separated. This can either be a result of doping of the material to form a p-n junction (as in semiconductor electroluminescent devices such as LEDs), or through excitation by the impact of high-energy electrons that is accelerated by a strong electric field (as with the phosphors in electroluminescent displays). Some examples of electroluminescent materials include powder ZnS doped with Cu or Ag, thin film ZnS doped with Mn, natural blue diamond (diamond with boron as dopant), III-V semiconductors such as InP, GaAs and GaN and inorganic semiconductors such as $[\text{Ru}(\text{bpy})_3]^{2+}(\text{PF}_6^-)_2$, where bpy is 2,2'-bipyridine. The backlights used in liquid crystal displays are powder phosphor-based electroluminescent panels. These panels provide a gentle, even illumination to the entire display while they are consuming relatively little power. This makes them convenient for battery-operated devices such as

wristwatches, computer controlled thermostats and pagers. Their gentle green-cyan glow seen everywhere in the technological world [17]. Figure 10 shows different LCD devices.



Figure 10: Different LCD devices [18, 19, 20].

4.2.4 Bioluminescence

Bioluminescence is defined as the production and emission of light by a living organism resulting from a chemical reaction during which chemical energy is converted into light energy. Its name is a hybrid word, originating from the Latin *lumen* “light” and the Greek *bios* for “living”. In most instances adenosine triphosphate (ATP) is involved. The chemical reaction that takes place can occur either inside or outside the cell. Bioluminescence occurs in marine vertebrates and invertebrates, as well as micro organisms and terrestrial animals. Ninety percent of deep-sea marine life is estimated to produce bioluminescence in some form. Most light-emission by marine life belongs in the green and blue light spectrum but some species emit red, infrared and even yellow bioluminescence. Land bioluminescence is less widely distributed, but they display a larger variety of colours. The best-known forms of land bioluminescence are fireflies and glow worms. Other insects, insect larvae, annelids, arachnids and even species of fungi have been noted to possess bioluminescent abilities [21]. Figure 11 and Figure 12 show forms of marine and land bioluminescence.

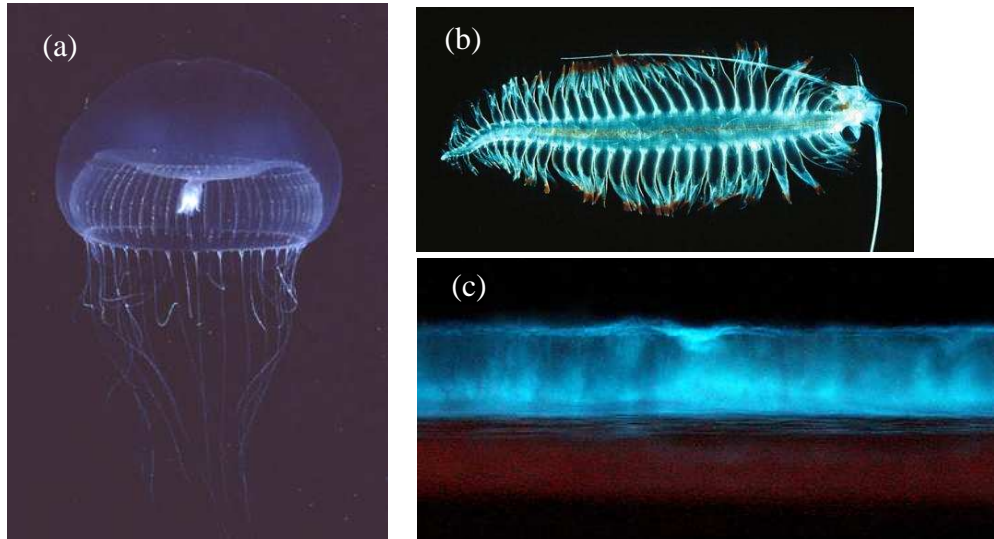


Figure 11: Marine bioluminescence. (a) *Aequorea Victoria* is a bioluminescent jellyfish [22], (b) *Tomopteris* is a genus of marine *planktonic polychaetes*. These species emit light when disturbed [23] and (c) Image of bioluminescent red tide event of 2005 at a beach in Carlsbad California showing brilliantly glowing crashing waves containing billions of *Lingulodinium polyedrum* dinoflagellates. [21].

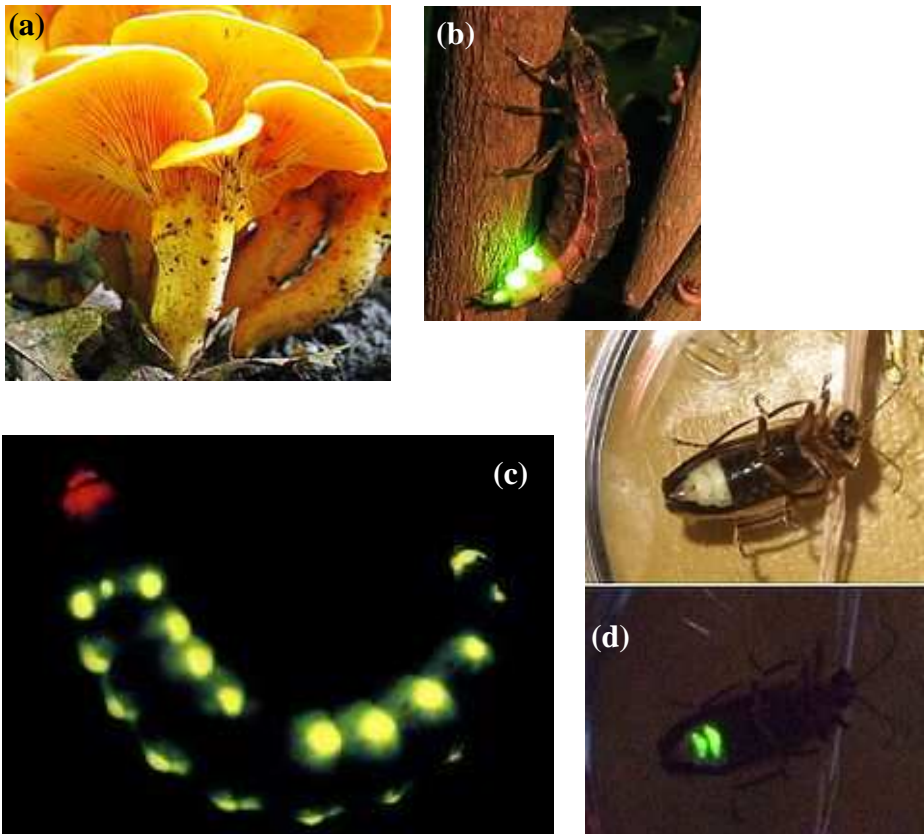
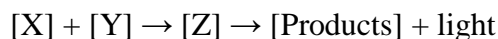


Figure 12: Land bioluminescence: (a) Jack o'lantern mushroom is an orange to red gill mushroom notable for its bioluminescent properties. It is very poisonous [24], (b) Female of *Lampyris noctiluca* [21], (c) the railroad worm (*Phrixothrix*) is quite distinct for having two different colours of luminescent organs. Like a tiny insect Christmas tree, their head glows red, while their body glows green [22] and (d) Firefly (species unknown) with and without flash [21].

4.2.5 Chemiluminescence

Chemiluminescence (also called chemoluminescence) is the emission of light (luminescence) together with a limited emission of heat, resulting from a chemical reaction. Given reactants X and Y, with an excited intermediate Z,



For example, if [X] is luminol and [Y] is hydrogen peroxide in the presence of a suitable catalyst we have:



where 3-APA is 3-aminophthalate and 3-APA[Z] is the excited state fluorescing as it decays to a lower energy level. The decay of the excited state [Z] to a lower energy level is responsible for the emission of light. In theory, one photon of light should be given off for each molecule of reactant, or in other words Avogadro's number of photons per mole. In actual practice, non-enzymatic reactions seldom exceed 1% quantum efficiency. An example of chemiluminescence is the luminol test, where forensic investigators use luminol to detect trace elements of blood left at a crime scene, as it reacts with the iron found in haemoglobin (Figure 13). When chemiluminescence takes place in living organisms, it is called bioluminescence. A light stick emits a form of light by chemiluminescence [25] (Figure 13).



Figure 13: Different types of chemiluminescence: light sticks [26, 27] and a luminol test done on a bloody shoe print [28].

4.2.6 Thermoluminescence

Thermoluminescence is also a form of luminescence. Absorbed light is re-emitted upon heating. Some minerals such as fluorite store energy when exposed to ultraviolet radiation. This energy is released in the form of light when the mineral is heated (Figure 14). The received radiation will be directly proportional to the amount of light that will be given off. Buried objects (e.g. pottery) that have been heated in the past can be dated by thermoluminescence dating, since the dose received from radioactive elements in the soil, cosmic rays etc is proportional to age (Figure 15). Thermoluminescent dosimeters make use of this phenomenon. The radiation dose received by a chip of suitable material that is carried around by a person or placed with an object can be measured in this way [29].



Figure 14: Chlorophane exhibiting thermoluminescence when heated [30].



Figure 15: Thermoluminescence dating can determine the age of antiquities [31].

4.2.7 Other types of luminescence [32]

- Electrochemiluminescence – luminescence by an electrochemical reaction.
- Crystalloluminescence – luminescence produced during crystallization.
- Cathodoluminescence – where a beam of electrons impacts on a luminescent material such as a phosphor.
- Mechanoluminescence – luminescence resulting from any mechanical action on a solid.
 - Triboluminescence – luminescence generated when bonds in a material are broken when that material is scratched, crushed or rubbed.
 - Fractoluminescence – luminescence generated when bonds in certain crystals are broken by fractures.
 - Piezoluminescence – luminescence produced by the action of pressure on certain solids.
- Radioluminescence – luminescence produced in a material by the bombardment of ionising radiation.
- Sonoluminescence – luminescence from imploding bubbles in a liquid when excited by sound.

Figure 16 shows the different types of other luminescence.

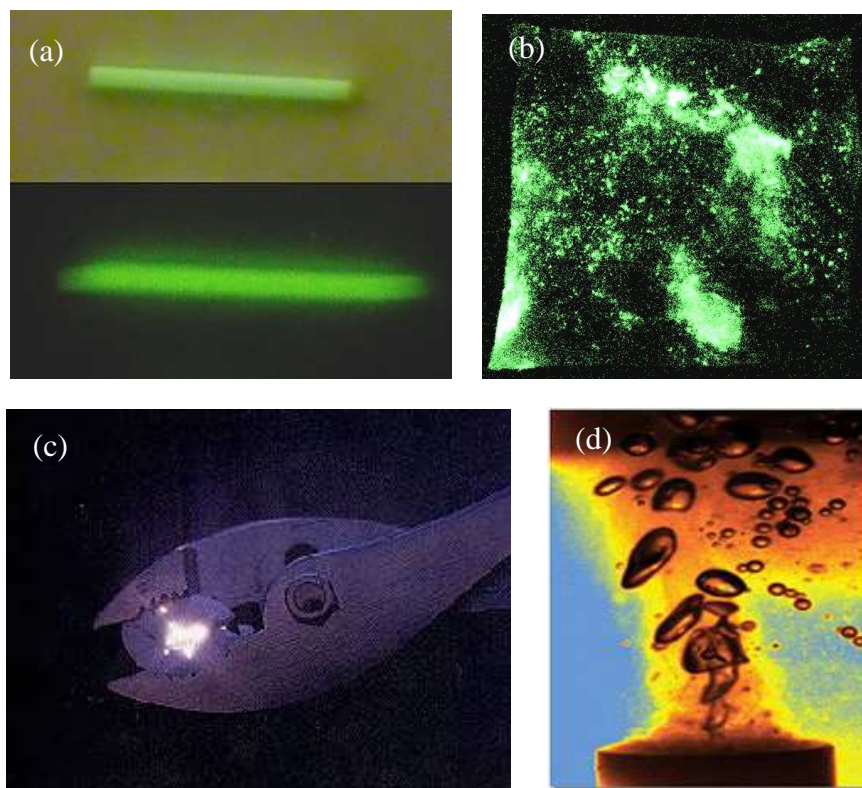


Figure 16: Different types of luminescence: (a) radioluminescence - a gaseous tritium light source [33], (b) mechanoluminescence - N-acetylanthranilic acid crystals crushed between two transparent windows [34], (c) triboluminescence – wintergreen lifesaver candy are generating light during chewing because the chemical bonds are tear apart [35] and (d) sonoluminescence – light emitted from collapsing gas bubbles in a liquid generated by ultrasound [36].

5. Applications of phosphors

The applications of phosphors can be classified as: (1) light sources represented by fluorescent lamps; (2) display devices represented by cathode ray tubes, flat panel displays and field emission displays; (3) detector systems represented by x-ray screens and scintillators; and (4) other simple applications, such as luminous paints with long persistent phosphorescence [1].

5.1 Fluorescent lamps

Phosphors make the fluorescent lamp work. A fluorescent lamp is a very efficient generator of ultraviolet energy at a wavelength of mostly 254 nm and sometimes at 185 nm. The fluorescent lamp phosphors will absorb the ultraviolet radiation and they will convert it into visible light. In the lamp industry when there is referred to the term “light” it also includes the near infrared and ultraviolet regions. A very fine powder form of the phosphor is applied as a uniform coating onto the inside surface of the lamp tube (Figure 17), resulting in a very effective light source.

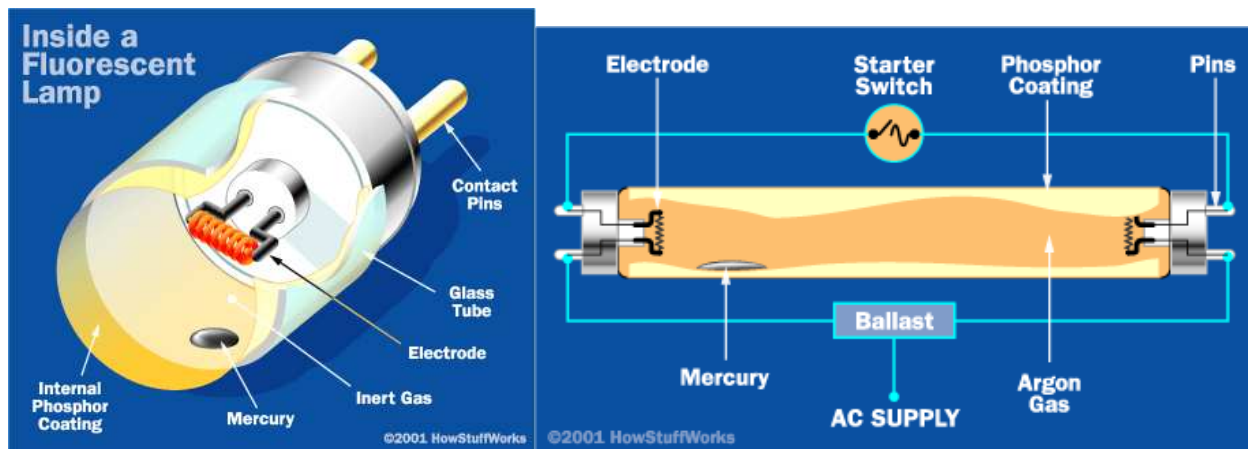


Figure 17: The inside of a fluorescent lamp [37].

The phosphor used for coating must be a powder to simplify the application to the inside of the tube. The phosphor powder is made into a paint that is then applied to the top inside of the vertical lamp tube and drained in a manner so as to form a very uniform coating. The phosphor coating is then dried and heated to near the melting point of the glass. This is done to burn off the organic components of the paint. To improve the adhesive properties of the phosphors binders, usually borates or very fine aluminium oxide may be added to the paint. It also prevents chipping of the coating. Table 1 shows some of the phosphors used in fluorescent lamps. These available phosphors can be blended to produce white light. Calcium halophosphate is the dominant phosphor in the lamp industry [5].

Table 1: Some phosphors used in fluorescent lamps.

Name	Formula	Activator	Emission Colour
Zinc Silicate	Zn_2SiO_4	Mn	Green
Zinc Beryllium Silicate	$(Zn, Be)_2SiO_4$	Mn	Orange
Cadmium Silicate	$CaO:SiO_2$	Pb, Mn	Salmon
Cadmium Borate	$CdO:B_2O_3$	Mn	Pink
Calcium Tungstate	$CaWO_4$	Pb	Blue
Magnesium Tungstate	$MgWO_4$	Self	Blue
Calcium Halophosphate	$Ca_{10}(PO_4)_6(F,Cl)_2$	Sb, Mn	White

5.2 Display devices

Emissive displays are electronic devices that involve the conversion of electrical energy to luminous energy as a function of the real image signal. These emissive displays can be converted into three major categories, namely projection, off-screen and direct-view. A projection display is an electronic device that utilizes a viewing screen that is separate from the optical source. An off-screen display is a device where the image is not viewed on a screen. A direct-view display is a device where the image is generated in the immediate proximity of the viewing screen. Direct view displays are classified into cathode ray tubes (CRTs) and flat panel displays (FPDs) [16]. CRTs have been the dominant display technology for many years, but the need for lower power consumption and portability opened the door for new technology.

5.2.1 Cathode ray tubes (CRTs)

A CRT consists out of a vacuum tube containing an electron gun (cathode) and a phosphor coated screen (Figure 18). The cathode is a heated filament and is the source of the electron beam. Electrons pour off the filament and into the vacuum where they get attracted by an anode. The electrons are then focussed and accelerated toward the screen by a focussing and

accelerating anode. Copper windings are wrapped around the tube and they act as steering coils. These coils create magnetic fields inside the tube and these magnetic fields steers the beam toward the screen. By varying the voltages in the coils, the electron beam can be positioned at any point on the screen. When the electron beam strikes the phosphor coated screen, a tiny bright visible spot is created on the screen. An image is formed when the beam is rastered across the screen. Colour CRTs have three electron guns, one for each primary colour. CRTs are used in oscilloscopes, television and computer monitors and radar targets. Typical values of cathode to anode distance range between 25 to 100 cm. CRTs are very bulky and when bigger screens are required the length of the tube must increase [39, 40].

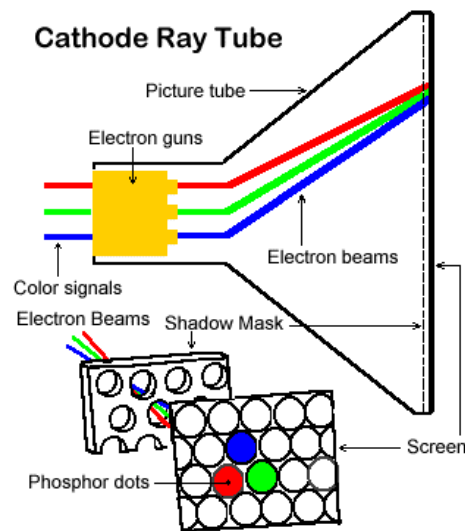


Figure 18: The basic components of a CRT used in televisions and computers [41].

5.2.2 Flat panel displays (FPDs)

Flat panel displays encompass a growing number of technologies enabling video displays that are much thinner and lighter than traditional television and video displays that use cathode ray tubes. They are usually less than 100 mm thick. FPDs require a small amount of power to accelerate the electrons from the cathode to the anode. They are defined as ideal displays because they are thin, have an even surface and low volume, a high resolution and contrast and are lightweight. They are used in many modern portable devices such as laptops, cellular phones and digital cameras [42].

Some examples of FPDs are:

- Plasma display panels (PDPs)
- Liquid crystal displays (LCDs)
- Organic light-emitting diode displays (OLEDs)
- Light-emitting diode display (LED)
- Electroluminescent displays (ELDs)
- Surface-conduction electron-emitter displays (SEDs)
- Field emission displays (FEDs) (also called Nano-emissive displays (NEDs))

Figure 19 – Figure 21 show some of the FPDs that are available.

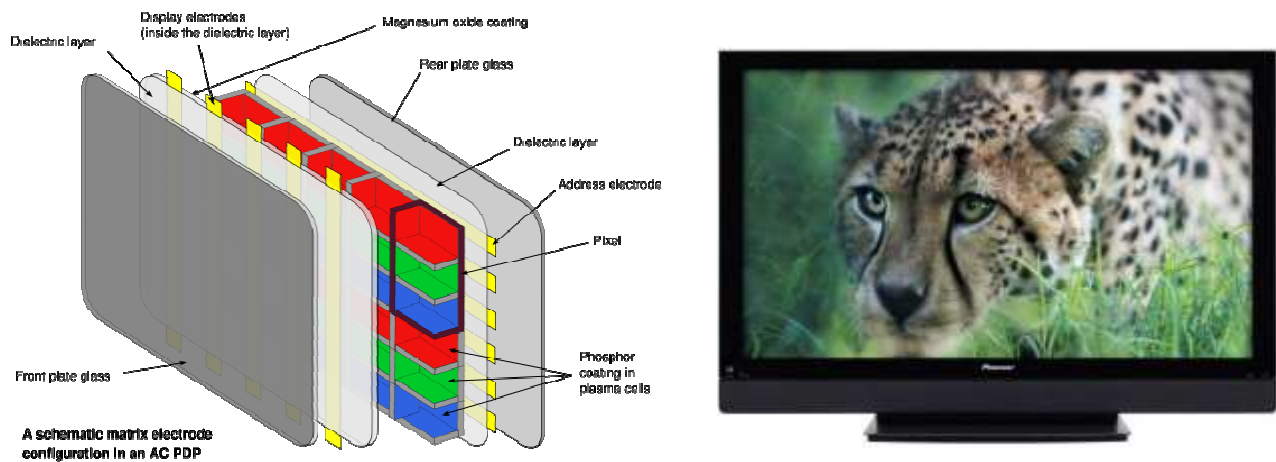


Figure 19: Schematic diagram of a plasma display and a plasma television [43].

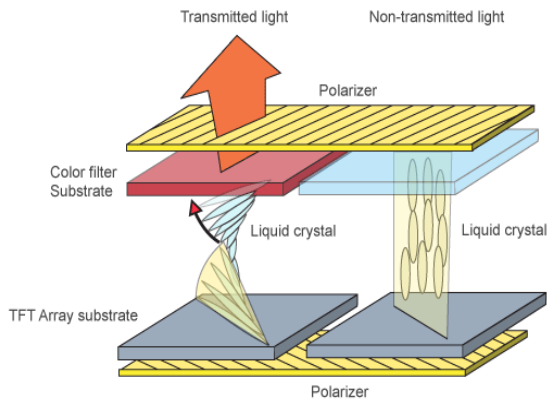


Figure 20: Schematic diagram of a LCD display [44] and a LCD television [45].

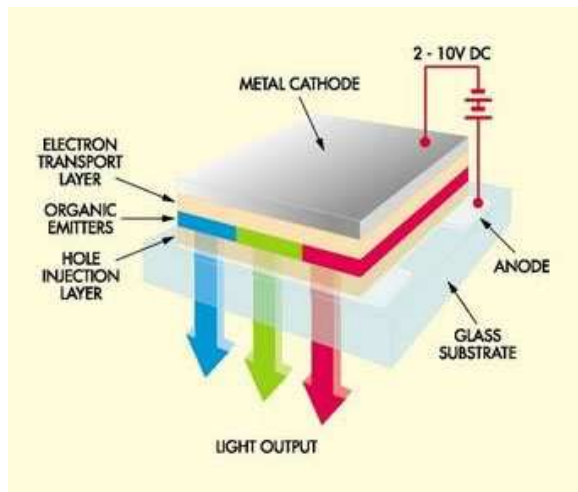


Figure 21: Schematic diagram of an OLED display [46] and an OLED television [47].

5.2.3 Field emission displays (FEDs)

Some believe field emission display (FED) technology will be the biggest threat to LCD's dominance in the emissive panel display arena. It has a low cost of manufacturing and is generally energy efficient since they are electrostatic devices that require no heat or energy when they are off. They have superior optical characteristics and won't age like current OLEDs. It has the emissive capabilities of CRTs while it is keeping perfect focus since it's a fixed pixel display like and LCD. FEDs is capitalising on the well-established cathode-anode-phosphor technology built into CRTs and is using this in combination with the dot matrix cellular construction of

LCDs. FEDs are using tiny "mini tubes" for each pixel, instead of using a single bulky tube like CRTs. The display can also be built in approximately the same size as an LCD screen. Each blue, green and red sub-pixel is effectively a miniature vacuum tube. Where the CRT uses a single gun for all pixels, a FED pixel cell has thousands of sharp cathode points, or microtips, at its rear. Materials such as molybdenum are used to make these microtips, from which electrons can be pulled very easily by a voltage difference, to strike blue, green and red phosphors at the front of the cell [48]. Figure 22 shows a schematic diagram of a FED display as well as a FED television.

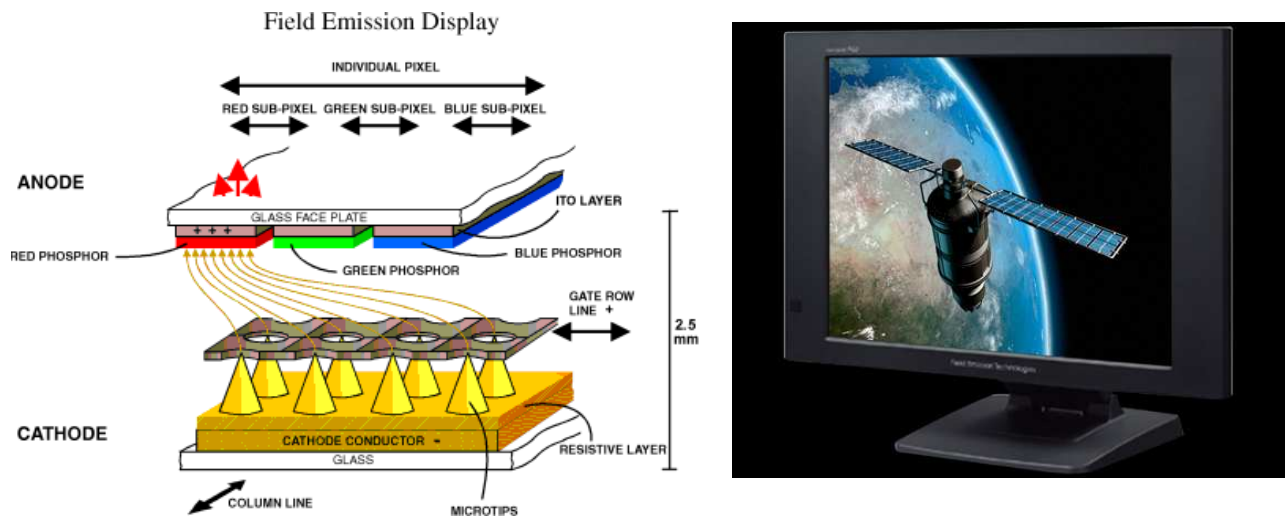


Figure 22: Schematic diagram of a FED display [49] and a FED television [50].

5.3 X-ray screens and scintillators

Since the discovery of x-rays in 1895 by Wilhelm Conrad Roentgen, there was a need to find materials efficient in converting x-rays to visible light. Simple photographic film was soon replaced by CaWO_4 powder and ZnS-based powders that are used until today. Scintillation detectors consist of a scintillator (or phosphor) material followed by an optical relay element and a photo detector (Figure 23 (a)). Wide band gap materials are used to convert x-rays into UV/visible photons. The entire scintillation conversion can be divided into three processes: conversion, transport and lastly luminescence. The conversion process involves an interaction of a high-energy photon with the material lattice. As a result many electrons and holes are created and thermalized in the conduction and valence bands. During the transport stage these charge carriers will migrate through the lattice. Their capture at trapping levels within the material's

forbidden gap will delay migration. Energy losses due to nonradiative recombination may also occur. Finally, the luminescence stage involves radiative recombination of the electron and hole trapped at the luminescence centre. There is a wide variety of materials investigated and used for x-ray detection. A summary of these materials are given in Table 2 [51].

Table 2: Summary of characteristics of selected phosphor materials [51].

Phosphor	Decay time (ns)	Efficiency (%)	Emission max. (nm)	Afterglow
ZnS:Ag	3.9	17-20	450	Very high
CaWO ₄	6.1	5	420	Very low
Gd ₂ O ₂ S:Tb	7.3	13-16	540	Very low
Gd ₂ O ₂ S:Pr,Ce,F	7.3	8-10	490	Very low
LaOBr:Tb	6.3	19-20	425	Low
YTaO ₄ :Nb	7.5	11	410	Low
Lu ₂ O ₃ :Eu	9.4	~8	611	Medium
SrHfO ₃ :Ce	7.7	2-4	390	Not reported

The main applications of scintillators are medical imaging, general flaw detection, high resolution 2D imaging and radio astronomy [51]. In medical imaging it can be used for many applications ranging from intra-oral radiography and mammography to chest radiography [52]. In astronomy thin layers of phosphors are used to do high resolution, soft x-ray imaging. Figure (b) shows a dual phosphor Alpha/Beta Scintillator with built in sample holder for simultaneous alpha/beta radiation sample counting.

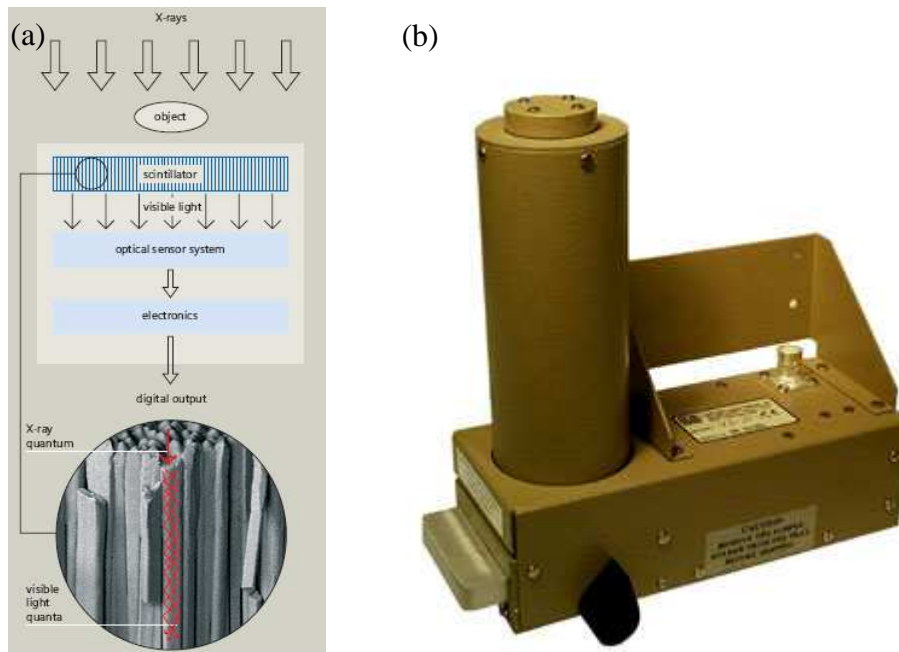


Figure 23: (a) Schematic diagram of a scintillator, which converts incoming x-rays into visible light [52] and (b) a dual phosphor Alpha/Beta Scintillator with built in sample holder for simultaneous alpha/beta radiation sample counting [53].

5.4 Other applications

5.4.1 “Glow-in-the-dark” materials

Phosphors, and especially long afterglow phosphors, have many applications as “glow-in-the-dark” materials. This range from luminescent paints, protective clothing, signs and house numbers.

5.4.1.1 Luminescent paints

Luminescent paints are used for a wide variety of applications. The main application of these paints is to illuminate things so that it can be visible in the dark. Cars can be painted so that they are visible on the open road, road signs and stripes on the road can be painted so that they are visible and even hospitals and police stations can be painted with luminescent paints so that they

are easily visible in places with poor lighting. Figure 24 shows a Smart car that is painted with green phosphor paint and some of these paints in different colours.



Figure 24: A Smart car painted with luminescent paint and some of these paints in different colours [54, 55].

5.4.1.2 Clothing

These days it is very important to be seen in the dark when you are jogging or walking in the streets. Wearing light coloured clothes can help, but wearing clothes that can glow in the dark are the best option. Some of the clothes that are available at the moment include bright green luminescent t-shirts and shoes (Figure 25).



Figure 25: Luminescent t-shirt and shoes [56, 57].

5.4.1.3 Signs and house numbers

Another important use of luminescent materials is to use it as signs and house numbers. During the daytime signs can easily be seen, but in poor light conditions or darkness, it is very difficult to see these signs. If the signs and house numbers could “glow-in-the-dark” it would be very easy to find them. In an emergency situation where you need to find the exit, escape route or fire extinguisher, it would be much easier if you could find the sign pointing to it. Emergency services, like paramedics, police and security companies, can also get to a call out faster if the house number were properly illuminated. Figure 26 shows some luminescent signs and house numbers and Figure 27 shows a homemade sign consisting of a polymer mixed with long afterglow phosphor powder. The sign is white during the day, but glows bright green during the night.



Figure 26: Luminescent signs and house numbers [58, 59].

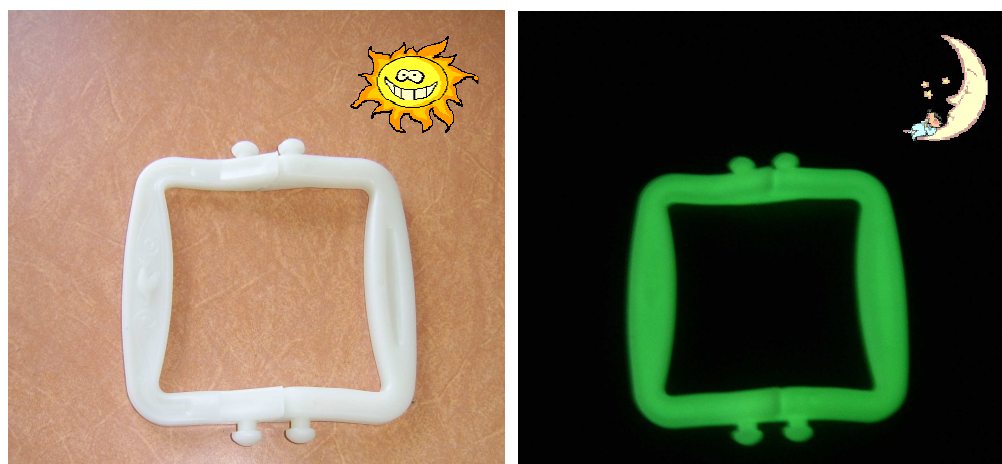


Figure 27: A homemade sign that glows bright green during the night.

5.4.1.4 Other applications.

Some of the other applications of long afterglow phosphors include luminescent toilet seats and door handles, luminescent balls and bikes and a luminescent rope. All these applications help with safety and ensure that objects can be used during a power failure or in poor light conditions.

Figure 28 shows some of these objects.



Figure 28: Some other applications of long afterglow phosphors [60, 61, 62, 63, 64].

5.4.2 Biological labelling

Quantum dots are used for bioimaging or biological labelling of cells. Quantum dots offer several enhancements over fluorescent dyes that are typically used for biological labelling. Organic dyes can exhibit a low quantum yield or brightness, because of molecular interactions with themselves, each other and the solvent. Another limitation is the loss of fluorescence that occurs when dye molecules react irreversibly with each other and the solvent, producing a non-fluorescent product. This process is known as photobleaching. Quantum dots have a reduced photobleaching effect and can therefore exhibit continuous fluorescence over a period of time. This makes quantum dots useful as biosensors, cellular labelling and *in vivo* and *in vitro* fluorescent detection [65].

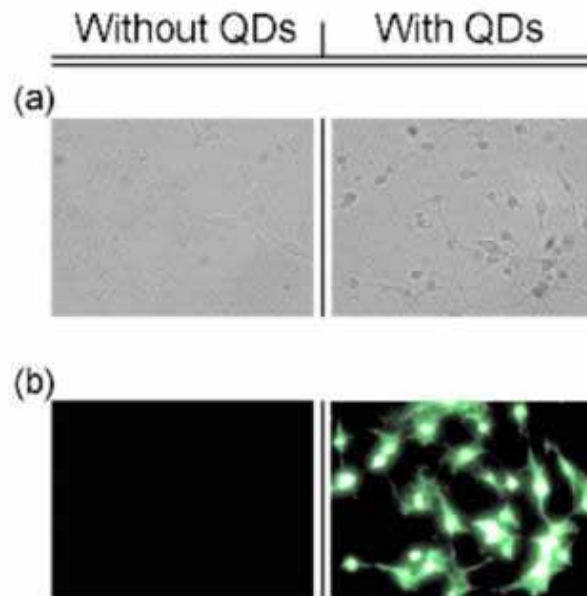


Figure 29: Silicon carbide quantum dots for fluorescence imaging of living cells [66].

Figure 29 shows chemically inert, biocompatible silicon carbide quantum dots for fluorescence imaging of living cells. SiC quantum dots have a major advance since all quantum dots used for imaging so far were toxic to cells [66].

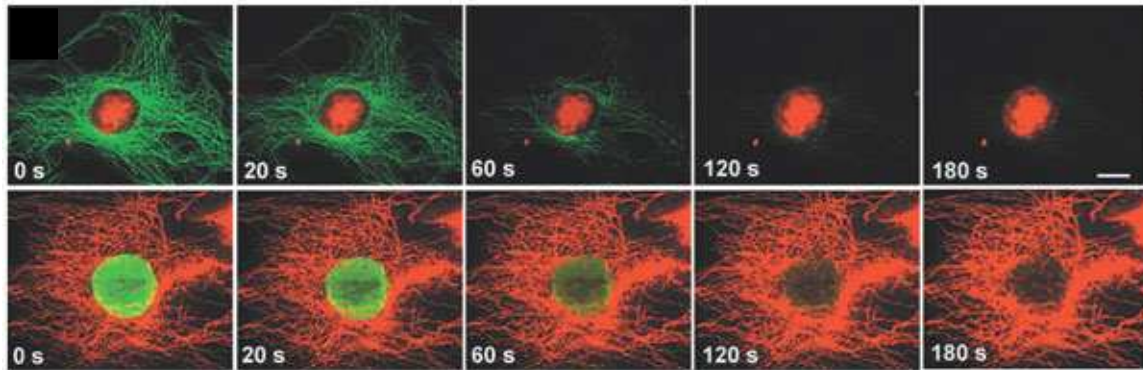


Figure 30: Cell labelling with quantum dots [67].

Figure 30 shows cell labelling with quantum dots and illustration of quantum dot photostability, compared with the dye Alexa 488. In the upper panels, the actin fibers are stained green with the dye and the nucleus is stained red with quantum dots. In the lower panel, the labelling is reversed [67].

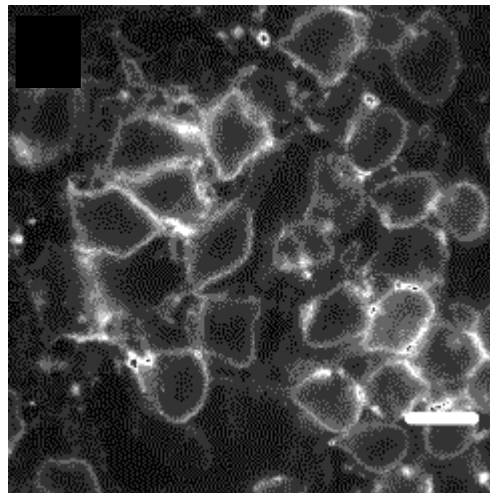


Figure 31: Quantum dots bound to leukaemia cells [68].

Figure 31 shows quantum dots bound to immunoglobulin-G antibodies attach to the surface of leukaemia cells, demonstrating a possible use in biological tagging [68].

Delivery of imaging and therapeutic agents to the brain is highly important for diagnosis and therapy of many brain diseases such as brain tumours. However, the delivery to these agents to the brain is often restricted by the blood-brain-barrier (BBB). This is a tight junction of endothelial cells that regulates the exchange of substances between brain and blood. The cell

membrane is another natural barrier that also can restrict transport of these agents. A method to overcome the cellular membrane barrier is provided by the use of membrane translocation peptides such as the TAT peptide. TAT (a cell penetrating peptide)-conjugated CdS:Mn/ZnS quantum dots (Qdots), intra-arterially delivered to a rat brain, rapidly (within a few minutes) labelled the brain tissue without manipulating the BBB. The Qdot loading was sufficiently high so that it allowed a gross fluorescent visualization of the whole rat brain using a low power hand-held UV lamp (Figure 32 and Figure 33). From histological data it can be clearly seen that TAT-conjugated Qdots migrated beyond the endothelial cell line and reached the brain parenchyma. Qdots without TAT were not able to label the brain tissue confirming the fact that TAT peptide was necessary to overcome the BBB [69].

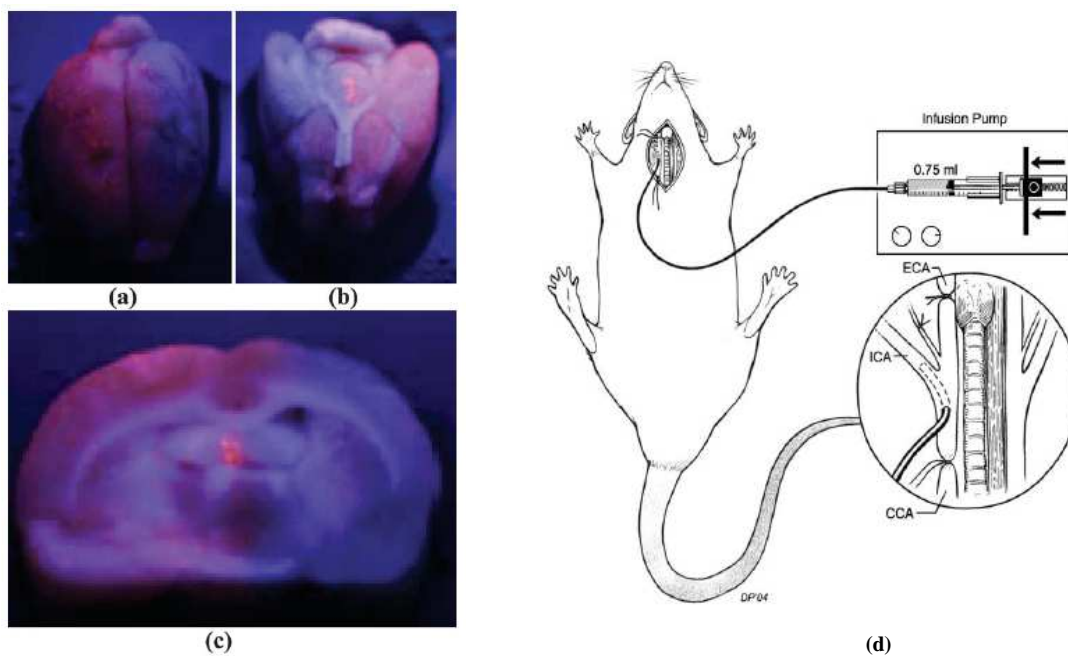


Figure 32: Gross views of a rat brain labelled with TAT-conjugated quantum dots; (a) and (b) represent dorsal views and (c) represents coronal section. Pink colour (left side in (a,c) and right side in (b)) originates primarily from quantum dot fluorescence and background blue colour (right side in (a,c) and left side in (b)) is due to the combination of UV excitation, auto fluorescence, and scattering lights. No filters were used for gross visualization of rat brain. (d) Schematic representation of the surgical procedure [69].

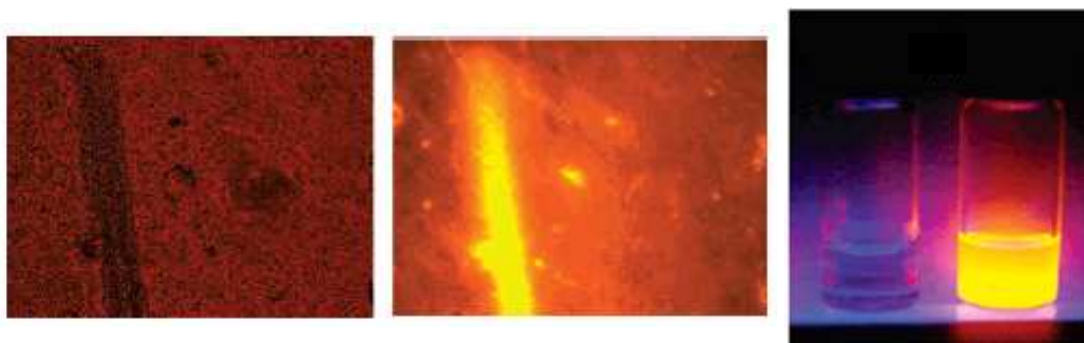


Figure 33: Branches of right middle cerebral artery: Transmission (left) and fluorescence (middle) images of a cross section of rat brain (magnification x 40). The artery was imaged by TAT-conjugated CdS:Mn/ZnS quantum dots (right) [70].

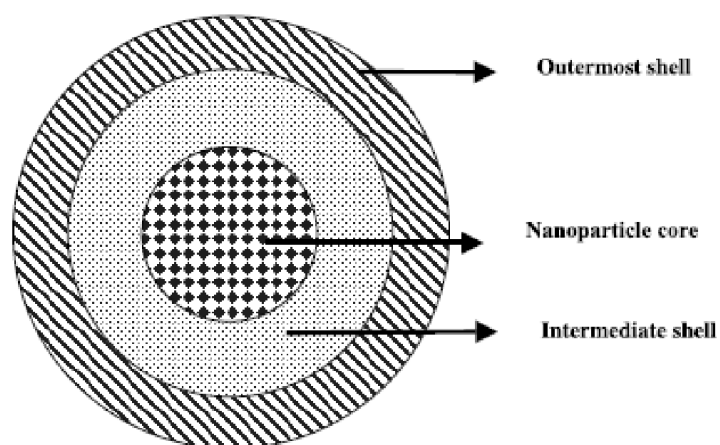


Figure 34: Schematic representation of a typical core-shell nanoparticle design. In some cases, the nanoparticle core is protected just by a single shell (i.e., there is no intermediate shell structure) [71].

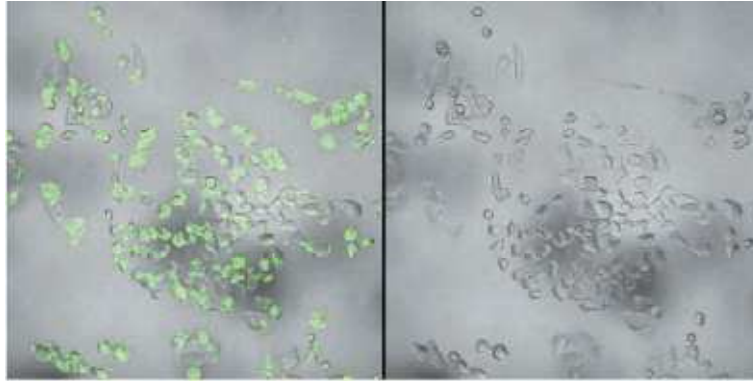


Figure 35: Fluorescence (left) and transmission (right) images of human lung cancer (A549) cells incubated with 200 nm size folate-conjugated fluorescein isothiocyanate (FITC) doped silica nanoparticles [71].

Semiconductor quantum dots have been extensively used for targeting cancer cells. Quantum dots are between 2 and 8 nm in size (Figure 34). They have a broad absorption band with a narrow and symmetric emission band and they typically emit in the visible to NIR spectral range. Quantum dot emission is due to a radiative recombination of an exciton (an electron-hole pair), which is characterized by a long lifetime (>10 ns) leading to the emission of a photon in a narrow and symmetric energy band. In comparison to traditional fluorescent molecules (fluorophores) or fluorescent proteins (e.g., GFP), quantum dots have several attractive optical features that are desirable for long-term, multi-target, and highly sensitive bioimaging applications (Figure 35) [71].

6. Types of phosphors

Phosphors are classified according to the transitions that take place when it is irradiated with either photons or electrons. The one group includes phosphors where the transition occurs in the band gap and the other group includes phosphors where transitions are localized in luminescent centres such as rare-earth elements. These are referred to as band gap and intra-atomic transitions respectively [16].

6.1 Band gap transition phosphors

A typical semiconductor consists out of a valence band and a conduction band. The energy gap between the bands is referred to as the band gap (Figure 36). The lower energy state or valence band is occupied by electrons originating from bound electrons of atoms. The higher energy bands or conduction bands are not occupied by electrons. The reason why these unoccupied states are called conduction bands is due to the fact that an electron in this band is almost freely mobile if it is excited from the valence band by some method: for example, by absorption of light quanta. In contrast, electrons in the valence band cannot be mobile because only two electrons (spin up and spin down) can occupy an electronic state. Electrons in the valence band must have empty states in order for them to move freely when an electric field is applied. After an electron is excited to the conduction band, a hole that remains in the valence band behaves as if it was a mobile particle with a positive charge [1].

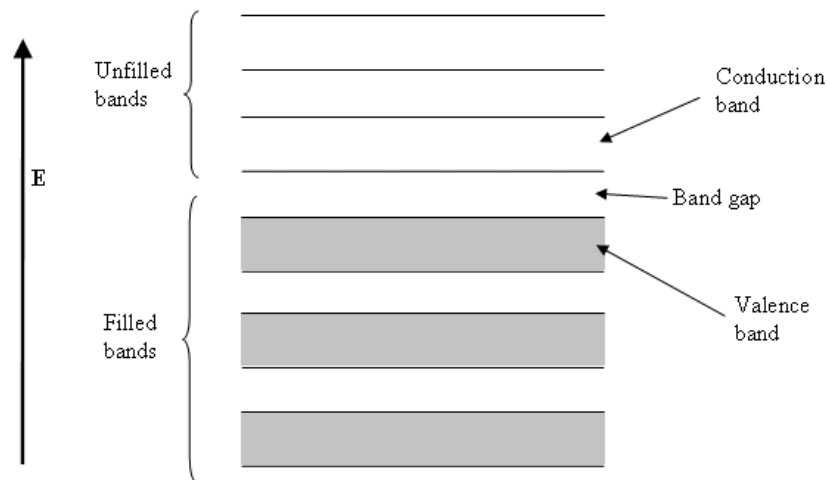


Figure 36: The different bands of a semiconductor [72].

Figure 36 shows a model of band gap transitions in a phosphor. Excitation occurs due to energy transfer from the incident, high energy, particles to the electrons in the valence band. If the transferred energy is high enough the electrons get excited to the higher energy levels or conduction band. Free electrons and free holes are now generated in the valence and conduction bands respectively. If the crystal is perfect, i.e. free from lattice defects and impurities, the free electrons and holes can recombine directly and emit photons ((a) in Figure 37). The energy of

these photons is equal to the band gap of the semiconductor. Localized energy levels or impurity levels are created in a crystal by the presence of activator impurities, incidental impurities and lattice defects. This provides effective recombination paths for the free electrons and holes as represented by (b), (c) and (d) in Figure 37. (b) Is the transition between a free electron in the conduction band and a hole trapped by an acceptor level. (c) Represents a transition between an electron in a deep donor level and a free hole in the valence band and (d) represent a transition between a donor and acceptor level. A number of luminescent processes in the ZnS:Ag,Cl (blue) ZnS:Cu,Al,Au (green) and ZnS:Mn (orange) phosphors occur according to (d) [16].

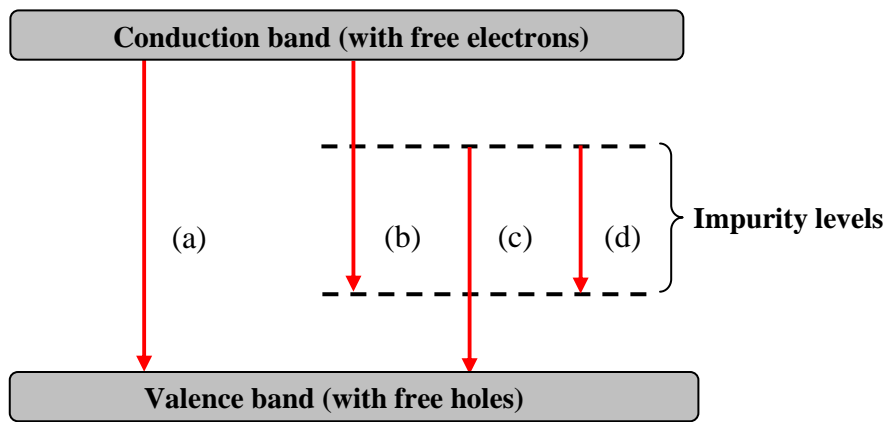


Figure 37: Model of band gap transitions in a phosphor [38].

6.2 Intra-atomic transition phosphors

Characteristic luminescence occurs by doping the host lattice with either transition (3d) or rare-earth (4f) metal ions (impurities) that substitute the host lattice cations. When a moving particle (electron or photon) collides with an atom an electron in the inner shell will be excited to a higher energy level. The electron relaxes to its original energy level and the extra energy is released in the form of a photon (Figure 38).

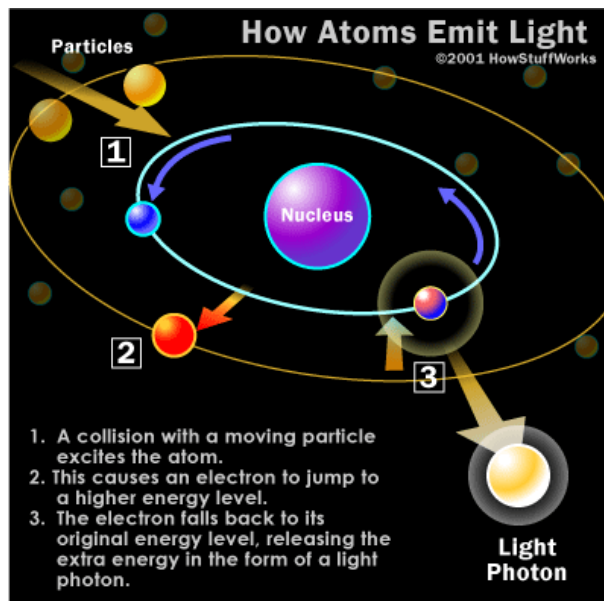


Figure 38: Schematic diagram of how an atom emits light [73].

Rare-earth ions from Ce^{3+} to Yb^{3+} (atomic numbers 58 - 70) have partially filled $4f$ orbitals with energy levels characteristic to each ion and shows a variety of luminescent properties around the visible region. Many of these ions are used as luminescent ions in phosphors. The levels are not much affected by the environment, because $4f$ electrons are shielded from external electric fields by the outer $5s^2$ and $5p^6$ electrons. This is in strong contrast with the transition metal ions, whose $3d$ electrons, that is located in the outer shell, are heavily affected by the environment or crystal field [1]. Figure 39 shows an energy level diagram of luminescent transitions within Eu^{3+} . The diagram shows that absorbed excitation (high energy electrons) induces transitions to higher f levels whereupon non-radiative transitions to the 5D_J ($J = 0, 1, 2, 3$) states occur. This is followed by radiative transitions to the ground state. Typical phosphors used in CRTs and FEDs consist of a host matrix doped with activators such as the rare-earths ($4f$) and transition metals ($3d$) [74].

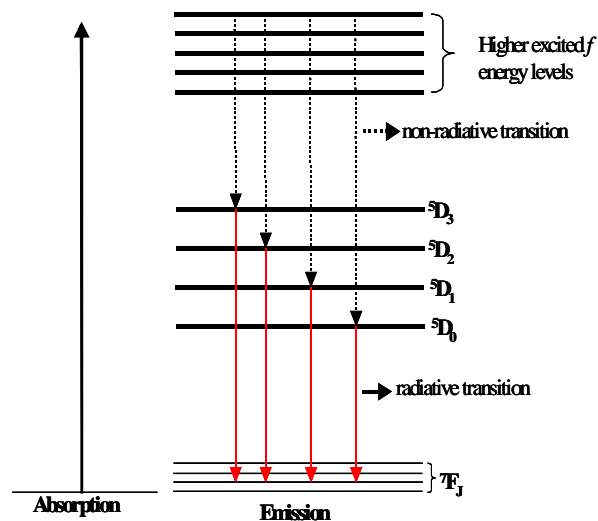


Figure 39: Intra-atomic luminescent transitions in Eu^{3+} ions [38].

7. ZnS

ZnS type phosphors are presently very important as CRT phosphors. These phosphors have a long history, dating back about 130 years. At the International Conference on Luminescence held in 1966 in Budapest, presentation titled “The Century of the Discovery of Luminescent Zinc Sulfide” was given, in which the history of luminescent ZnS was discussed. In 1866, a young French chemist, Théodore Sidot, succeeded in growing tiny ZnS crystals by a sublimation method. Although his original purpose was to study crystal growth, the crystals grown exhibited phosphorescence in the dark. The experiments were repeated, the observations confirmed and a note to the Academy of Science of Paris was presented. This note was published by Becquerel. These phosphorescent ZnS (zinc-blende) crystals were thereafter called Sidot’s blende. From present knowledge, one can conclude that Sidot’s blende contained a small quantity of copper as an impurity responsible for the phosphorescence [1].

Zinc sulfide is a trimorphous mineral consisting of sphalerite, wurtzite and matraite.

7.1 Sphalerite

The mineral sphalerite is the chief ore of zinc. It consists largely of zinc sulphide in crystalline form, but almost always contains variable iron. When the iron content is sufficiently high it is an opaque black variety, marmatite. It is usually found in association with pyrite, galena and other sulphides along with dolomite, calcite and fluorite. The mineral will crystallize in the cubic crystal system. In the crystal structure, zinc and sulphur atoms are tetrahedrally coordinated. This structure is closely related to the structure of diamond (Figure 40). The hexagonal analogue is known as the wurtzite structure. The lattice constant for zinc sulfide in the zinc-blende crystal structure is 0.596 nm, calculated from geometry and ionic radii of 0.074 nm (zinc) and 0.184 nm (sulfide). It forms ABCABD layers. Its colour is usually yellow, brown or grey to grey-black, and it may be shiny or dull (Figure 41). Some of its characteristic is that it has a yellow to light brown streak, a hardness of 3.5 - 4 and a specific gravity of 3.9 - 4.1. The refractive index of sphalerite is 2.37. Some specimens of sphalerite are also fluorescent in ultraviolet light [75].

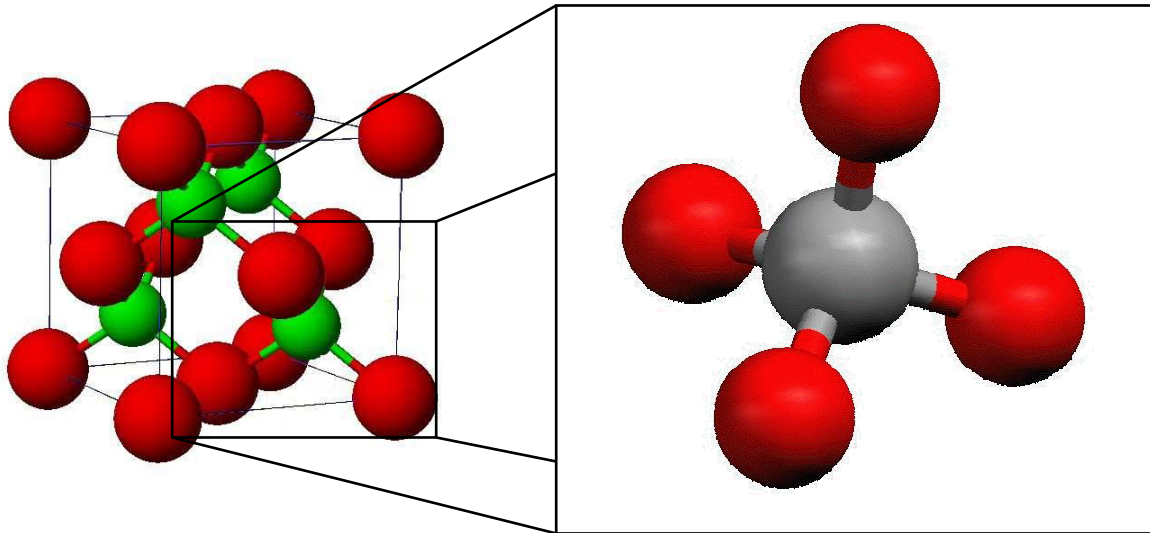


Figure 40: Zinc blende crystal structure [76] and tetrahedral arrangement [77].



Figure 41: Different types of sphalerite [76, 79, 75, 80].

7.2 Wurtzite

Wurtzite is a zinc sulfide mineral, a less frequently encountered mineral form of sphalerite. Its crystal structure is called the hexagonal wurtzite crystal structure, to which it lends its name (Figure 42). This structure is a member of the hexagonal crystal system and consists of tetrahedrally coordinated zinc and sulphur atoms that are stacked in an ABABAB pattern. The unit cell parameters of wurtzite are $a = b = 3.81 \text{ \AA}$ and $c = 6.23 \text{ \AA}$. Its colour ranges from brownish black, orange brown, reddish brown to black (Figure 43). It can be characterized by a hardness of 3.5 – 4, a light brown streak and a specific gravity of 4.0 [81]. It occurs in hydrothermal deposits associated with sphalerite, chalcopyrite, pyrite, barite and marcasite. It was first described for an occurrence in Příbram, Czech Republic in 1861 and named after the French chemist Charles-Adolphe Wurtz [82].

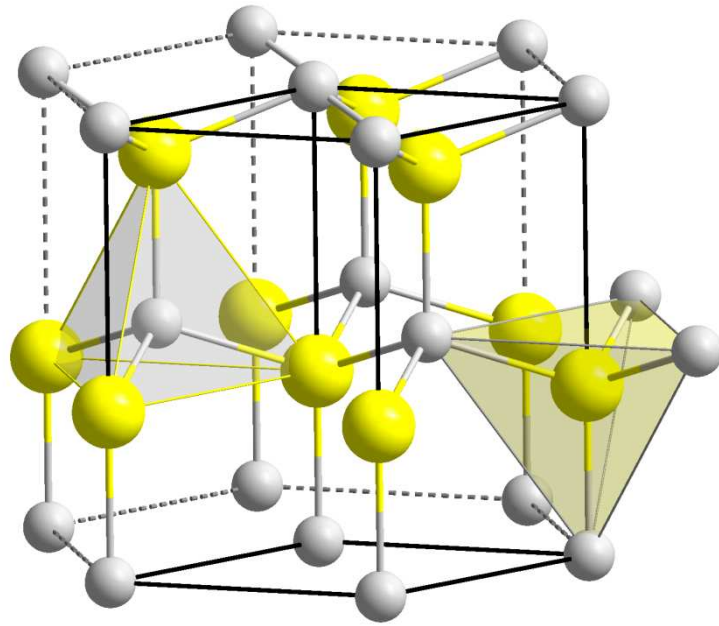


Figure 42: The hexagonal wurtzite crystal structure [83].



Figure 43: Different types of wurtzite [84, 85, 86].

7.3 Matraite

Matraite is the rarest form of zinc sulfide. It has a hexagonal crystal structure, a hardness of 3.5 - 4, a yellow white streak and a brownish yellow colour (Figure 44). It was named after the Matra Mountains in Hungary [87].

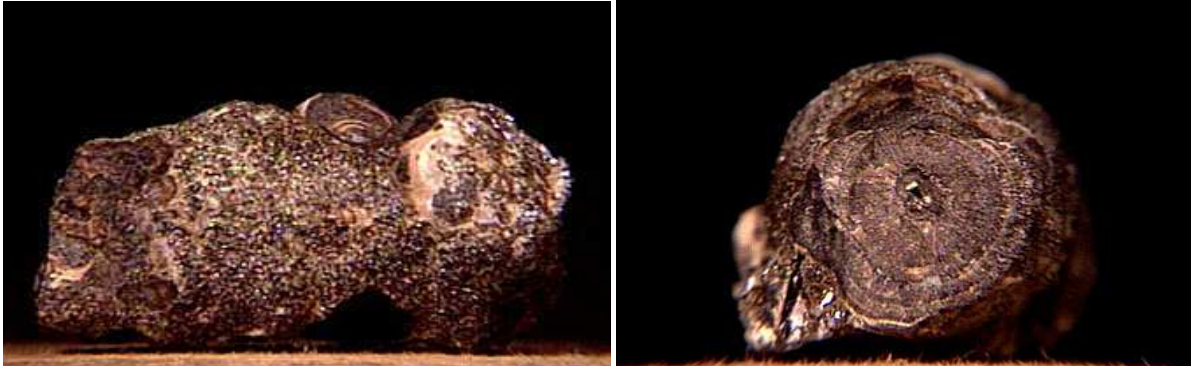


Figure 44: Matraite [84].

References

- 1 S. Shionoya and W.M. Yen, Phosphor Handbook, CRC Press LLC, Boca Raton, (1999) p 3-4, 5-6, 178, 186, 231-232 847-848.
- 2 The Discovery of Luminescence: "The Bolognian Stone", [online]. Available from http://www.isbc.unibo.it/Files/10_SE_BoStone.htm [Accessed 8 June 2009].
- 3 E.N. Harvey, A history of Luminescence, American Philosophical Society, (1957) p 18.
- 4 C.C. Kang, R.S. Liu, J.C. Chang and B. J. Lee, Chem. Mater. **15** (2003) 3966.
- 5 R. Kane and H. Sell, Revolution in Lamps: A Chronicle of 50 Years of Progress, 2nd edition, The Fairmont Press, Georgia (2001) p93.
- 6 The Science of PDT, [online]. Available from <http://www.bmb.leeds.ac.uk/pdt/science.htm#top> [Accessed 21 September 2009].
- 7 Fluorescence and Phosphorescence, [online]. Available from http://www.physik.unibas.ch/Praktikum/VPII/Fluoreszenz/Fluorescence_and_Phosphorescence.pdf [Accessed 9 June 2009].
- 8 UV-Vis Luminescence Spectroscopy: Theoretical principles, [online]. Available from <http://teaching.shu.ac.uk/hwb/chemistry/tutorials/molspec/lumin1.htm> [Accessed 9 June 2009].
- 9 Luminescence, [online]. Available from <http://www.uvminerals.org/luminese.htm> [Accessed 9 June 2009].
- 10 Heated screw, [online]. Available from <http://www.photographersdirect.com/buyers/stockphoto.asp?imageid=1742197> [Accessed 10 June 2009].
- 11 Light bulb, [online]. Available from <http://www.freefoto.com/preview/11-12-52> [Accessed 10 June 2009].
- 12 Sun, [online]. Available from <http://www.daviddarling.info/encyclopedia/S/Sun.html> [Accessed 10 June 2009].
- 13 Fluorescence, [online]. Available from <http://en.wikipedia.org/wiki/Fluorescence> [Accessed 10 June 2009].
- 14 Fluorescent light bulbs, [online]. Available from <http://urbngreen.com/?m=200806> [Accessed 10 June 2009].
- 15 Neon open sign, [online]. Available from <http://www.neonclick.de/index.htm> [Accessed 10 June 2009].

- 16 Phosphorescence, [online]. Available from <http://en.wikipedia.org/wiki/Phosphorescence> [Accessed 10 June 2009].
- 17 Electroluminescence, [online]. Available from <http://en.wikipedia.org/wiki/Electroluminescence> [Accessed 10 June 2009].
- 18 Calculator, [online]. Available from <http://www.diytrade.com/china/4/products/3223048/CALCULATOR.html> [Accessed 11 June 2009].
- 19 Casio PAS410B-5V Pathfinder Watch, [online]. Available from <http://salestores.com/casiopas.html> [Accessed 11 June 2009].
- 20 LCD Music Alarm Clock, [online]. Available from <http://www.made-in-china.com/china-products/productviewixmEpjtConQL/LCD-Music-Alarm-Clock-w-Aurora-Flash-Backlight-ETA-280-.html> [Accessed 11 June 2009].
- 21 Bioluminescence, [online]. Available from <http://en.wikipedia.org/wiki/Bioluminescence> [Accessed 11 June 2009].
- 22 Living Lights: A Glowing Compendium, [online]. Available from <http://curiousexpeditions.org/?p=233> [Accessed 11 June 2009].
- 23 Bioluminescence: Colours With, For and by Life, [online]. Available from <http://www.sciencelay.com/Biology/Zoology/Bioluminescence-Colours-With-for-and-by-Life.612487> [Accessed 11 June 2009].
- 24 Jack o'lantern mushroom, [online]. Available from <http://www.treknature.com/gallery/photo86591.htm> [Accessed 11 June 2009].
- 25 Chemoluminescence, [online]. Available from <http://en.wikipedia.org/wiki/Chemoluminescence> [Accessed 12 June 2009].
- 26 How light sticks work, [online]. Available from http://118.98.213.22/choirul/how/light_stick/light-stick.htm [Accessed 12 June 2009].
- 27 AmeriGlo 6" Safety Light Stick, [online]. Available from http://www.thefirestore.com/store/product.cfm/pid_4741_ameriglo_6_safety_light_stick_8_hour_tactical_blue_or_white/ [Accessed 12 June 2009].
- 28 Luminol against crime, [online]. Available from http://newcuriosity.blogspot.com/2008_09_01_archive.html [Accessed 12 June 2009].
- 29 Thermoluminescence, [online]. Available from <http://en.wikipedia.org/wiki/Thermoluminescence> [Accessed 12 June 2009].

- 30 Thermoluminescence, [online]. Available from <http://www.geocities.com/rainforest/9911/thermo.htm> [Accessed 12 June 2009].
- 31 Archaeological applications, [online]. Available from <http://www.hko.gov.hk/education/dbcp/radiation/eng/r20.htm> [Accessed 12 June 2009].
- 32 Luminescence, [online]. Available from <http://en.wikipedia.org/wiki/Luminescence> [Accessed 12 June 2009].
- 33 Radioluminescence, [online]. Available from <http://en.wikipedia.org/wiki/Radioluminescence> [Accessed 15 June 2009].
- 34 Mechanoluminescence Event Yields Novel Emissions, Reactions, [online]. Available from <http://www.sciencedaily.com/releases/2007/05/070508190022.htm> [Accessed 15 June 2009].
- 35 Candy Science: Chewing Light, [online]. Available from <http://brightest-kidz.squarespace.com/journal/2008/2/8/candy-science-chewing-light.html> [Accessed 15 June 2009].
- 36 Light From Gas Bubbles: Sonoluminescence Measured, [online]. Available from <http://www.nsf.gov/od/lpa/news/02/pr0263.htm> [Accessed 15 June 2009].
- 37 How Fluorescent Lamps Work, [online]. Available from <http://home.howstuffworks.com/fluorescent-lamp.htm/printable> [Accessed 15 June 2009].
- 38 O.M. Ntwaeaborwa, PhD Thesis, University of the Free State, South Africa (2006) p7, 15-16.
- 39 Cathode ray tube, [online]. Available from http://en.wikipedia.org/wiki/Cathode_ray_tube [Accessed 5 June 2009].
- 40 The Cathode Ray Tube, [online]. Available from <http://electronics.howstuffworks.com/tv3.htm> [Accessed 5 June 2009].
- 41 Computer basics, [online]. Available from <http://www.jegsworks.com/Lessons/lesson5/lesson5-4.htm> [Accessed 5 June 2009].
- 42 Flat panel display, [online]. Available from http://en.wikipedia.org/wiki/Flat_panel_display [Accessed 12 June 2009].
- 43 Plasma TV, [online]. Available from <http://www.plasmatelly.com/> [Accessed 16 June 2009].

- 44 TFT-LCD: What is it?, Available from http://www.cmo.com.tw/opencms/cmo/technology/TFTLCDx_What_is_itx/?__locale=en [Accessed 16 June 2009].
- 45 Dell websites drop LCD TV line-up, [online]. Available from http://www.reghardware.co.uk/2006/02/03/dell_site_drops_lcd_tv/ [Accessed 16 June 2009].
- 46 OLED, [online]. Available from <http://www.scienceofspectroscopy.info/edit/index.php?title=OLED> [Accessed 16 June 2009].
- 47 Sony talks up 'world's first' OLED TV, [online]. Available from http://www.reghardware.co.uk/2007/10/01/sony_talks_first_oled_tv/ [Accessed 16 June 2009].
- 48 Field Emission Displays, [online]. Available from http://www.pctechguide.com/43FlatPanels_FEDs.htm [Accessed 5 June 2009].
- 49 Field Emission Displays (FEDs), [online]. Available from <http://groups.csail.mit.edu/graphics/classes/6.837/F98/Lecture1/Slide20.html> [Accessed 16 June 2009].
- 50 FED, [online]. Available from http://www.televisions.com/News/Sony_spin-off_gives_up_development_of_FED.php [Accessed 16 June 2009].
- 51 Scintillators and phosphor materials: Latest developments and applications, [online]. Available from VILLAOLMO.MIB.INFN.IT/ICATPP9TH_2005/RADIATION_DAMAGE/MIHOKOVA.DOC [Accessed 15 June 2009].
- 52 Solid Screen® X-ray Scintillators, [online]. Available from http://health.siemens.com/med/rv/images/solid_screen.pdf [Accessed 15 June 2009].
- 53 Ludlum Sample Counters <http://www.deqtech.com/Ludlum/Categories/sample-counters.htm> [Accessed 15 June 2009].
- 54 2007 Smart fortwo Luminescent Paint, [online]. Available from http://digiads.com.au/car-news/latest-SMART-news/2007_Smart_fortwo_Luminescent_Paint_200701/photos_0.html [Accessed 17 June 2009].
- 55 Glow in The Dark Ink and Paint, [online]. Available from <http://www.made-in-china.com/showroom/santana44/product-detailHoemBgCPXzhp/China-Glow-in-The-Dark-Ink-and-Paint.html> [Accessed 17 June 2009].
- 56 Glow in the dark tees, [online]. Available from <http://n-sb.org/index.php/2007/03/21/nike-glow-in-the-dark-tees/> [Accessed 17 June 2009].

- 57 Nike 'Illumination' Pack, [online]. Available from <http://english.mashkulture.net/2007/03/01/nike-illumination-pack/> [Accessed 17 June 2009].
- 58 Signs & Tape, [online]. Available from <http://www.glonation.com/signs-and-tape.html> [Accessed 17 June 2009].
- 59 Glow in the Dark Numbers, [online]. Available from http://www.solarpowernumbers.com/Glow_In_The_Dark_Numbers.htm [Accessed 17 June 2009].
- 60 Glow in the Dark Toilet Seat, [online]. Available from <http://www.acpau.com.au/product.php?productid=16406&cat=293&bestseller> [Accessed 17 June 2009].
- 61 Luminous football, golf ball, baseball, [online]. Available from http://www.diytrade.com/china/4/products/2395176/glow_in_the_dark_ball_series.html [Accessed 17 June 2009].
- 62 Glow in the Dark Rope, [online]. Available from <http://www.glowingproducts.com/rope.html> [Accessed 17 June 2009].
- 63 Glow in the dark bike, [online]. Available from <http://bmxmuseum.com/forums/viewtopic.php?id=80362&action=new> [Accessed 17 June 2009].
- 64 Glow-in-the-Dark Doorknob Grips, [online]. Available from <http://www.gearfuse.com/tag/glow-in-the-dark/> [Accessed 17 June 2009].
- 65 S.O. Oluwafemi, PhD Thesis, University of Zululand, South Africa (2008) p45-49.
- 66 SiC Quantum Dots Image Live Cells, [online]. Available from <http://www.nano.org.uk/news/sep2008/latest1599.htm> [Accessed 18 June 2009].
- 67 The use of nanocrystals in biological detection, [online]. Available from <http://www.nature.com/nbt/journal/v22/n1/full/nbt927.html> [Accessed 18 June 2009].
- 68 "Cornell dots", [online]. Available from <http://www.news.cornell.edu/stories/May05/CUdots.ws.html> [Accessed 18 June 2009].
- 69 S. Santra, H. Yang, J.T. Stanley, P.H. Holloway, B.M. Moudgil, G. Walter and R.A. Mericle, Chem. Commun.(2005) 3144-3145.
- 70 S. Santra, H. Yang, P.H. Holloway J.T. Stanley and R.A. Mericle, J. Am. Chem. Soc, **127** (2005) 1657.
- 71 S. Santra, D. Dutta, G.A. Walter and B.M. Moudgil, Technology in Cancer Research & Treatment, **4** (2005) 594, 599.

- 72 Band gap, [online]. Available from http://www.all-science-fair-projects.com/science_fair_projects_encyclopedia/Band_gap [Accessed 22 June 2009].
- 73 How X-rays Work, [online]. Available from <http://www.howstuffworks.com/x-ray.htm/printable> [Accessed 22 June 2009].
- 74 A.M. Srivastava and C.R. Ronda, Phosphors, *Electrochem. Soc. Inter*, (2003) 48.
- 75 Sphalerite, [online]. Available from <http://en.wikipedia.org/wiki/Sphalerite> [Accessed 24 June 2009].
- 76 Zincblende (Zinc sulfide, ZnS) structure [online]. Available from <http://www.seas.upenn.edu/%7Echem101/sschem/ionicsolids.html> [Accessed 17 April 2009].
- 77 Classic Molecular Modeling [online]. Available from <http://chemlab.truman.edu/CHEM121Labs/MolecularModeling1.htm> [Accessed 17 April 2009].
- 78 Sphalerite (Zinc Sulfide), [online]. Available from <http://ohiohistorycentral.org/entry-images.php?rec=1344> [Accessed 24 June 2009].
- 79 Stock photo: Sphalerite with chert, [online]. Available from <http://www.sxc.hu/photo/303672> [Accessed 24 June 2009].
- 80 Marmatite Gallery, [online]. Available from <http://www.mindat.org/gallery.php?min=6294> [Accessed 24 June 2009].
- 81 General Wurtzite Information, [online]. Available from <http://webmineral.com/data/Wurtzite.shtml> [Accessed 24 June 2009].
- 82 Wurtzite, [online]. Available from <http://en.wikipedia.org/wiki/Wurtzite> [Accessed 24 June 2009].
- 83 Wurtzite crystal structure, [online]. Available from <http://www.answers.com/topic/wurtzite> [Accessed 24 June 2009].
- 84 Mineral Collection Images, [online]. Available from <http://www.cs.cmu.edu/~adg/adg-psimages.html> [Accessed 24 June 2009].
- 85 Collecting Wurtzite Crystals Negley, Ohio, [online]. Available from <http://www.vasichkominerals.com/wurtz.htm> [Accessed 24 June 2009].
- 86 Wurtzite, [online]. Available from <http://hyperphysics.phy-astr.gsu.edu/hbase/Minerals/wurtzite.html> [Accessed 24 June 2009].

87 Matraite, [online]. Available from [http://www.mineralatlas.com/mineral%20general%20descriptions /M/matraitepcd.htm](http://www.mineralatlas.com/mineral%20general%20descriptions/M/matraitepcd.htm) [Accessed 24 June 2009].

Chapter 3

Theory of characterization techniques.

The powders that were investigated in this study were characterized using scanning electron microscopy (SEM), energy dispersive x-ray spectroscopy (EDS), transmission electron microscopy (TEM), x-ray diffraction (XRD), UV-Vis spectroscopy, photoluminescence (PL), cathodoluminescence (CL), Auger electron spectroscopy (AES) and residual gas analyses (RGA). The theory of these characterization techniques can be found in this chapter. It also gives the experimental setup and layout of the methods used for characterization.

1. Scanning electron microscopy (SEM)

1.1 Theory

Scanning electron microscopy (SEM) is used to inspect the topographies of specimens at very high magnifications (Figure 1). The magnification can go to more than 300 0000 x. During SEM analysis, a beam of electrons is focussed on a spot volume of the specimen. The electron beam has energies that range from a few keV to 50 keV and it is focussed by two condenser lenses into a beam with a very fine spot size. This beam then passes through the objective lens, where pairs of coils deflect the beam either linearly or in a raster fashion over a rectangular area of the sample surface (Figure 2). When the primary electron beam strikes the surface of the sample it is scattered by atoms in the sample. Through this scattering events, the primary beam spreads effectively and fills a teardrop-shaped volume (Figure 3), know as the interaction volume, and this extends about 1 to 5 μm into the surface. Secondary electrons are emitted from interactions in this region, they are then detected, converted to a voltage and amplified to produce an image.

More than one type of signal can be produced by SEM and they include secondary electrons, back-scattered electrons (BSEs), characteristic x-rays, cathodoluminescence, specimen current and transmitted electrons. Specialized detectors are required for the detection of these signals and they are not usually all present on a single machine [1].

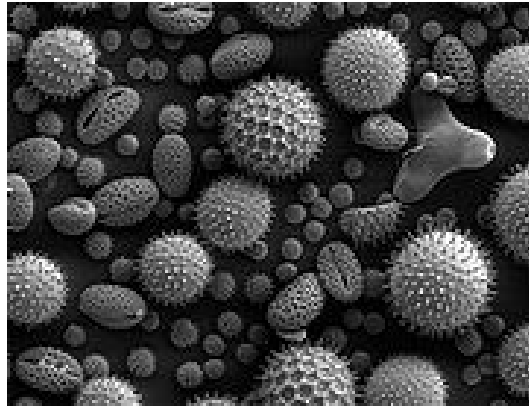


Figure 1: SEM micrograph of pollen [1].

The SEM and EDS system used in this study is shown in Figure 4.

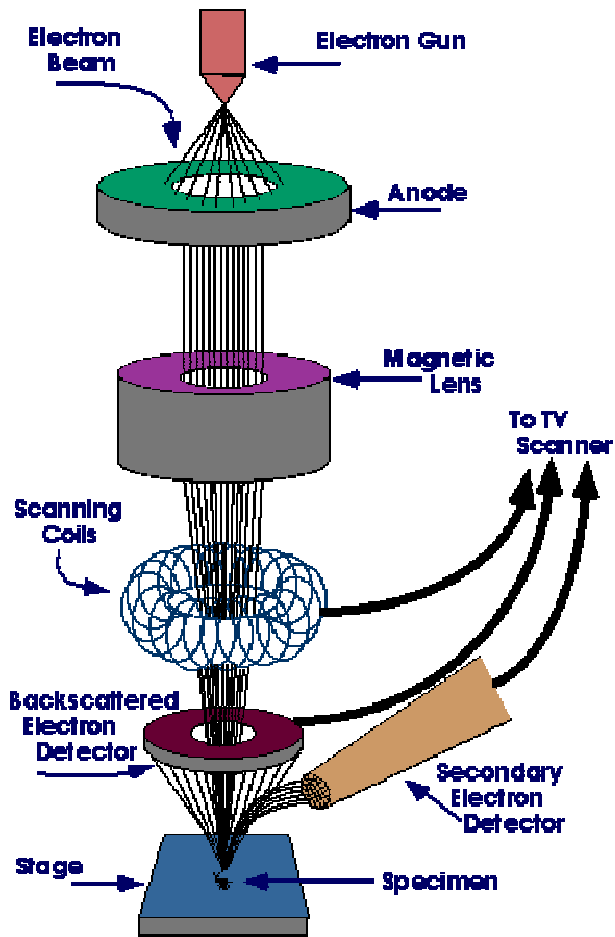


Figure 2: Schematic diagram of a typical scanning electron microscope [2].

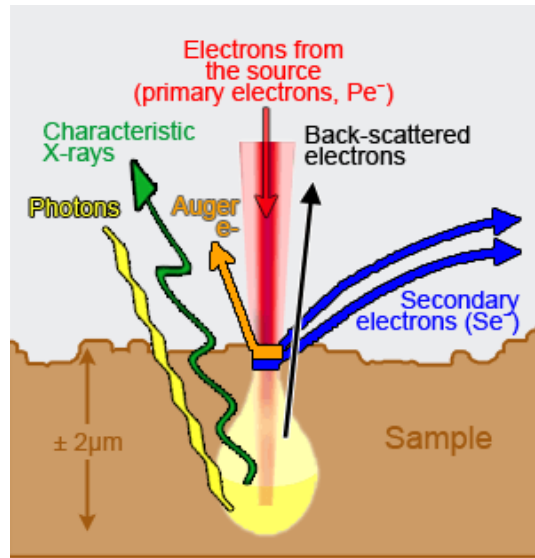


Figure 3: Electrons produced in SEM [3].



Figure 4: SEM system at the Centre for Microscopy at UFS.

2. Energy dispersive x-ray spectroscopy (EDS)

2.1 Theory

The chemical composition of the synthesized powders used in this research study was determined by EDS analysis. EDS is an analytic technique and is used for elemental analysis or chemical composition of a sample. When a sample is bombarded with electrons it can emit x-

rays, which can be analysed. By measuring the intensity distribution and energy of the x-ray signal generated by a focussed electron beam impinging on a sample, the chemical analysis of the sample can be obtained. The source of the electron beam is the electron gun of a scanning electron microscope.

To stimulate a measurable response from a specimen, an electron or photon beam is aimed down into the sample to be characterized. At rest, an atom within the sample contains ground state or “unexcited” electrons, situated in probability shells around the nucleus. The incident beam, however, excites an electron in an inner shell, prompting its ejection and resulting in the formation of a hole within the atom’s electronic structure. An electron from an outer, higher-energy shell then fills the hole (Figure 5), and the excess energy is released in the form of an x-ray (Figure 6). The release of x-rays creates spectral lines that are highly specific to individual elements; thus, by analyzing the x-ray emission data the sample in question can be characterized [3].

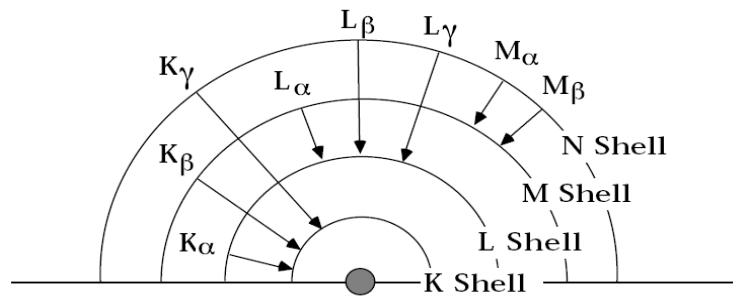


Figure 5: The probability shells around the nucleus [4].

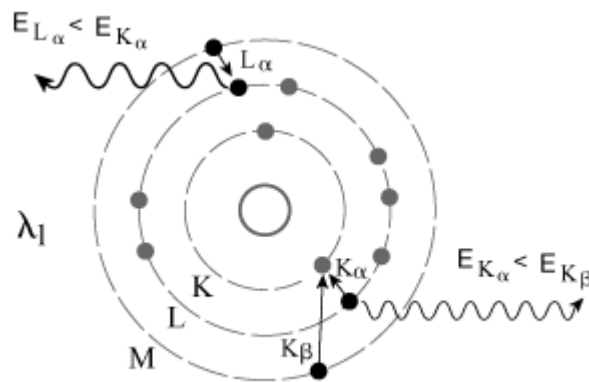


Figure 6: Characteristic x-ray radiation [5].

An EDS spectrum is given as the output of an EDS analysis (Figure 7). This spectrum is a plot of how frequently an x-ray is received for each energy level and it is given in counts per second. It normally displays peaks that correspond to energy levels from which the most x-rays have been received. Each peak is characteristic of an element.

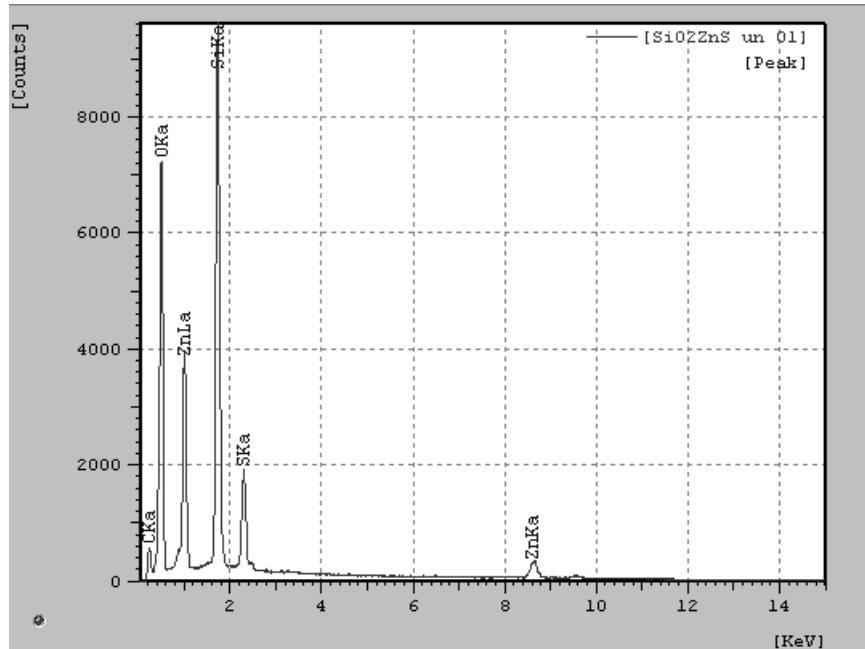


Figure 7: Example of an EDS spectrum of SiO₂:ZnS nano phosphors.

3. Transmission electron microscopy (TEM)

3.1 Theory

Transmission electron microscopy is a microscopy technique whereby a beam of electrons is transmitted through a very thin sample and interacting with the sample as it passes through. The interaction of the electrons transmitted through the sample is forming an image. This image is magnified and then focussed onto a fluorescent screen or it can be detected by a CCD camera.

The imaging capability of TEMs has a significantly higher resolution than that of light microscopes, because of the small de Broglie wavelength of electrons. The instrument is therefore enabled to examine fine detail - even as small as a single layer of atoms. TEM is used

in a range of scientific fields as a major analysis method, in both biological and physical sciences. Applications of TEM are in material science, pollution and semiconductor research, virology, and cancer research.

The operation of the TEM requires an ultra high vacuum and a high voltage (300 kV). The electrons are emitted by a source and then it is focused and magnified by a set of magnetic lenses (Figure 8). The imaged that is formed is either shown on a fluorescent screen or on a monitor and it is printed on photographic film. The resolution power is usually restrained by the technique with which the preparation was achieved and the quality of the lens system. Today's transmission electron microscopes offer resolutions up to 0.1nm at 300kV and probe diameters up to 0.34nm.

TEM exploits three different interactions of electron beam-specimen; unscattered electrons (transmitted beam), elastically scattered electrons (diffracted beam) and inelastically scattered electrons. Different types of images are obtained in TEM, using the apertures properly as well as the different types of electrons. As a result, diffraction patterns are shown because of the scattered electrons. If the unscattered beam is selected, we obtain the Bright Field Image. Dark Field Images are attained if diffracted beams are selected by the objective aperture [6]. Figure 8 shows a schematic diagram of the layout of a typical TEM and Figure 9 shows the sample holders that are used in TEMs.

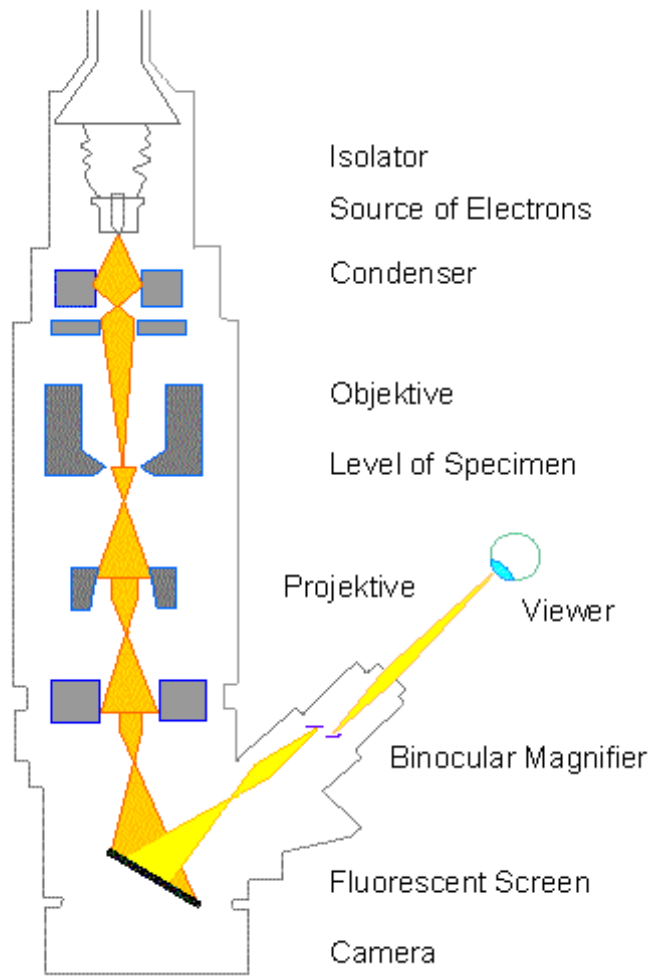


Figure 8: Schematic diagram of a TEM [7].

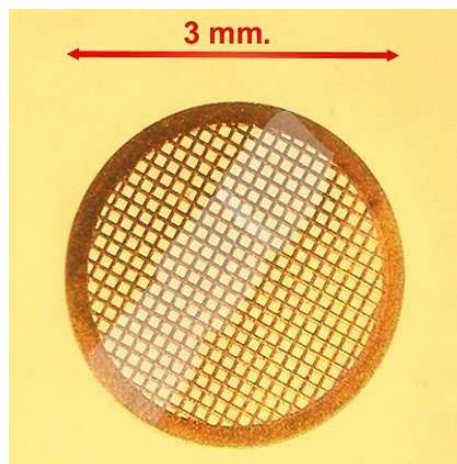


Figure 9: TEM sample support mesh “grid”, with ultramicrotomy sections [8].

Figure 10 shows the TEM at the Centre for Microscopy at UFS.



Figure 10: TEM system at the Centre for Microscopy at UFS.

4. X-ray diffraction (XRD)

4.1 Crystal structure

Solid matter consists out of two types of material: amorphous and crystalline. In an amorphous sample the atoms are arranged in a random way (similar to what we find in a liquid). Glasses are an example of amorphous materials. In a crystalline sample the atoms are arranged in a regular or ordered pattern and there is a smallest volume element that, by repetition in three dimensions, can describe the crystal (just like a brick wall can be described by the shape and orientation of a single brick). This smallest volume element is called a unit cell. The dimensions of this unit cell can be described by three axes namely: a, b and c and the angles between the axis are α , β and γ . A schematic diagram of the unit cell is given in Figure 11.

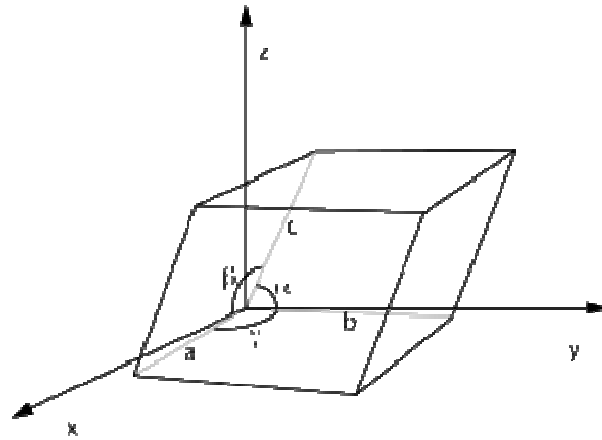


Figure 11: A unit cell from a three dimensional lattice [9].

About 95% of all solid materials can be described as crystalline. When x-rays interact with a crystalline substance a diffraction pattern is formed. This pattern of a pure substance is therefore acting as a fingerprint of that substance. The powder diffraction method is used for identification and characterization of polycrystalline phases.

When an electron is placed in an alternating electromagnetic field, it will oscillate with the same frequency as the field. The electrons around an atom will start to oscillate with the same frequency as the incoming beam when an x-ray beam hits the atom. Destructive interference will be found in almost all the directions, that is, the combining waves is out of phase and there will be no resultant energy leaving the sample. The atoms in a crystal are however arranged in an ordered way and constructive interference will therefore occur in a very few directions. These waves will be in phase and there will be well defined x-ray beams leaving the sample at various directions. A diffracted beam may be therefore described as a beam composed of a large number of scattered rays mutually reinforcing one another.

This model is very complex to handle mathematically and it is preferred to talk about x-ray reflections from a series of parallel planes inside the crystal. The Miller indices h, k, l define the orientation and interplanar spacings of these planes. The a axis of the unit cell will be cut into h sections, the b axis into k sections and the c axis into l sections by a given set of planes with indices h, k, l . When the planes are parallel to the corresponding axis it is indicated by a zero.

4.2 Bragg's Law

Bragg's law is the basis of XRD analysis. With this law it is possible to make accurate quantifications of experimental results in the determination of crystal structures. The law was derived by English physicist Sir W.H. Bragg and his son Sir W.L. Bragg in 1913. It was used to explain why the cleavage faces of crystals appear to reflect x-ray beams at certain angles of incidence.

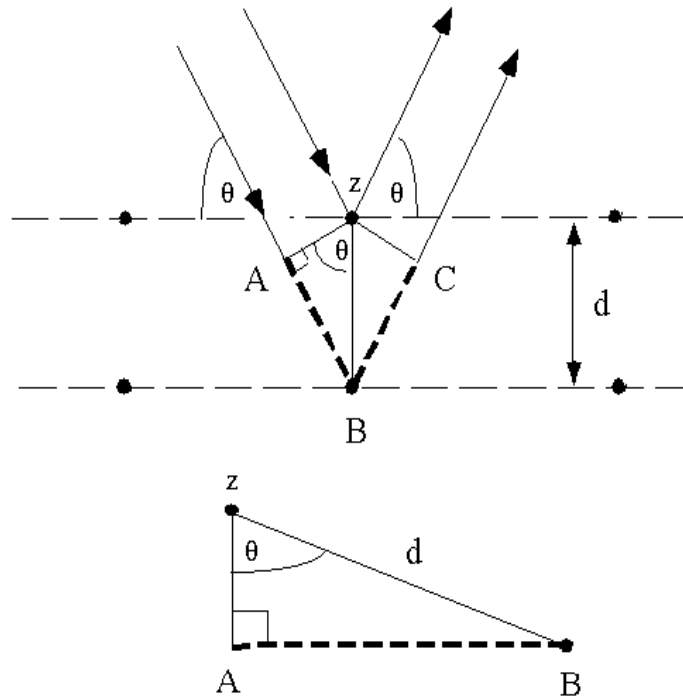


Figure 12: Deriving Bragg's law using the reflection geometry and applying trigonometry.
[10].

The lattice planes in the simple crystal in Figure 12 are separated by a distance d . Bragg's law is given by

$$n\lambda = 2d \sin \theta \quad (1)$$

The angle between the transmitted and diffracted beams will always be equal to 2θ because of the geometry of the Bragg's condition. This angle can be obtained readily in experimental situations and the results of x-ray diffraction are therefore given in terms of 2θ . It is however very important to remember that the angle that is used in the Bragg's equation must correspond to the angle between the incident radiation and the diffracting plane, i.e. θ [10].

5. UV-Vis spectroscopy

5.1 Theory

Several processes are possible when a sample is stimulated by the application of an external electromagnetic radiation source. The radiation can for example be reflected or scattered. What is important is that some of the radiation can be absorbed and promote some of the sample into the excited state (Figure 13). In absorption spectroscopy the amount of light that is absorbed is measured as a function of wavelength. Both qualitative and quantitative information can be obtained from the sample using this method.

Every molecular species is capable of absorbing its own characteristic frequencies of electromagnetic radiation. In this process energy is transferred to the molecule and results in a decrease in the intensity of the electromagnetic radiation that is incident on the sample. The radiation is thus attenuated because of absorption. The Beer-Lambert law or just Beer's law (absorption law) is quantitatively giving how the amount of attenuation depends on the concentration of the absorbing molecule as well as the path length over which the absorption occurs. When light traverses through a medium that contains an absorbing analyte, intensity decreases will occur when the analyte becomes excited. For a sample with a certain concentration, the longer the path length of the light (length of the medium through which the light passes), the more absorbers will be in the path and the greater the attenuation. Also, for a given path length, the higher the concentration of the absorbers the stronger the attenuation of the light beam.

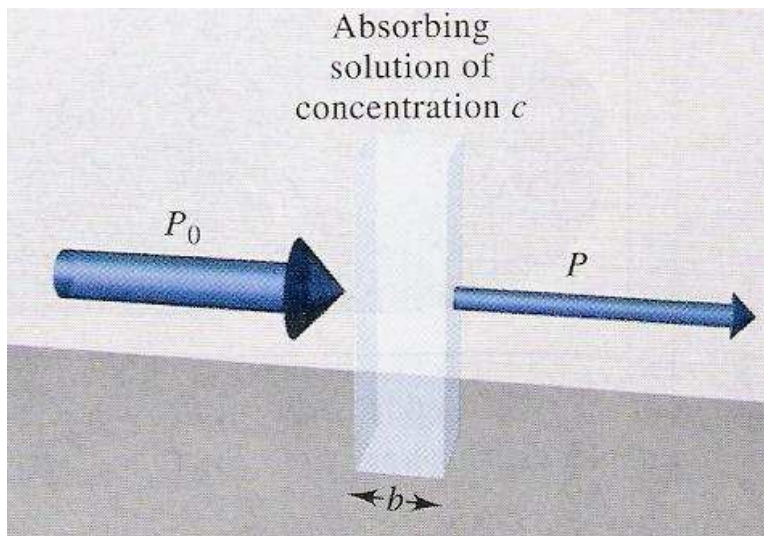


Figure 13: Attenuation of a beam of radiation by an absorbing solution. The larger arrow on the incident beam signifies a higher radiant power than is transmitted by the solution. The path length of the solution is b , and the concentration is c [11].

Figure 13 is a schematic diagram showing the attenuation of a parallel beam of monochromatic radiation passing through an absorbing solution of thickness b centimetres and a concentration of c moles per litre. The interactions between the photons and absorbing particles cause the radiant power of the beam to decrease from P_0 to P . The fraction of incident radiation transmitted by the solution is the transmittance T of the solution, as shown in equation 2. Transmittance is often expressed as a percentage called the percent transmittance.

$$T = \frac{P}{P_0} \quad (2)$$

The absorbance A of a solution is translated to the transmittance in a logarithmic manner, as shown in equation 3. When the absorbance of a solution increases the transmittance will decrease.

$$\begin{aligned} A &= -\log T \\ &= \log \frac{P_0}{P} \end{aligned} \quad (3)$$

5.2 Beer's Law

Absorbance is directly proportional to the concentration of the absorbing species c and to the path length b of the absorbing medium, according to Beer's law. This is expressed by equation 4.

$$\begin{aligned} A &= \log \frac{P_0}{P} \\ &= abc \end{aligned} \quad (4)$$

with a a proportionally constant called the absorptivity. Absorbance is a unit less quantity so the units of the absorptivity must cancel the units of b and c . If b has the units of cm and c have the units of g L⁻¹, then absorptivity must have the units of L g⁻¹ cm⁻¹. When b is expressed in cm and the concentration in moles per litre, the proportionality is called the molar absorptivity and is given the special symbol, ϵ . Thus

$$A = \epsilon bc \quad (5)$$

where ϵ has the units of L mol⁻¹ cm⁻¹ [11].

5.3 Tauc's relation

The band gap of the powder samples can be determined using Tauc's relation [12]. This is a direct relation between the measured energy and the band gap. Figure 14 shows a schematic diagram of the absorption process that takes place in a double beam UV-Vis spectrophotometer.

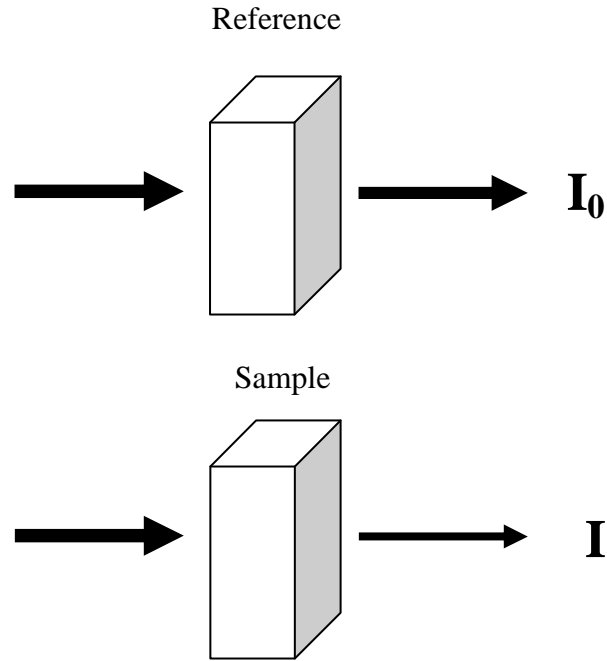


Figure 14: Schematic diagram of the absorption process.

In Figure 14 the intensity of the beam that is measured after it had passed through the reference is referred to as I_0 and the measured intensity of the beam passing through the sample is I . The relation between I and I_0 is given by equation 6

$$I = I_0 e^{(-\alpha x t)} \quad (6)$$

where α is the absorption coefficient, x is the concentration and t is the path length of the cuvette (10 mm in this case). Equation 6 can be rewritten in this form

$$\frac{I}{I_0} = e^{(-\alpha x t)} \quad (7)$$

By taken logs on both sides of equation 7 it can be rewritten as

$$\log\left(\frac{I}{I_0}\right) = -\alpha x t \quad (8)$$

and by making α the subject of the formula a relation for the absorption coefficient can be found in terms of known parameters. This relation is given in equation 9

$$\begin{aligned}\alpha &= -\frac{1}{xt} \log\left(\frac{I}{I_0}\right) \\ &= \frac{1}{xt} \log\left(\frac{I_0}{I}\right)\end{aligned}\tag{9}$$

The absorbance that is measured with the equipment is equal to $\frac{1}{xt} \log\left(\frac{I_0}{I}\right)$. It is also equal to the absorption coefficient, so the absorption coefficient is therefore equal to the measured absorbance and can be used directly in Tauc's relation without any conversion.

Tauc's relation [12] is given by

$$\begin{aligned}(\alpha h\nu) &\approx (h\nu - E_g)^n \\ (\alpha h\nu)^{1/n} &\approx (h\nu - E_g)\end{aligned}\tag{10}$$

where α is the absorption coefficient, $h\nu$ is the photon energy and E_g is the band gap of the material. n indicates the type of transition. The value of n for allowed direct, allowed indirect, forbidden direct and forbidden indirect transitions are $1/2$, 2 , $3/2$, and 3 [13, 14]. When $(\alpha h\nu)^{1/n} \approx 0$ then $0 \approx h\nu - E_g$ and this means that $h\nu \approx E_g$. From this it can be seen that by extrapolating the linear portion of the graph and making $(\alpha h\nu)^{1/n} \approx 0$ the band gap of the material can be obtained.

Absorption and percentage transmittance measurements were performed on the powders using a Shimadzu UV-1700 PharmaSpec UV-Vis spectrophotometer (Figure 15).



Figure 15: The Shimadzu UV-1700 PharmaSpec UV-Vis spectrophotometer.

6. Photoluminescence spectroscopy (PL)

6.1 Theory

Photoluminescence is a non-destructive, contactless method of probing the electron structure of materials. Photo-excitation occurs when light is directed onto a sample and it gets absorbed and imparts excess energy into the material. One of the ways this excess energy can be dissipated by the sample is through the emissions of light. This process is called luminescence. When the luminescence is accompanied by photo-excitation it is called photoluminescence (Figure 16). Various important material properties give a direct measure of the spectral content and intensity of this photoluminescence.

Electrons within the material moving into permissible excited states are caused by photo-excitation. Excess energy is released when these electrons return to their equilibrium states, and this may include the emission of light (radiative process) or a non-radiative process (Figure 16). The energy of the emitted light relates to the difference in the energy levels between the two electron states that is involved in the transition between the excited and equilibrium state. The relative contribution of the radiative process is related to the quantity of the emitted light.

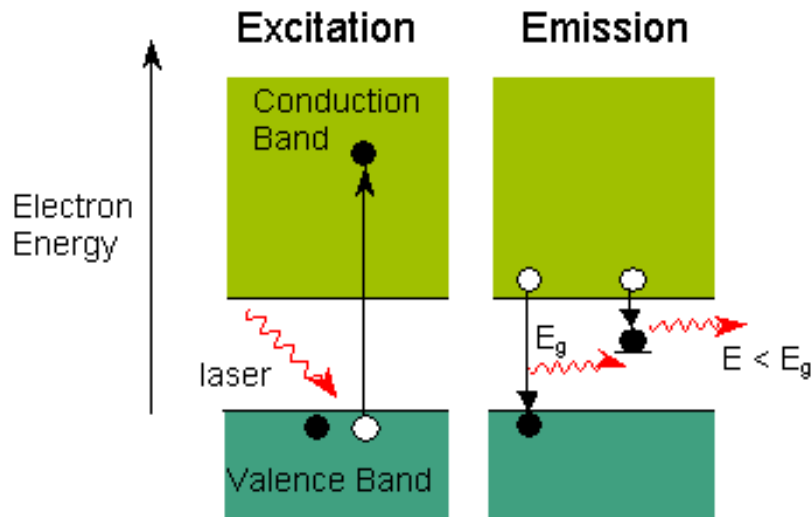


Figure 16: E_g is the band gap energy. On the left a high energy laser photon kicks an electron from its orbit. The electron loses some energy until it reaches the bottom of the conduction band. Two possible transitions are shown on the right hand diagram. On the left the electron combines immediately with a hole in the valence band, emitting a photon of energy E_g . On the right it gets stuck in a 'mid-gap' state (impurity level) emitting a lower energy photon [15].

Photoluminescence can be used in many different ways:

6.1.1 Determination of the band gap.

The most common radiative transition in semiconductors is between states in the conduction and valence bands, with the energy difference between these bands being known as the band gap. When working with new compound semiconductors the determination of the band gap is particularly useful.

6.1.2 Detection of impurity levels and defects.

Localized defect levels are also involved in radiative transitions in semiconductors. Specific defects can be identified by using the photoluminescence energy associated with these levels and their concentration can be determined by the amount of photoluminescence.

6.1.3 Mechanisms of recombination.

Recombination or the return of electrons to their equilibrium state, can involve both radiative and non-radiative processes. The dominant recombination process directly relates to the amount of photoluminescence and its dependence on the level of photo-excitation and temperature. The understanding of the underlying physics of the recombination mechanism is greatly assisted by the analysis of the photoluminescence [16].

The PL measurements were done using either a 325 nm HeCd (26mW) laser as an excitation source (Figure 17 and Figure 18) or a Cary Eclipse fluorescence spectrophotometer (Figure 19).



Figure 17: PL system at NMMU with a 325 nm HeCd (26mW) laser as an excitation source.

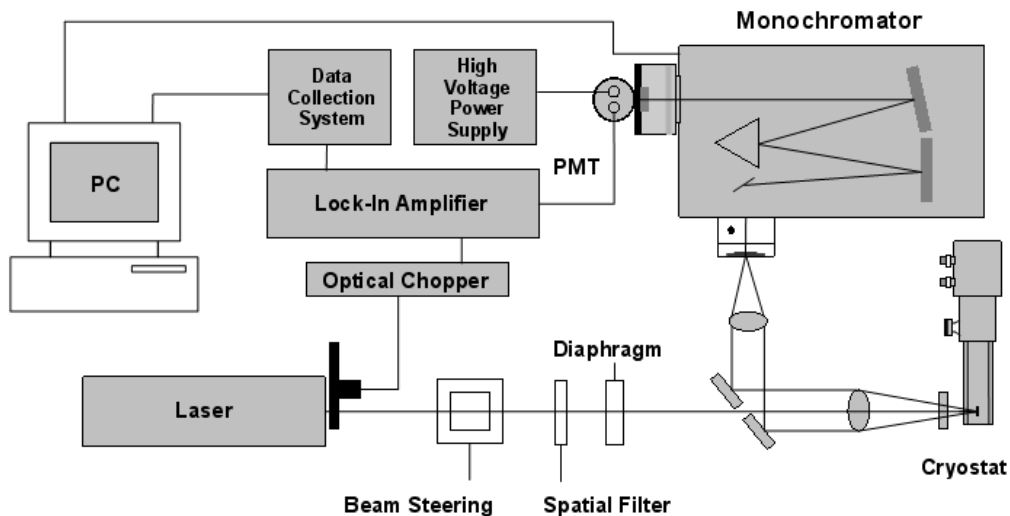


Figure 18: Schematic diagram of the PL system at NMMU.



Figure 19: Cary Eclipse fluorescence spectrophotometer.

7. Cathodoluminescence (CL)

7.1 Theory

Cathodoluminescence is an electrical and optical phenomenon where an electron gun generates a beam of electrons and this beam then impact on a luminescent material such as a phosphor, causing it to emit visible light. The screen of a television is the most common example (Figure 20).

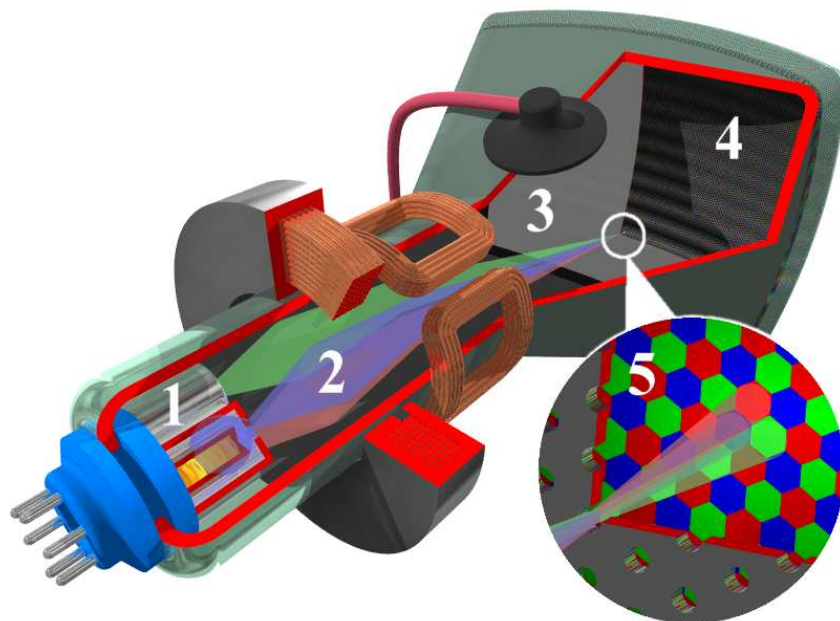


Figure 20: The inside of a television or computer screen. 1-3 shows the cathode ray tube (CRT) and 4 and 5 shows the phosphor coated screen [17].

Cathodoluminescence occurs when a high energy electron beam impinges on a semiconductor, which will excite electrons from the valence band to the conduction band, leaving a hole in the valence band. With electron-hole recombination it is possible for a photon to be emitted. The energy (colour) of the photon and the probability that a photon and not a phonon will be emitted depends on the material, its defect states and purity. Any non-metallic material or semiconductors can be examined in this case. A highly focussed electron beam impinges on a sample and the sample emits light from a localized area. An optical system (such as an elliptical mirror) collects this light. A fiber optic will transfer the light out of the microscope, where it will be separated by a monochromator and then detected by a photomultiplier tube.

Direct band gap semiconductors are most easily examined by this technique, but indirect band gap semiconductors such as silicon also emit weak levels of light, and can be examined as well. In the case of a semiconductor specimen, the cathodoluminescence energy is equivalent to the energy gap between the valence and conduction band (band gap) [18].

CL data were collected for 24 hr with a S200/PC2000/USB2000/HR2000 spectrometer type using OOI Base 32 computer software. Figure 21 shows the whole system (ESCA system) that can record a CL, AES and RGA spectrum simultaneously.



Figure 21: The ESCA system.

8. Auger electron spectroscopy (AES)

8.1 Theory

Auger electron spectroscopy (AES) is a surface analytical technique and it can determine the chemical composition of the surface layers of a sample. An electron beam excites the sample and the beam can be focussed into a fine probe. The Auger effect is an electronic process at the heart of AES resulting from the intra- and interstate transitions of electrons in an excited atom. When an atom is probed by an electron beam (energy range 2keV - 50keV), an electron from the core is removed leaving behind a hole (the ionization step in Figure 22). An outer shell electron then fills the core hole (the relaxation step in Figure 22). The electron that moves to the lower energy level (core state) loses an amount of energy that is equal to the difference in orbital energies. The energy that is lost can either appear as an x-ray photon or it can be transferred to another electron which is then ejected from the atom (step 3 in Figure 22). This ejected electron is called the Auger electron. This electron then moves through the solid and loses some of its energy through inelastic collision with bound electron in the solid. If the Auger electron is however released sufficiently close to the surface, it can escape the surface with little or no loss in energy and can be detected by an electron spectrometer.

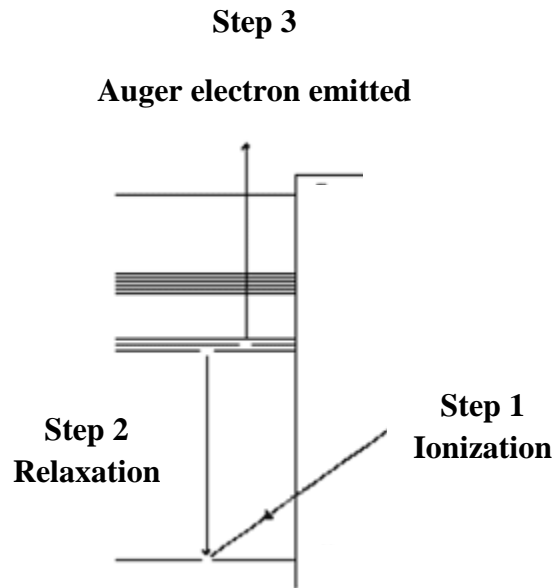


Figure 22: Schematic diagram of the Auger effect [19].

The characteristic kinetic energy (E_{KLM}) of the ejected electron is (Figure 23):

$$E_{KLM} = E_K - E_L - E_M \quad (11)$$

where E_K , E_L and E_M are the energies of the respective shells. The kinetic energy of the ejected electron is independent of the mechanism of initial hole formation. The type of element determines the energies of the different orbitals (shells) of the atom. The composition of the surface of a sample can therefore be determined. The probability of the emission of a characteristic Auger electron from a lighter element is higher than for heavy elements, because in heavy elements the electrons in the 1s shell are more tightly bound to the nucleus, and the AES technique is therefore more sensitive to the lighter elements. AES must be performed under ultra high vacuum (UHV) conditions (pressures of 10^{-9} - 10^{-10} Torr) to prevent gasses from absorbing and scattering the very low energy Auger electrons and to prevent the formation of a thin “gas layer” on the surface of the specimen degrading analytical performance [20].

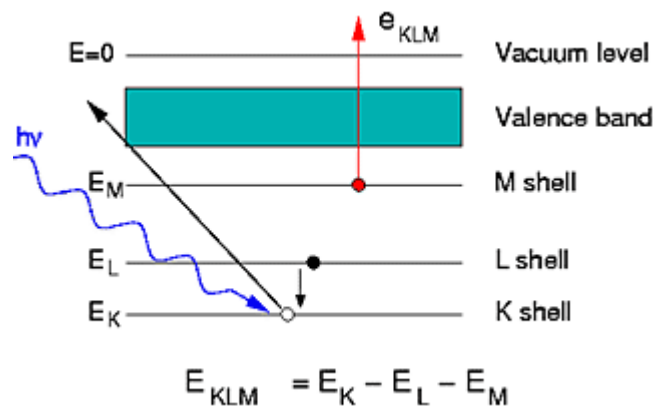


Figure 23: Diagram showing the characteristic kinetic energy of the ejected electron [21].

The AES spectra were recorded in an ultrahigh vacuum (UHV) chamber with a PHI Model 549 system (Figure 21).

9. Residual gas analysis (RGA)

9.1 Theory

Residual gas analysis is used to identify the gasses that are present in vacuum environments. In this study RGA was used to determine the different kind of gas species present in the vacuum environment during AES and CL measurements. Residual gas analysers operate by creating a beam of ions from samples of the gas being analysed. This results in a mixture of ions and they are then separated into individual species through their charge-to-mass ratios. A typical RGA has three major parts: ionizer, mass analyser and ion detector. The output spectrum of an RGA shows the relative intensities of the various gas species that are present. This output is known as a mass spectrum or mass scan.

The molecules of the analysed gas are turned into ions by an ionizer through electron impact ionization. An electron beam is used to strike the gas atoms to ionize them. A hot emission filament generates this ionizing electron beam and it is extracted by means of an electric field. Reactive gasses like oxygen can easily destroy this hot filament and that is why RGA's operate at pressures of less than 10^{-4} Torr.

The mass analyser distinguishes the ions from the gas from each other in terms of their masses. Various mass separation techniques exist, but the mass analysers used in RGAs usually employ the RF quadrupole (Figure 24). This quadrupole has four cylindrical rods that are provided with combinations of DC and AC voltages of varying frequency. For a given applied frequency only ions that possess the right mass-to-charge ratio can reach the ion collector. For the detection of ions at less sensitive ranges a Faraday cup may be used, but for ion detection at higher sensitivities, an electron multiplier is required.

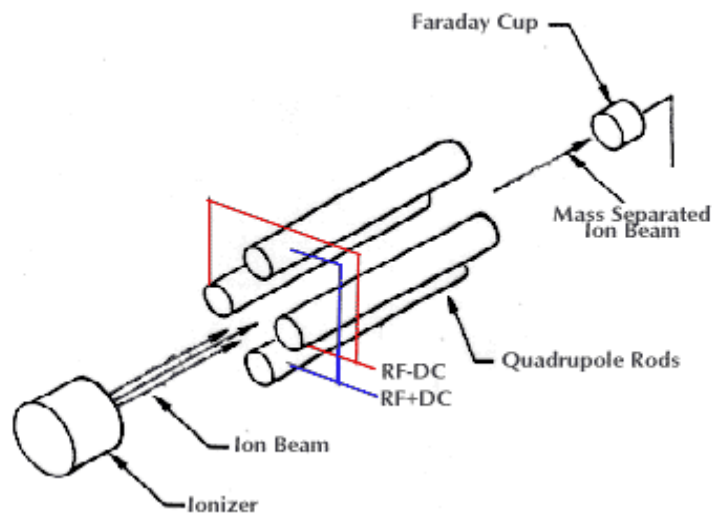


Figure 24: Schematic diagram of a RF quadrupole [22].

The mass spectra are usually represented as a chart with a mass-to-charge ratio on the x-axis and the relative intensities on the y-axis (Figure 25). The peaks that are exhibited by a mass spectrum must be interpreted properly since these can be ambiguous in certain cases, such as when two different molecules exhibit the same mass. By knowing how the two different molecules with the same mass would dissociate into smaller fragments of different mass-to-charge ratios (known as cracking patterns) allows for absolute identification of the gas.

In the semiconductor industry, RGA is used in identifying vapours, gases, or residues for the purpose of finding leaks in vacuum systems and eliminating contaminants that causes process problems or product failures [23].

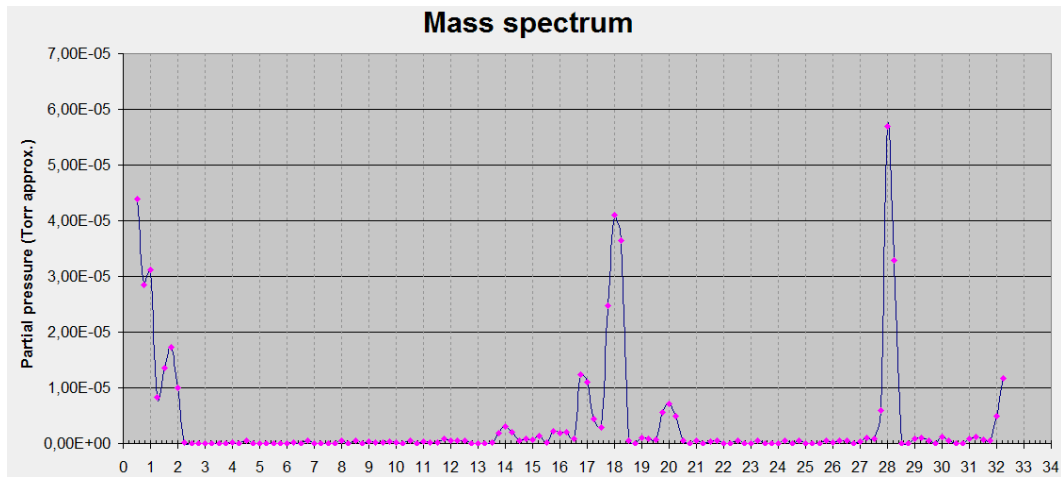


Figure 25: Example of a RGA mass spectrum [24].

RGA was performed to determine the volatile gas species during electron bombardment of a sample, by using the Anavac-2 mass analyser (Figure 21).

References

- 1 Scanning electron microscope, [online]. Available from http://en.wikipedia.org/wiki/Scanning_electron_microscope [Accessed 15 May 2009].
- 2 Scanning electron microscope (SEM), [online]. Available from <http://www.purdue.edu/REM/rs/sem.htm> [Accessed 15 May 2009].
- 3 Electrons in Scanning electron microscopy, [online]. Available from <http://www.vcbio.science.ru.nl/en/fesem/info/principe/> [Accessed 12 May 2009].
- 4 Introduction to XEDS in the AEM, [online]. Available from <http://209.85.229.132/search?q=cache:nImyTkuTBRUJ:tpm.amc.anl.gov/Lectures/XEDSAEMShortCourse.pdf+Recall+that+for+each+atom+every+shell+has+a+unique+level+determine+by+atomic+configuration+for+that+element.&cd=1&hl=en&ct=clnk&gl=za> [Accessed 13 May 2009].
- 5 Energy Dispersive X-ray Spectroscopy (EDS/EDX), [online]. Available from <http://www.thermo.com/com/cda/technology/detail/1,,12700,00.html> [Accessed 13 May 2009].
- 6 The Transmission Electron Microscope (TEM) <http://www.biologie.uni-hamburg.de/b-online/e03/03e.htm> [Accessed 13 May 2009].
- 7 The Transmission Electron Microscope (TEM), [online]. Available from <http://www.biologie.uni-hamburg.de/b-online/ge03/14.gif> [Accessed 26 May 2009].
- 8 Specimen stage, [online]. Available from http://en.wikipedia.org/wiki/Transmission_electron_microscope [Accessed 26 May 2009].
- 9 Crystal structure [online] available from <http://wpcontent.answers.com/wikipedia/commons/thumb/5/5e/UnitCell.png/300px-UnitCell.png> [Accessed 4 May 2009].
- 10 Bragg's Law and diffraction, [online]. Available from <http://www.eserc.stonybrook.edu/ProjectJava/Bragg/> [Accessed 25 May 2009].
- 11 D.A. Skoog, D.M. West, F.J. Holler and S.R. Crouch, Fundamentals of Analytical Chemistry 8th edition, Brooks/Cole – Thomson Learning, USA, (2004) p. 715 - 720.
- 12 J. Tauc, R. Grigorovici and A. Vancu, Phys. Status Solidi, **15** (1966) 627.
- 13 V. Kumar, R. Kumar, S.P. Lochab and N. Singh, Nucl. Instr. and Meth. in Phys. Res. B, **262** (2007) 197.
- 14 R.Sarkar, C.S. Tiwary, P. Kumbhakar, S. Basu and A.K. Mitra, Physica E, **40** (2008) 3116.

- 15 Photoluminescence [online] available from <http://www.macdiarmid.ac.nz/news/success/Reeves.php> [Accessed 4 May 2009].
- 16 Photoluminescence spectroscopy, [online]. Available from http://www.nrel.gov/pv/measurements/photoluminescence_spectroscopy.html [Accessed 25 May 2009].
- 17 What's inside your computer, [online]. Available from <http://lions-wing.net/lessons/hardware/hard.html> [Accessed 18 May 2009].
- 18 Cathodoluminescence, [online]. Available from <http://en.wikipedia.org/wiki/Cathodoluminescence> [Accessed 18 May 2009].
- 19 Auger electron spectroscopy (AES), [online]. Available from <http://www.phy.com/techniques/aes.html> [Accessed 18 May 2009].
- 20 Auger electron spectroscopy, [online]. Available from http://en.wikipedia.org/wiki/Auger_electron_spectroscopy [Accessed 26 May 2009].
- 21 AES (Auger Electron Spectroscopy), [online]. Available from <http://lasuam.fmc.uam.es/lasuam/glossary.php#aes> [Accessed 20 May 2009].
- 22 Basic vacuum concepts, [online]. Available from <http://www.fnrf.science.cmu.ac.th/theory/vacuum/Basic%20Vacuum%20Concepts.html> [Accessed 21 May 2009].
- 23 Residual Gas Analysis (RGA), [online]. Available from <http://www.siliconfareast.com/rga.htm> [Accessed 21 May 2009].
- 24 Set up of mass spectrometer and first mass Spectrum, [online]. Available from http://es.geocities.com/queralv/LastResults/Set_Up_Of_Mass_Spectroscopy_And_First/Set_Up_Of_Mass_Spectroscopy_And_First.htm [Accessed 21 May 2009].

Chapter 4

Luminescent mechanism of ZnS:Mn²⁺

In this chapter the luminescent mechanism of ZnS:Mn²⁺ is discussed. An explanation of the ⁴T₁-⁶A₁ transition of Mn²⁺ is given as well as an explanation of the terms involved. The role of the Tanabe-Sugano diagrams in explaining the terms involved is given as well as how the Russell-Saunders coupling scheme and the Ligand field theory can explain the Tanabe Sugano diagrams. By using the energy dispersion and configurational coordinate model the blue and red shift in the excitation and emission spectra of ZnS and ZnS:Mn²⁺ are explained.

1. Introduction

When ZnS is doped with Mn²⁺ orange emission is observed. This orange emission is due to the ⁴T₁-⁶A₁ transition of Mn²⁺. These transitions were explained in terms of the Tanabe-Sugano diagrams for the *d*⁵ level and the Ligand field theory by different researchers [1-5].

2. Orgel (Correlation) diagrams

Orgel diagrams shows the energies of all possible terms for a given d electron configuration as a function of the ligand field splitting Δ [6]. It shows the energy levels of both high spin octahedral and tetrahedral transition metal ions. It only shows the spin allowed transitions [7]. The left and right sides of the diagram represents two extremes. The left hand side is for a free ion (no field) and LS coupling determines the energies of the terms or microstates. The right hand side is for a coordinate ion (ligand field) and the ligand field splitting determines the energy of the terms or microstates.

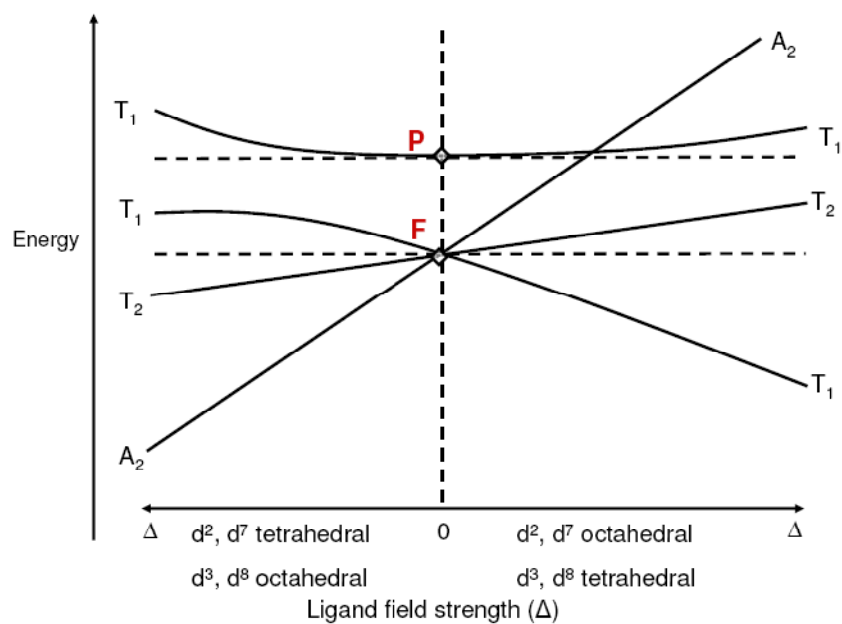
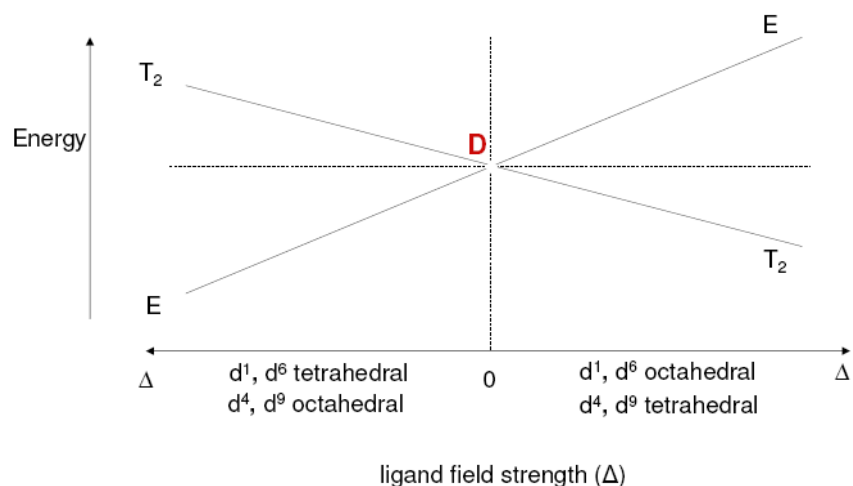


Figure 1: a) Orgel diagram for complexes with D ground terms and b) Orgel diagram for complexes with F and P ground terms [8].

In Figure 1 (a) the Orgel diagram for a complex with D ground terms is shown. Only one electronic transition is expected and its energy corresponds directly to D. d^1 , d^6 tetrahedral and d^4 , d^9 octahedral complexes are covered on the left hand side and on the right hand side d^4 , d^9 tetrahedral and d^1 , d^6 octahedral. Figure 1 (b) shows the diagram for complexes with F ground terms. Three electronic transitions are expected and D may not correspond directly to the transition energy. d^2 , d^7 tetrahedral and d^3 , d^8 octahedral complexes are covered on the left hand

side and d^3 , d^8 tetrahedral and d^2 and high spin d^7 octahedral complexes are covered on the right hand side.

3. Tanabe-Sugano diagram for a d5 ion

The Orgel diagrams lack some features necessary for practical quantitative use. Calculations of electronic state energies as a function of ligand field strength are available and this can be used for quantitative fitting of observed spectra. Tanabe and Sugano has taken these results and compiled the Tanabe-Sugano diagrams [3] and they are used to interpret spectra for ions of all types, from d^2 to d^8 . The Tanabe-Sugano diagrams are a modified form of the Orgel diagrams and they are able to predict the transition energies for both low spin (strong field) and high spin (weak field) complexes, as well as for both spin-allowed and spin forbidden transitions. The energy of the electronic states is expressed as E/B (y-axis) and this is plotted against the ligand field strength Δ/B (x-axis). E is the term energy, B is the Racah parameter and Δ is the ligand field splitting energy.

The Racah parameter can be explained as follows [9]: when you have a multi-electron atom, there exists some electrostatic repulsion between these electrons. This repulsion is not the same for each atom and varies from atom to atom, depending on the orbitals they occupy and the number and spin of the electrons. The three parameters A , B and C , which are known as the Racah parameters, express the total repulsion of an atom. Giulio Racah first described them in 1942 [10]. They can be obtained empirically from gas-phase spectroscopic studies of atoms. In transition-metal chemistry they are often used to describe the repulsion energy associated with an electronic term. Since $C \approx 4B$, terms with energies that depend on both B and C can be plotted on the same diagrams.

The zero energy of the diagrams is always taken as the ground state term (lowest term) therefore the energy is a relative energy with respect to the ground state. Some diagrams are therefore discontinuous (see $d^4 - d^7$) when the ground term is changed [11]. This happens when the ligand field becomes strong enough to favour electron pairing.

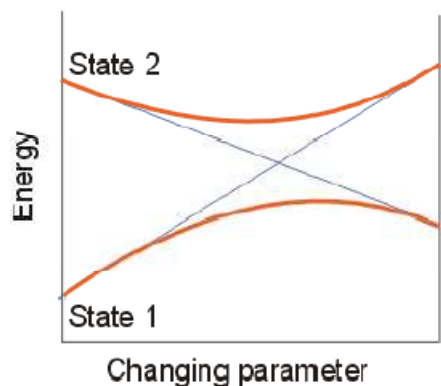
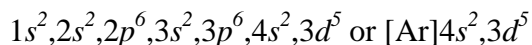


Figure 2: Illustration of the noncrossing rule: This rule states that if two states of the same symmetry are likely to cross with the change of a parameter (thin lines), they will avoid crossing and will mix together (thick lines) [11]

Curved lines are observed for both the Orgel and Tanabe-Sugano diagrams. This is due to mixing of terms of the same symmetry type. These states obey the noncrossing rule which states that if the increasing ligand field causes two weak field terms of the same symmetry to approach, they will bend apart from each other and do not cross. They will mix generating a lower and higher energy state.

Mn has 25 electrons. The electron configuration for Mn is [12]:



Mn^{2+} has 23 electrons. The electron configuration for Mn^{2+} is:

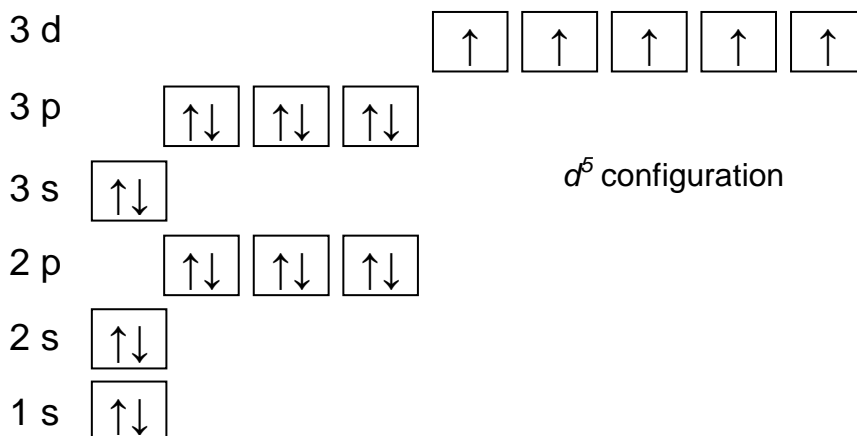
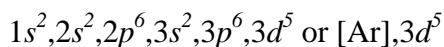


Figure 3: Aufbau diagram of Mn^{2+} .

From the electron figuration and the Aufbau diagram of Mn^{2+} (Figure 3) it can be seen that Mn^{2+} has a d^5 configuration and is therefore a d^5 ion. The Tanabe-Sugano diagram for a d^5 ion can thus be used to describe the states and terms of Mn^{2+} .

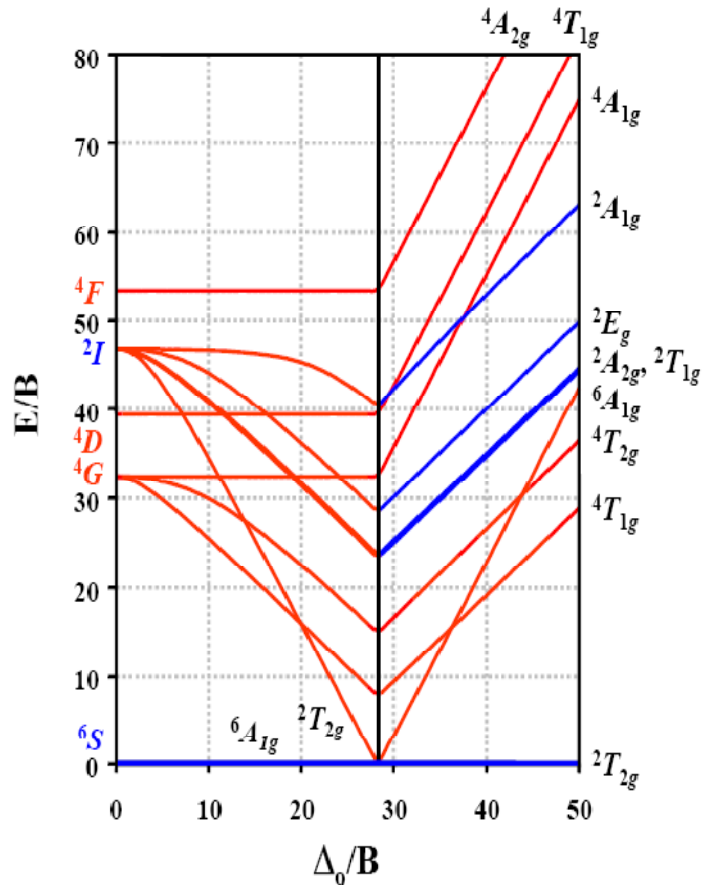


Figure 4: The Tanabe-Sugano diagram for a d^5 ion [13].

As is the case for the Orgel diagrams, the Tanabe-Sugano diagrams (Figure 4) have also two extremes. The left side can be described by die Russell-Saunders coupling scheme and the right side by the Ligand field theory.

4. Russell-Saunders or LS coupling scheme.

4.1 Quantum numbers

4.1.1 Principle quantum number (n)

This number largely determines the size and energy of the orbitals. Electrons in an atom reside in shells and these shells are characterized by a particular value of n . $n = 1, 2, 3, \dots$. The main shells are labelled as follow: K ($n = 1$), L ($n = 2$), M ($n = 3$), etc (Figure 5).

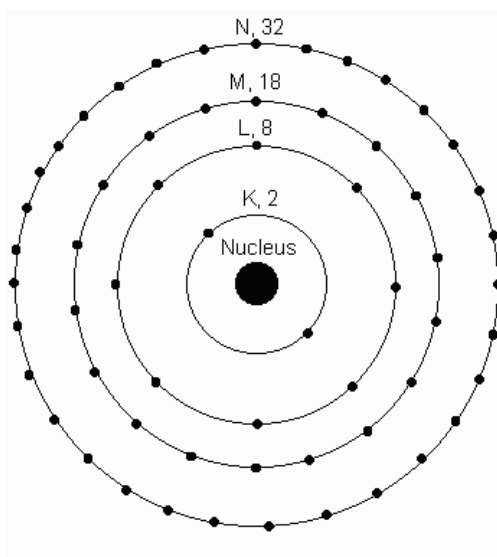


Figure 5: Diagram of the shells of an atom [14].

4.1.2 Azimuthal or Orbital quantum number (l)

This number determines the shape of the orbital. The electrons in each shell can occupy an orbital and these orbitals are described by the orbital quantum number (l). $l = 0, 1, 2, 3, \dots, (n - 1)$. The orbitals are traditionally termed s, p, d, f, etc.

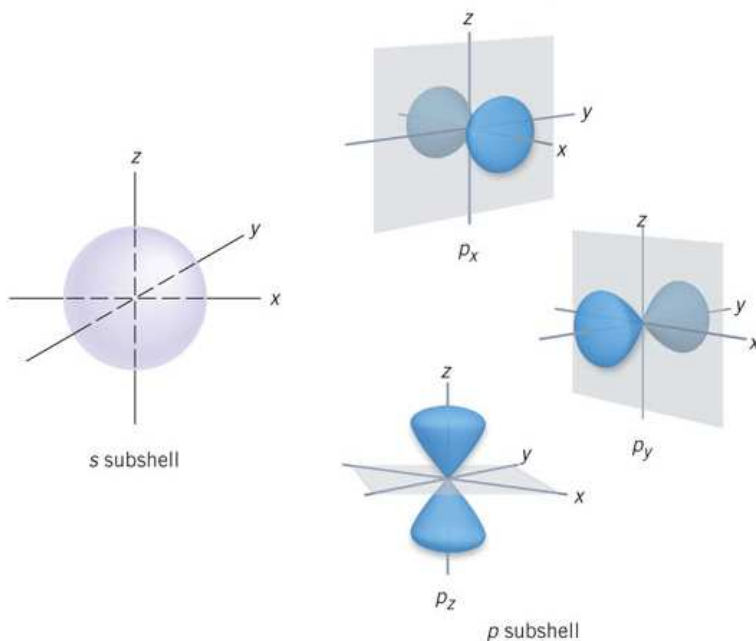
4.1.3 Magnetic quantum number (m_l)

m_l is a subset of l and describes orbitals orientation in space. It denotes the available energy levels within the subshells (Figure 6). The allowed values of $m_l = l, l - 1, l - 2, \dots, 1, 0, -1, \dots, -(l - 2), -(l - 1), -l$.

Table 1 gives the relationship between the different quantum numbers for each orbital.

Table 1: Relationship between quantum numbers.

Orbital	Values	Number of values for m_l
S	$l = 0, m_l = 0$	1
P	$l = 1, m_l = -1, 0, 1$	3
D	$l = 2, m_l = -2, -1, 0, +1, +2$	5
F	$l = 3, m_l = -3, -2, -1, 0, +1, +2, +3$	7
G	$l = 4, m_l = -4, -3, -2, -1, 0, +1, +2, +3, +4$	9



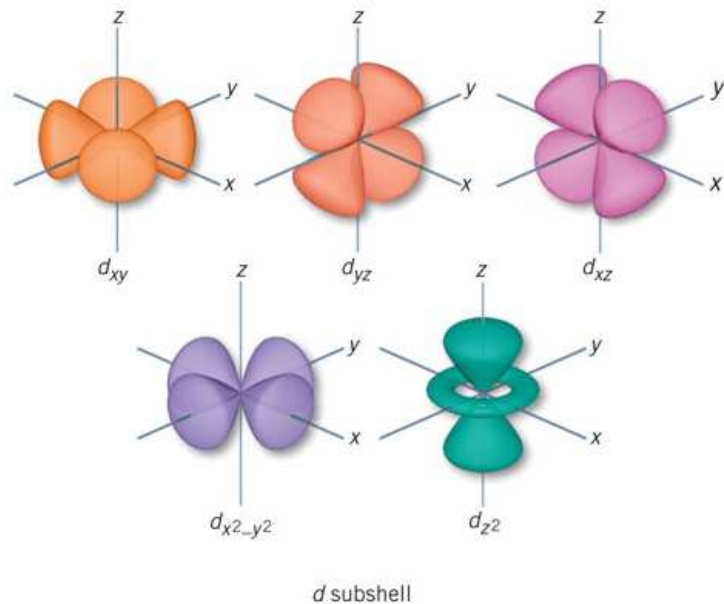


Figure 6: Diagram of the s, p and d subshells [15].

4.1.4 Spin quantum number (m_s)

m_s is the fourth quantum number and it indicates the orientation of the spin axis of an electron. The Pauli Exclusion Principle states that “no two electrons in the same atom can have identical values for all four of their quantum numbers.” This means that only two electrons can occupy a subshell of an orbital and these electrons must have opposite spins (up and down spins). The value of m_s is either $+\frac{1}{2}$ or $-\frac{1}{2}$ (Figure 7).

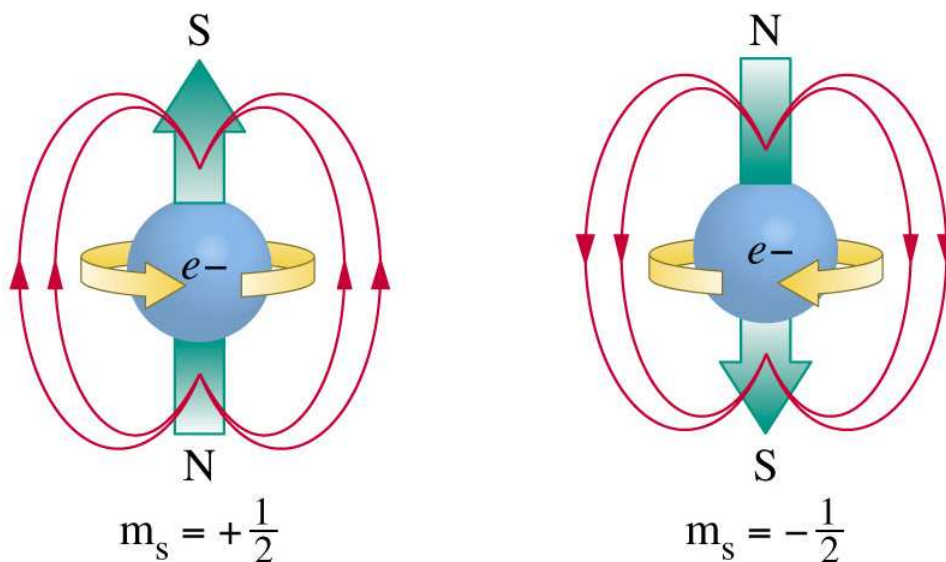


Figure 7: Schematic diagram illustrating the orientation of the spin of an electron. Because of the spin the electron can be treated as a tiny magnet [16].

4.2 Coupling types

In the case of Russell-Saunders coupling three types of interactions can occur:

- Spin-spin coupling or coupling of spin momenta.
- Orbit-orbit coupling or coupling of orbital angular momenta.
- Spin-orbit coupling or coupling of spin and orbital angular momenta.

4.2.1 Spin-spin coupling (S)

The resultant spin quantum number of a system of electrons is S . Electrons in the same orbital can only have two relative orientations: spinning in opposite direction and spinning in the same direction. The spins can be added vectorially and the resultant lies in the same straight line as the component vectors. The spins also combine vectorially in a many electron atom. When there is an even number of electrons S takes on an integral number and for an odd number of electrons it takes on a half integral value. S is the resultant spin angular momentum vector and it is related to the quantum number S by the expression

$$\mathbf{S} = \sqrt{S(S+1)}\hbar \quad (1)$$

where $S = \pm 1/2$.

$$\begin{aligned} \therefore \mathbf{S} &= \sqrt{\left(\frac{1}{2}\left(\frac{1}{2}+1\right)\right)}\hbar \\ &= \frac{\sqrt{3}}{2}\hbar \end{aligned} \quad (2)$$

and the z component (Figure 8) of the spin angular momentum is [17]:

$$S_z = \pm \frac{1}{2}\hbar \quad (3)$$

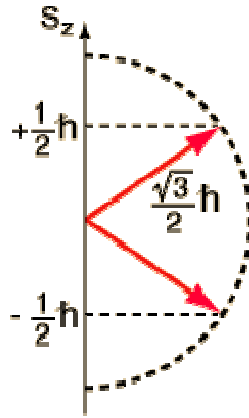


Figure 8: Diagram showing the different components of the spin angular momentum [17].

4.2.2 Orbit-orbit coupling (L)

A vector can represent the orbital angular momentum and the resultant angular orbital momentum is a vector combination of the angular momentum of all occupied orbitals in the atom. In a two electron atom each electron occupied orbital has its own angular momentum, but it is also affected by the other occupied orbitals angular momentum, because they are coupled together by electrostatic forces between the electrons and the nucleus and between the electrons them self. The angular momentums therefore act upon each other, and cause precession around the direction of the resultant angular momentum (Figure 9). This remains constant in magnitude and direction by the principle of conservation of angular momentum. L is the resultant angular

momentum of the whole occupied orbital system. l is the vector quantity for a single electron and it is expressed by

$$l = \sqrt{l(l+1)}\hbar \quad (4)$$

and for many electrons:

$$L = \sqrt{L(L+1)}\hbar \quad (5)$$

where L is the quantum number of the resultant orbital angular momentum. l , the angular momentum vector, makes a constant angle with the direction of \mathbf{L} , therefore precession of each orbital angular momentum takes place about the direction of \mathbf{L} in space. It does not precess if one of the individual l 's is already parallel to \mathbf{L} . For an s orbital $l = 0$ (see orbital quantum number). The angular momentum of two p orbitals can combine in one of three ways: $\mathbf{L} = 0$, l or $2l$ (Figure 10).

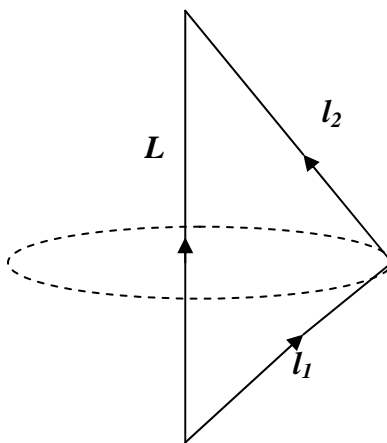


Figure 9: Coupling of orbital angular momenta (Redrawn from reference [18], p89).

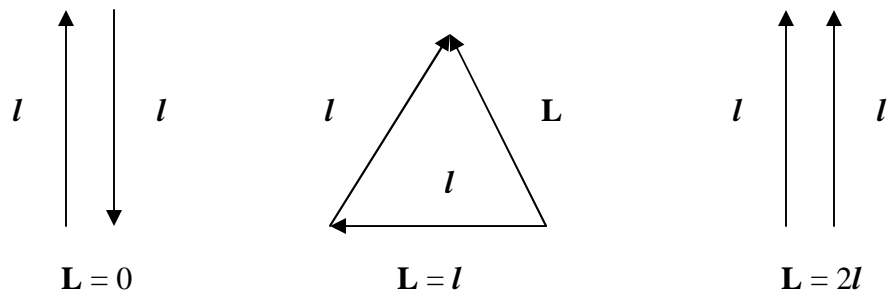


Figure 10: Vectorial combination of orbital angular momenta, showing three possible values for L (Redrawn from reference [18], p89).

4.2.3 Spin-orbit coupling (J)

For a single electron it is clear that the coupling of its spin and orbital angular momenta must be by means of their magnetic field, because there is no electrostatic coupling between them. The coupling between spin and orbital angular momenta is therefore magnetic. The coupling of angular momenta in an atom can theoretically be described by either the Russell-Saunders (LS) coupling or the jj coupling.

4.3 Russell-Saunders (LS) coupling

The resultant spin angular momentum (\mathbf{S}) is given by the electrostatically coupled separate spin angular momenta. The resultant orbital angular momentum (\mathbf{L}) is given by the electrostatically coupled separate orbital angular momenta. \mathbf{S} and \mathbf{L} are coupled magnetically. When they are combined vectorially they give the resultant angular momentum of the atom \mathbf{J} . This is related to the quantum number J by the expression:

$$\mathbf{J} = \sqrt{J(J+1)}\hbar \quad (6)$$

$J = (L - S), (L - S + 1), \dots, (L + S - 1), (L + S)$. From these values of J it can be clearly seen why this form of coupling is called LS coupling. This applies, in general, to the lighter elements (Figure 11).

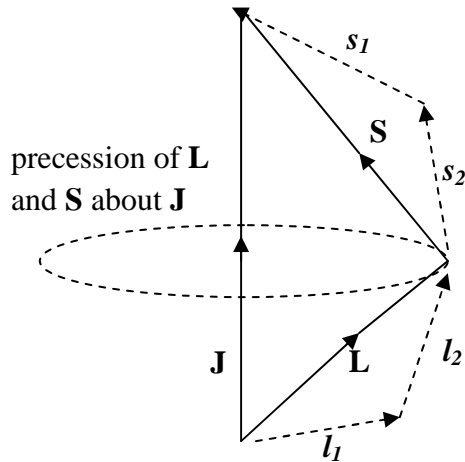


Figure 11: Russell-Saunders (LS) coupling. (Redrawn from reference [18], p90).

4.4 jj coupling

For each electron the spin and orbital angular momentum are coupled magnetically together and this gives the resultant angular momentum of the electron **j** (Figure 12). This is related to the quantum number *j* by the expression:

$$\mathbf{j} = \sqrt{j(j+1)}\hbar \quad (7)$$

Magnetically combination of all the **j**'s gives the resultant angular momentum of the atom (**J**). This method of coupling applies to the heavy elements where the electrostatic coupling between the electrons is small.

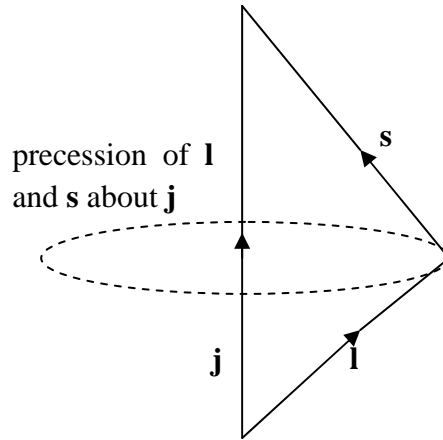


Figure 12: Coupling of l and s for a single electron. (Redrawn from reference [18], p91).

L and S precess round J in the case of the Russell-Saunders coupling. The separate j 's precess round J in the case of jj coupling (Figure 13). The direction and magnitude of J remains constant in both cases.

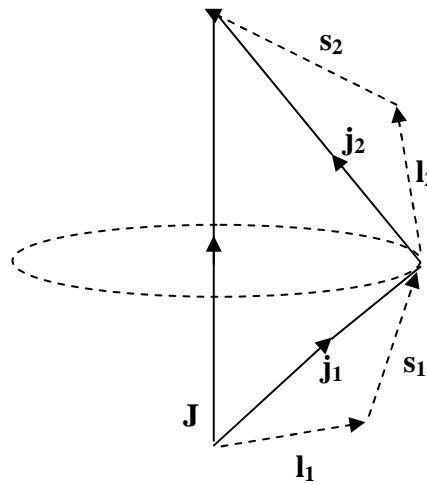


Figure 13: jj coupling. j_1 and j_2 precess around J (Redrawn from reference [18], p91).

4.5 Term symbols

The arrangement of electrons is represented by the term symbol. This symbol shows how the electrons in a d^n configuration are distributed among the 5 d orbitals. Their electronic arrangements will differ in energy depending on the extent to which the d electrons interact (e.g. suffer coulombic repulsions) [19]. The term symbol is defined as

$$2S+1 \mathbf{L}_J \quad (8)$$

The values of **S**, **L** and **J** are determined as follows:

• **S**

S is the total spin of an atom and it is the vector sum of the spin angular momenta of the individual electrons [20]

$$\mathbf{S} = \Sigma m_s \quad (9)$$

$m_s = +1/2$ if it is spin up and $m_s = -1/2$ if it is spin down (Figure 7). $2S + 1$ is the multiplicity of an atom and this is the total spin of an atom. The values for $2S + 1$ are:

$$\begin{array}{cccccc} S = & 0 & 1/2 & 1 & 3/2 & 2 & 5/2 \dots \\ 2S + 1 = & 1 & 2 & 3 & 4 & 5 & 6 \dots \end{array}$$

The value of $2S + 1$ shows the multiplicity of the atom. For $2S + 1 = 1$ it is a singlet, for $2S + 1 = 3$ a triplet and for $2S + 1 = 6$ a sextet.

• **L**

L is the total orbital angular momentum and it is the vector sum of the individual orbital momenta of the electrons [20]

$$\mathbf{L} = \Sigma m_l \quad (10)$$

By analogue with the notations s, p, d, \dots for the orbitals with $l = 0, 1, 2, \dots$, the total angular momenta is denoted by the upper-case equivalents:

$$\begin{array}{cccccc} L = & 0 & 1 & 2 & 3 & 4 \dots \\ & S & P & D & F & G \end{array}$$

• **J**

The total spin-orbit angular momentum is denoted by **J** (equation 6). The quantum number **J** can take the following values: $(L - S)$, $(L - S + 1)$, ..., $(L + S - 1)$, $(L + S)$. For the different values of L and S the values for J can be: 0, 1, 2 ... or $1/2$, $3/2$, $5/2$... There are $(2S+1)$ possible values of J for $S < L$ and $(2L + 1)$ values of J for $L > S$.

Term symbol for the ground state

The ground state refers to free ions. In this case we are looking at free transition metal ions (no ligands). Hund's rules must be obeyed in this order:

1. The ground state has a maximum **S** value; that is the maximum number of unpaired electrons.
2. It has a maximum **L** value (assuming rule 1 is already obeyed).
3. It has a minimum **J** if the shell is less than half full and maximum **J** if the shell is more than half full.

Table 2: Ground terms for the free ions of d^n .

d^n	2	1	0	-1	-2	L	S	Ground Term
d^1	↑					2	1/2	2D
d^2	↑	↑				3	1	3F
d^3	↑	↑	↑			3	3/2	4F
d^4	↑	↑	↑	↑		2	2	5D
d^5	↑	↑	↑	↑	↑	0	5/2	6S
d^6	↑↓	↑	↑	↑	↑	2	2	5D
d^7	↑↓	↑↓	↑	↑	↑	3	3/2	4F

d^8	$\uparrow\downarrow$	$\uparrow\downarrow$	$\uparrow\downarrow$	\uparrow	\uparrow	3	1	3F
d^9	$\uparrow\downarrow$	$\uparrow\downarrow$	$\uparrow\downarrow$	$\uparrow\downarrow$	\uparrow	2	1/2	2D

Table 2 gives the values of the ground terms for the free ions of d^n . The terms are determined as follow:

- **S** is the sum of the unpaired electrons each using a value of 1/2 ($\uparrow = +1/2$, $\downarrow = -1/2$ and $\uparrow\downarrow = 0$). For d^7 $S = 0 + 0 + 1/2 + 1/2 + 1/2 = 3/2$
- The value of **L** is the sum of the labels for each column. For d^7 $L = (2 \times 2) + (1 \times 2) + 0 - 1 - 2 = 3$
- The ground term for d^7 is therefore 4F

4.6 Microstates

Each atom or ion has its own unique set of quantum numbers. For example: The configuration of a $2p^2$ ion is $n = 2$; $l = 1$, $m_l = -1, 0, 1$; $m_s = \pm 1/2$. Many configurations can fit that description. These configurations are called microstates and they have different energies because of their inter-electronic repulsions. The number of microstates is given by [21]

$$W = \frac{N!}{n_0! n_1! \dots n_k!} \quad (11)$$

where $N!$ is the total number of electrons in the outer shell, and n is the number of electrons.

The number of microstates for the hydrogen atom is $\frac{2!}{1! \times 1!} = 2$

The number of microstates for the carbon atom is $\frac{6!}{2! \times 4!} = 15$

The number of microstates for or a d^3 configuration is $\frac{10!}{3! \times 7!} = 120$

The number of microstates for or a d^5 configuration is $\frac{10!}{5! \times 5!} = 252$

From this we can see that the number of microstates increase for more complex atoms and ions. The different terms for each atom or ion can be determined from the microstates. To do this a certain stepwise method is used (the method is explained for a Carbon atom [8]):

1. Define $S = M_s = \sum m_s (S, S - 1, \dots, 0, \dots, -S)$ and $L = M_l = \sum m_l (-L, \dots, 0, \dots, +L)$ [19].
2. Determine the possible values of M_s and M_l for the specific atom or ion.

For a Carbon atom:

$$n = 1$$

$$l = 1$$

$$m_s = \pm 1/2$$

$$m_l = -1, 0, +1$$

$$M_s = -1, 0, 1$$

$$M_l = -2, -1, 0, 1, 2$$

3. Each microstate is described by using the notation (m_l^\pm, m_s^\pm) where + means $m_s = +1/2$ and – means $m_s = -1/2$ [22].
4. Draw a table of M_l vs M_s and fill in the microstates (a Carbon atom has 15 microstates (Table 3)).

Table 3: Microstates for a carbon atom.

		M_s		
		-1	0	1
M_l	+2		$1^+ 1^-$	
	+1	$1^- 0^-$	$1^+ 0^-$ $1^- 0^+$	$1^+ 0^+$
	0	$-1^- 1^-$	$-1^+ 1^-$ $0^+ 0^-$ $-1^- 1^-$	$-1^+ 1^+$
	-1	$-1^- 0^-$	$-1^+ 0^-$ $-1^- 0^+$	$-1^+ 0^+$
	-2		$-1^+ -1^-$	

5. The terms are determined by looking at the values of M_l .
 - The largest M_l value is +2, so $L = 2$ which is a D term. The multiplicity is determined by the value of M_s . In this case $M_s = 0$, so $2S + 1 = 1$. The term is therefore 1D .
 - The next M_l value is +1, so $L = 1$ which is a P term. $M_s = 0, \pm 1$, so $2S + 1 = 3$. The term is therefore 3P .
 - The remaining M_l value is 0, so $L = 0$ which is a S term. $M_s = 0$, so $2S + 1 = 1$. The term is therefore 1S .
6. The number of coulombs is an indication of the spin multiplicity.

M_s

		-1	0	1	
	+2		X		
	+1	X	X	X	X
	0	X	X	X	X
M_l	-1	X	X	X	X
	-2		X		

The blue block shows the 1D term.

The red block shows the 3P term.

The green block shows the 1S term.

This method of determining the microstates can be used for any atom or ion. In Table 4 the term symbols that were determined from the microstates for the p^1 - p^5 and d^1 - d^9 configurations are given.

Table 4: Terms symbols for the different configurations [23].

Configuration	Terms
p^1, p^5	2P
p^2, p^4	$^3P, ^1D, ^1S$
p^3	$^4S, ^2P, ^2D$
d^1, d^9	2D
d^2, d^8	$^3P, ^3F, ^1S, ^1D, ^1G$
d^3, d^7	$^2P, ^2D, ^2D, ^2F, ^2G, ^2H, ^4P, ^4F$
d^4, d^6	$^1S, ^1S, ^1D, ^1D, ^1F, ^1G, ^1G, ^1I, ^3P, ^3P, ^3D, ^3F, ^3F, ^3G, ^3H, ^5D$
d^5	$^2S, ^2P, ^2D, ^2D, ^2D, ^2F, ^2F, ^2G, ^2G, ^2H, ^2I, ^4P, ^4D, ^4F, ^4G, ^6S$

5. Ligand field theory

The Ligand field theory describes the orbital arrangement, bonding and other characteristics of coordination complexes. It is the representation of the application of molecular orbital theory to transition metal complexes. A transition metal has one s, three p and five d orbitals. These orbitals have appropriate energy to form bonds with ligands. The geometry of the complex (octahedral, tetrahedral, square planar) plays a big role in Ligand field theory and most explanations are given for octahedral complexes. These complexes have six ligands, which are bond to a metal centre (Figure 14).

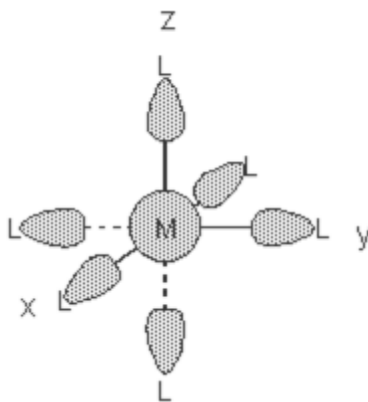
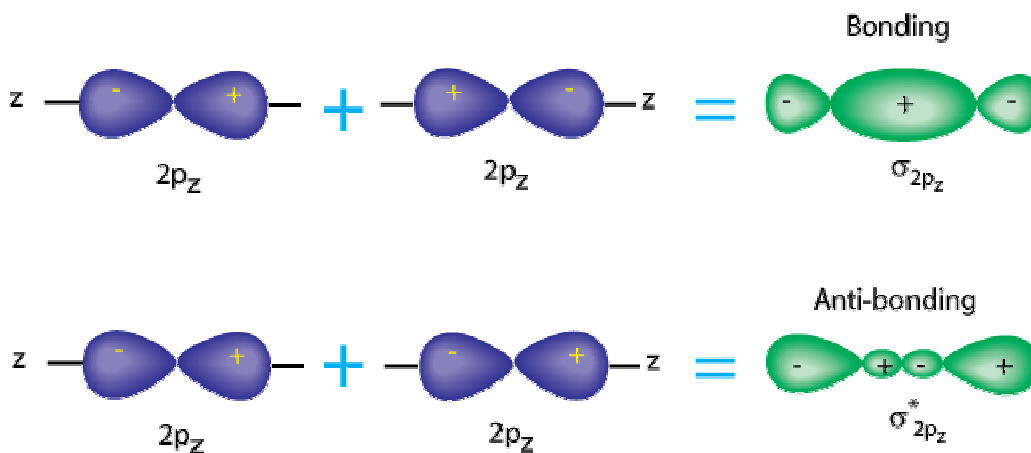


Figure 14: Diagram showing the 6 ligands (L) of an octahedral complex bonded to a metal centre (M) [24].

A ligand is an ion, atom or molecule that is bonded to a central metal. It generally involves the formal donation of one or more of its electrons. Two types of bonding can take place namely σ and π bonding (Figure 15 and Figure 16).



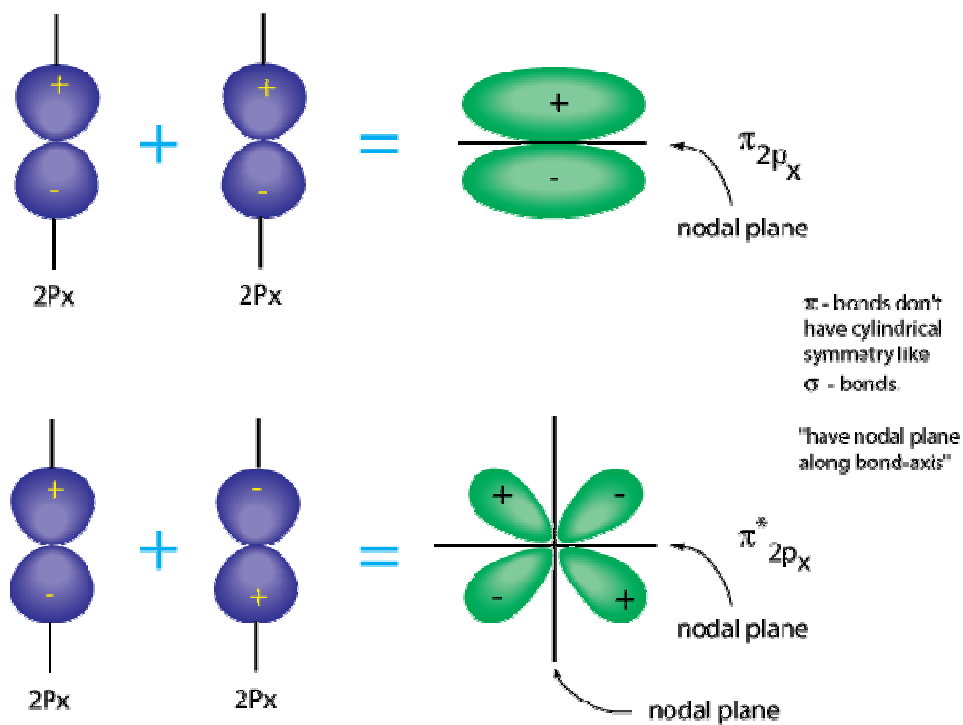


Figure 15: Diagram showing the σ and π bonds for p orbitals [25].

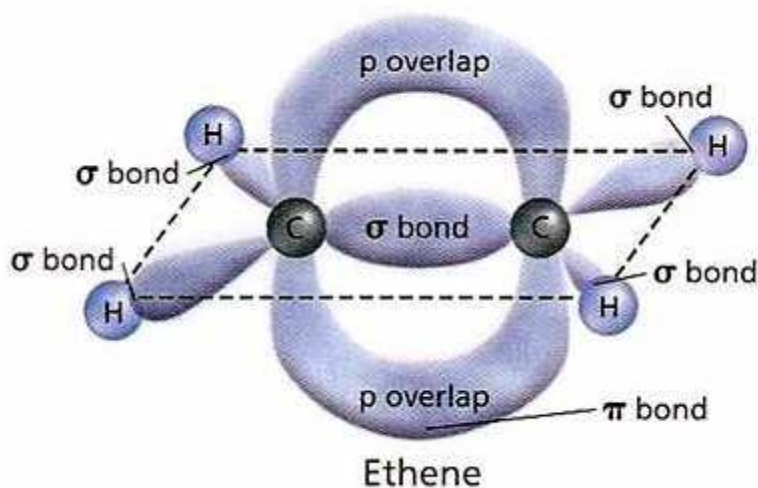


Figure 16: Diagram showing the σ and π bonds in ethene [26].

The crystal structure of ZnS is zinc blende. The zinc blende structure consists of tetrahedral structures that are bonded together (Figure 17). Also, Zn and Mn have their valence electrons

occupying the d orbital. From here on we will only focus on tetrahedral symmetry and splitting of the d orbitals and how the Ligand field theory applies to it.

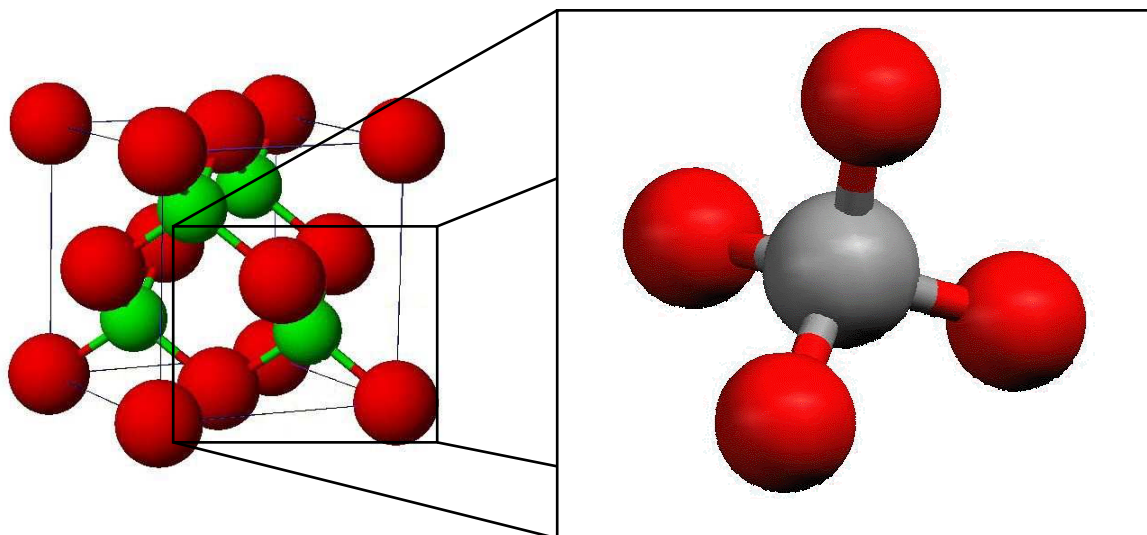


Figure 17: Zinc blende crystal structure [27] and tetrahedral arrangement [28].

Figure 18 shows the five different d orbitals: d_{xy} , d_{yz} , d_{xz} , d_z^2 and $d_{x^2-y^2}$, and the combination of all five.

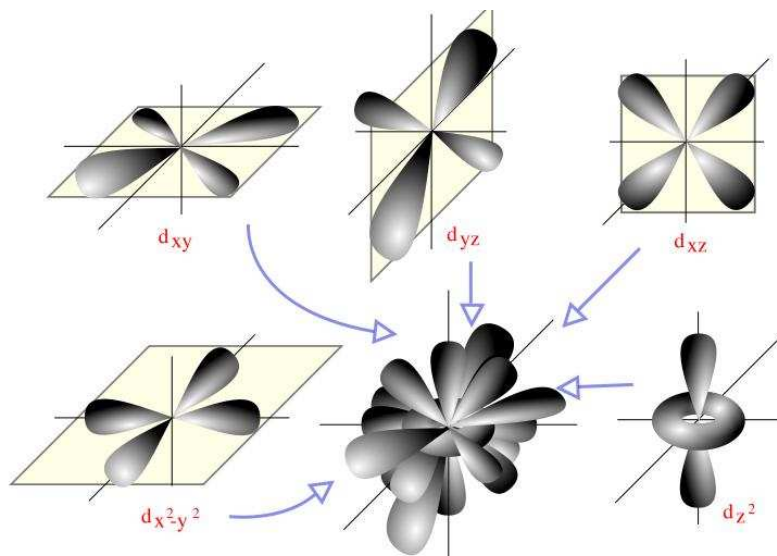


Figure 18: The five d orbitals [29].

When it is a free ion, the energy of all five the orbitals will be the same, but when the ion is bonded to ligands there is a splitting in energy. From Figure 19 it can be seen for the d_{z^2} and $d_{x^2 - y^2}$ orbitals that the ligand neatly fits in between the orbitals. There is no overlap of the orbitals and the ligand and these two orbitals are at a lower energy than that of a free ion. In the case of the d_{xy} , d_{yz} and d_{xz} orbitals the ligands and orbitals overlap causing them to be at a higher energy than that of a free ion.

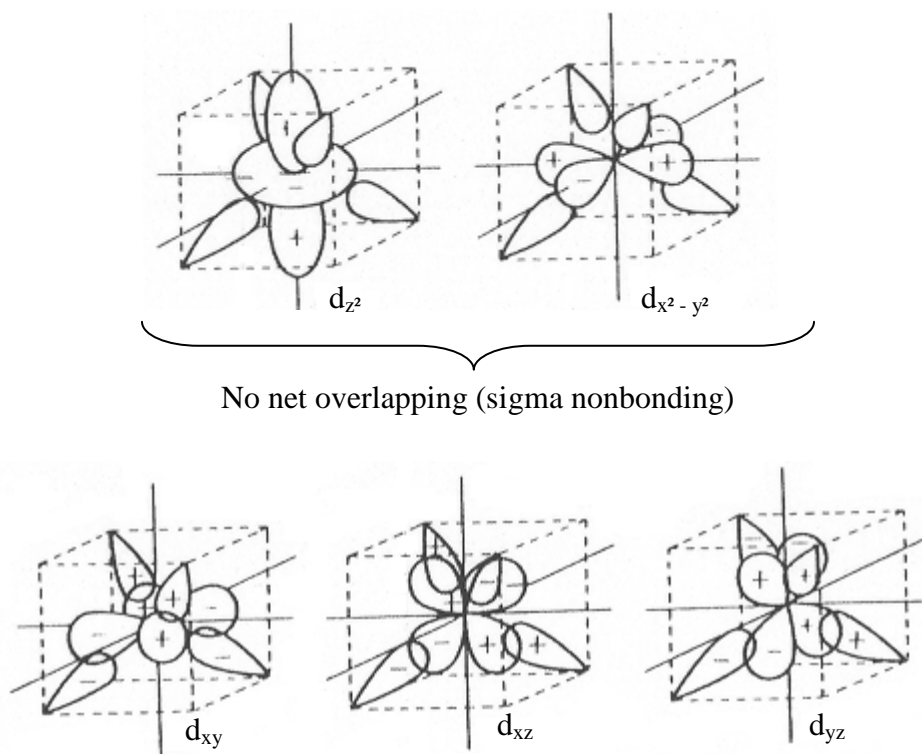


Figure 19: Tetrahedral sigma overlap for the d orbitals of transition metals [30].

When a ligand field is applied, the five d orbitals of a free ion or atom splits up into the doubly degenerate e_g and triply degenerate t_{2g} sets (Figure 20). The symbols that are assigned to these orbitals are as follows: for a singly degenerate orbital the symbol used is either a or b, for a doubly degenerate orbital it is e and for a triply degenerate orbital it is t [12].

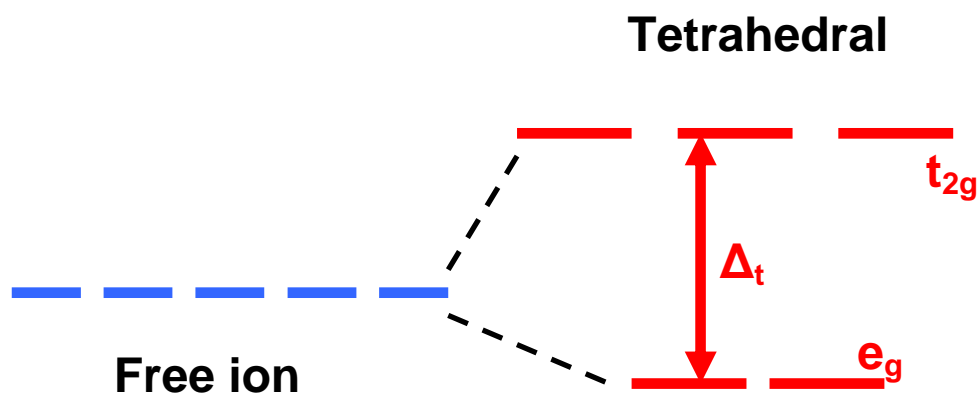


Figure 20: Energy splitting of the d orbitals in a ligand field.

When a ligand is applied to an ion or atom the ground state term symbol is split in its presence. There is no effect on its spin and the multiplicity will therefore remain the same. The term will be split in the same way as atomic orbitals. Table 5 gives a correlation between the free ion terms and their terms in the presence of a ligand field.

Table 5: Correlation between atomic and ligand field terms [8, 20].

Atomic term	Ligand field components
S	A_{1g}
P	T_{1g}
D	$T_{2g} + E_g$
F	$T_{1g} + T_{2g} + A_{2g}$
G	$A_{1g} + E_g + T_{1g} + T_{2g}$
H	$E_g + 2 \times T_{1g} + T_{2g}$
I	$A_{1g} + A_{2g} + E_g + T_{1g} + T_{2g}$

An A term is singly degenerate, an E term doubly degenerate and a T term triply degenerate [12, 19]. The subscripts 1 and 2 are used to distinguish between states that have the same degeneracy.

The subscripts g and u are used for molecules that have a centre of symmetry. g shows states whose wave functions are even (from the German *gerade*) and u shows states whose wave functions are uneven (*ungerade*), with respect to inversion through the centre of symmetry.

Just as the d orbitals of an atom is split by the application of a ligand field into t_{2g} and e_g orbitals, so is a D term split into a T_{2g} and E_g term. In a tetrahedral or octahedral complex the energy of the t_{2g} set of orbitals is always lower than that of the e_g set of orbitals. When a D term is split by a ligand field, the E_g term is the ground term in some complexes and in other complexes the T_{2g} term is lower.

For A and E terms there is no orbital angular momentum, i.e. $L = 0$, but a T term describes an electronic configuration with orbital angular momentum, i.e. $L = 1$. The ground state term symbol can be predicted by considering whether or not we have orbital angular momentum for a particular electronic configuration. Let's consider the d^1 configuration (Figure 21) [19]:

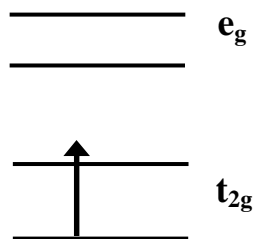


Figure 21: d^1 electronic configuration.

The t_{2g} set (d_{xy} , d_{xz} and d_{yx} orbitals) is degenerated and has the same shape, so these orbitals are able to rotate into one another. If the one orbital rotates into another and there is an electron in that orbital, it will result in that electron rotating around the nucleus. This electron would have orbital angular momentum associated with it. The term symbol is 2D for a free d^1 atom. This D term symbol will split up into ${}^2T_{2g}$ and 2E_g , when a ligand field is applied. An E term does not have orbital angular momentum, while a T term has some, and therefore we have a ${}^2T_{2g}$ ground term. A d^3 configuration has a ${}^4A_{2g}$ ground term and a d^4 has a 5E_g ground term [19]. This method of working out the terms symbols only applies to high spin complexes.

6. Band theory [31]

A crystal consists of a periodic configuration of atoms and this is called the crystal lattice. If we look at the electronic states in these crystals, we can see that in an isolated state, the electrons of the atoms exist in discrete energy levels and the atomic wave functions characterize the states of these bound electrons. Because of the overlaps between the electronic wave functions belonging to different atoms, their discrete energy levels will have finite spectral width in the condensed state. This is due to the fact that electrons can become itinerant between atoms, and they then finally fall into delocalized electronic states which is called electronic energy bands and these bands also obey the symmetry of the crystals. In these energy bands, the states with lower energies are occupied by electrons originating from bound electrons of atoms and are called valence bands. Electrons originating from bound electrons of atoms occupy the states with lower energy of these energy bands, and these states are called valence bands. Energy bands having higher energies are unoccupied and are called conduction bands. Usually there is no electronic state between the top of the valence band and the bottom of the conduction band in materials having crystal symmetry (rock-salt, zinc blende or wurtzite structures), and this region is called the band gap. The conduction band is called like that because of the fact that an electron that is excited from the valence band, for example by absorption of light quanta, to the conduction band is almost freely mobile. Only two electrons (spin up and spin down) can occupy an electronic state and electrons in valence bands can therefore not be mobile, because of this fundamental property of electrons. When an electric field is applied it is necessary for electrons in the valence band to have empty states in order for them to move freely. A hole remains in the valence band when an electron is excited to the conduction band, and this hole behaves as if it was a mobile particle with a positive charge and is called a positive hole. A schematic description of these excitations is given in Figure 22 and Figure 23.

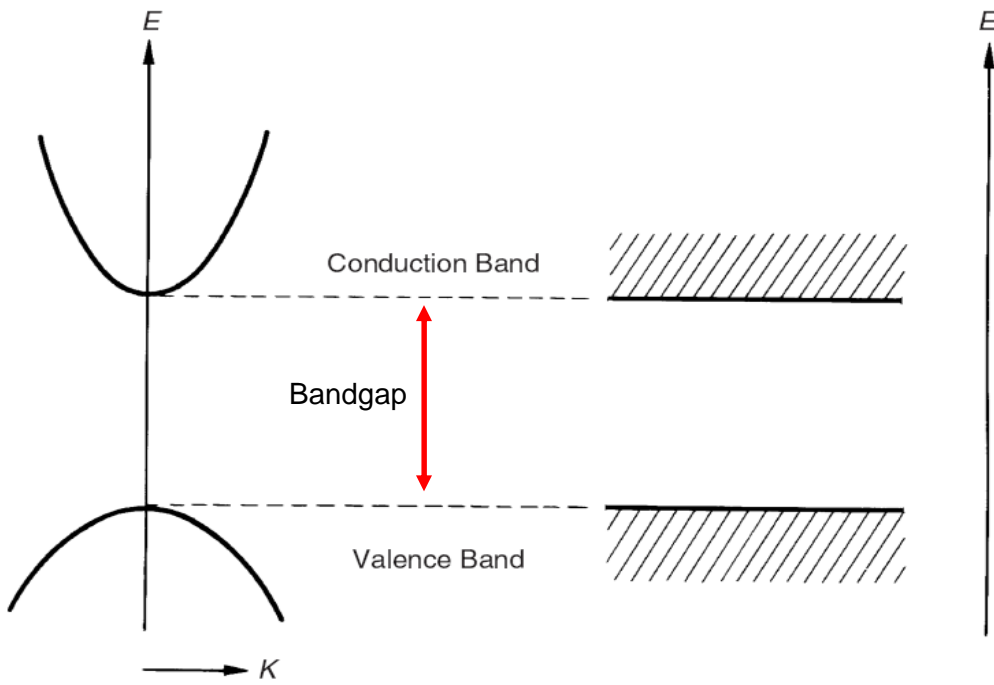


Figure 22: The energy states for a single particle as a function of the wave vector K in a direct band gap semiconductor. (Redrawn from reference [31] p23)

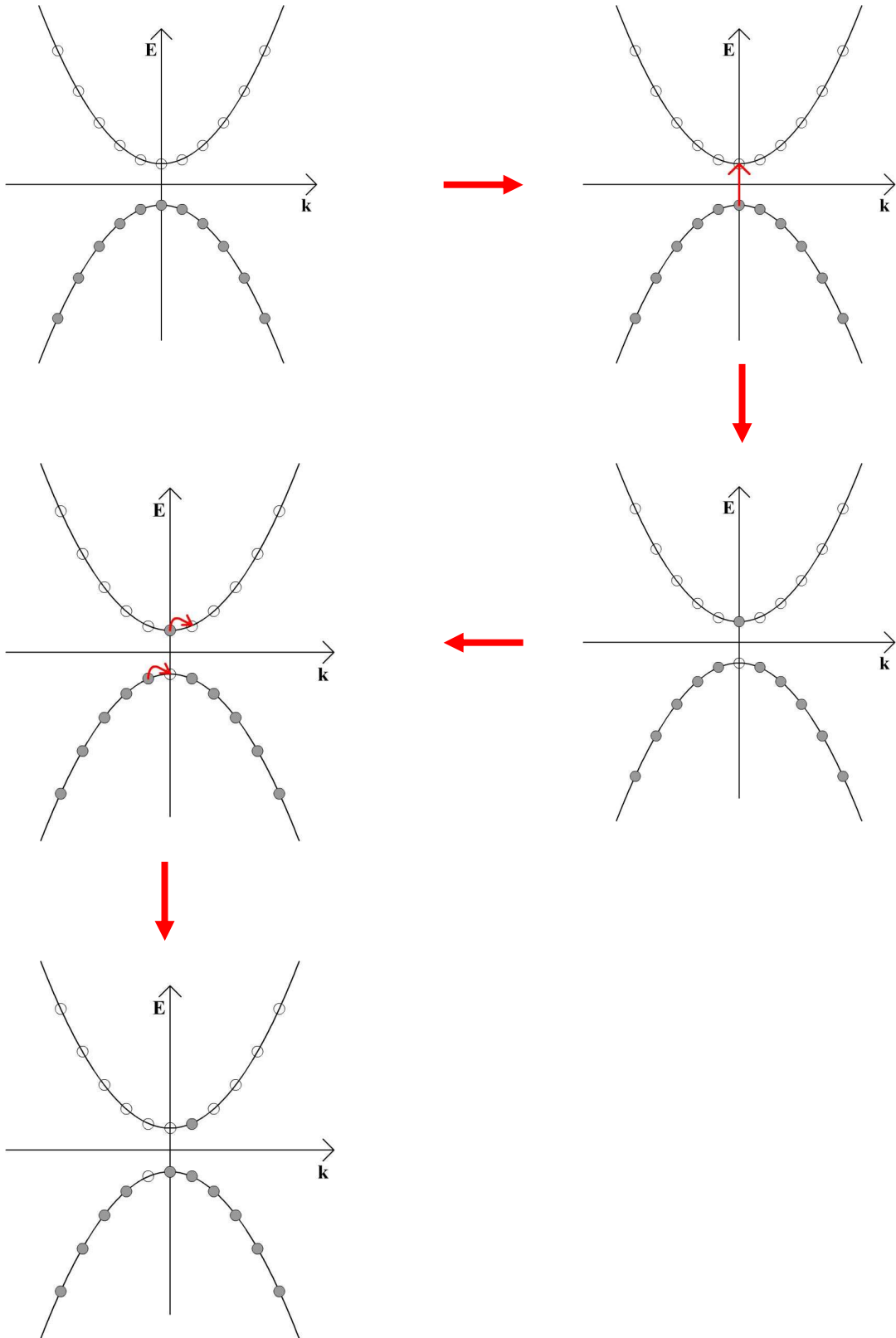


Figure 23: Schematic description of the excitations [32].

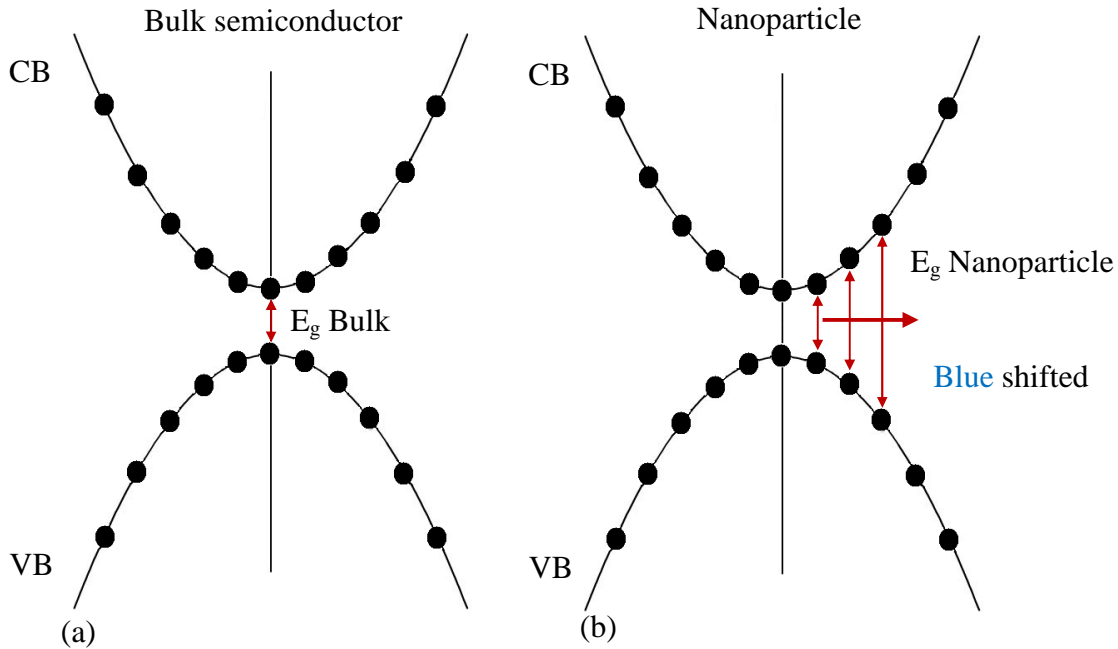


Figure 24: Energy dispersion for (a) the bulk semiconductor case compared to that of (b) the Nanoparticle case [33].

A band gap separates the energy bands for electrons and holes. In a semiconductor, the dispersion relations for the energy of electrons and holes are parabolic at first approximation. Only for electrons (holes) occupying the levels that lie at the bottom (top) of the conduction (valence) band does this approximation hold true. Each parabola represents a quasi-continuous set of electron (hole) states along a given direction in k -space. An energy gap (E_g bulk) separates the lowest unoccupied energy band and the highest occupied energy band, as shown in Figure 24. For a bulk semiconductor this band gap can range from a fraction of an eV up to a few eV [33]. It might be expected that the energy dispersion relations are still parabolic in a nanoparticle. Only discrete energy levels can exist in a nanoparticle, so each of the original parabolic bands of the bulk case is now fragmented into an ensemble of points. Quantum confinement has a remarkable effect on the nanoparticles. The more confined the charge carriers are the larger the separation between the individual bands and it also leads to a greater zero-point energy [33]. The band gap of nanoparticles is therefore blue shifted.

This can also be seen from the Brus equation [34]

$$\Delta E_g = E_{g(\text{powder})} - E_{g(\text{bulk})} = \left[\frac{\hbar^2 \pi^2}{2\mu r^2} \right] - \left[\frac{1.8e^2}{\epsilon r} \right] \quad (12)$$

where E_g is the band gap, μ is the reduced electron-hole effective mass, ϵ is the dielectric constant and r is the crystalline radius. From this equation it can be seen that if the radius of the particle gets smaller, the band gap gets larger (equation 12 a).

$$\Delta E_g \propto \frac{1}{r} \quad (12 \text{ a})$$

7. Configurational coordinate model [31, 35].

The configurational coordinate model is used to describe optical properties, such as the effect of lattice vibrations and the shape of the absorption and emission bands. This model represents the total energy of a luminescent centre as a function of the distance between an impurity atom and the first nearest neighbour. The configurational coordinate (Q) is the distance that characterizes the interactions between an atom and its first nearest neighbour. The two curves (Figure 25) are the ground state U_g and the excited state U_e of the dopant ion and are given by the following relations.

$$U_g = K_g \frac{Q^2}{2} \quad (13)$$

$$U_e = K_e \frac{(Q - Q_0)^2}{2} + U_0 \quad (14)$$

where K_g and K_e are the force constants of the chemical bond, Q_0 is the interatomic distance at the equilibrium of the ground state and U_0 is the total energy at $Q = Q_0$. The model can explain several factors qualitatively. These are:

1. Stokes Law: the fact that the absorption energy is in most cases higher than that of the emission energy. The Stokes' shift refers to the energy difference between the two.
2. The emission and absorption band widths, their shapes and temperature dependence.
3. The thermal quenching of luminescence – only qualitative explanation.

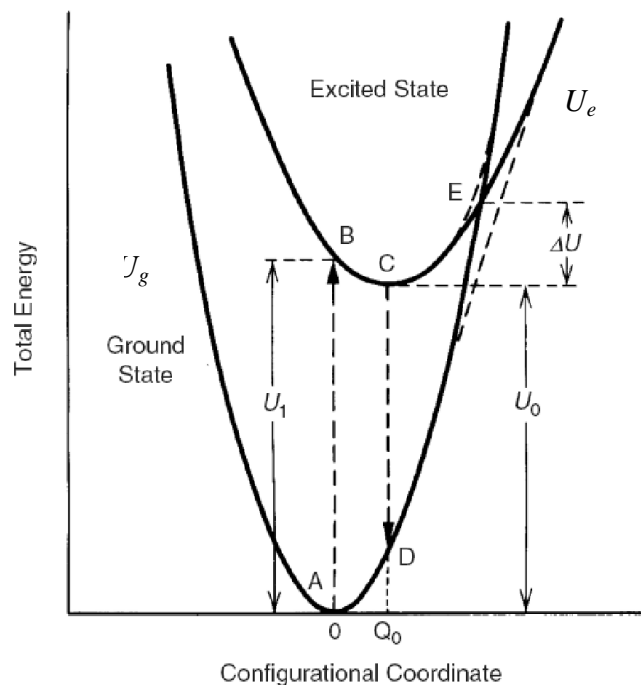


Figure 25: Schematic illustration of the configurational coordinate model. The broken lines AB and CD indicate the absorption and emission of light, respectively [31].

The luminescent centre will undergo a transition from A to B to the excited state U_e during irradiation or excitation (absorption of energy). The system is now in a higher vibrational state and will therefore relax to the more stable configuration C. The excess energy will be dissipated to the lattice in the form of heat. Light will be emitted by the luminescent centre through a transition from C to D and it will again be in the ground state U_g . The state is still in a higher vibrational level in the ground state and it will come to its minimum energy position through a nonradiative transition from D to A, completing the cycle. When the two curves intersect an electron in the excited state can cross over the intersection at E, assisted by thermal energy, and can reach the ground state through a nonradiative transition.

References

1. M. Tanaka, *J. Lumin.* **100**, (2002) 166.
2. M. Jain, J.L. Roberts, in: M. Jain (Ed.), *Diluted Magnetic Semiconductors*, World Scientific, Singapore, 1991, 31.
3. Y. Tanabe and S. Sugano, *J. Phys. Soc. Japan* **9**, (1954) 753 - 767.
4. D.S. McClure, *J. Chem. Phys.* **39**, (1963) 2850.
5. H. Yang, J. Zhao, L. Song, L. Shen, Z. Wang, L. Wang and D. Zhang, *Mater. Lett.* **57**, (2003) 2290.
6. Correlation diagrams [online]. Available from http://www.chembio.uoguelph.ca/schlaf/text_files/CHEM_3650_Lecture_Notes/6_3_Spectra3_ok.pdf [Accessed 7 April 2009].
7. Calculations using Orgel diagrams [online]. Available from <http://wwwchem.uwimona.edu.jm:1104/courses/Tanabe-Sugano/TScalcs.html> [Accessed 7 April 2009].
8. Coordination Chemistry Electronic Spectra of Metal Complexes [online]. Available from <http://academic.brooklyn.cuny.edu/chem/howell/inorganic%202006/710%20Lecture%2010.ppt> [Accessed 17 April 2009].
9. Racah parameter [online]. Available from http://en.wikipedia.org/wiki/Racah_parameter [Accessed 17 April 2009].
10. G. Racah, *Phys. Rev.* **62**, (1942) 438.
11. Tanabe-Sugano Diagrams [online]. Available from http://www.chembio.uoguelph.ca/schlaf/text_files/CHEM_3650_Lecture_Notes/6_3_Spectra3_ok.pdf [Accessed 17 April 2009].
12. F.A. Cotton, G. Wilkinson and P.L. Gaus, *Basic Inorganic Chemistry* 3rd edition, John Wiley & Sons Inc., New York, (1995) p. 52, 522.
13. d^5 Tanabe-Sugano diagram [online]. Available from <http://www.albion.edu/chemistry/abbethune/356/F07/tanabesugano.htm> [Accessed 27 April 2009].
14. Structure of atoms [online]. Available from <http://earthsci.org/education/teacher/basicgeol/miner/miner.html> [Accessed 8 April 2009].
15. The third shell [online]. Available from http://www.sci.uidaho.edu/chem101/Lecture%20photos/fig5_12Orbitals.jpg [Accessed 8 April 2009].
16. Quantum numbers [online]. Available from <http://www.kentchemistry.com/links/AtomicStructure/quantumnumbers.htm> [Accessed 9 April 2009].

17. Electron spin [online]. Available from <http://hyperphysics.phy-astr.gsu.edu/hbase/spin.html#c1> [Accessed 9 April 2009].
18. P.J. Durrant and B. Durrant, Introduction to Advanced Inorganic Chemistry, Longmans, Green and Co Ltd, London, (1962) p89 – 91.
19. S.M. Owen and A.T. Brooker, A Guide to Modern Inorganic Chemistry, Longman Scientific & Technical, UK, (1991) p157, 158, 159, 160.
20. D.F. Shriver, P.W. Atkins and C.H. Langford, Inorganic Chemistry, Oxford University Press, Oxford, (1990) p435, 436, 443.
21. The Boltzmann Distribution [online]. Available from [http://garfield.chem.elte.hu/Turanyi/oktatas/gyogyszerez/optical%20spectroscopy%20\(lecture%20notes\)/03Boltzm.doc](http://garfield.chem.elte.hu/Turanyi/oktatas/gyogyszerez/optical%20spectroscopy%20(lecture%20notes)/03Boltzm.doc) [Accessed 15 April 2009].
22. Terms for the d^3 configuration [online]. Available from <http://bilbo.chm.uri.edu/CHM501/lecture3.html> [Accessed 27 April 2009].
23. Atomic Term Symbols [online]. Available from http://www.chem.ufl.edu/~itl/4412/ppt/atom_levels.ppt [Accessed 15 April 2009].
24. Electronic Absorption Spectroscopy of Metal Complexes [online]. Available from <http://www.wpi.edu/Academics/Depts/Chemistry/Courses/General/AppendixJ.html> [Accessed 17 April 2009].
25. Molecular Orbital Theory [online]. Available from <http://grandinetti.org/Teaching/Chem121/Lectures/MOTheory/index.html> [Accessed 17 April 2009].
26. Sigma and Pi Bonds [online]. Available from <http://www.megamolecules.com/products.htm> [Accessed 17 April 2009].
27. Zincblende (Zinc sulfide, ZnS) structure [online]. Available from <http://www.seas.upenn.edu/%7Echem101/sschem/ionicsolids.html> [Accessed 17 April 2009].
28. Classic Molecular Modeling [online]. Available from <http://chemlab.truman.edu/CHEM121Labs/MolecularModeling1.htm> [Accessed 17 April 2009].
29. D orbitals [online]. Available from http://en.wikibooks.org/wiki/File:D_orbitals.svg [Accessed 17 April 2009].
30. W.W. Porterfield, Inorganic Chemistry A Unified Approach, Addison-Wesley, USA, (1984), p429.

31. S. Shionoya and W.M. Yen, Phosphor Handbook, CRC Press, Boca Raton, (1999) p21 - 23, 36 - 38.
32. Charge Carriers in Semiconductors [online]. Available from http://www.doitpoms.ac.uk/tlplib/semiconductors/charge_carriers.php [Accessed 21 April 2009].
33. G. Schmid, Nanoparticles: From Theory to Application, Wiley-VCH, Verlag GmbH & Co. KGaG, Weinheim, (2004) p21 - 22.
34. B. Bhattacharjee, D. Ganguli, K. Iakoubovskii, A. Stesmans and S. Chaudhuri, Bull. Mater. Sci. **25**, (2002) 179.
35. D.R. Vij, Luminescence of Solids, Springer, USA, (1998) p 273 -274.

Chapter 5

Preparation of ZnS:Mn²⁺ and SiO₂-ZnS:Mn²⁺ nano particle phosphors and structural and chemical analysis of these phosphors.

1. Introduction

Significant progress has been made in recent years in an attempt to understand the fundamental concepts of synthesizing ZnS:Mn²⁺. The different chemical processes include the sol-gel process, chemical precipitation method, micro-emulsion method, precipitation in a solid polymer matrix, the liquid-solid-solution (LSS) technique, the flux method, inorganic synthesis method, colloidal chemical method, the competitive reaction chemistry method, coprecipitation reaction method [1-8]. Different starting materials were used in these methods. The sources of Zn²⁺ ions include Zn(NO₃)₂·6H₂O, Zn(CH₃COO)₂·2H₂O, ZnSO₄·7H₂O or ZnCl₂. CH₃CSNH₂, NH₂CSNH₂, C₂H₅OSH, H₂S or Na₂S could be used as the source of S²⁻ ions. MnCl₂ or Mn(CH₃COO)₂ was used for the Mn²⁺ doping ions. Three common solvents were used in the different synthesis techniques namely de-ionized water, methanol or ethanol. Some of the methods suggest adding a stabilizer to stabilize the nano particles formed during the reaction and to control their growth [8]. Some of these stabilizers are α -methacrylic acid (MA), hydroxypropyl cellulose (HPC) and polyvinylpyrrolidone (PVP). In some of the techniques only ZnS:Mn²⁺ were synthesized, but others used a capping or coating agent. These agents include tetramethoxysilane (TMOS), SiO₂, 3-methacryloxypropyl trimethoxysilane (MPTS), acrylic acid (AA) and polyvinyl alcohol (PVA). The use of these capping and coating agents is to protect the nano particles that had formed and to enhance the luminescence of these materials.

This chapter presents an overview of the synthesis of ZnS:Mn²⁺ and SiO₂-ZnS:Mn²⁺ nano phosphors, with different concentrations of Mn²⁺. The samples were characterized with scanning electron microscopy (SEM), energy dispersive x-ray spectroscopy (EDS), transmission electron microscopy (TEM) and x-ray diffraction (XRD).

2. Experimental

2.1 Preparation of ZnS:Mn²⁺ nano particles

ZnS:Mn²⁺ sols were prepared by using the chemical precipitation method described by Lu et al. [2]. The synthesis was carried out using Zn(CH₃COO)₂·2H₂O, Mn(CH₃COO)₂ and Na₂S as starting materials. Zn(CH₃COO)₂·2H₂O and Mn(CH₃COO)₂ were dissolved in ethanol with stirring at 150°C. A 1:1 ethanol to deionized water solution of Na₂S was added to the Zn²⁺ and Mn²⁺ solution drop by drop with vigorous stirring at 75°C. The resulting white precipitate was centrifuged and washed using a mixture of toluene and ethanol in 2:1 volume ratio. The washed ZnS:Mn²⁺ precipitate was divided into two parts. One part was dried at 120°C for two hours, ground using pestle and mortar and finally annealed at 600°C for two hours. The other part was dispersed in ethanol for mixing with SiO₂. A flow diagram describing the preparation of ZnS:Mn²⁺ is shown in Figure 1 and Figure 2.

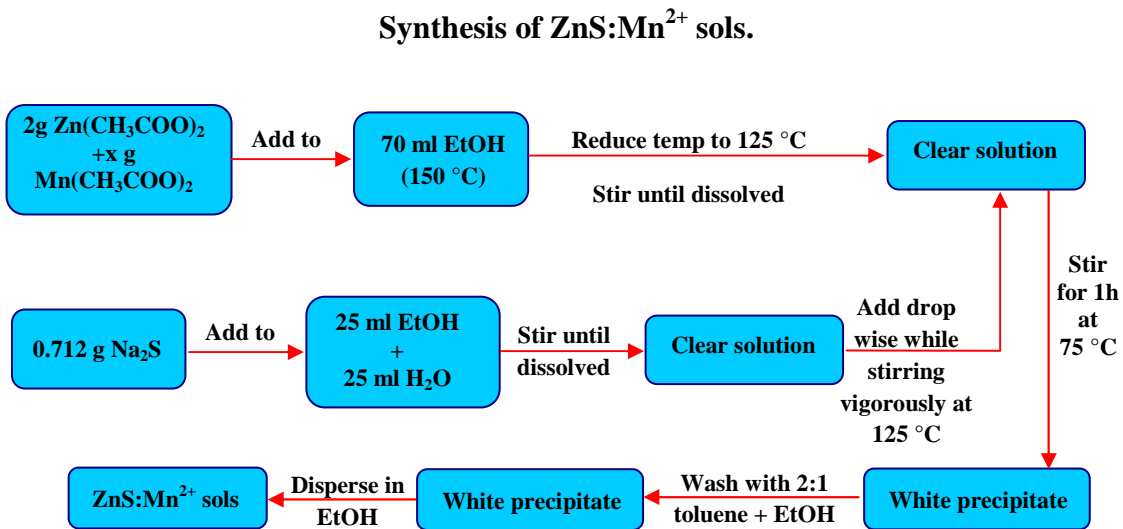


Figure 1: A flow diagram for the preparation of ZnS:Mn²⁺ sols.

Synthesis of ZnS:Mn²⁺ powders.

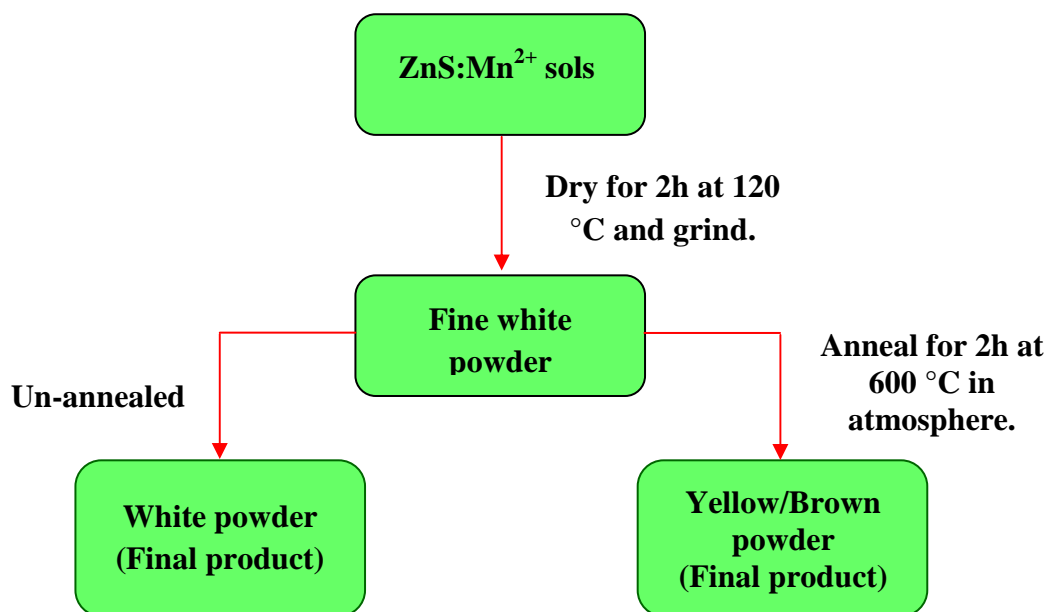


Figure 2: A flow diagram for the preparation of ZnS:Mn²⁺ powders.

2.2 Preparation of SiO₂-ZnS:Mn²⁺ nano particles

SiO₂ sols were prepared by using the method described by Ntwaeaborwa et al. [9], by mixing 10 g of tetraethylorthosilicate (TEOS) with 14 ml of deionized water, 8 ml of ethanol and 5 ml of 0.15 M HNO₃ (catalyst). The mixture was stirred at room temperature for 1 hour until a transparent solution formed. The ZnS:Mn²⁺ sol dispersed in ethanol was added to the SiO₂ sol drop by drop with vigorous stirring at room temperature. The mixture was stirred for 24 hours until a gel formed. The gels were dried in air at room temperature for 3 days. The resulting white solids were then ground and sieved to get a fine white powder, which was also annealed at 600°C for two hours. The concentration of Mn²⁺ in ZnS:Mn²⁺ and SiO₂-ZnS:Mn²⁺ was varied from 2 – 20 mol%. The synthesis process is illustrated in Figure 3.

electron microscope (FESEM) at the CSIR, with an accelerating voltage of 25kV, was used to record the 100000 x magnification image of ZnS.

3.1.1 Commercially available ZnS:Mn²⁺ phosphor powders

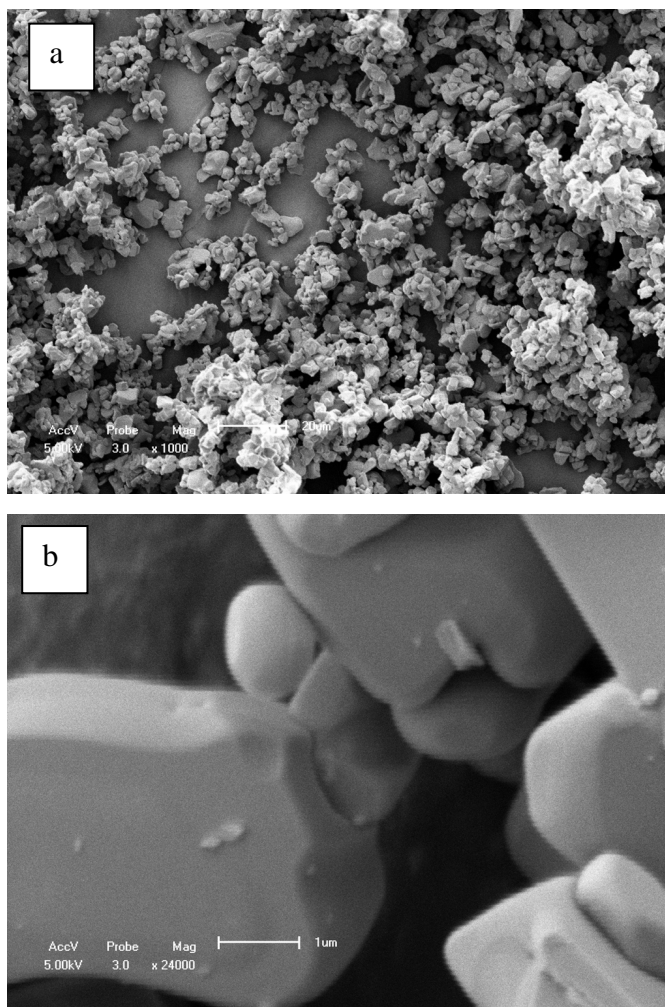


Figure 4: a) SEM image of the ZnS:Mn²⁺ commercial powders taken with an accelerating voltage of 5kV and a magnification of 1000x and b) the same surface area with a magnification of 24000x.

Figure 4 shows the SEM image of the commercially available phosphor powders. From Figure 4, it can be seen that the phosphor powders were slightly agglomerated. At higher magnification, it can be seen that no nano particles exists and that all the particles are non-uniform in shape. The particles are single crystals and don't consists of subunits.

3.1.2 Synthesized ZnS and ZnS:Mn²⁺

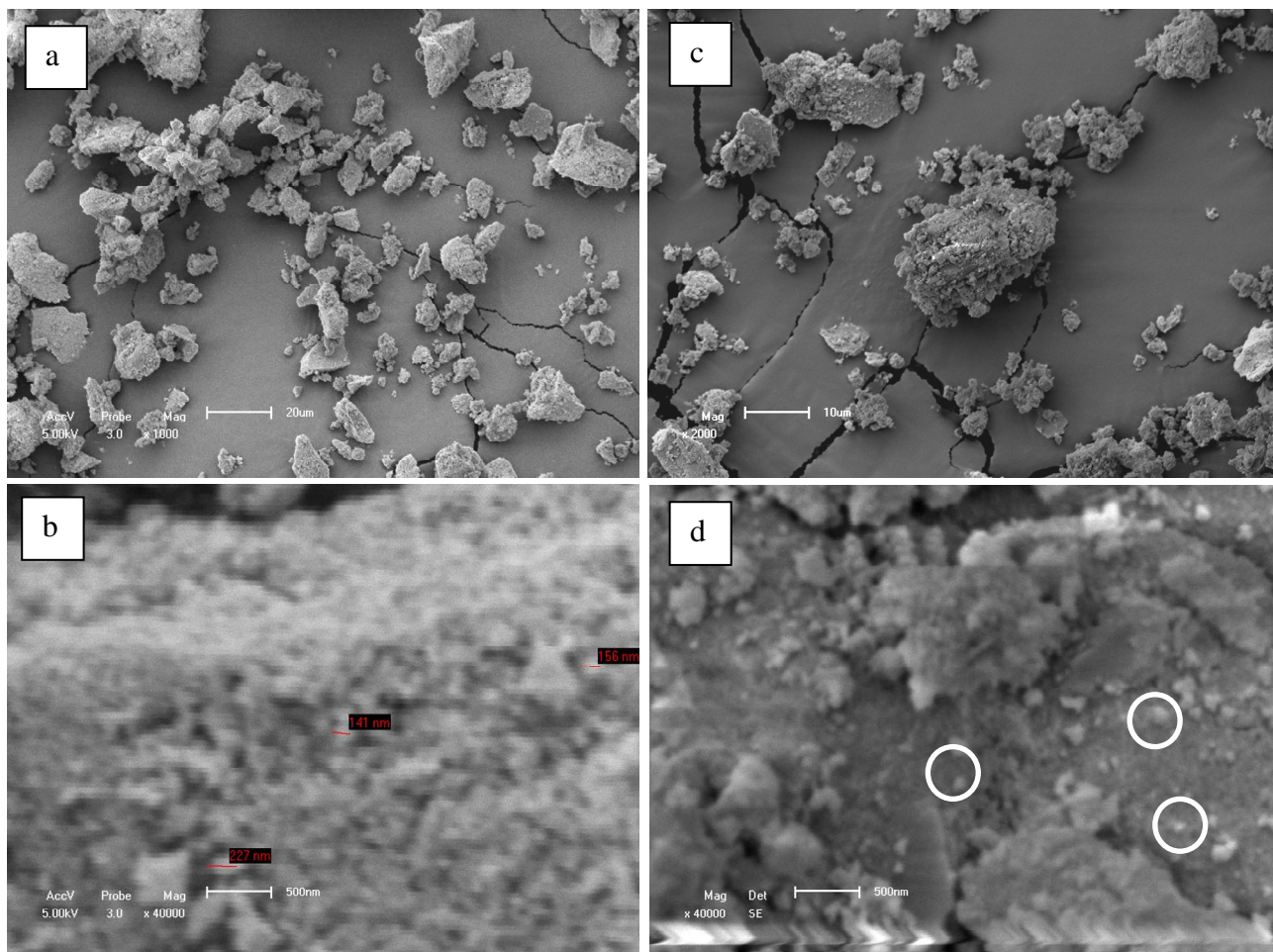


Figure 5: SEM image of the synthesized ZnS and ZnS:Mn²⁺ powders taken with an accelerating voltage of 5 kV. (a) ZnS at a magnification of 1000x and (b) the same surface area with a magnification of 40000x, showing the nano particles. (c) ZnS:Mn²⁺ at a magnification of 2000x and (d) the same surface area with a magnification of 40000x, showing the nano particles.

Figure 5 shows the SEM image of synthesized ZnS and ZnS:Mn²⁺ nano particles. From Figure 5, it can be seen that the particles were highly agglomerated. At higher magnification, it can be seen that nano particles formed (white circles in Figure 5d). The average particle size is 100 - 200 nm. Because SEM can often only determine the particle size of secondary particles, it is assumed that the secondary particles of ZnS and ZnS:Mn²⁺ consist of primary particles that are in the range of 3 nm, as estimated by Scherrer's equation.

3.1.3 Synthesized SiO₂:ZnS

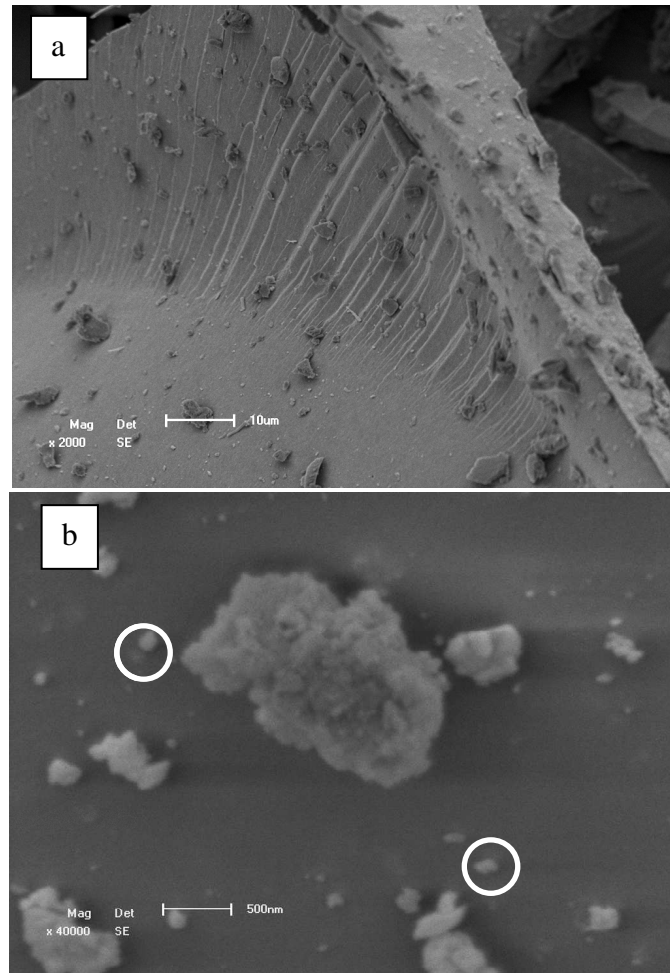
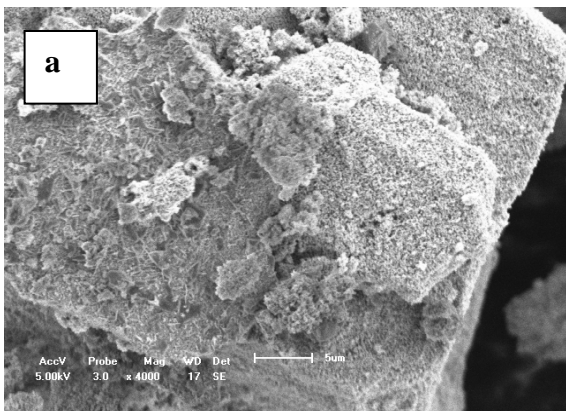
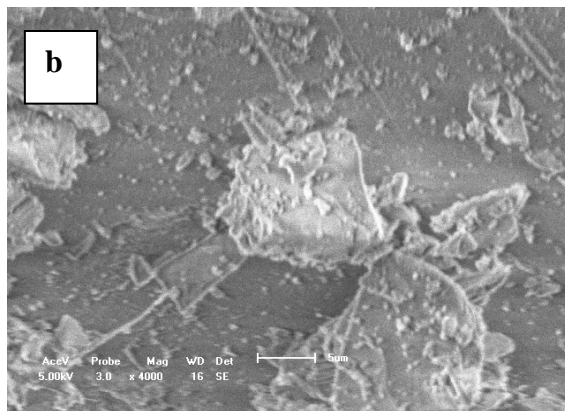


Figure 6: a) SEM image of the synthesized SiO₂:ZnS powders taken with an accelerating voltage of 5 kV and a magnification of 2000x and b) the same surface area with a magnification of 40000x, showing the nano particles.

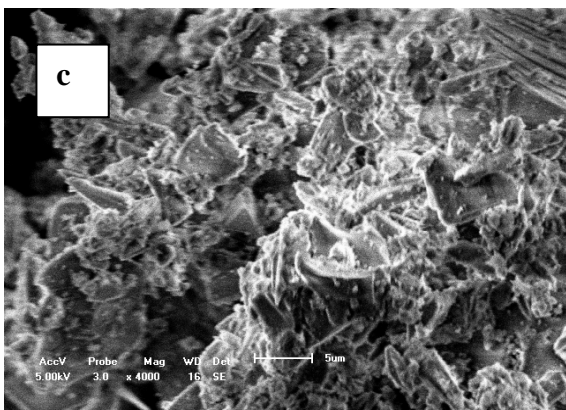
Figure 6 shows the SEM image of synthesized SiO₂:ZnS particles. From Figure 6 a, it can be seen that big SiO₂:ZnS particles had formed showing a glass like structure with some fracture lines on the left side of the particle. Smaller particles that are clinging to the big particle are also observed. At higher magnification, it can be seen that these small particles consists of an agglomeration of nano particles (white circles in Figure 6b). The average particle size of these agglomerated particles is 100 - 1000 nm.



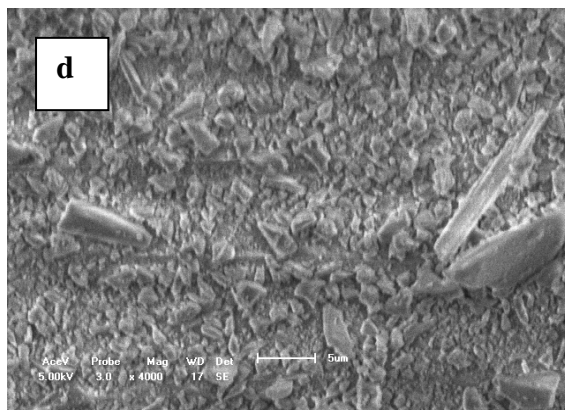
ZnS 600°C 4000x



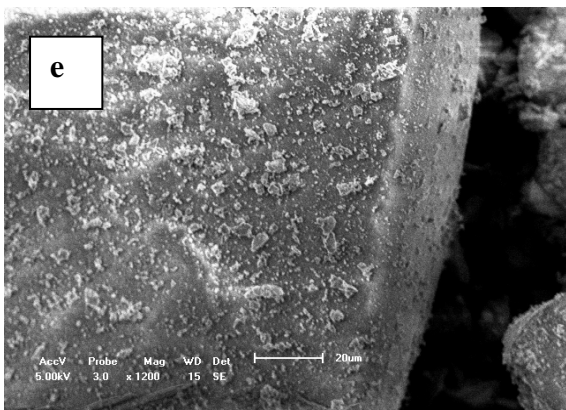
SiO₂ 600°C 4000x



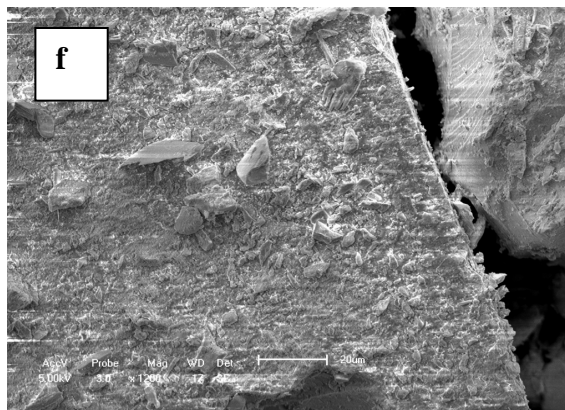
SiO₂:Mn²⁺ un-annealed 4000x



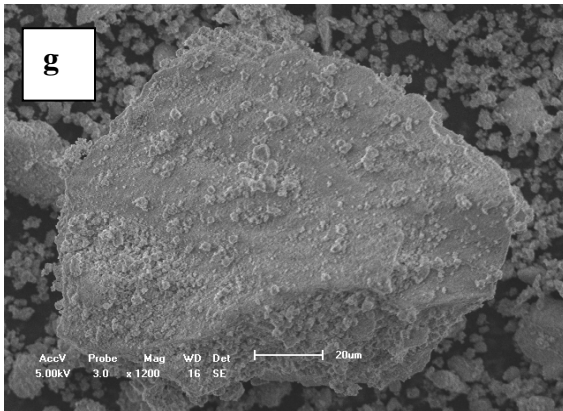
SiO₂:Mn²⁺ 600°C 4000x



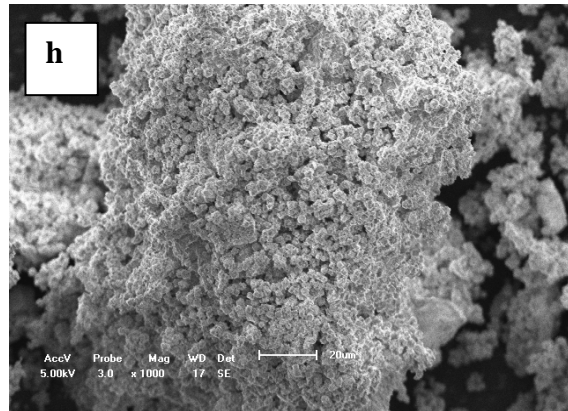
SiO₂:ZnS un-annealed 1200x



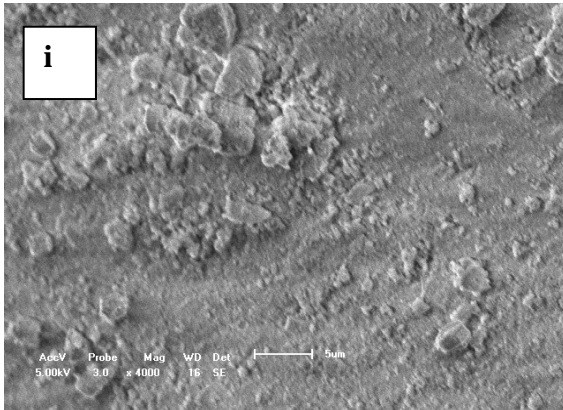
SiO₂:ZnS 600°C 1200x



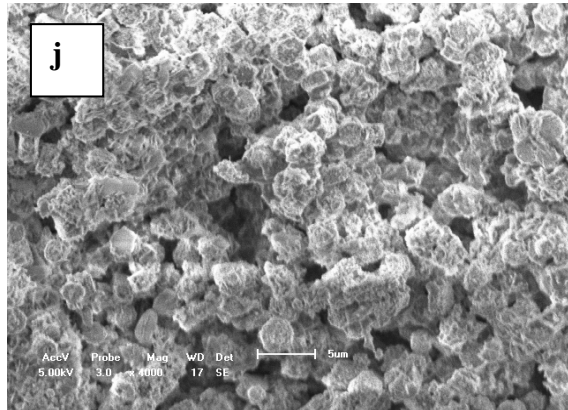
ZnS:Mn²⁺ 20 mol% un- annealed 1200x



ZnS:Mn²⁺ 20 mol% 600°C 1200x



ZnS:Mn²⁺ 20 mol% un- annealed 4000x



ZnS:Mn²⁺ 20 mol% 600°C 4000x

Figure 7: SEM images of different synthesized powders taken with an accelerating voltage of 5 kV.

Figure 7 shows the SEM images of different synthesized powders. Figure 7 (a) shows the SEM image of ZnS powders annealed at 600°C. Big particles had formed with some smaller structures, that are in the range of 5 µm, can be seen on these particles. The smaller structures are most likely agglomerated secondary particles. Figure 7 (b) shows the SEM image of annealed SiO₂. It can be seen that glasslike particles had formed with some smaller particles that are clinging to the surface of the big particles. Figure 7 (c) shows the SEM image of an-annealed SiO₂:Mn²⁺ and (d) shows the SEM image of annealed SiO₂:Mn²⁺. No change was observed in the morphology with the addition of Mn²⁺ to the SiO₂. Big particles had again formed with some

smaller particles clinging to it. The structures that were observed from these smaller particles could be due to crushing of the samples. Figure 7 (e) and (f) show the SEM images of un-annealed and annealed SiO₂:ZnS. Both these samples consist out of big particles with some smaller particles that can be seen on the surface of the big particles. Annealing of SiO₂:ZnS did not change the surface morphology. Figure (g), (h), (i) and (j) show the SEM images of un-annealed and annealed ZnS:Mn²⁺ 20 mol%. The un-annealed sample's surface morphology corresponds to that of the 2 mol% of Mn²⁺ sample. The particles are also agglomerated and most likely consist out of smaller secondary particles. The morphology of the annealed sample shows a drastic change from that of the un-annealed sample. Spherical structures had formed that are ~ 5 μm in diameter. At 1200x magnification it can be seen that the powder again consists out of big particles, but these particles are composed out of these spherical structures. These spherical structures are clearly visible at 4000x magnification.

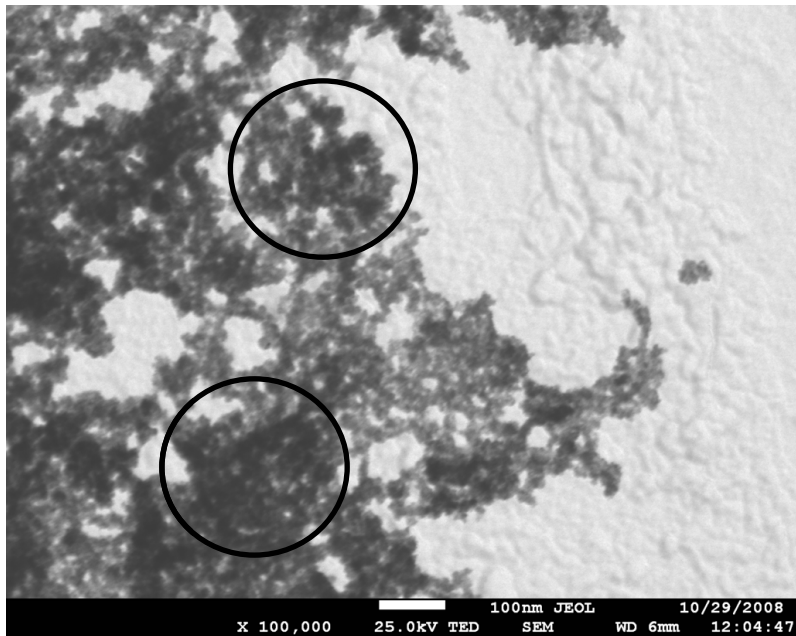


Figure 8: FESEM image of synthesized ZnS. The accelerating voltage is 25 kV and the magnification is 100000 x.

Figure 8 shows the FESEM image of synthesized ZnS nano particles. A cluster of agglomerated particles can clearly be seen (black circles in Figure 8). At higher magnifications it would be possible to see that these agglomerated particles consist out of smaller particles that must be ~ 100 nm or smaller in size.

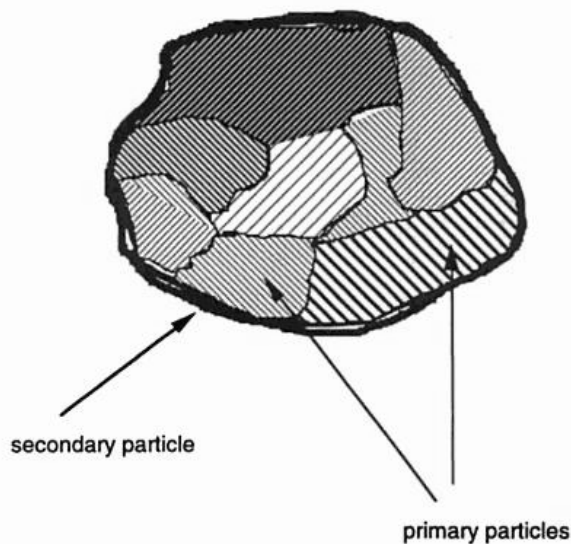


Figure 9: Schematic diagram showing the secondary and primary particles [10].

Particles can consist out of two units. It can be a single unit like a single crystal or it may consist of subunits [10]. From Figure 9 it can be seen that the individual subunits are the primary particles and agglomerates of these subunits or primary particles are called secondary particles. By doing SEM measurements, only the size of the secondary particles can be determined [10]. For crystalline materials like ZnS the size of the primary particles can be estimated by the amount of line broadening of the x-ray line, by performing dark-field imaging (Figure 10(a)) by transmission electron microscopy (TEM) or from lattice imaging (Figure 10(b)) by high-resolution transmission electron microscopy (HRTEM).

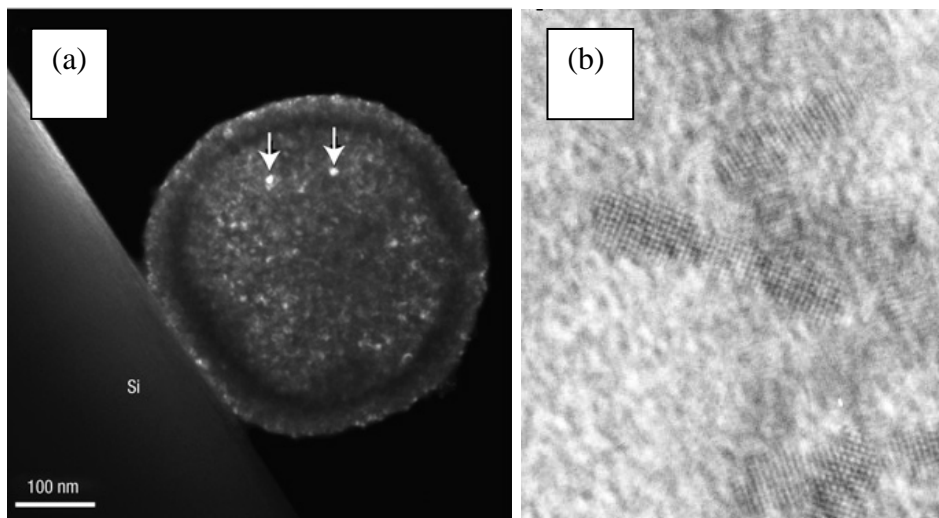


Figure 10: a) TEM dark field image of CdS nanospheres [11] and b) HRTEM Lattice Image of CdSe Rods [12].

3.2 EDS results

EDS spectra were obtained with an x-ray spectrometer attached to a Shimadzu SSX550 at the Centre for microscopy (CCEM) at the University of the Free State, to determine the chemical composition of the samples. An accelerating voltage of 15kV was used.

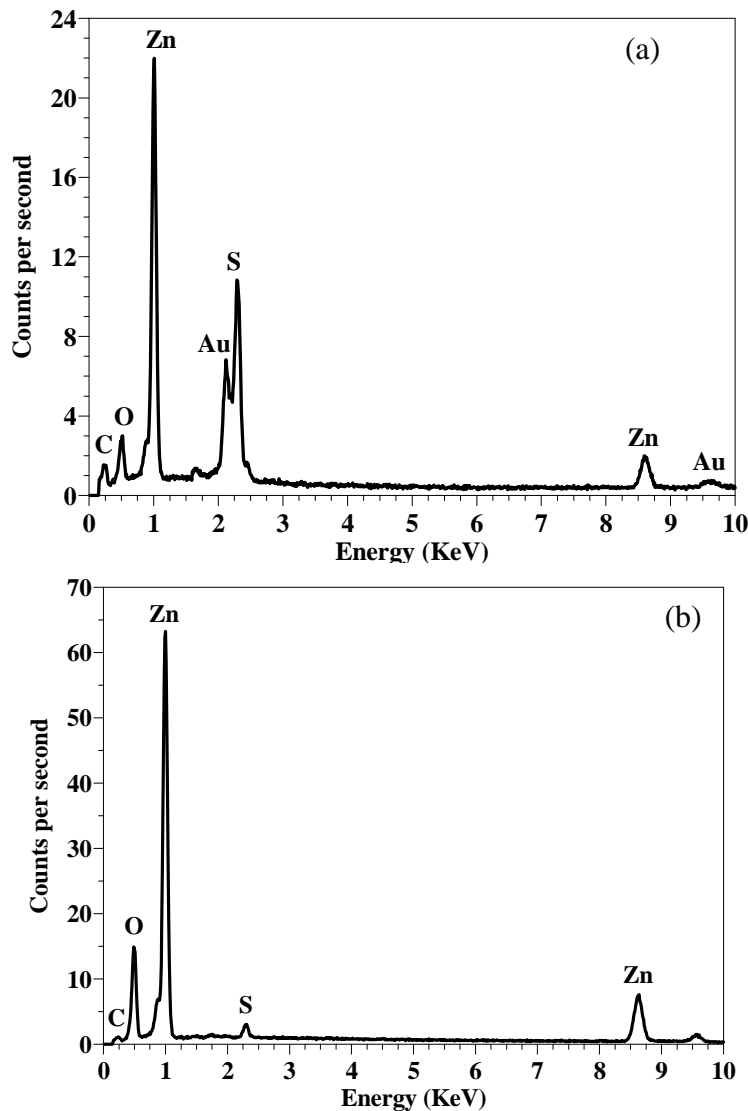


Figure 11: EDS spectra for a) un-annealed and b) annealed ZnS. The accelerating voltage was 15 kV.

Figure 11 shows the EDS spectra for un-annealed and annealed ZnS. The un-annealed sample was coated with an Au coating of ~ 10nm to prevent charging. Figure 11 shows peaks corresponding to Zn, S, O, Au, and C, depicting the characteristic chemical composition of the synthesized ZnS nano particles. The C peak is due to contamination of the sample or it is coming from the carbon tape on which the samples were mounted. The Au peak is due to coating. XRD data indicates that for the un-annealed sample mainly ZnS had formed, with a small amount of ZnO present in the sample and for the annealed sample mainly ZnO had formed, with a small amount of ZnS present in the sample. The presence of ZnS as well as ZnO is confirmed by the

Zn, S and O peaks. Table 1 shows the weight % of the different elements that were present. The relative O concentration increased during annealing, while the relative S concentration decreased. From this we can conclude that the amount of ZnO in the annealed sample is much higher than that of the un-annealed sample.

The determination of the concentration of the different elements in the samples is only relative. It is limited to the spot that was analyzed and is not a true representation of the whole sample. The samples that were coated with Au are showing a relative Au concentration of ~ 25%. The thickness of the Au coating is in the order of 10 nm, while the sample is more than 2 μm thick. It can therefore be seen that the concentrations are not a true representation of the concentration of elements in the samples. Some elements are also more sensitive to the EDS detector than others and can therefore not be compared directly.

Table 1: Listed EDS results for the un-annealed and annealed ZnS samples.

	Weight %				
	C	O	Zn	S	Au
ZnS un-annealed	10	15	34	16	25
ZnS 600 °C	3	27	69	1	-

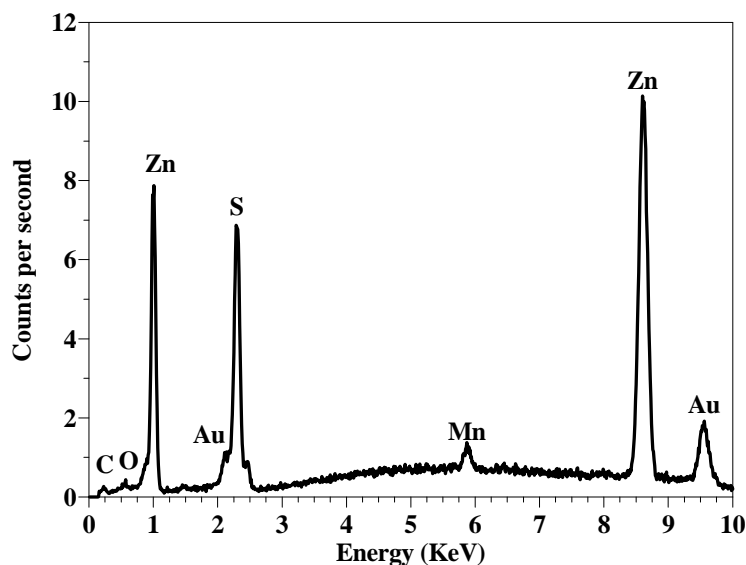


Figure 12: EDS spectrum of commercially available ZnS:Mn²⁺ phosphor powders. The accelerating voltage is 15 kV.

Figure 12 shows the EDS spectrum of commercially available ZnS:Mn²⁺ phosphor powders. Zn, S, O, Mn, Au, and C peaks are present. The very small O peak is an indication that almost no ZnO was formed during sample preparation. The Zn and S peaks depict the characteristic chemical composition of the commercial phosphor. The concentration of dopants is normally too small to detect with EDS, but in this case a small Mn peak is observed suggesting that the amount of Mn present in the commercial phosphor is high (> 5 wt %).

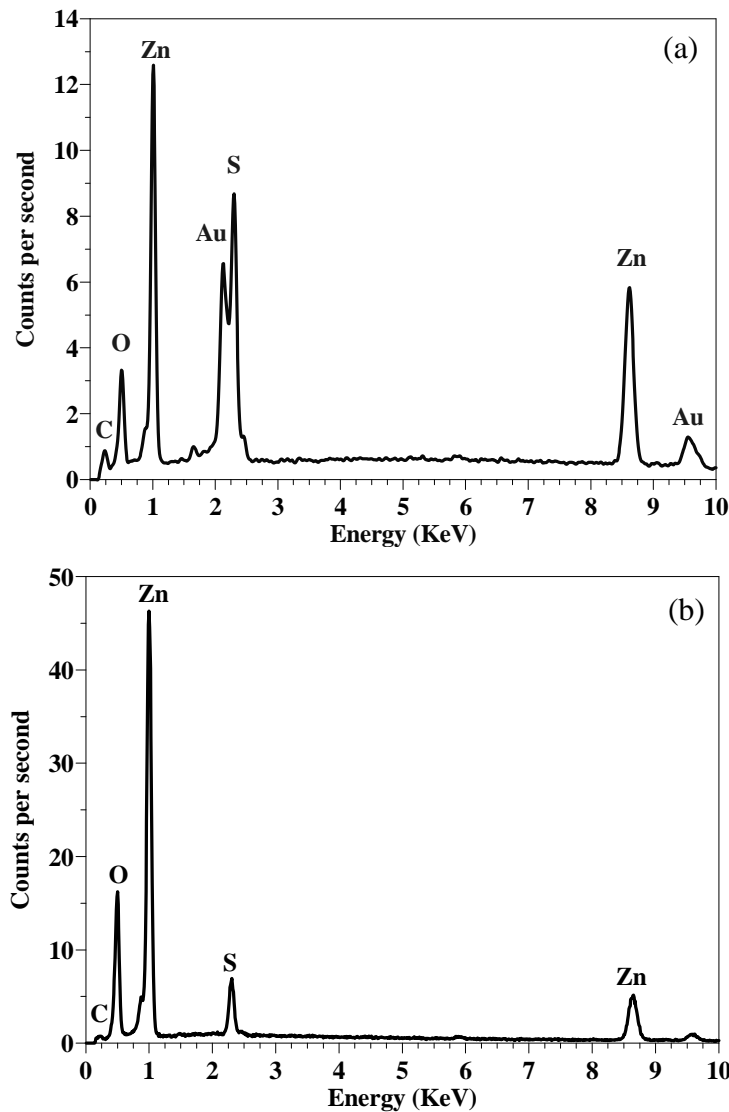


Figure 13: EDS spectra for a) un-annealed and b) annealed ZnS:Mn²⁺ doped with 2 mol% of Mn²⁺. The accelerating voltage was 15 kV.

Figure 13 shows the EDS spectra of un-annealed and annealed ZnS:Mn²⁺ doped with 2 mol% Mn²⁺. The presence of both ZnS and ZnO in the samples is confirmed with the Zn, S and O peaks. Small C and Au peaks are also present. From Table 2 it can be seen that the relative concentration of O is much higher for the annealed sample, indicating that ZnS was oxidized to ZnO during the annealing process.

Table 2: Listed EDS results for the un-annealed and annealed ZnS:Mn²⁺ samples.

	Weight %				
	C	O	Zn	S	Au
ZnS:Mn ²⁺ un-annealed	3	8	55	7	27
ZnS:Mn ²⁺ 600 °C	3	33	59	5	-

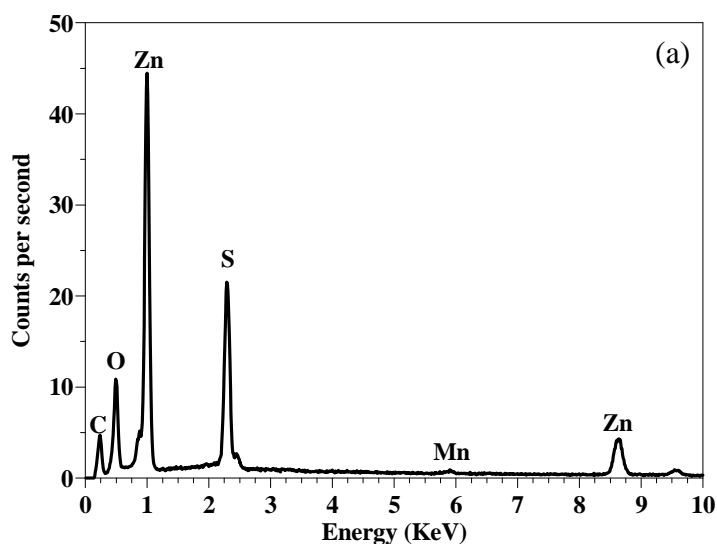


Figure 14 a): EDS spectrum for un-annealed ZnS:Mn²⁺ doped with 20 mol% of Mn²⁺. The accelerating voltage was 15 kV.

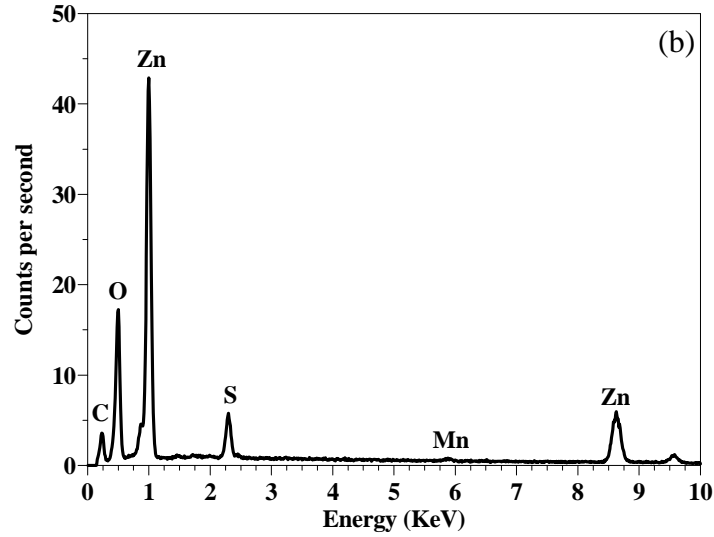


Figure 14 b): EDS spectrum for annealed ZnS:Mn²⁺ doped with 20 mol% of Mn²⁺. The accelerating voltage was 15 kV.

Figure 14 shows the EDS spectra of un-annealed and annealed ZnS:Mn²⁺ 20 mol%. The presence of ZnS and ZnO in the samples is confirmed by the Zn, S and O peaks. Due to the high concentration of Mn²⁺ (20 mol%), a small Mn peak is visible in the spectra. From Table 3 it can be seen that for the un-annealed sample the weight % of Mn was 1% and in the annealed sample the amount of Mn was too small to detect.

Table 3: Listed EDS results for the un-annealed and annealed ZnS:Mn²⁺ 20 mol% samples.

	Weight %				
	C	O	Zn	S	Mn
ZnS:Mn ²⁺ 20 mol% un-annealed	15	26	44	14	1
ZnS:Mn ²⁺ 20 mol% 600 °C	9	33	55	3	0

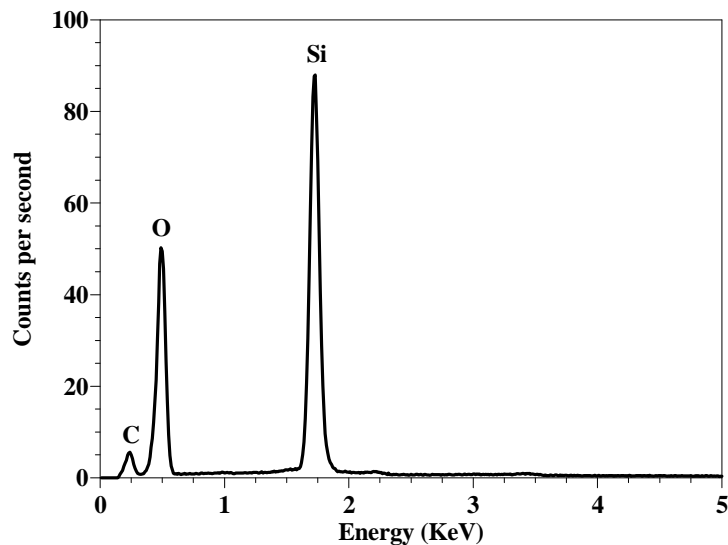


Figure 15: EDS spectrum of annealed SiO₂. The accelerating voltage is 15 kV.

The observed peaks in Figure 15 confirm that the sample consists of SiO₂ with the presence of a small amount of carbon contamination which is due to the carbon tape the samples were mounted on.

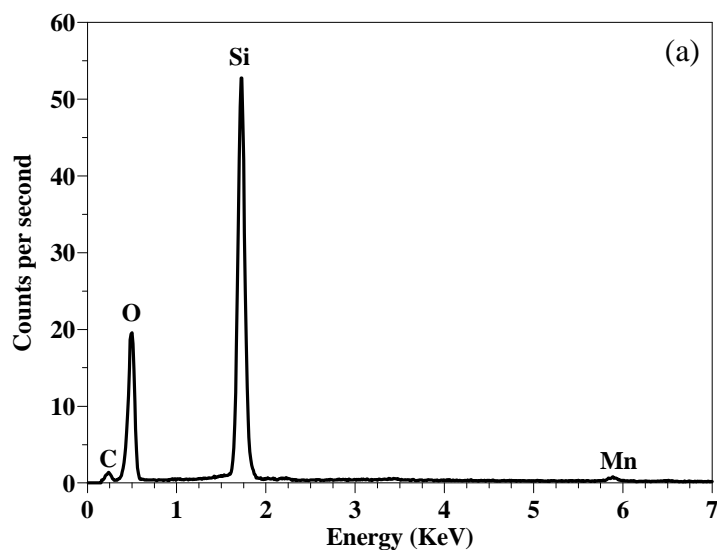


Figure 16 a): EDS spectrum for un-annealed SiO₂:Mn²⁺ doped with 10 mol% of Mn²⁺. The accelerating voltage is was kV.

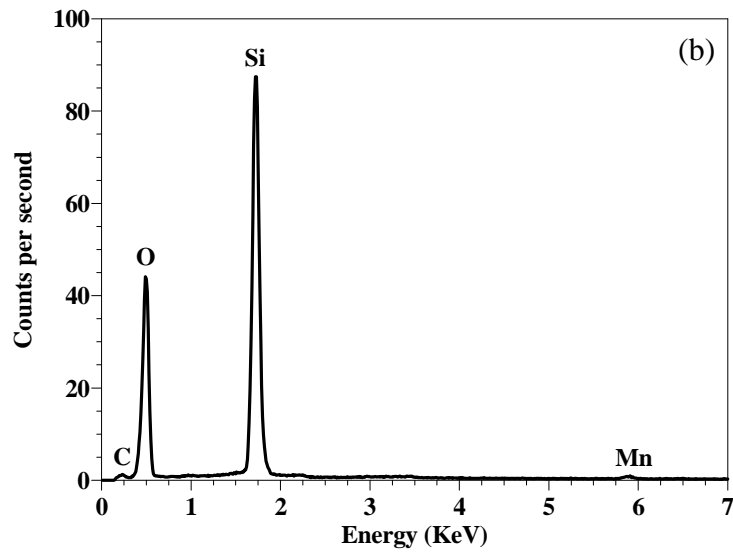


Figure 16 b): EDS spectrum for annealed $\text{SiO}_2:\text{Mn}^{2+}$ doped with 10 mol% of Mn^{2+} . The accelerating voltage was 15 kV.

Figure 16 shows the EDS spectra of un-annealed and annealed $\text{SiO}_2:\text{Mn}^{2+}$ 10 mol%. The samples consist of SiO_2 as the observed Si and O peaks confirm with small traces of Mn^{2+} ions as depicted in the spectra.

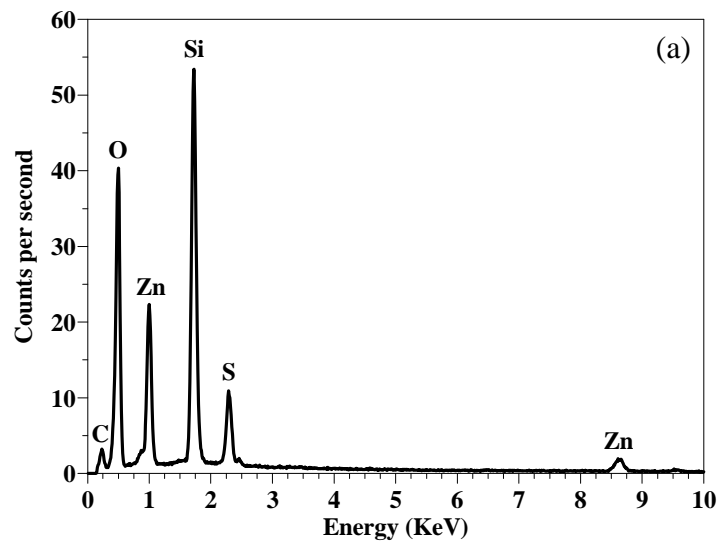


Figure 17 a): EDS spectrum for un-annealed $\text{SiO}_2:\text{ZnS}$. The accelerating voltage was 15 kV.

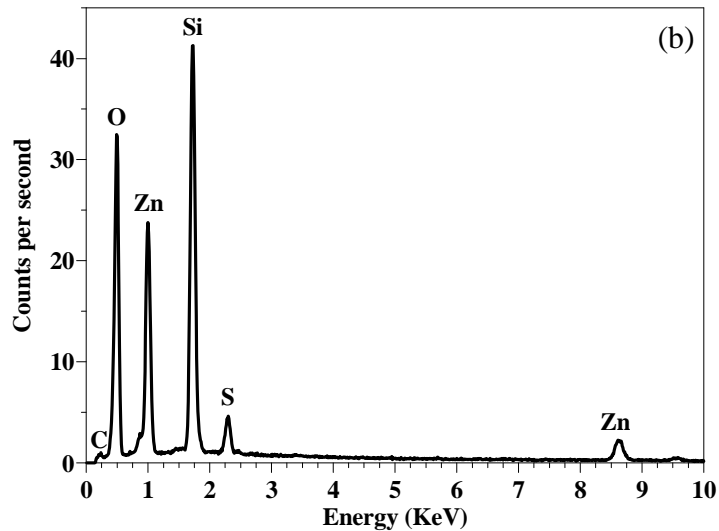


Figure 17 b): EDS spectrum for annealed $\text{SiO}_2:\text{ZnS}$. The accelerating voltage is 15 kV.

Figure 17 shows the EDS spectra of un-annealed and annealed $\text{SiO}_2:\text{ZnS}$. The presence of ZnS is confirmed with the Zn and S peaks while the presence of SiO_2 is confirmed with the Si and O peaks.

3.3 TEM results

The particle size and crystal structure of the synthesized ZnS powders were determined with TEM using a JEM 2100F TEM at the University of Pretoria and a Phillips CM100 at the CCEM. The ZnS samples were prepared as described in section 2.1. The prepared samples were dispersed in ethanol. 3mm Holey carbon copper grids were dipped into the ethanol mixture and the grids were allowed to dry. The TEM measurements were then taken.

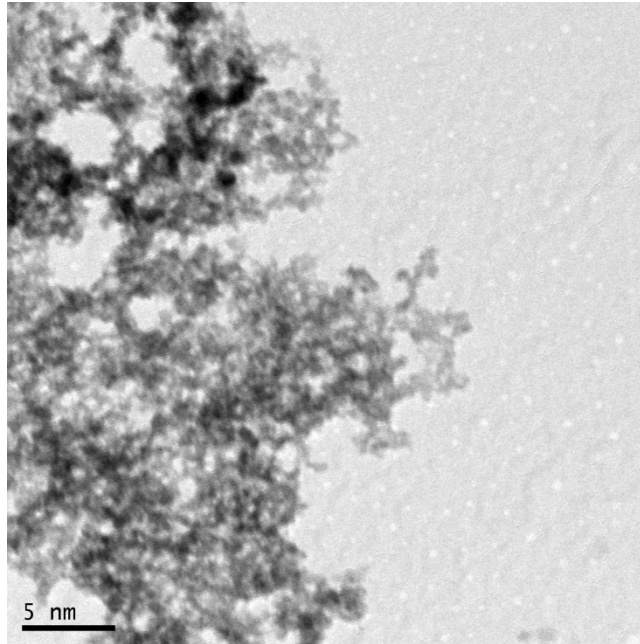


Figure 18: HRTEM image of synthesized ZnS nano particles with average particle size of 2 – 4 nm in diameter.

Figure 18 shows the HRTEM image of synthesized ZnS nano particles. It shows a agglomeration of nano particles. The average particle size estimated from the HRTEM image was ~2 - 4 nm in diameter, which is consistent with the particle size calculated from the XRD data.

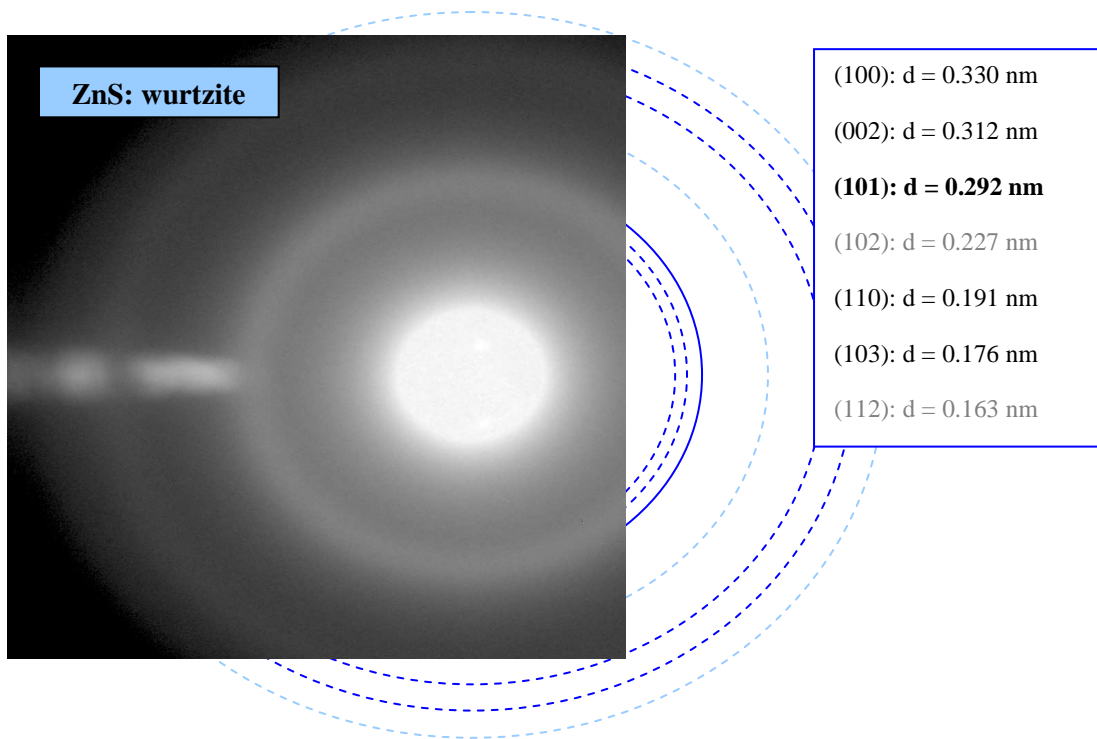


Figure 19: Electron diffraction pattern showing the ZnS wurtzite structure.

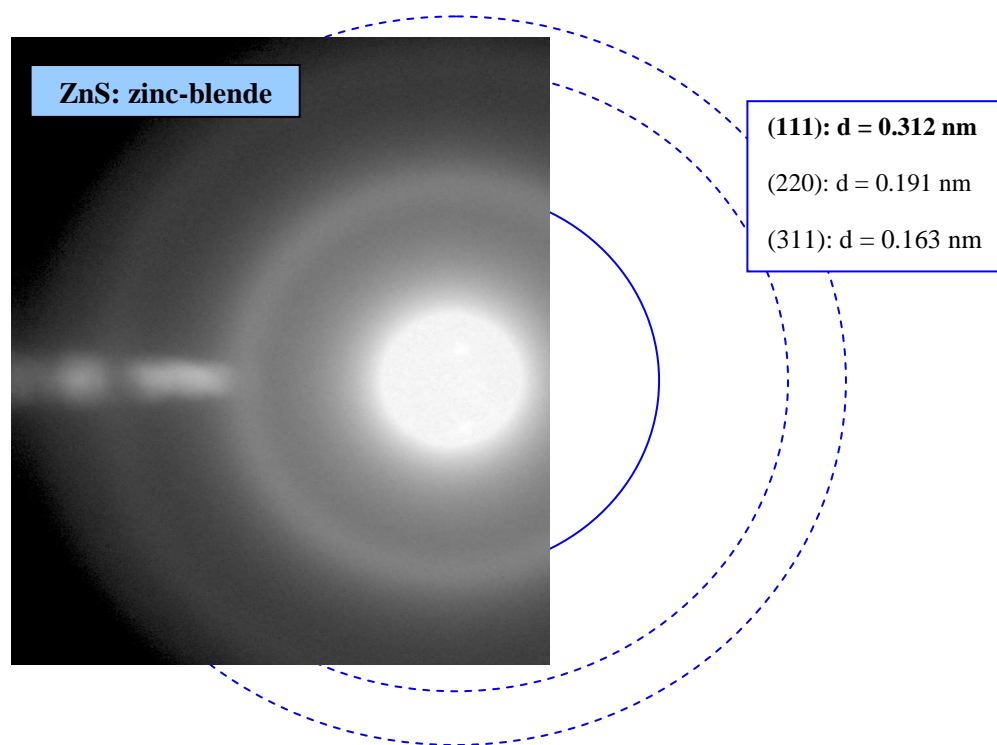


Figure 20: Electron diffraction pattern showing the ZnS zinc blende structure.

Figure 19 and 20 show the electron diffraction pattern of ZnS. The diffraction pattern consists of a central halo, with concentric broad rings around it. In Figure 19 the rings correspond to reflections from the (1 0 0), (0 0 2), (1 0 1), (1 0 2), (1 1 0), (1 0 3) and (1 1 2) planes and in Figure 20 the rings correspond to reflections from the (1 1 1), (2 2 0) and (3 1 1) planes. This confirms that both the hexagonal wurtzite and the cubic zinc blende crystallographic structures of ZnS nano particles are present.

3.4 XRD results

The crystal structure and particle size were determined with XRD, using a Siemens Diffractometer D5000 equipped with a Cu K α source ($\lambda = 1.504 \text{ \AA}$). All the powder samples were sieved to obtain an average secondary particle size of 212 μm .

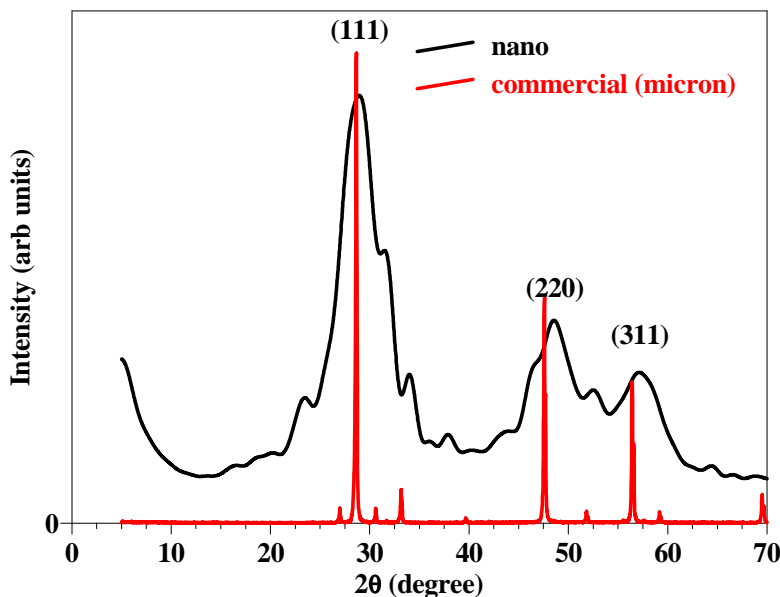


Figure 21: XRD spectra of commercially available ZnS:Mn²⁺ particles and synthesized ZnS:Mn²⁺ particles (x 50).

The XRD spectra for commercial micron-size and synthesized nano-size ZnS:Mn²⁺ particles are shown in Figure 21. The sharp peaks of the commercial particles show that it is highly crystalline and the particles are in the micron size. The three diffraction peaks positions corresponds to the lattice planes of (1 1 1), (2 2 0) and (3 1 1) matching the zinc blende (sphalerite) ZnS crystal structure (JCPDS 5-566). For the synthesized particles broadening of the peaks are observed, due

to smaller particle sizes. Strain factors as well as broadening due to the instrument could also contribute to the broadening of the peaks. The XRD pattern of the synthesized nano ZnS:Mn²⁺ particles resembles that of the commercial particles. Manganese impurities did not contribute to any additional diffraction peaks and it indicates that the Mn²⁺ ions were well dispersed in the ZnS matrix [13] and their concentration was relatively low.

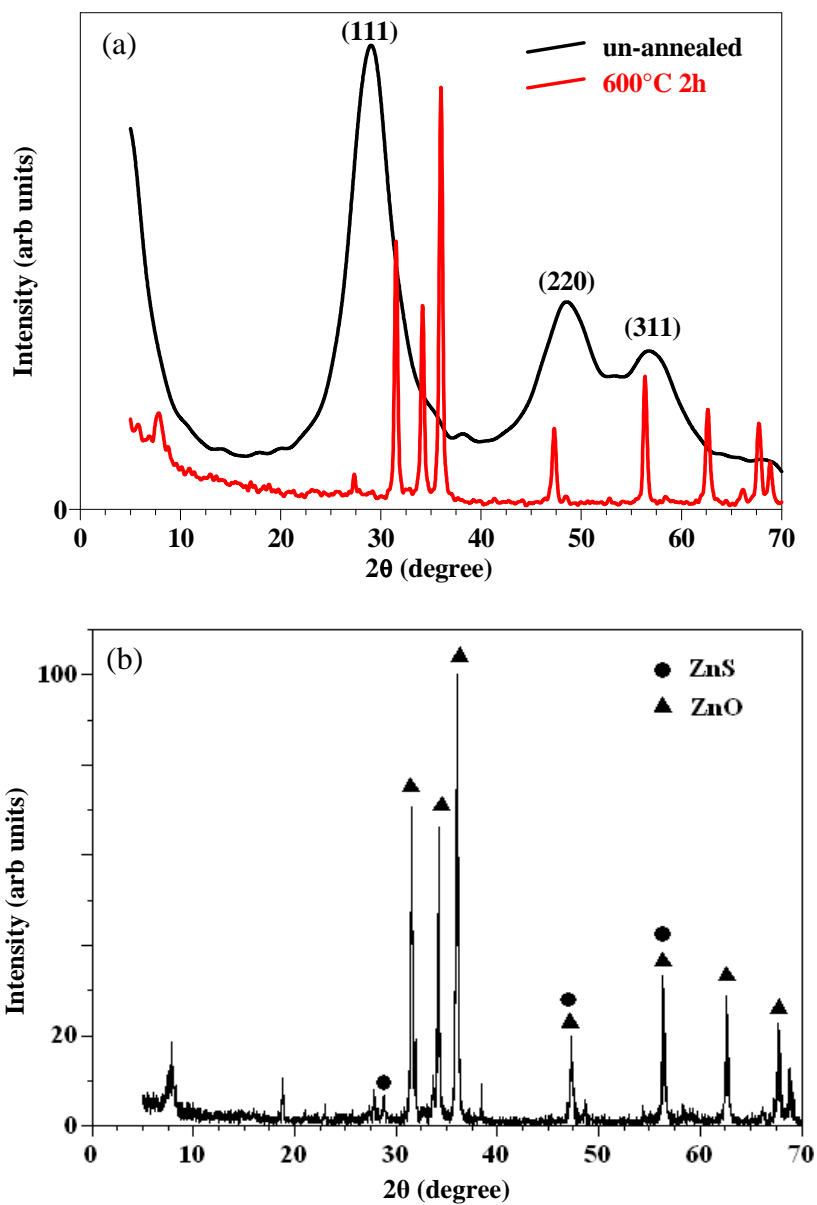


Figure 22: a) XRD spectra of un-annealed and annealed ZnS and b) peak positions of ZnS and ZnO for the annealed sample.

In Figure 22 the difference between the un-annealed and annealed samples are shown. For the un-annealed sample the diffraction peaks are broad, which is an indication of smaller particle sizes. The average particle size of the ZnS nano particles were estimated from the broadened XRD peak using Scherrer's equation [14]:

$$t = \frac{k\lambda}{B \cos \theta} \quad (1)$$

where t is the mean particle size, k is Scherrer's constant ~ 0.9 , λ the wavelength of the x-rays, θ is the angle of diffraction and B is the half peak width at full maximum of the peak after correcting for peak broadening which is caused by the diffractometer. B can be represented as

$$B^2 = B_{obs}^2 - B_m^2 \quad (2)$$

where B_{obs}^2 is the measured peak width and B_m is the peak broadening due to the instrument [15]. By making use of the (1 1 0) peak the average particle size was calculated as 3 ± 1 nm.

In Figure 22 (b) the diffraction peaks correspond to the lattice planes of (1 0 0), (0 0 2), (1 0 1), (1 0 2), (1 1 0), (1 0 3) and (1 1 2) (JCPDS 5-664) and are consistent with the hexagonal wurtzite crystal structure of ZnO. Some diffraction peaks of ZnS blende were also detected in the spectrum. This indicates that during annealing zinc reacted with oxygen in the atmosphere and ZnO was formed. For the annealed sample there is a narrowing of the peaks. The average particle size was calculated as ~ 50 nm. Similar observations were reported in ref [16].

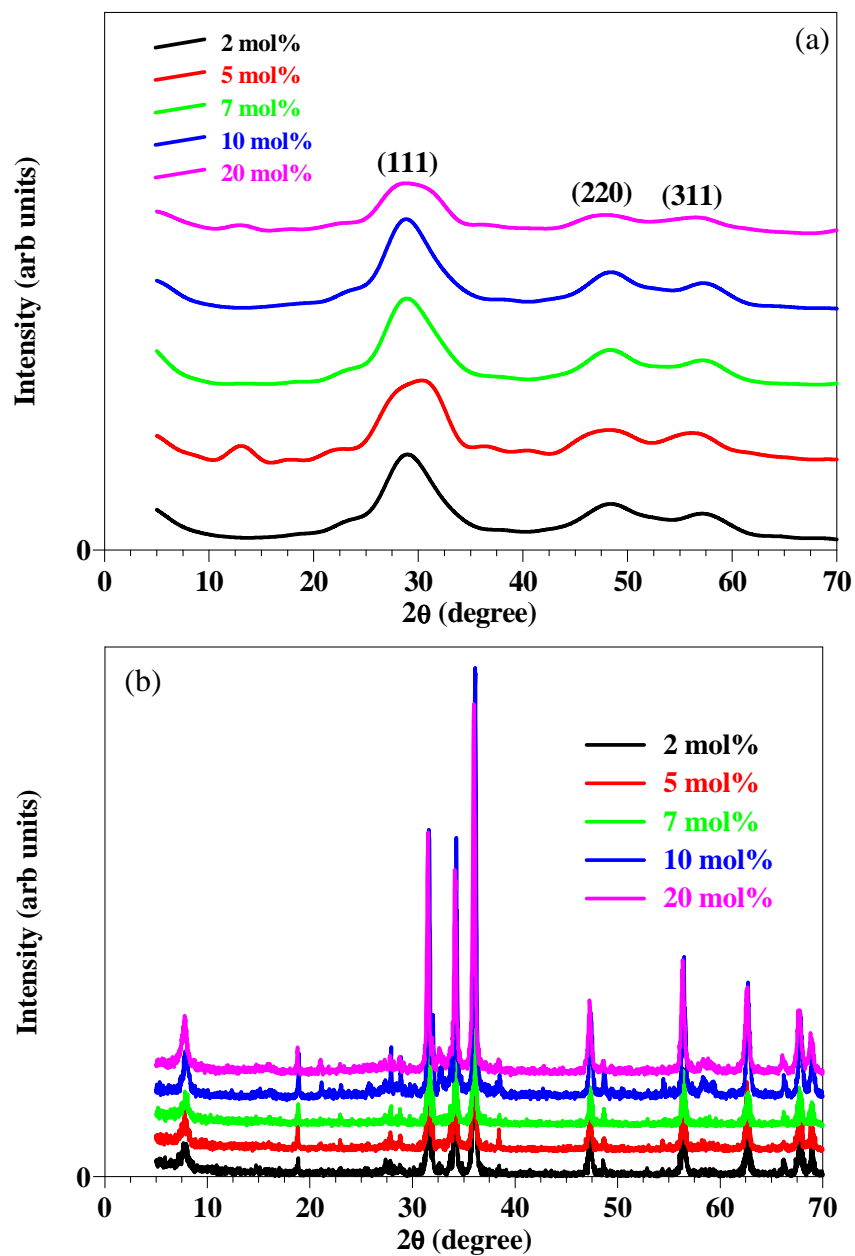


Figure 23: XRD spectra of a) un-annealed and b) annealed $ZnS:Mn^{2+}$.

In Figure 23 the XRD spectra for the (a) un-annealed and (b) annealed samples are shown. The un-annealed samples are showing no change in the peak position with a change in the Mn^{2+} concentration. The crystal structure of all the samples is consistent with the zinc blende structure of ZnS. The average particle size for the un-annealed $ZnS:Mn^{2+}$ samples were calculated as 3 ± 1 nm from Scherrer's equation. For the annealed samples there is again no change in the peak

positions with an increase in the Mn^{2+} concentration. The diffraction peaks corresponds mainly to that of the wurtzite crystal structure of ZnO, but some peaks of the zinc blende ZnS crystal structure are also observed. It can also be seen that the annealed samples are more crystalline than the un-annealed samples. The average particle size was calculated as ~ 50 nm.

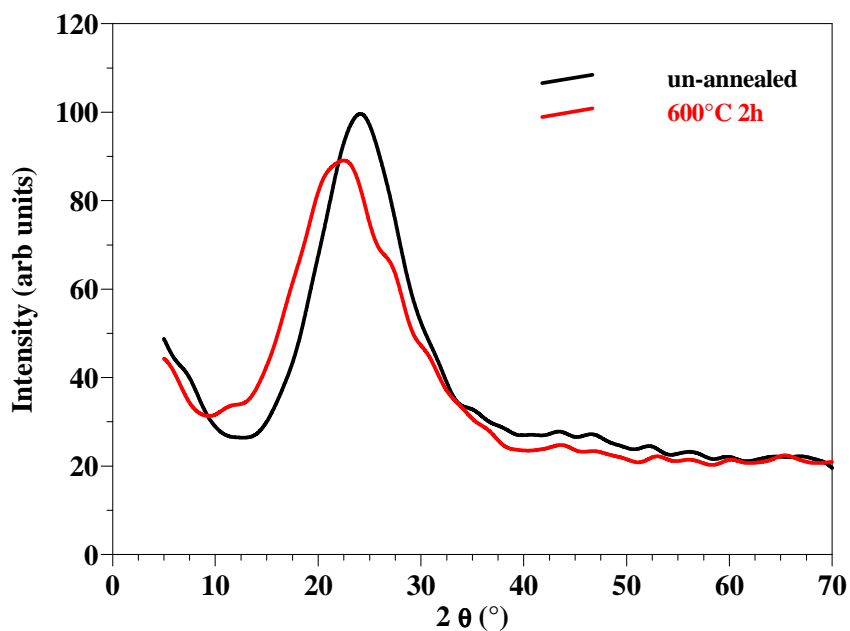


Figure 24: XRD spectra of un-annealed and annealed SiO_2 .

The spectra in Figure 24 show a broad diffraction peak for both the un-annealed and annealed SiO_2 samples. This broad peak is due to the high amorphous scattering background from the SiO_2 . A slight shift in the spectrum of the annealed sample is observed. Impurities might have been introduced to the SiO_2 matrix during the annealing process causing the observed shift.

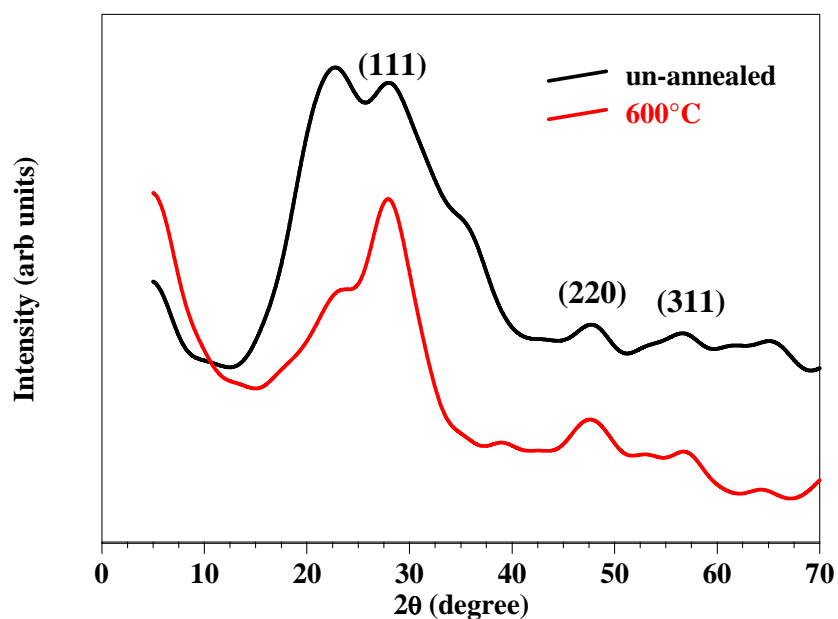


Figure 25: XRD spectra of un-annealed and annealed SiO₂:ZnS.

Figure 25 shows the XRD spectra for un-annealed and annealed SiO₂:ZnS. Small diffraction peaks corresponding to the diffraction planes of ZnS are detected around 48° and 56° for both samples. The (111) peak of ZnS is also observed for both samples. This peak is sitting inside the high amorphous scattering background of the SiO₂ matrix.

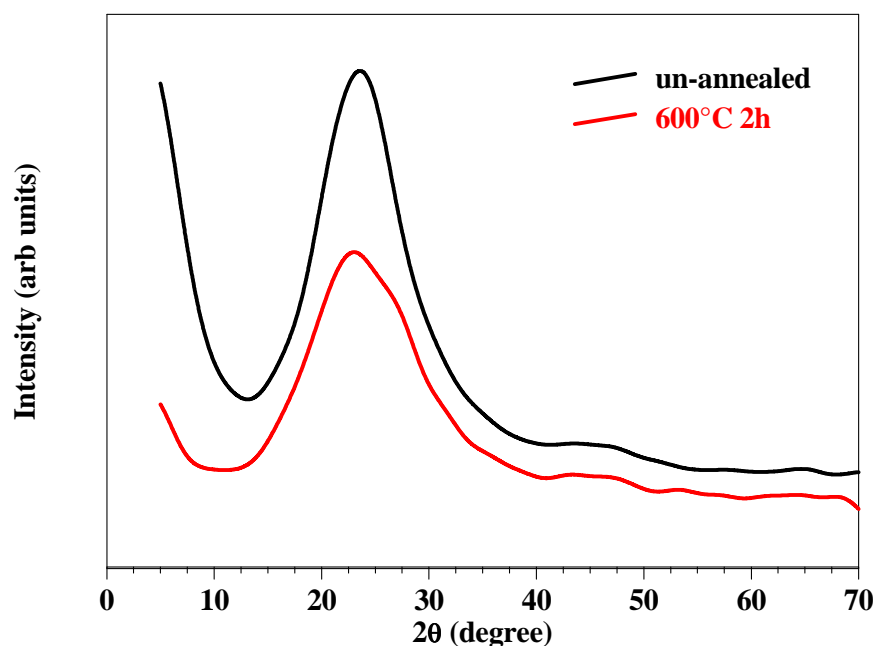


Figure 26: XRD spectra of un-annealed and annealed $\text{SiO}_2:\text{Mn}^{2+}$.

In Figure 26 the XRD spectra for un-annealed and annealed $\text{SiO}_2:\text{Mn}^{2+}$ is shown. The only diffraction peak that is detected is the broad amorphous peak from the SiO_2 matrix (Figure 25). Manganese impurities did not contribute to diffraction peaks or shifts in the peak position and it indicates that the Mn^{2+} ions were well dispersed in the SiO_2 matrix [13] and their concentration was relatively low.

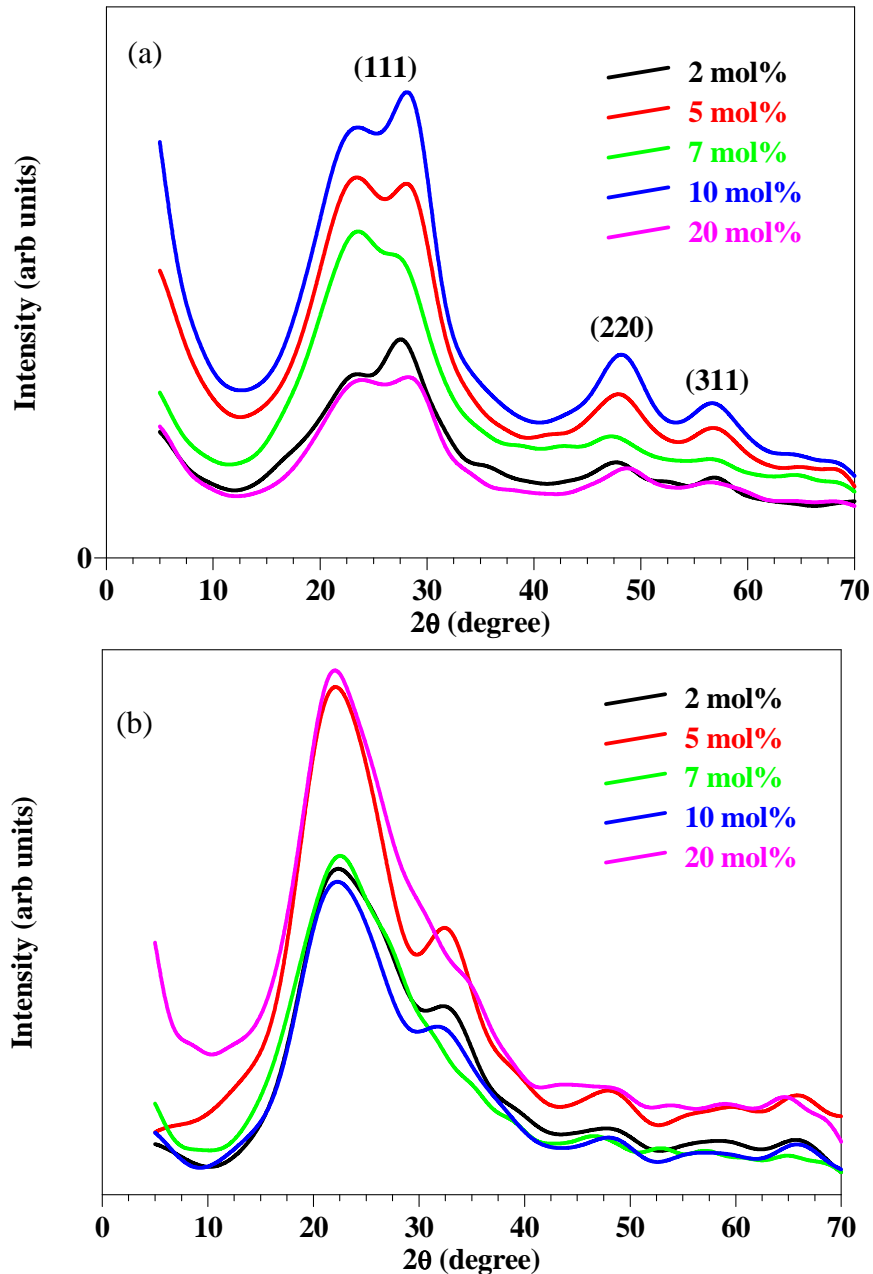


Figure 27: XRD spectra of a) un-annealed and b) annealed SiO₂-ZnS:Mn²⁺.

Figure 27 shows the XRD spectra for un-annealed and annealed SiO₂-ZnS:Mn²⁺. For the un-annealed samples the diffraction peaks of ZnS can clearly be seen indicating that the ZnS:Mn²⁺ particles were not well dispersed through the SiO₂ matrix. The broad peak between 20° and 30° is a combination of the broadened ZnS diffraction peak and the amorphous SiO₂ matrix peak. No change in the peak position is observed with a change in the Mn²⁺ concentration. For the annealed samples small diffraction peaks that are associated with ZnS and ZnO are detected. The

broad peak between 20° and 30° is a combination of the broadened ZnS/ZnO diffraction peak and the amorphous SiO₂ matrix peak.

4. Conclusion

From the SEM results it can be seen that the synthesized ZnS and ZnS:Mn²⁺ consist of secondary particles that were agglomerated to form bigger particles. The average size of the secondary particles was 100 - 200 nm. The commercial ZnS:Mn²⁺ powder shows micron size particles with slight agglomeration. All the samples that contain SiO₂ show glass like structures. With the addition of Mn²⁺ to the SiO₂, needle like structures were formed. The annealed ZnS:Mn²⁺ 20 mol% sample shows some spherical structures. These spheres are again agglomerated secondary particles. The FESEM image confirms that the particles were agglomerated and that the secondary particles were in the order of 100 nm in size.

All the EDS results show that the desired samples had formed. The results also confirmed that for the un-annealed samples the amount of ZnS was higher than that of ZnO. In the case of the annealed samples ZnS were oxidized to ZnO during annealing. For the low doping concentrations of Mn²⁺ no Mn peak was observed. For the high doping concentrations (10 and 20 mol%) a small Mn peak was observed. C was present in all the samples. This is due to either contamination or the presence of the carbon tape on which the samples were mounted.

The TEM results show that the primary ZnS particle's size is $\sim 2 - 4$ nm. It shows an agglomeration of nano particles. The electron diffraction pattern of ZnS confirmed that both the cubic zinc blende and the hexagonal wurtzite crystallographic structures were present.

The XRD results confirmed that for the un-annealed samples cubic zinc blende ZnS had formed. There was also a broadening in the peaks indicating a decrease in the particle size. The average particle size was calculated using Scherrer's equation and it was found to be 3 ± 1 nm. For the annealed samples both cubic zinc blende ZnS and hexagonal wurtzite ZnO had formed. This is an indication that during annealing the samples reacted with oxygen in the air to form ZnO. The peaks narrowed and the average particle size increased to ~ 50 nm. With the addition of Mn²⁺ to the ZnS, there was no change in the position of the peaks. The manganese impurities therefore did not contribute to any additional diffraction peaks or shifts in the peak position. This is an

indication that the Mn^{2+} ions were well dispersed in the ZnS matrix [13] and that their concentration was relatively low. A broad amorphous peak belonging to the SiO_2 matrix was observed in the samples containing SiO_2 .

References

1. B. Bhattacharjee, D. Ganguli, S. Chaudhuri and A.K. Pal, *Thin Solid Films*, **422** (2002) 98.
2. S.W. Lu, B.I. Lee, Z.L. Wang, W. Tong, B.K. Wagner, W. Park and C.J. Summers, *J. Lumin.* **92** (2001) 74.
3. D. Son, D. Jung, J. Kim, T. Moon, C. Kim and B. Park, *Appl. Phys. Lett.* **90** (2007) 101910-1.
4. H.S. Batti, R. Sharma and N.K. Verma, *Physica B*, **382** (2006) 39.
5. A.B. Cruz, Q. Shen, T. Toyoda, *Mater. Sci. Eng. C*, **25** (2005) 762.
6. C. Jin, J. Yu, L. Sun, K. Dou, S. Hou, J. Zhao, Y. Chen and S. Huang, *J. Lumin.* **66&67** (1996) 315.
7. H. Yang and P.H. Holloway, *J. App. Phys.* **93** (2003) 586.
8. W.Q. Peng, S.C. Qu, G.W. Cong, X.Q. Zhang and Z.G. Wang, *J. Cryst. Growth*, **282** (2005) 180.
9. O.M. Ntwaeaborwa, H.C. Swart, R.E. Kroon, P.H. Holloway and J.R. Botha, *J. Phys. Chem. Sol.* **67** (2006) 1750.
10. G.M. Chow and K.E. Gonsalves, *Nanomaterials: synthesis, properties and applications*, edited by A.S. Edelstein and R.C. Cammarata, Institute of Physics, Bristol, 2001, 56.
11. As-prepared hollow nanocrystalline CdS nanospheres, [online]. Available from http://www.nature.com/nmat/journal/v7/n12/fig_tab/nmat2295_F1.html [Accessed 4 November 2009].
12. CdSe Quantum Dots and Rods, [online]. Available from <http://www.nhn.ou.edu/cspin/research/nuggets/nugget2.html> [Accessed 4 November 2009].
13. W.Q. Peng, S.C. Qu, G.W. Cong, Z.G. Wang, *J. Crystal Growth* **279**, 456 (2005).
14. B.D. Cullity, *Elements of X-Ray Diffraction*, Addison-Wesley, Reading, MA, 1978.
15. Crystallite size measurement using Xray Diffraction, [online]. Available from <http://chms.engineering.ucdavis.edu/students/undergraduates/labs/files/XRD-CSize1.pdf> [Accessed 17 November 2009].
16. Y. Tong, Z. Jiang, C. Wang, Y. Xin, Z. Haung, S. Liu and C. Li, *Mat. Lett.* **62**, 3386 (2008).

Chapter 6

Luminescent properties of ZnS:Mn²⁺ and SiO₂-ZnS:Mn²⁺ nanoparticle phosphors.

The luminescent properties of ZnS:Mn²⁺ and SiO₂-ZnS:Mn²⁺ are discussed in this chapter. It starts with the absorption and transmittance of the different samples and then shows how Tauc's relation was used to calculate the band gap of the different samples. This is followed by the photoluminescence (PL) data for the different samples and it finishes off with the Auger electron spectroscopy (AES) and residual gas analysis (RGA) data of the different samples and the degradation study and cathodoluminescence (CL) of commercial ZnS:Mn²⁺.

1. Absorption

The absorption measurement was performed on the powders using a Shimadzu UV-1700 PharmaSpec UV-Vis spectrophotometer. The powders were first dispersed in ethanol and placed in a quartz cuvette. The absorption characteristics were measured after the powders were dissolved. Ethanol was used as the reference sample.

1.1 Synthesized ZnS

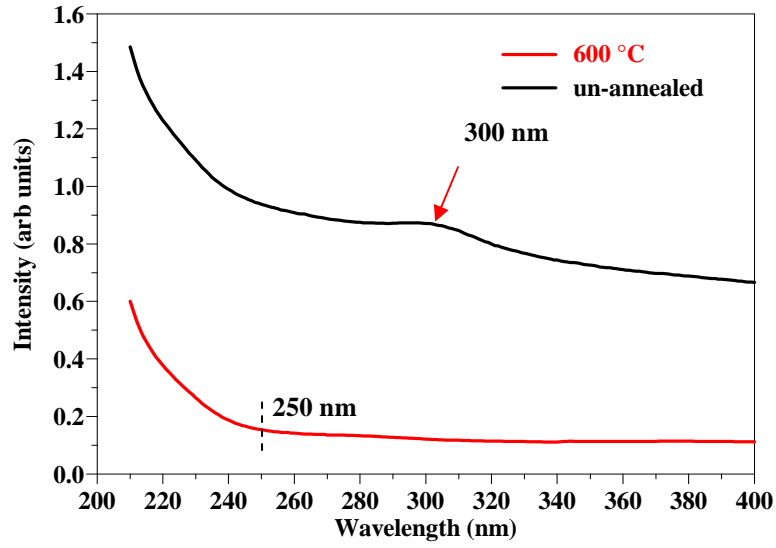


Figure 1: Absorption spectra of the un-annealed and annealed ZnS.

Figure 1 shows the absorption spectra of the un-annealed and annealed ZnS. The characteristic absorption peak due to ZnS nanoparticles appears in the wavelength range 220-340 nm and this peak's position reflects the band gap of the material. For the un-annealed ZnS an absorption peak appears at around 300 nm. This peak is blue-shifted from the absorption edge of bulk ZnS (345 nm) [1]. For the annealed sample the absorption edge starts at ~250 nm.

1.2 Commercial ZnS:Mn²⁺

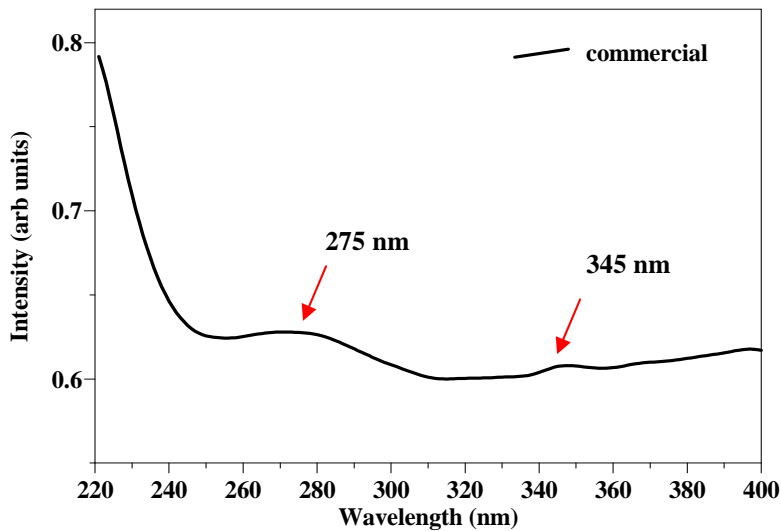


Figure 2: Absorption spectrum of commercial ZnS:Mn²⁺.

Figure 2 shows the absorption spectrum of commercial ZnS:Mn²⁺. Two peaks are observed for the absorption spectrum. One at 345 nm and the other one at 275 nm. The peak at 345 nm corresponds to absorption over the band gap (~3.66 eV) and the one at 275 nm can be assigned to an excitonic transition and proves the existence of ZnS [2]. There is no shift in the peak from the absorption edge of bulk ZnS, confirming that the particle size of the commercial phosphor is in the μm range.

1.3 Synthesized ZnS:Mn²⁺ (un-annealed)

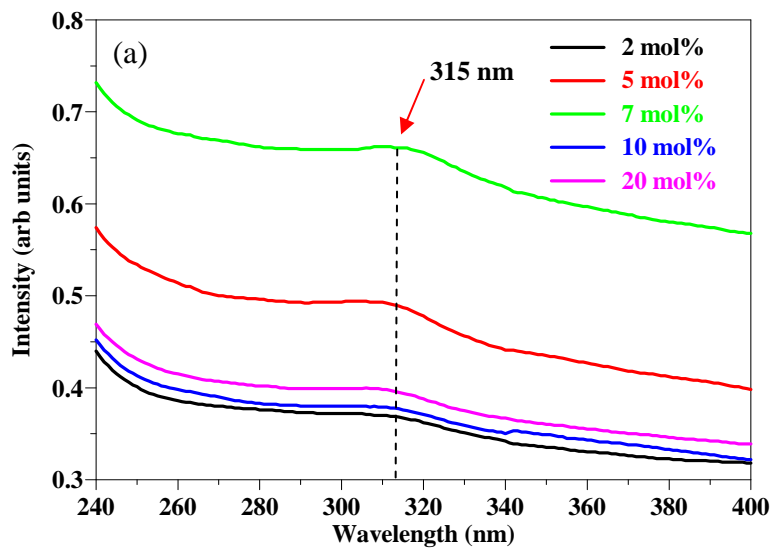


Figure 3: Absorption spectra of un-annealed ZnS:Mn²⁺ with different concentrations of Mn²⁺.

Figure 3 shows the absorption spectra of un-annealed ZnS:Mn²⁺. A broad peak is observed at 312 nm for all the different samples. This peak is blue-shifted from the absorption edge of bulk ZnS (345 nm). This blue-shift is due to quantum confinement effects. From Figure 4 it can also be seen that there is no regular trend in the absorption intensity for the different mol% samples.

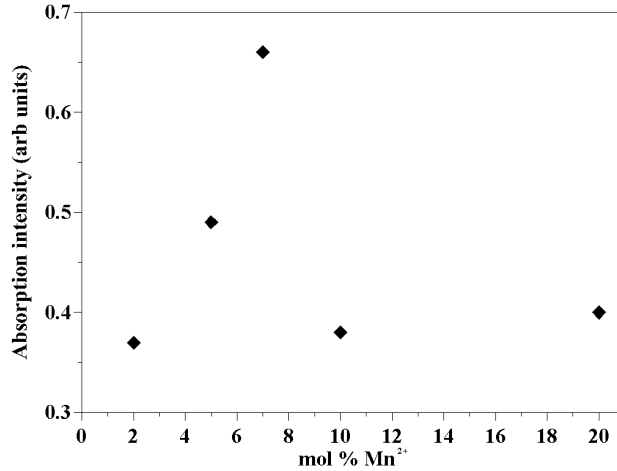


Figure 4: Graph of mol% Mn²⁺ as a function of absorption intensity for un-annealed ZnS:Mn²⁺.

1.4 Synthesized ZnS:Mn²⁺ (annealed)

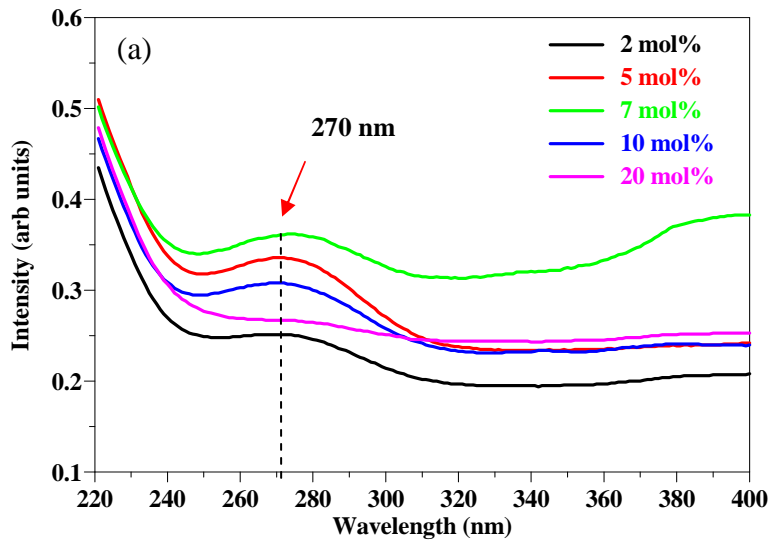


Figure 5: Absorption spectra of annealed ZnS:Mn²⁺.

Figure 5 shows the absorption spectra of annealed ZnS:Mn²⁺. A broad peak is observed at ~270 nm for all the samples. This peak is due to excitonic transitions [2] and proves the existence of ZnS in the samples. This peak is blue-shifted from both the absorption edge of bulk ZnS (345 nm) and bulk ZnO (387 nm). This shift is due to quantum confinement effects. From Figure 6 it can again be seen that there is no regular trend in the absorption intensities of the different samples. These results correspond with that of the un-annealed samples.

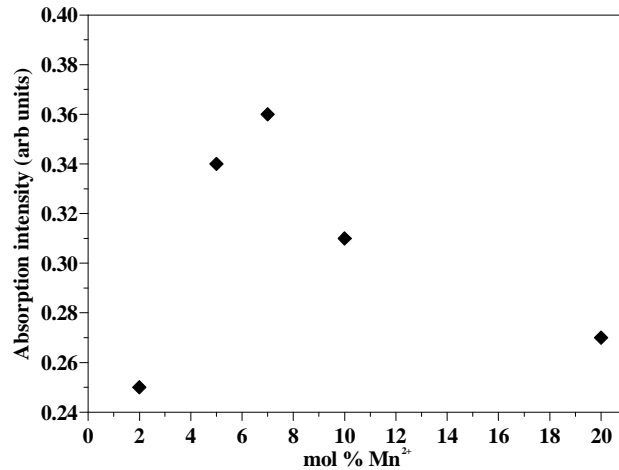


Figure 6: Graph of mol% Mn²⁺ as a function of absorption intensity for annealed ZnS:Mn²⁺.

1.5 Synthesized SiO₂

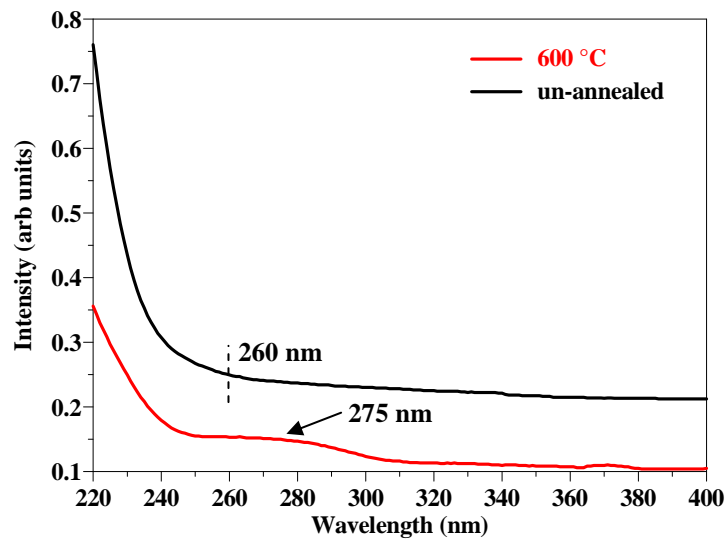


Figure 7: Absorption spectra of un-annealed and annealed SiO₂.

Figure 7 shows the absorption spectra of un-annealed and annealed SiO₂. The un-annealed sample shows an absorption edge at ~260 nm, while the annealed sample shows a broad absorption peak at ~275 nm. The absorption of the un-annealed sample is higher than that of the annealed sample.

1.6 Synthesized $\text{SiO}_2:\text{Mn}^{2+}$

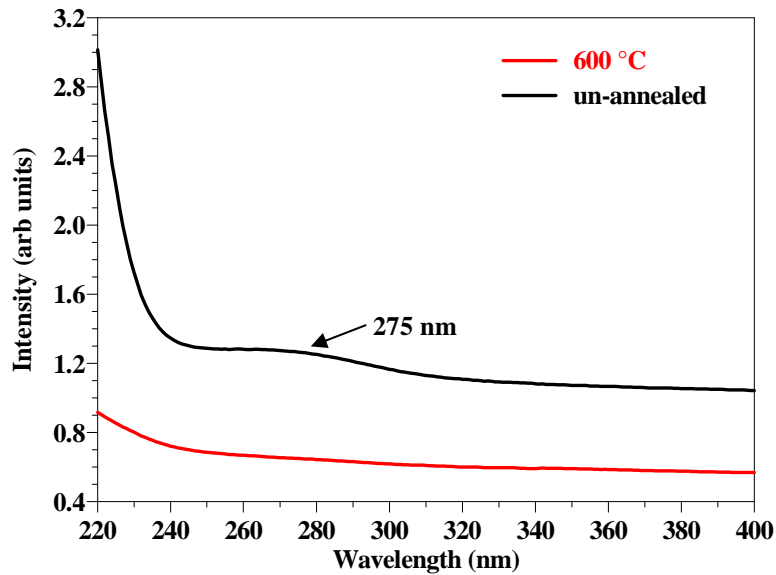


Figure 8: Absorption spectra of un-annealed and annealed $\text{SiO}_2:\text{Mn}^{2+}$.

Figure 8 shows the absorption spectra of un-annealed and annealed $\text{SiO}_2:\text{Mn}^{2+}$. The un-annealed sample shows a broad absorption peak ~ 275 nm, while no peak could be observed for the annealed sample. The addition of Mn^{2+} causes the absorption edge of the un-annealed sample to red-shift with 50 nm.

1.7 Synthesized SiO₂:ZnS

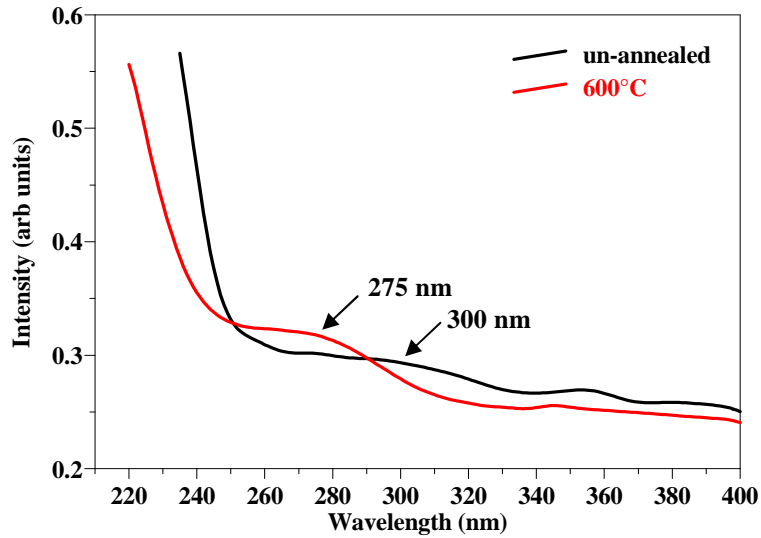


Figure 9: Absorption spectra of un-annealed and annealed SiO₂:ZnS.

Figure 9 shows the absorption spectra of un-annealed and annealed SiO₂:ZnS. The un-annealed sample shows a broad absorption peak at 300 nm. This is due to the presence of ZnS nano particles in the SiO₂ matrix. The peak is blue-shifted from that of bulk ZnS (345 nm). The annealed sample shows a broadened peak at around 275 nm. This peak is due to excitonic transitions and proves the existence of ZnS particles in the SiO₂ matrix.

1.8 Synthesized SiO₂-ZnS:Mn²⁺ (un-annealed)

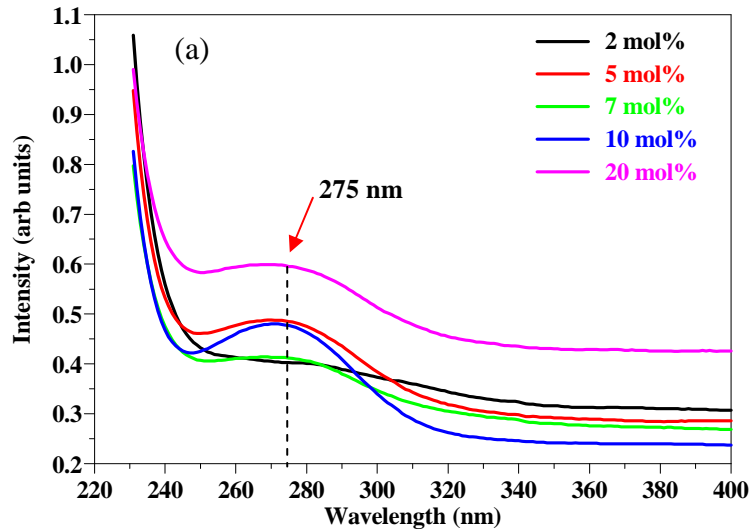


Figure 10: Absorption spectra of un-annealed SiO₂-ZnS:Mn²⁺.

Figure 10 shows the absorption spectra of un-annealed SiO₂-ZnS:Mn²⁺. All the samples show a broad peak at around 275 nm. The 2 mol% sample's peak is overshadowed by the 7 mol% sample. This broad absorption peak is due to excitonic transitions and proves the presence of ZnS in the samples. This peak is blue-shifted from the absorption edge of bulk ZnS (345 nm). It is due to quantum confinement effects. The 20 mol% sample has the highest absorption intensity (Figure 11).

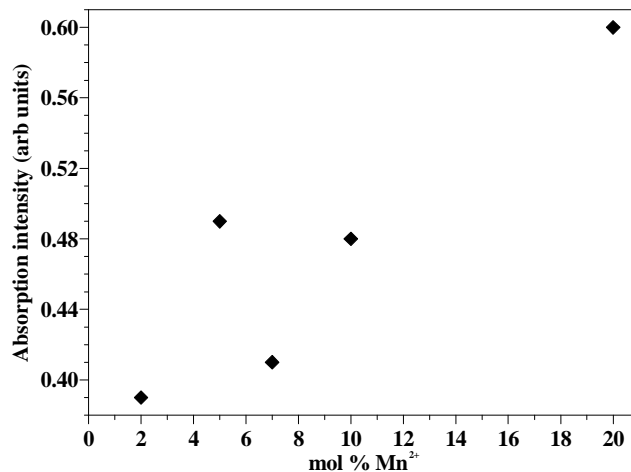


Figure 11: Graph of mol% Mn²⁺ as a function of absorption intensity for un-annealed SiO₂-ZnS:Mn²⁺.

1.9 Synthesized $\text{SiO}_2\text{-ZnS:Mn}^{2+}$ (annealed)

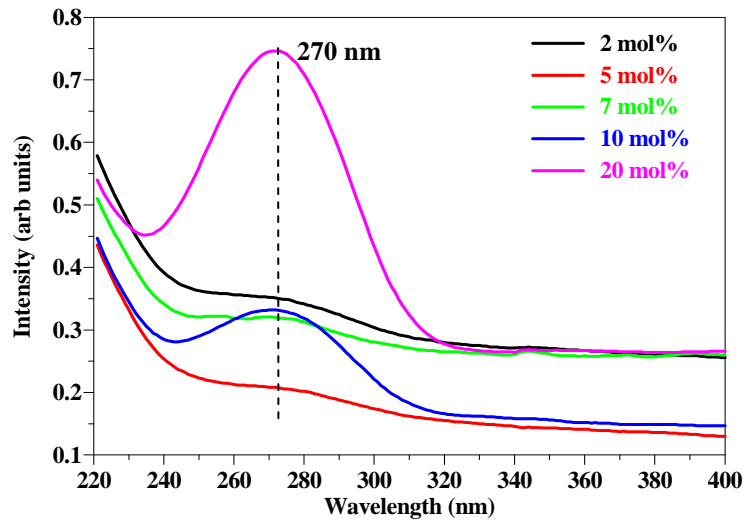


Figure 12: Absorption spectra of annealed $\text{SiO}_2\text{-ZnS:Mn}^{2+}$.

Figure 12 shows the absorption spectra of annealed $\text{SiO}_2\text{-ZnS:Mn}^{2+}$. All the samples are showing a broad absorption peak at ~ 270 nm. The 2 – 7 mol% sample's peak are overshadowed by the 10 and 20 mol % sample's peaks. The absorption peaks are blue-shifted from that of bulk ZnS (345) and bulk ZnO (387 nm). This is due to quantum confinement effects. Figure 13 is showing how the absorption intensity is varying with Mn^{2+} concentration. The 20 mol% sample has the highest absorption intensity of all the samples.

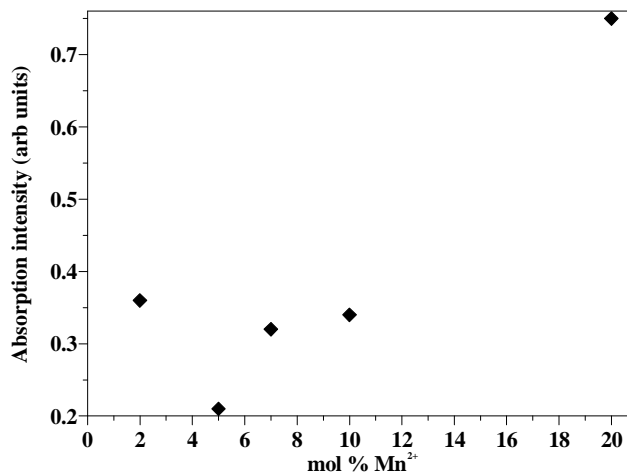


Figure 13: Graph of mol% Mn^{2+} as a function of absorption intensity for annealed $\text{SiO}_2\text{-ZnS:Mn}^{2+}$.

2. Band gap determination

2.1 Determination of the band gap of the commercial and synthesized samples.

Tauc's relation was used to determine the band gap of the synthesized powders. The value of n is $\frac{1}{2}$, because ZnS is a direct band gap material [1]. The linear part of the graph was extrapolated to $(\alpha h\nu)^{1/n} \approx 0$ to determine the bandgap.

2.1.1 Commercial ZnS:Mn²⁺

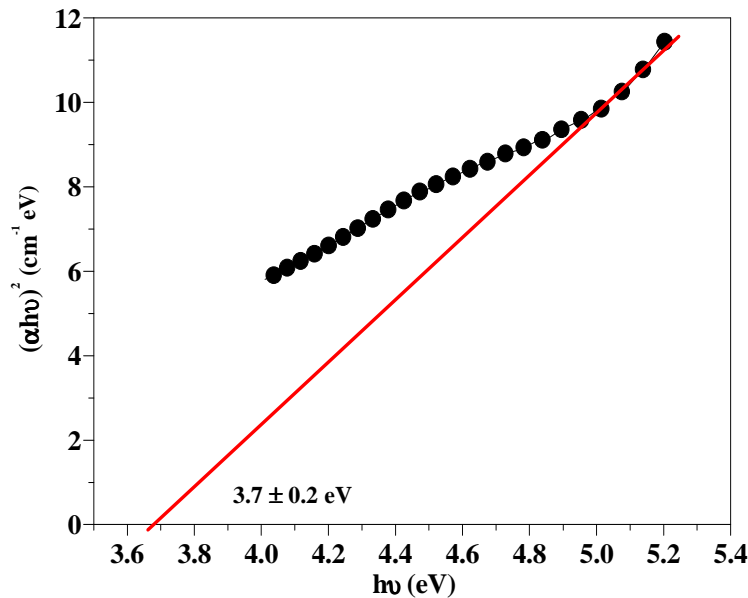


Figure 14: Band gap determination of commercial ZnS:Mn²⁺.

From Figure 14 it can be seen that the band gap of commercial ZnS:Mn²⁺ was determined as 3.7 ± 0.2 eV. This corresponds well to the theoretical value of 3.66 eV [11]. It is also an indication that the particle size of the commercial phosphor were in the μm range.

2.1.2 Un-annealed ZnS

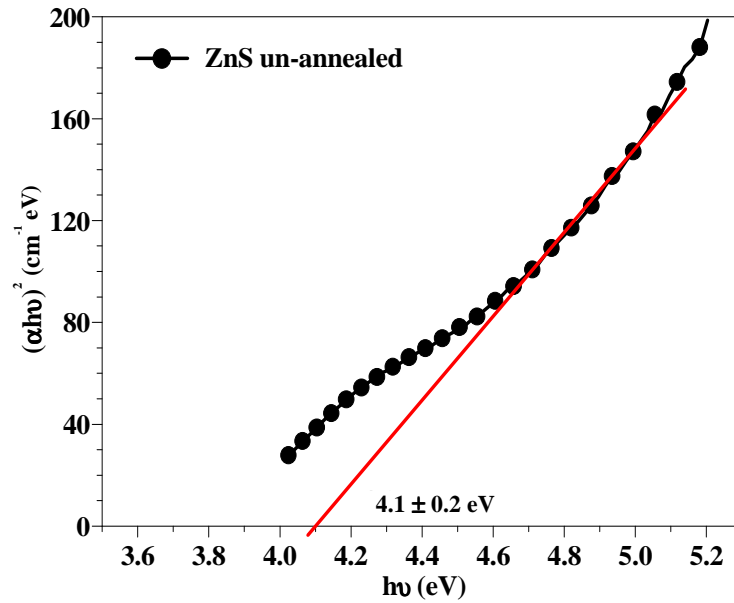


Figure 15: Band gap determination of un-annealed ZnS.

From Figure 15 it was determined that the band gap of un-annealed ZnS is $4.1 \pm 0.2 \text{ eV}$. There is a blue shift in the band gap of 0.44 eV from that of bulk ZnS (3.66 eV). This is an indication that the particle size had decreased to nm range.

2.1.3 Annealed ZnS

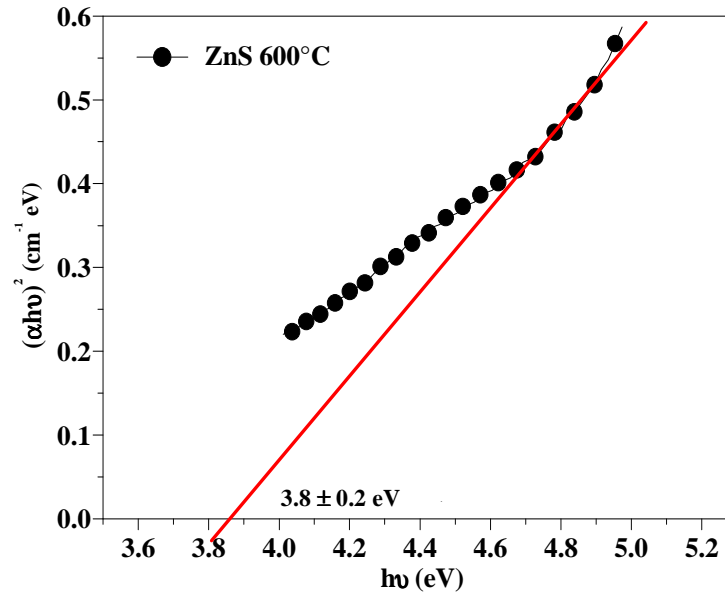


Figure 16: Band gap determination of annealed ZnS.

Figure 16 shows that the band gap of annealed ZnS is determined as $3.8 \pm 0.2 \text{ eV}$. There is a blue shift of 0.19 eV from that of bulk ZnS. From the XRD result it could be seen that the particle sizes of the annealed ZnS are bigger than those of the un-annealed sample and the blue shift in the band gap is therefore also smaller.

2.1.4 Un-annealed ZnS:Mn²⁺

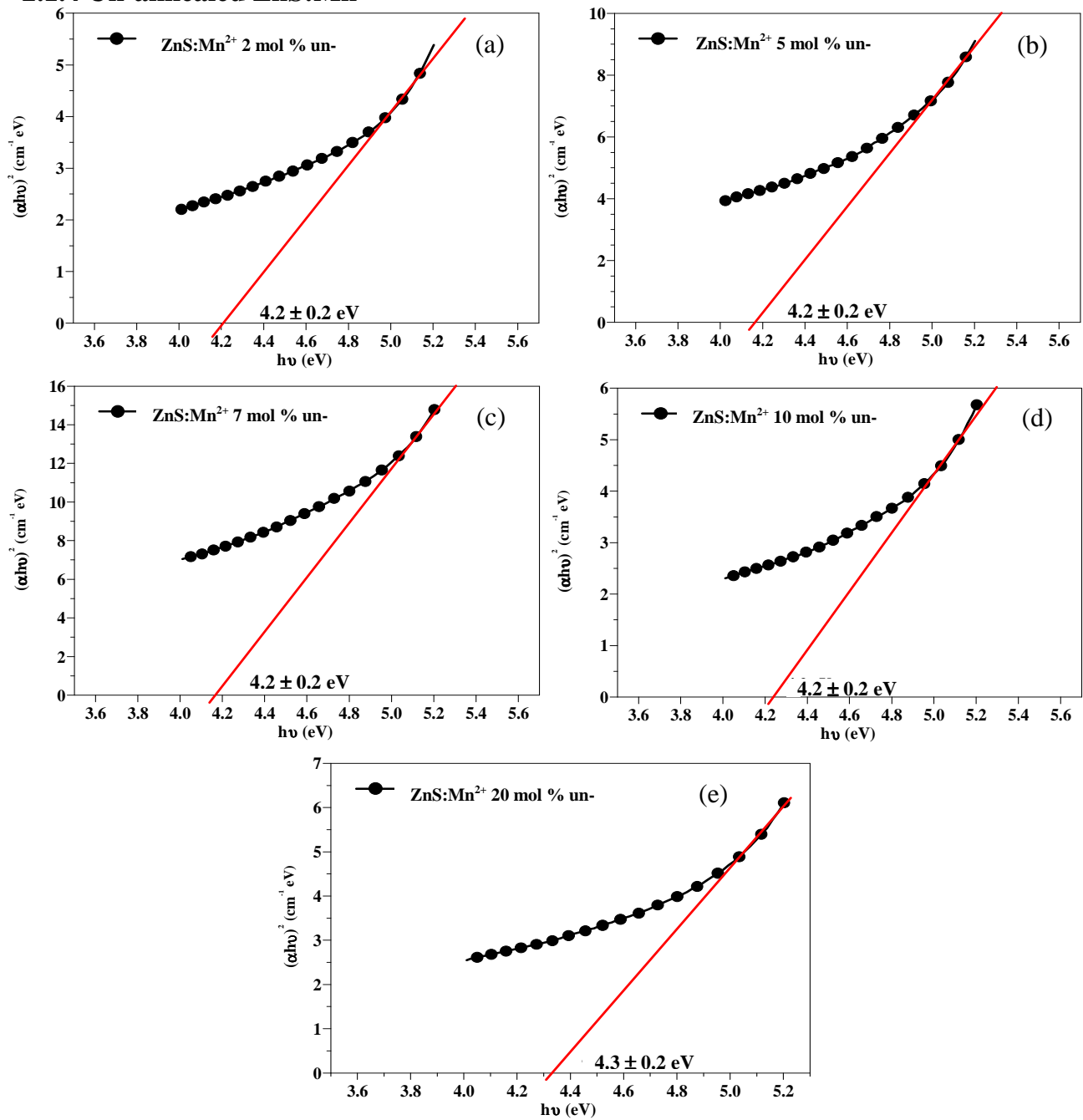


Figure 17: (a-e) band gap determination of different mol% of un-annealed ZnS:Mn²⁺.

Figure 17 a-e shows the band gap of the different mol% of un-annealed ZnS:Mn²⁺. The values of the band gaps are listed in Table 1. It can be seen that with the addition of Mn²⁺ to the ZnS matrix the band gap increases slightly from 4.1 eV to 4.2 eV. In the 20 mol% samples there was an even bigger increase in the band gap to 4.3 eV. This increase of the band gap is an indication that the particle size decreased even more from that of bulk ZnS.

Table 1: Band gaps of different mol% of un-annealed ZnS:Mn²⁺.

mol%	Band gap
2	4.2 ± 0.2 eV
5	4.2 ± 0.2 eV
7	4.2 ± 0.2 eV
10	4.2 ± 0.2 eV
20	4.3 ± 0.2 eV

2.1.5 Annealed ZnS:Mn²⁺

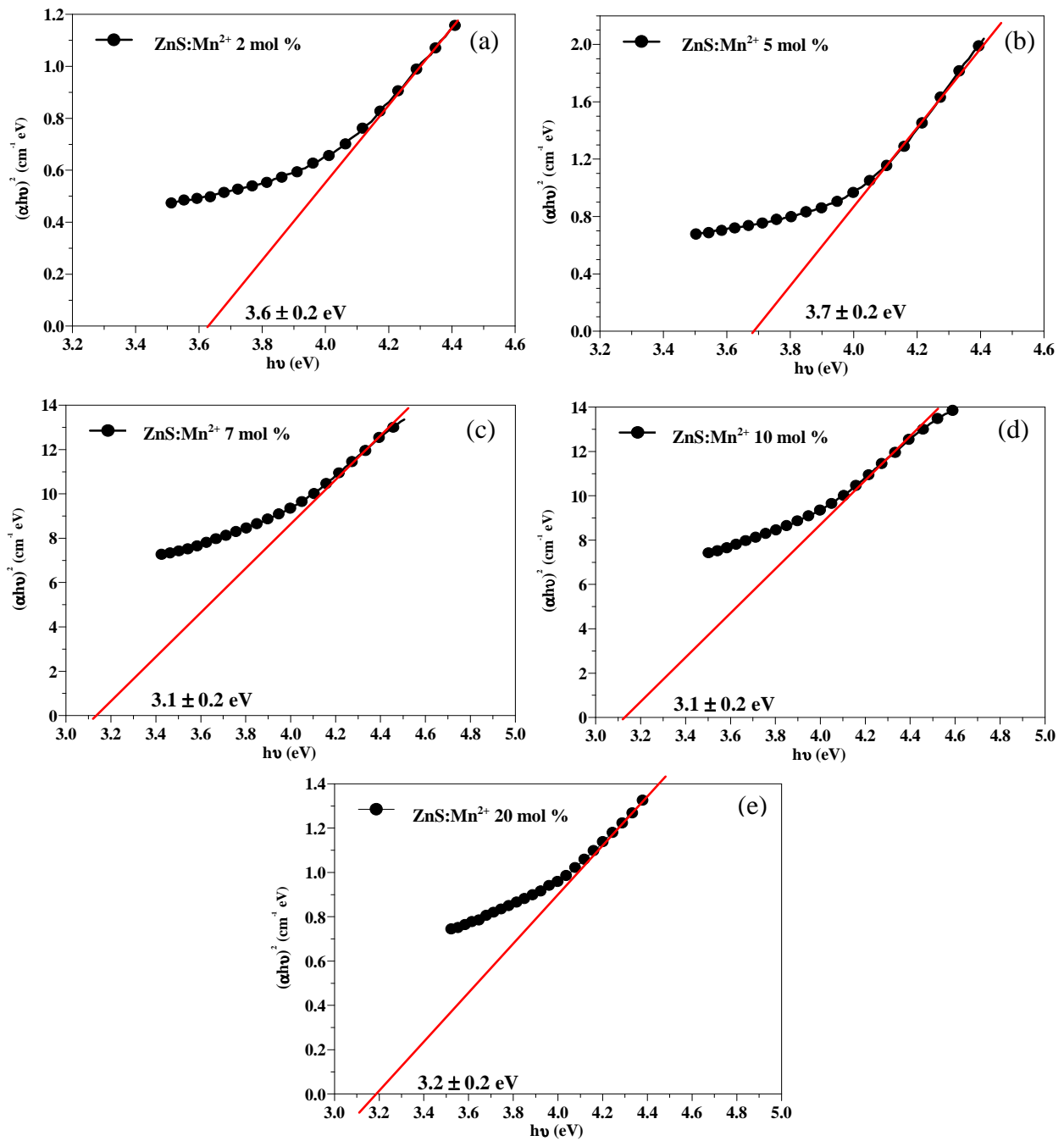


Figure 18: (a-e) band gap determination of different mol% of annealed ZnS:Mn²⁺.

Figure 18 a-e shows the band gap of the different mol% of annealed ZnS:Mn²⁺. The values are tabulated in Table 2. From the XRD and EDS results it can be seen that mostly ZnO had formed during annealing. The 2 and 5 mol% samples have a band gap that more or less corresponds to that of bulk ZnS (3.66 eV). In the case of the 7, 10 and 20 mol% samples, the band gap correspond to that of bulk ZnO (3.2 eV) [11]. From the XRD results it could also be seen that the particle size increased with annealing and we therefore expect no or a slight blue shift in the band gap of the annealed samples.

Table 2: Band gaps of different mol% of annealed ZnS:Mn²⁺.

mol%	Band gap
2	3.6 ± 0.2 eV
5	3.7 ± 0.2 eV
7	3.1 ± 0.2 eV
10	3.1 ± 0.2 eV
20	3.2 ± 0.2 eV

3. Particle size

When the sizes of the nanoparticles become comparable to the Bohr excitonic radius (a_B), a quantum confinement effect is expected from these particles. The Bohr [4] radius is given by

$$a_B = 4\pi\epsilon\hbar^2 \left[1/m_e^* + 1/m_h^* \right] / e^2 \quad (6)$$

where ϵ is the dielectric constant, and m_e^* and m_h^* are the effective masses of electrons and holes, respectively. Using the values of $\epsilon = 8.76$, $m_e^* = 0.34 m_0$ and $m_h^* = 0.23m_0$ [5] the excitonic Bohr radius of ZnS is found to be 2.5nm.

The radius of the particles can be calculated using the Brus equation [6]:

$$\Delta E_g = E_{g(\text{powder})} - E_{g(\text{bulk})} = \left[\frac{\hbar^2 \pi^2}{2\mu r^2} \right] - \left[1.8e^2 / \epsilon r \right] \quad (7)$$

where ΔE_g is the blue shift of the band gap, μ is the reduced electron-hole effective mass and r is the crystallite radius. In the case of ZnS the bulk values of all the materials parameters are known [11]. For nanoparticles, this results in a relation between the particle radius r , in nanometers, and the band gap E , in electron volts. This relation [7] is given by

$$r(E) = \frac{0.32 - 2.9\sqrt{E - 3.49}}{2(3.50 - E)} \quad (8)$$

Table 3: Calculated particle radius of the different un-annealed samples.

Sample	Particle radius (r)
ZnS	1.6 ± 0.5 nm
ZnS:Mn ²⁺ 2 mol%	1.5 ± 0.5 nm
ZnS:Mn ²⁺ 5 mol%	1.5 ± 0.5 nm
ZnS:Mn ²⁺ 7 mol%	1.5 ± 0.5 nm
ZnS:Mn ²⁺ 10 mol%	1.5 ± 0.5 nm
ZnS:Mn ²⁺ 20 mol%	1.4 ± 0.5 nm

The radii of the particles correspond well to that of the Bohr excitonic radius of ZnS. The r values (Table 3) were comparable to the particle sizes obtained from the XRD and TEM results.

4. Photoluminescence

The PL spectra for the different samples were taken using a 325 nm HeCd (26mW) laser as an excitation source and a Cary Eclipse spectrophotometer equipped with a 15W Xenon flash lamp that flashes at a rate of 80 flashes per second with an average pulse width of 2-3 μ s. The effect of the Mn^{2+} concentration, addition of SiO_2 and annealing at 600 $^{\circ}C$ were investigated.

4.1 Commercial $ZnS:Mn^{2+}$

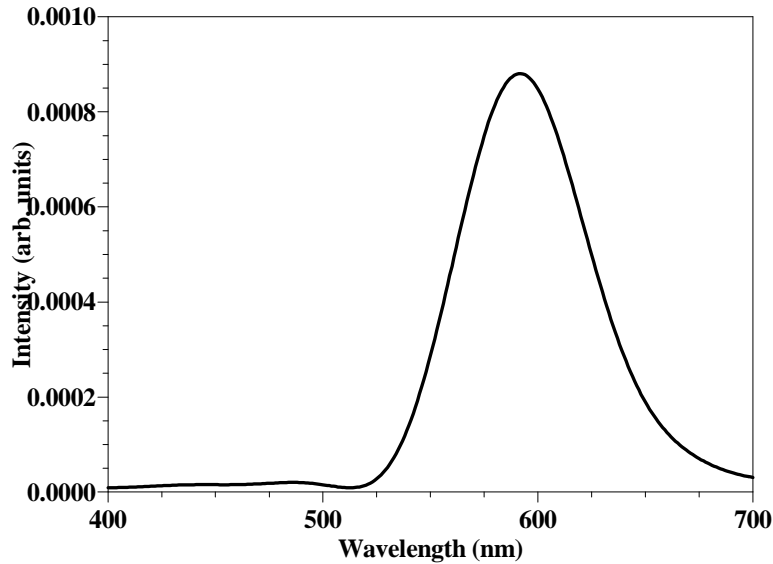


Figure 19: PL spectrum of commercially available $ZnS:Mn^{2+}$.

Figure 19 shows the PL spectrum of commercially available $ZnS:Mn^{2+}$, collected with a 325 nm He/Cd laser. The spectrum has a broad peak with a maximum at 595 nm which corresponds to the characteristic ${}^4T_1 \rightarrow {}^6A_1$ transition of Mn^{2+} ions [8]. A peak at 450 nm associated with band gap emission of ZnS were not observed in this case.

4.2 Synthesized ZnS

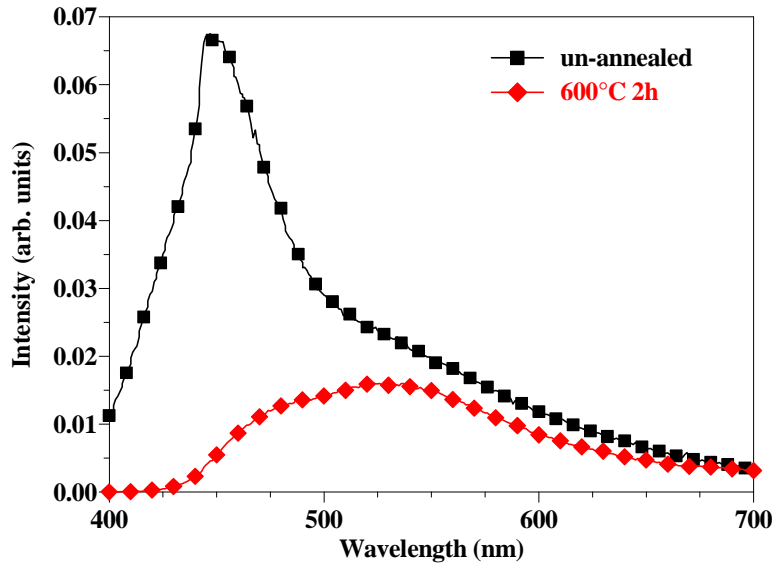


Figure 20: PL spectra of un-annealed and annealed ZnS.

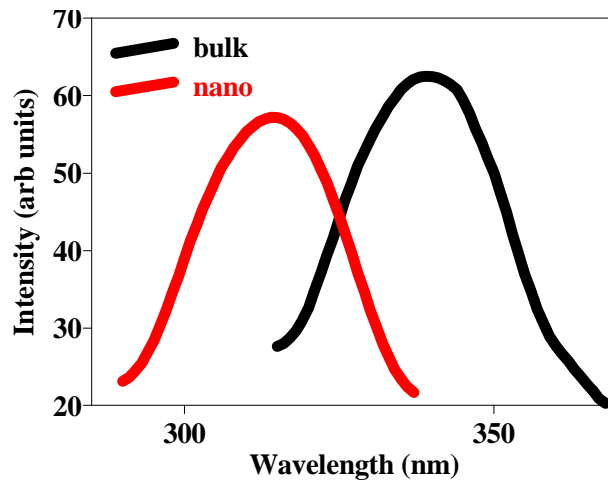


Figure 21: Excitation spectra of bulk and nano ZnS for 600 nm emission.

Figure 20 shows the PL spectra of un-annealed and annealed ZnS, collected with a 325 nm He/Cd laser. The un-annealed sample has a peak at 450 nm, which corresponds to band gap emission of ZnS. This emission is in the blue region and is characteristic of ZnS. The annealed sample shows a broad peak with its maximum at ~ 550 nm. This peak is a combination of the 450 nm ZnS peak and a peak which is associated with defects emission from ZnO. Because the intensity of the ZnO emission is higher than that of ZnS, it is another clear indication that ZnO had formed during the annealing process.

Figure 21 shows the excitation spectra for bulk and nano ZnS, collected with a Cary Eclipse spectrophotometer equipped with a Xenon lamp. The excitation peak for nano ZnS is observed at ~ 310 nm, which corresponds well to the data obtained from the absorption spectra for nano ZnS (303 nm). The peak for bulk ZnS has a maximum at ~ 340 nm. This corresponds well to the peaks observed by Murase et al [9]. It can clearly be seen from this data that there was a blue shift in the peak position for the nano ZnS. The cause of this shift will be discussed in detail in chapter 7.

4.3 Synthesized ZnS:Mn²⁺ (un-annealed)

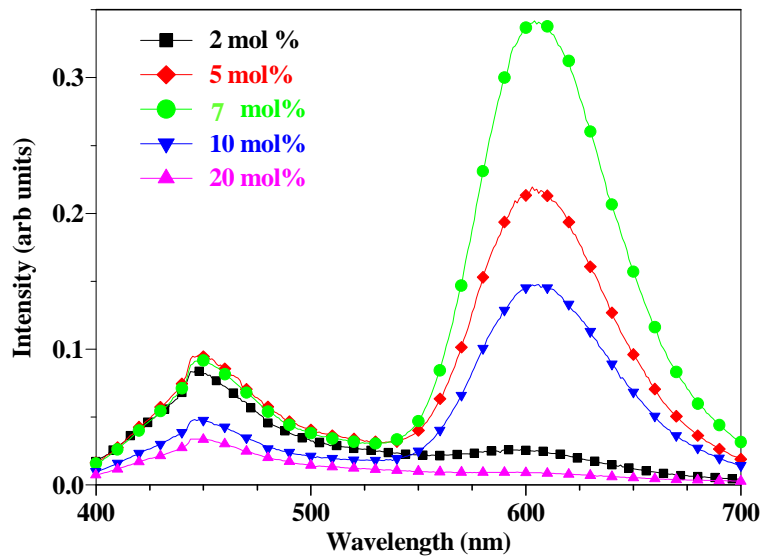


Figure 22: PL spectra of un-annealed ZnS:Mn²⁺.

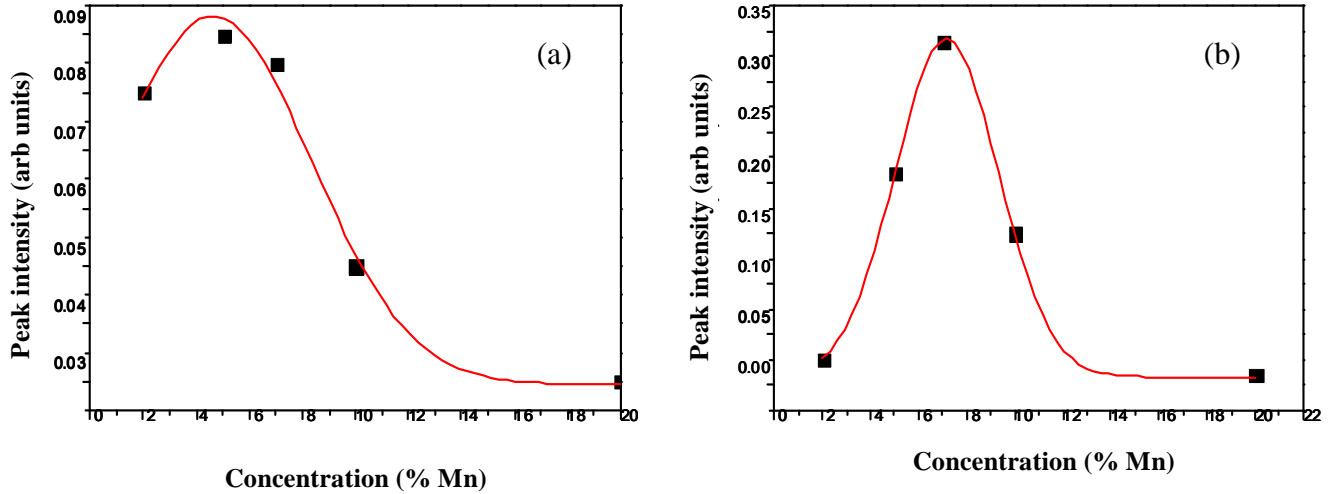


Figure 23: Gaussian function showing the peak intensity as a function of concentrations for a) the 450 nm peak and b) the 600 nm peak.

In Figure 22 the emission spectra of the un-annealed ZnS:Mn²⁺ with different concentrations of Mn²⁺ ions are shown. The spectra were collected using a 325 nm He/Cd laser. Two peaks are observed at 450 and 600 nm. The 450 nm peak corresponds to excitonic emission of ZnS and the 600 nm peak corresponds to the characteristic ⁴T₁ → ⁶A₁ transition of Mn²⁺ ions [8]. There was an intensity increase with an increase in Mn²⁺ concentration from 2 - 7 mol% and a decreased in intensity for the 10 and 20 mol% Mn²⁺ concentrations (Figure 23 a and b). The decrease in PL intensity at higher concentrations can be ascribed to concentration quenching effects [10].

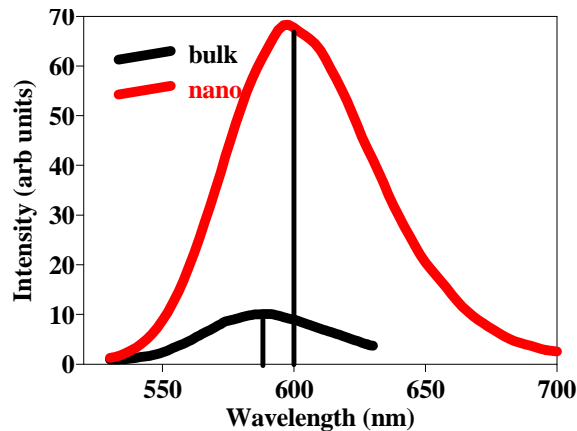


Figure 24: Emission spectrum of bulk and nano ZnS:Mn²⁺ at 325 nm excitation.

Figure 24 shows the emission spectra of bulk and nano ZnS:Mn²⁺, collected with a Cary Eclipse spectrophotometer equipped with a Xenon lamp. The peak for bulk ZnS:Mn²⁺ is observed at 590 nm and that of nano ZnS:Mn²⁺ is observed at 600 nm. It can clearly be seen from this data that there was a red shift of 10 nm in the peak position for the nano ZnS:Mn²⁺. The reason for this shift is explained in detail in chapter 7.

4.4 Synthesized ZnS:Mn²⁺ (annealed 600°C 2h)

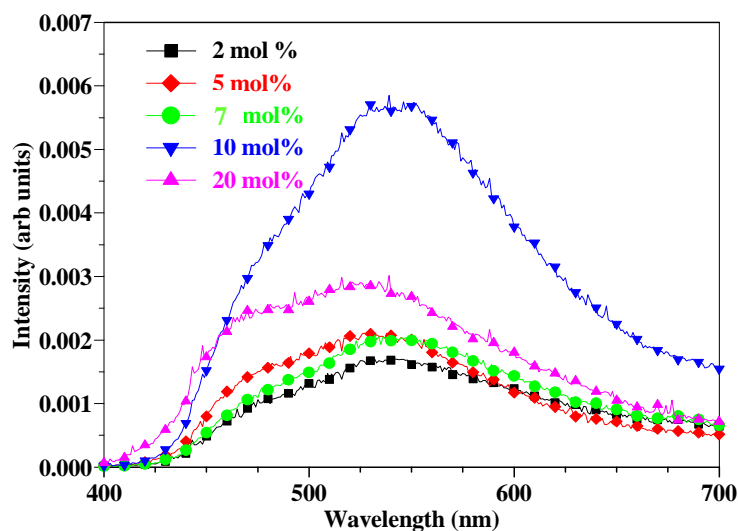


Figure 25: PL spectra of annealed ZnS:Mn²⁺.

Figure 25 shows the emission spectra for the annealed ZnS:Mn²⁺. The spectra were collected using a 325 nm He/Cd laser. A broad emission peak is observed with its maximum at ~ 550 nm. These emission spectra are again a combination of the 450 nm ZnS peak and a peak that can be associated with defects emission of ZnO [11]. This is a further confirmation that ZnO was formed during the annealing process. The maximum PL intensity was obtained when ZnS was doped with 10 mol% of Mn²⁺ and the least intensity was observed from the 20 mol% Mn²⁺ co-doping.

4.5 Synthesized SiO₂

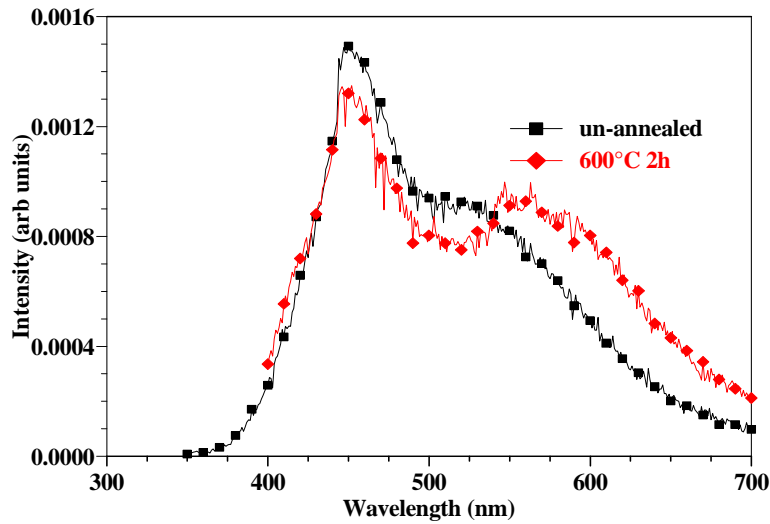


Figure 26: PL spectra of un-annealed and annealed SiO₂.

In Figure 26 the PL emission spectra, collected with a 325 nm He/Cd laser, of the as prepared and annealed SiO₂ are shown. The main emission peak for both samples was stable at ~450 nm. A shoulder was observed at ~525 nm from the as prepared sample and it was red shifted to ~550 nm in the annealed sample. These emissions are associated with either structural defects or charge transfer between Si and O atoms [12].

4.6 Synthesized SiO₂:ZnS

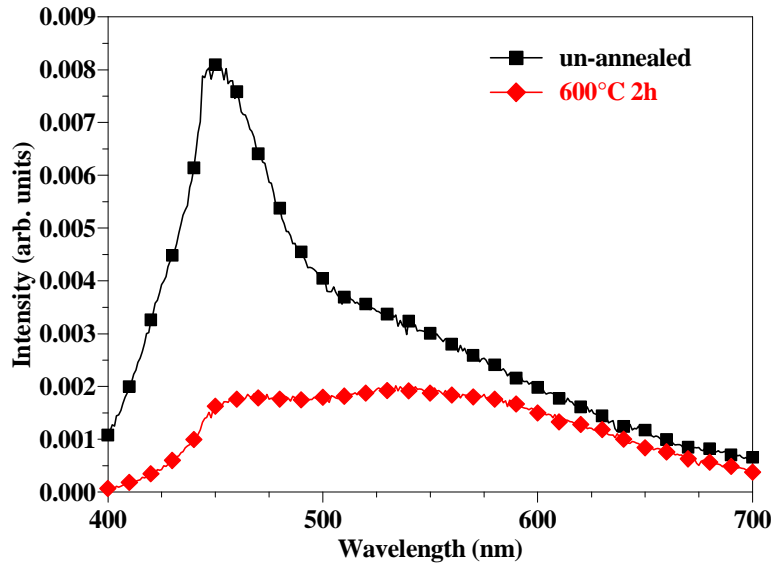


Figure 27: PL spectra of un-annealed and annealed SiO₂:ZnS.

In Figure 27 the emission spectra for the un-annealed and annealed samples of SiO₂:ZnS are shown. These spectra were collected using a 325 nm He/Cd laser. For the un-annealed sample the main emission peak is at ~450 nm. This peak corresponds to both the 450 nm peak of ZnS and SiO₂ (Figure 20 and Figure 26). A shoulder was observed at ~525 nm, which corresponds to the one observed in Figure 26. The observed emission was green, indicating a mixture of emission from ZnS and SiO₂. The annealed sample has a broad emission peak from ~450 nm - 600 nm. This peak is a mixture of the main SiO₂ peak at ~450 nm, the blue-shifted shoulder at ~550 nm, the 450 nm emission peak of ZnS and the 550 nm emission peak of ZnO. From the XRD and EDS data in chapter 5, it can be seen that this sample is a mixture of SiO₂, ZnS and ZnO, so the resulting emission is the mixture of the three.

4.7 Synthesized SiO₂-ZnS:Mn²⁺ (un-annealed)

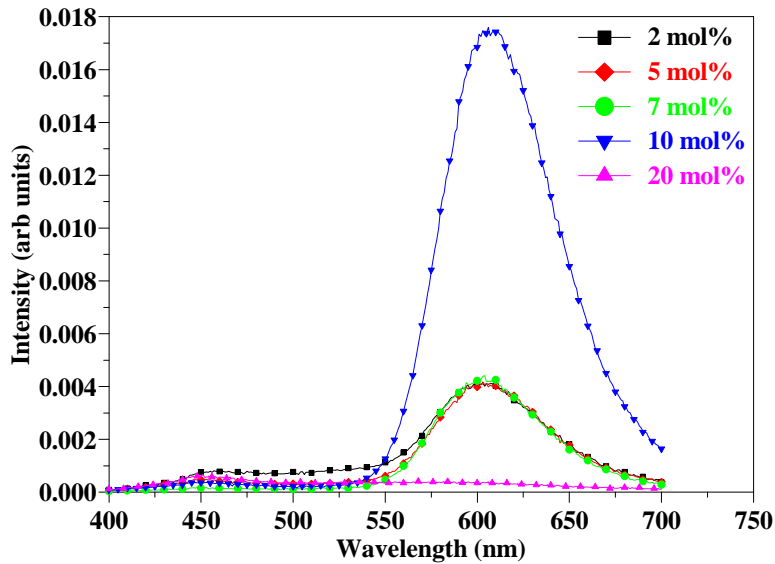


Figure 28: PL spectra of un-annealed SiO₂-ZnS:Mn²⁺.

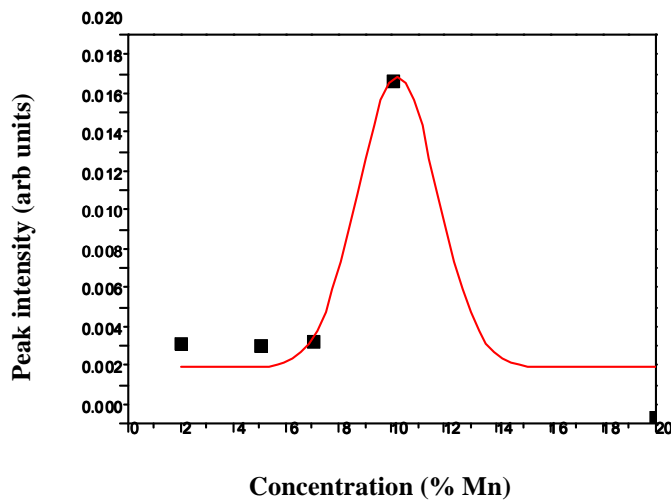


Figure 29: Gaussian function showing the peak intensity as a function of concentrations for the 600 nm peak.

Figure 28 shows the PL emission spectra of SiO₂-ZnS:Mn²⁺, collected using a 325 nm He/Cd laser. The main emission peak was again observed at 600 nm and it may be associated with the characteristic ⁴T₁ → ⁶A₁ transition of Mn²⁺ ions. A small peak similar to the ZnS band gap emission was also detected at 450 nm. PL intensity was maximized for the 10 mol% Mn²⁺ and it

was quenched when the concentration was increased to 20 mol%, probably due to concentration quenching effects again [10]. The intensity of the 2, 5 and 7 mol% were almost the same (Figure 29).

4.8 Synthesized SiO₂-ZnS:Mn²⁺ (annealed 600°C 2h)

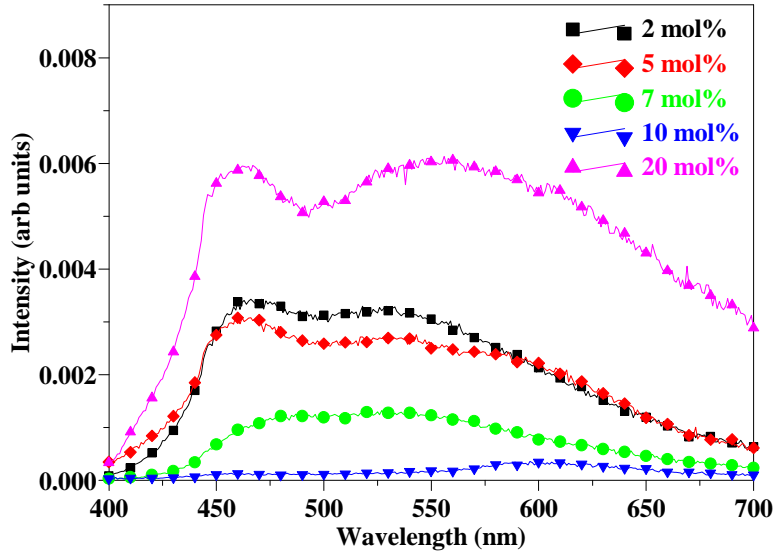


Figure 30: PL spectra of annealed SiO₂-ZnS:Mn²⁺.

In Figure 30 the emission spectra observed for different concentration of Mn²⁺ in SiO₂-ZnS:Mn²⁺. These spectra were collected using a 325 nm He/Cd laser. For the 2, 5 and 20 mol% samples two peaks were observed – one at 450 nm and a broad peak at 550 nm. The peak at 450 nm is most probably associated with band gap emission from ZnS. It can however also correspond to the SiO₂ peak in Figure 26. The peak at 550 nm can be ascribed to defects emission of ZnO, which was most probably formed as a result of a chemical reaction between Zn and O atoms during annealing of the sample [12]. For the 7 mol% sample a broad emission peak is observed, but it is believed that this peak also consists of a combination of ZnS, SiO₂ and ZnO emission peaks. For the 10 mol% sample the emission peaks are suppressed due to the high intensity of the peaks coming from the other samples. A peak at ~ 600 nm is observed. This peak is also present in the 20 mol % sample. This peak is believed to be coming from Mn²⁺ emission.

5. Auger electron spectroscopy (AES) and cathodoluminescence (CL).

The AES spectra were recorded in an ultra high vacuum (UHV) chamber using a PHI Model 549. A 2keV electron beam, with a beam current of 10 μ A and a beam size of 220 μ m was used. RGA was performed to determine the volatile gas species during electron bombardment of the sample. An Anavac-2 mass analyzer was used to measure the RGA. The CL data were collected for 24 hr with a S200/PC2000/USB2000/HR2000 spectrometer type using OOI Base 32 computer software.

5.1 Auger spectra

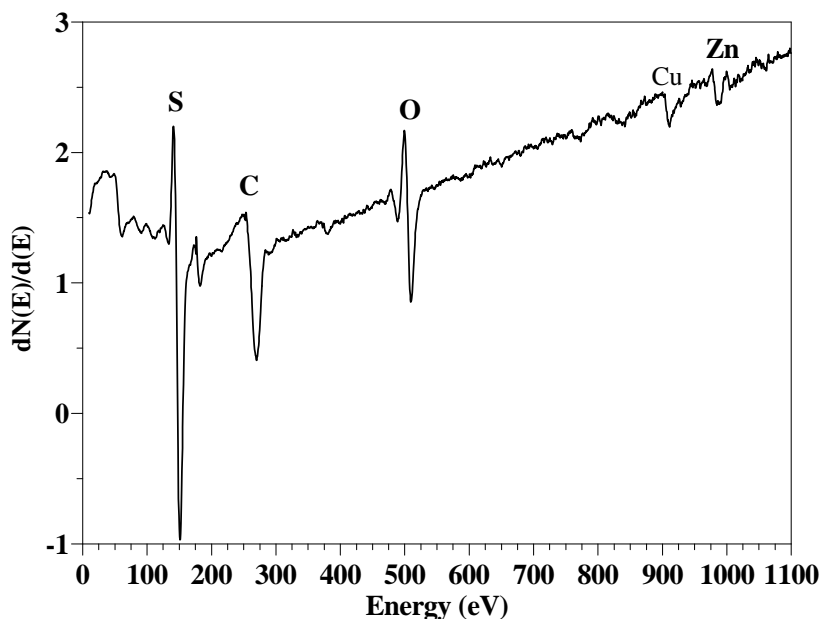


Figure 31: AES spectrum of commercial ZnS:Mn^{2+} .

Figure 31 shows the AES spectrum of commercial ZnS:Mn^{2+} . Peaks are observed at 152 eV, 273 eV, 503 eV, 920 eV and 994 eV. The 152 and 994 eV peaks correspond to the elements sulphur and zinc, coming from the ZnS matrix. No peaks for manganese were observed at 589 eV, indicating that the amount of Mn on the surface was below the AES detection limit. The 273 eV peak corresponds to carbon and the 503 eV peak to oxygen. The C peak is an indication of contamination from adventitious carbon and the O peak is an indication that some ZnO is present on the surface. The peak at 920 eV is coming from the copper sample holder.

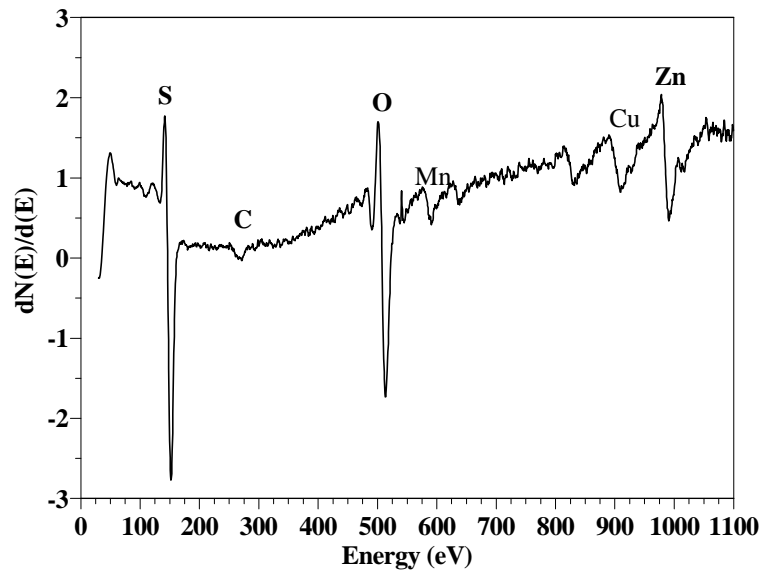


Figure 32: AES spectrum of synthesized ZnS:Mn²⁺.

Figure 32 shows the AES spectrum of synthesized ZnS:Mn²⁺. The peaks at 152 eV and 994 eV are associated with the sulphur and zinc peaks of the ZnS matrix. The peak at 589 eV corresponds to manganese. This peak might be present due to the segregation of the Mn to the surface of the sample. The small carbon peak at 273 eV is an indication that there was less contamination from adventitious carbon. The large oxygen peak at 503 eV is an indication that ZnO is present on the surface. The peak at 920 eV is due to the copper sample holder.

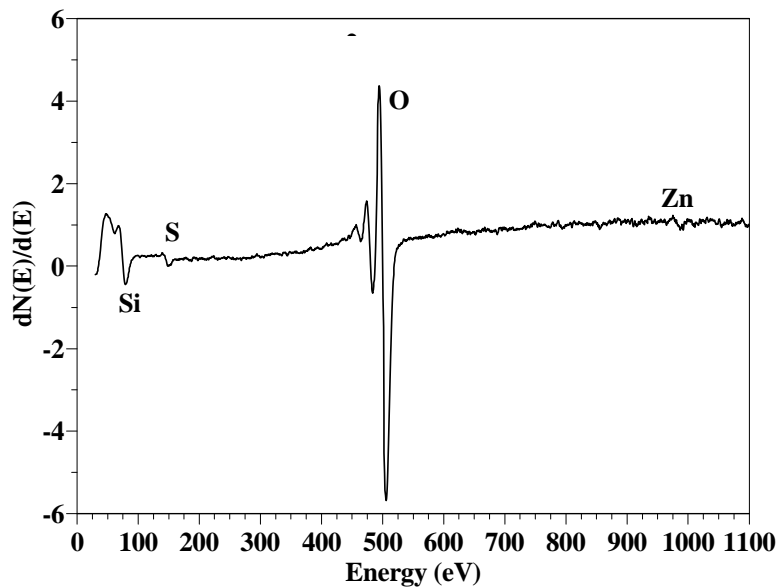


Figure 33: AES spectrum of synthesized SiO₂-ZnS:Mn²⁺.

Figure 33 shows the AES spectrum of synthesized $\text{SiO}_2\text{-ZnS:Mn}^{2+}$. Peaks at 92 eV, 152 eV, 503 eV and 994 eV are observed. The 152 eV and 994 eV peaks are an indication that sulphur and zinc are present on the surface and this is due to the presence of ZnS. However, the concentration of the S and Zn peaks is very low, indicating that a small concentration of ZnS is present on the surface. The peak at 92 eV is associated with silicon and the one at 503 eV with oxygen. These two peaks are due to the presence of SiO_2 on the surface. Because of the low concentration of ZnS on the surface it is assumed that the SiO_2 partially encapsulates the ZnS:Mn^{2+} . No carbon peak was observed and the absence of this peak suggests that there was no contamination from adventitious carbon.

5.2 Residual gas analysis (RGA) spectra.

RGA was used to determine the residual gases in the vacuum system. A RGA spectrum was recorded with the electron beam either switched on or off.

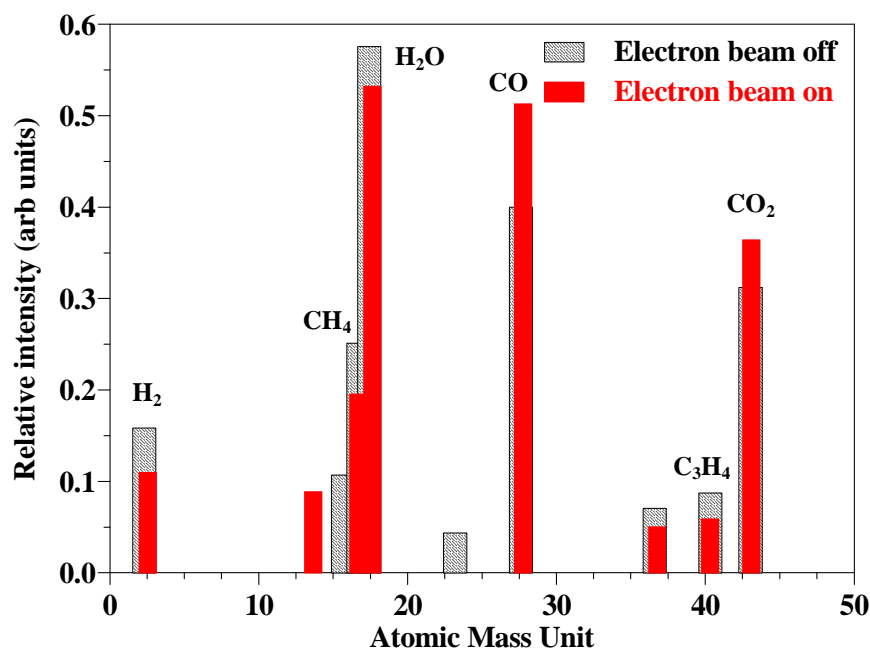


Figure 34: RGA spectra of commercial ZnS:Mn^{2+} .

Figure 34 shows the RGA spectra of commercial ZnS:Mn^{2+} taken at base pressure of 1×10^{-8} Torr when the beam was off and after a few minutes with the beam on. Residual gasses such as H_2 , CH_4 , H_2O , CO , C_3H_4 and CO_2 were present. The amount of H_2 , CH_4 , H_2O and C_3H_4

decreased when the beam was switched on, while the amount of CO and CO₂ increased when the beam was switched on. This change in the gasses is due to electron beam induced surface chemical reactions. The increase in the carbon containing gasses can be attributed to the fact that carbon is leaving the surface of the sample under electron beam bombardment in the form of CO and CO₂.

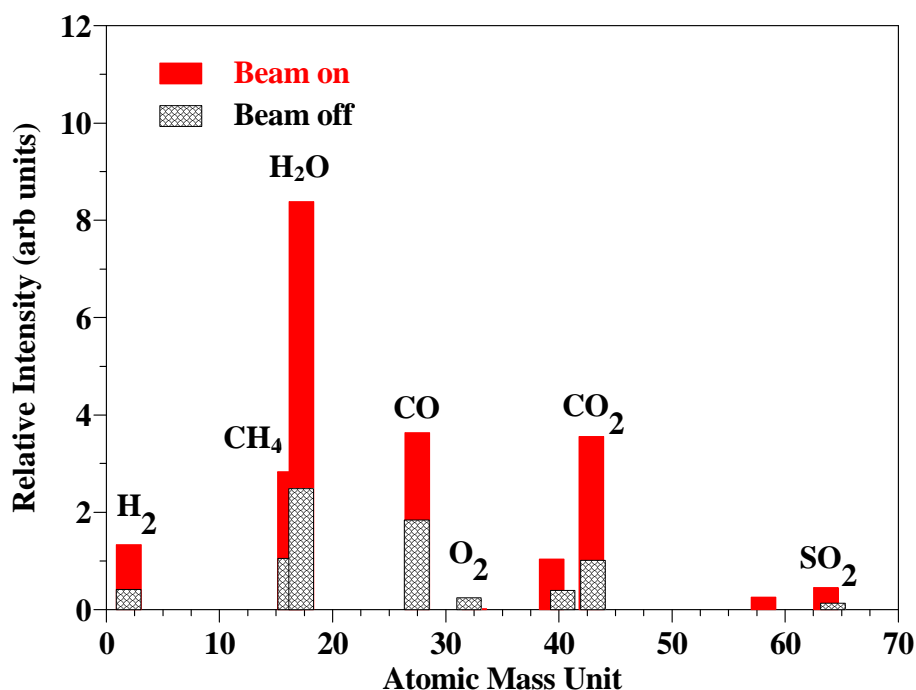


Figure 35: RGA spectra of synthesized ZnS:Mn²⁺.

Figure 35 shows the RGA spectra of synthesized ZnS:Mn²⁺ taken at base pressure of 1×10^{-8} Torr when the beam was off and after a few minutes with the beam on. Residual gasses such as H₂, CH₄, H₂O, CO, O₂, C₃H₄, CO₂ and SO₂ are present. The amount of all the gasses, except O₂, increases when the beam is switched on. The increase is attributed to electron beam induced surface chemical reactions. The increase in SO₂ is due to the fact that sulphur is leaving the surface under electron bombardment and it is reacting with the oxygen, which is also leaving the surface, to form SO₂.

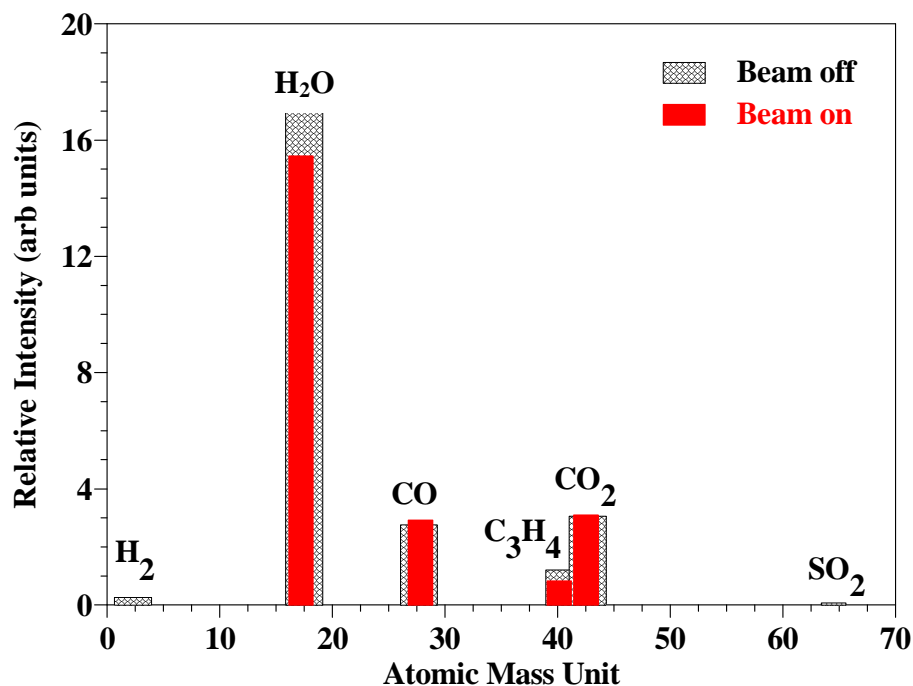


Figure 36: RGA graph of synthesized SiO₂-ZnS:Mn²⁺.

Figure 36 shows the RGA spectra of synthesized SiO₂-ZnS:Mn²⁺ taken at base pressure of 1×10^{-8} Torr when the beam was off and after a few minutes with the beam on. Residual gasses such as H₂, H₂O, CO, C₃H₄ and CO₂ are present. The amount of H₂, OH and C₃H₄ decreased when the beam was switched on, while the amount of CO and CO₂ stayed the same. Almost no SO₂ was detected.

5.3 Degradation of commercial ZnS:Mn²⁺

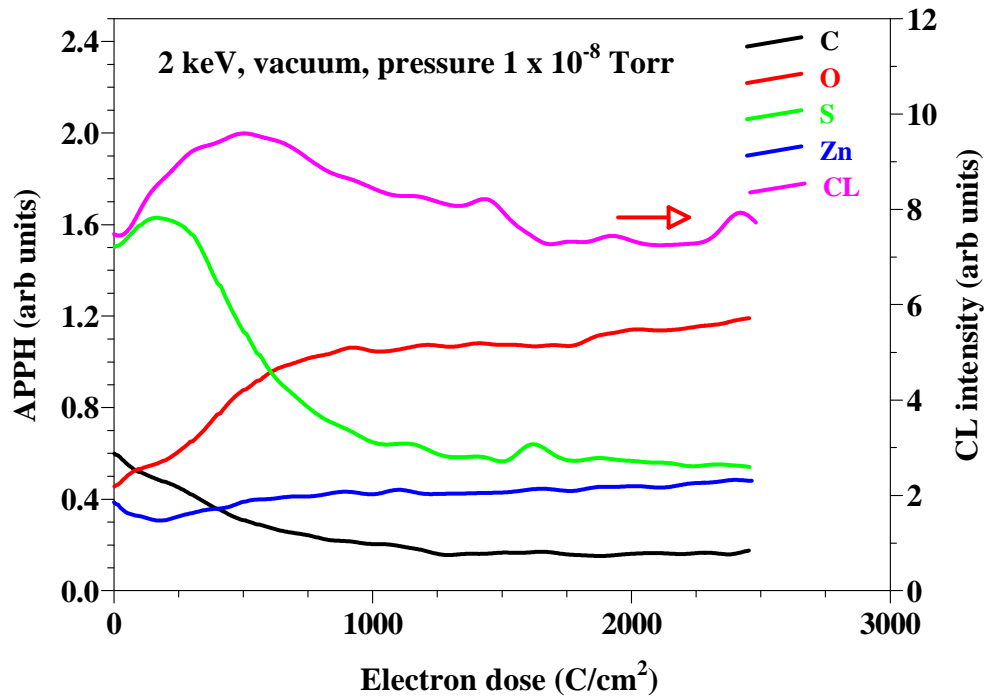


Figure 37: The CL intensity of commercial ZnS:Mn²⁺ powder and APPHs of C, O, S and Zn as a function of electron dose during degradation at a base pressure of 1×10^{-8} Torr.

Figure 37 shows the Auger peak-to-peak heights (APPHs) of C, O, S and Zn and the CL intensity as a function of electron dose during degradation at 1×10^{-8} Torr. The graph depicts the electron stimulated surface chemical reaction (ESSCR) mechanism [13]. The Auger peak of C immediately started to decrease exponentially when the surface was exposed to electron beam. The C on the surface of commercial ZnS:Mn²⁺ is from adventitious atmospheric contamination [14]. Initially the Auger peak of S increased. This is due to the removal of C from the surface. The S then started to decrease exponentially, while the O increased after most of the C was removed from the surface. The Zn peak increases marginally before stabilizing for the duration of the experiment.

The ESSCR mechanism for ZnS states that the C and S are reduced and O increases on the surface [15]. The reduction of S and C are due to desorption by formation of volatile SO_x and CO_x [16]. The increase in O is due to the formation of ZnO or ZnSO₄ on the surface. The initial step is the core level ionization of the Zn atoms through the interatomic Auger cross transition

stimulated by the electron beam. This leaves the S atom with a net positive charge surrounded by positive metal ions. This occurs simultaneously with the electron beam dissociation of O_2 to reactive O^- species. As soon as the adventitious C is depleted from the surface as volatile CO_x compounds, S is then released as SO_x , with an apparent accumulation of O that forms the non-luminescent ZnO or $ZnSO_4$ layer [17]. Figure 38 shows the ESSCR mechanism for the formation of ZnO and Figure 39 shows the mechanism for the formation of $ZnSO_4$. The formation of the different gas layers is attributed to the different gas species present in the vacuum system during degradation [18].

Figure 40 shows the CL spectra of commercial $ZnS:Mn^{2+}$ before degradation, after 3 hours and after degradation at 1×10^{-8} Torr. When examining the CL intensity as a function of electron dose in Figure 40, we can see that there was an initial increase in the CL intensity. This increase is due to the removal of the carbon layer on the surface. After approximately three hours, when all the carbon is removed from the surface, the CL intensity reaches a maximum. The $ZnS:Mn^{2+}$ then starts to degrade according to the ESSCR mechanism. A non-luminescent ZnO or $ZnSO_4$ layer starts to form on the surface accounting for the decrease in the CL intensity. Because the experiment was performed in vacuum and not in an oxygen atmosphere, the CL intensity of $ZnS:Mn^{2+}$ did not decrease to 0, but stabilized after 12 hours.

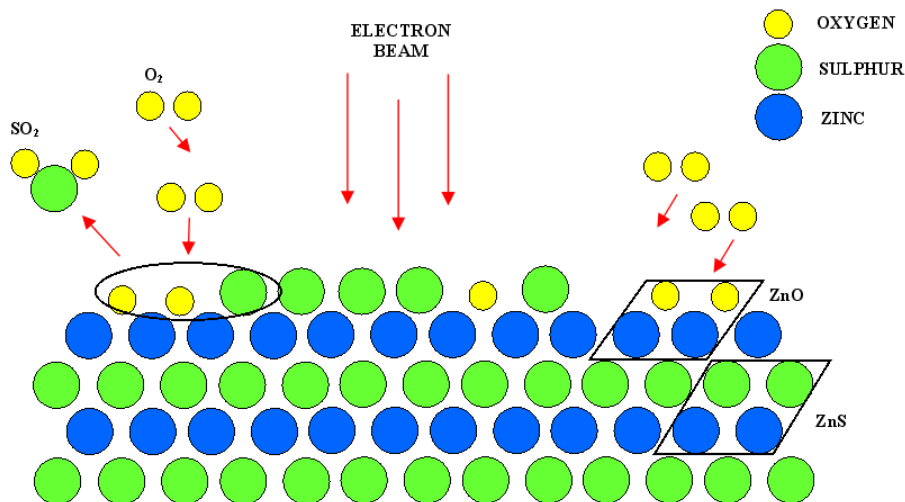


Figure 38: The ESSCR mechanism for the formation of ZnO [18].

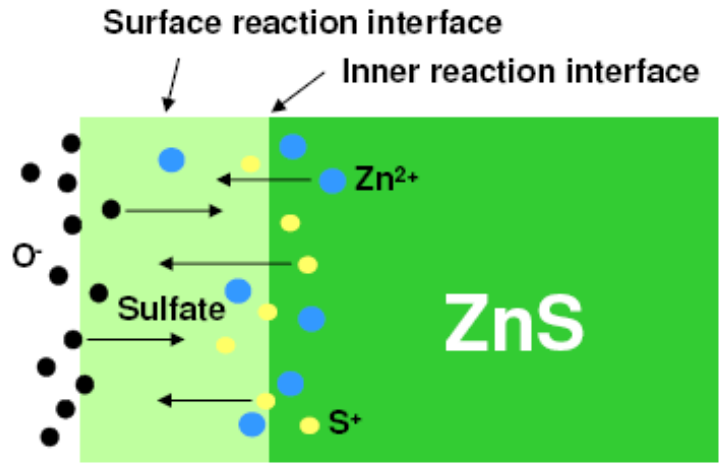


Figure 39: The mechanism for the formation of ZnSO₄ [18].

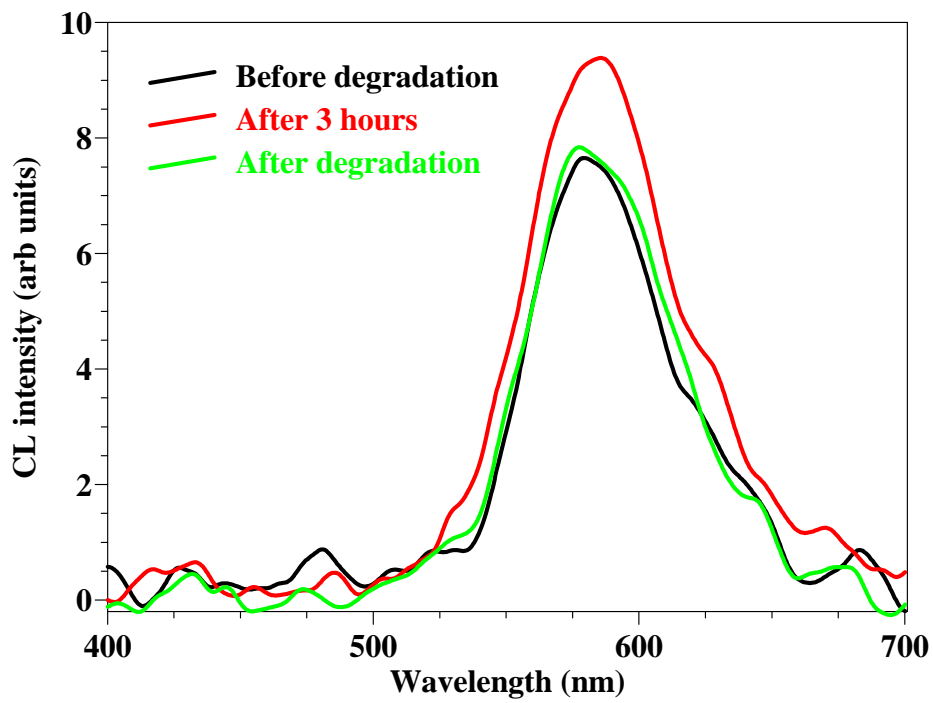


Figure 40: CL spectra of commercial ZnS:Mn²⁺ before degradation, after 3 hours and after degradation at 1×10^{-8} Torr.

6. Conclusion

Absorption measurements were performed on the samples to determine their fundamental absorption peaks and edges. For un-annealed ZnS the absorption peak is at 300 nm. This peak is blue-shifted from the absorption edge of bulk ZnS (345 nm). By using Tauc's relation the band gap of synthesized ZnS was determined as $\sim 4.1 \pm 0.2$ eV. This is a blue-shift in the band gap of 0.44 ± 0.2 eV from that of bulk ZnS (3.66 eV). For commercial ZnS:Mn²⁺ two absorption peaks were observed. One at 345 nm and the other at 275 nm. The peak at 345 nm corresponds to absorption over the band gap (3.66 eV) and the one at 275 nm can be assigned to an excitonic transition that proves the existence of ZnS. The band gap was determined as 3.7 ± 0.2 eV and there is almost no shift from that of bulk ZnS confirming that the particle size of the commercial phosphor is in the μm range. For un-annealed ZnS:Mn²⁺ an absorption peak at 312 nm was observed. This is again a blue-shift from that of bulk ZnS. For the annealed samples a peak at 270 nm were observed. This peak is due to excitonic transitions and proves the existence of ZnS in the samples. For the un-annealed SiO₂-ZnS:Mn²⁺ samples a broad absorption peak at 275 nm were observed. This is again an indication that ZnS is present in the samples. For the annealed SiO₂-ZnS:Mn²⁺ samples the absorption peak was observed at the same position, indicating that annealing of the samples did not changed their absorption. The radii of the un-annealed ZnS:Mn²⁺ samples were determined with the Brus equation. The average particle radius was ~ 1.5 nm, corresponding to XRD and TEM results.

One PL peak at 595 nm was observed for the commercial ZnS:Mn²⁺ sample. This peak corresponds to the ⁴T₁-⁶A₁ transition of Mn²⁺. For the un-annealed ZnS sample a peak at 450 nm was observed. This peak corresponds to band gap emission on ZnS. In the case of the un-annealed ZnS:Mn²⁺ samples the two peaks were again observed, but the Mn²⁺ peak showed a red-shift of 5 nm to 600 nm. This is due to the quantum confinement of the samples. For the un-annealed SiO₂-ZnS:Mn²⁺ samples these two peaks were also observed. For the annealed ZnS sample a broad peak at 550 nm were observed. This peak corresponds to defect emission from ZnO. This is an indication that the ZnS was converted to ZnO during annealing. Un-annealed SiO₂ has two peaks at 450 nm and 525 nm and annealed SiO₂ has two peaks at 450 nm and 550 nm. These emissions are associated with either structural defects or charge transfer between Si and O atoms. The PL emission for annealed SiO₂-ZnS:Mn²⁺ shows two peaks: one at

450 nm and one at 550 nm. The 450 nm corresponds to the 450 nm peak of SiO₂, and the 550 nm peak can be ascribed to defect emission from ZnO.

S, C, O and Zn peaks were observed for the AES spectrum of commercial ZnS:Mn²⁺. No Mn peak was observed because the amount of Mn on the surface was below the AES detection limit. For the synthesized ZnS:Mn²⁺ sample the same peaks were observed. For synthesized SiO₂-ZnS:Mn²⁺ Si, S, O and Zn peaks were observed. RGA analysis is showing that H₂, H₂O, O, OH, CO, O₂, C₃H₄, CO₂ and SO₂ gasses are present in the system. Degradation of the commercial ZnS:Mn²⁺ sample was according to the ESSCR mechanism. The S peak decreased while the O peak increased. The C peak also decreased. The decrease in the S and C peak is due to desorption by formation of volatile SO_x and CO_x. The increase in O is due to the formation of ZnO or ZnSO₄ on the surface.

References

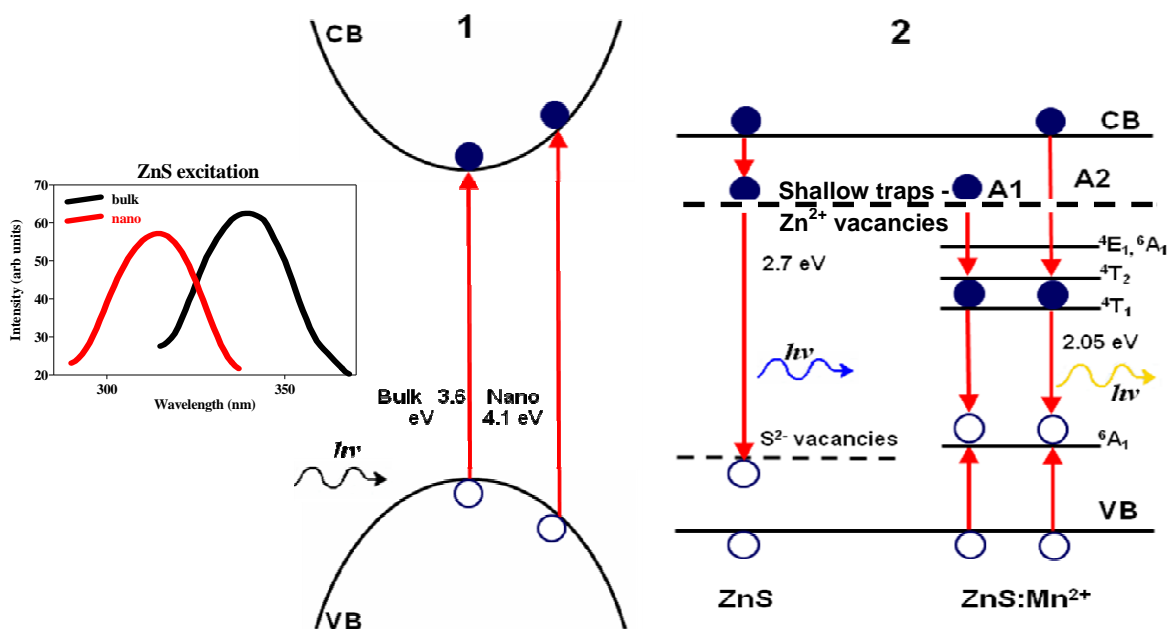
1. B.S. Rema Devi, R. Raveendran and A.V. Vaidyan, *Pramana – J. Phys.*, **68** (2007) 685.
2. U. Sohling, G. Jung, D.U. Saenger, S. Lu, B. Kutsch and M. Mennig, *J. Sol-Gel Sci. Tech.* **13** (1998) 686.
3. D.R. Lide, *Handbook of Chemistry and Physics*, 74th ed., CRC Press, Boca Raton, FL, 1994.
4. B. Bhattacharjee, D. Ganguli, K. Iakoubovskii, A. Stesmans and S. Chaudhuri, *Bull. Mater. Sci.* **25** (2002) 179.
5. Landolt-Bornstein, *Numerical data and functional relationship in science and technology* (Berlin: Springer Verlag) **22a** (1987) 168.
6. L.E. Brus, *J. Chem. Phys.* **80** (1984) 4403.
7. J. F. Suyver, S. F. Wuister, J. J. Kelly, and A. Meijerink, *Nano Lett.* **1** (2001) 429.
8. R.N. Bhargava, D. Gallagher, X. Hong and N. Nurmikko, *Phys. Rev. Lett.* **72** (1994) 416.
9. N. Murase, R. Jagannathan, Y. Kanematsu, M. Watanabe, A. Kurita, K. Hirata, T. Yazawa and T. Kushida, *J. Phys. Chem. B*, **103** (1999) 758.
10. K.H. Yoon, J.K. Ahn and J.Y. Cho, *J. Mater. Sci.* **36** (2001) 1376.
11. O.M. Ntwaeaborwa and P.H. Holloway, *Nanotechnology* **16** (2005) 867.
12. O.M. Ntwaeaborwa, H.C. Swart, R.E. Kroon, J.R. Botha, J.M. Ngaruiya, P.H. Holloway, in *Photoluminescence Research Progress*, editors: H.K. Wright and G.V. Edwards (Nova Publishers, New York) (2008) pp 287-306.
13. P.H. Holloway, J.S. Sebastian, T.A. Trottier and H.C. Swart, *Solid State Technol.* (1995) 47.
14. L. Oosthuizen, H.C. Swart, P.E. Viljoen, P.H. Holloway and G.L.P. Berning, *Appl. Surf. Sci.* **120** (1997) 11.
15. K.T. Hillie and H.C. Swart, *Appl. Surf. Sci.* **183** (2001) 306.
16. H.C. Swart, J.S. Sebastian, T.A. Trottier, S.L. Jones and P.H. Holloway, *J. Vac. Sci. Technol. A*, **14** (3) (1996) 1697.
17. K.T. Hillie and H.C. Swart, *Appl. Surf. Sci.* **193** (2002) 78.
18. H.C. Swart, *phys. Stat. sol. (c)*, **1** (9) (2004) 2355.

Chapter 7

Luminescent mechanism of ZnS, ZnS:Mn²⁺ and ZnO.

This chapter presents the luminescent mechanism of ZnS, ZnS: Mn²⁺ and ZnO. The excitation mechanism of ZnS bulk and nano semiconductors are discussed in part 1. The ZnS and ZnS:Mn²⁺ emission mechanism is discussed in part 2, while part 3 shows the emission mechanism of bulk and nano ZnS:Mn²⁺ according to the configuration coordinate model. The luminescent mechanism of ZnO is briefly explained at the end of the chapter.

1. Luminescent mechanism of ZnS and ZnS:Mn²⁺



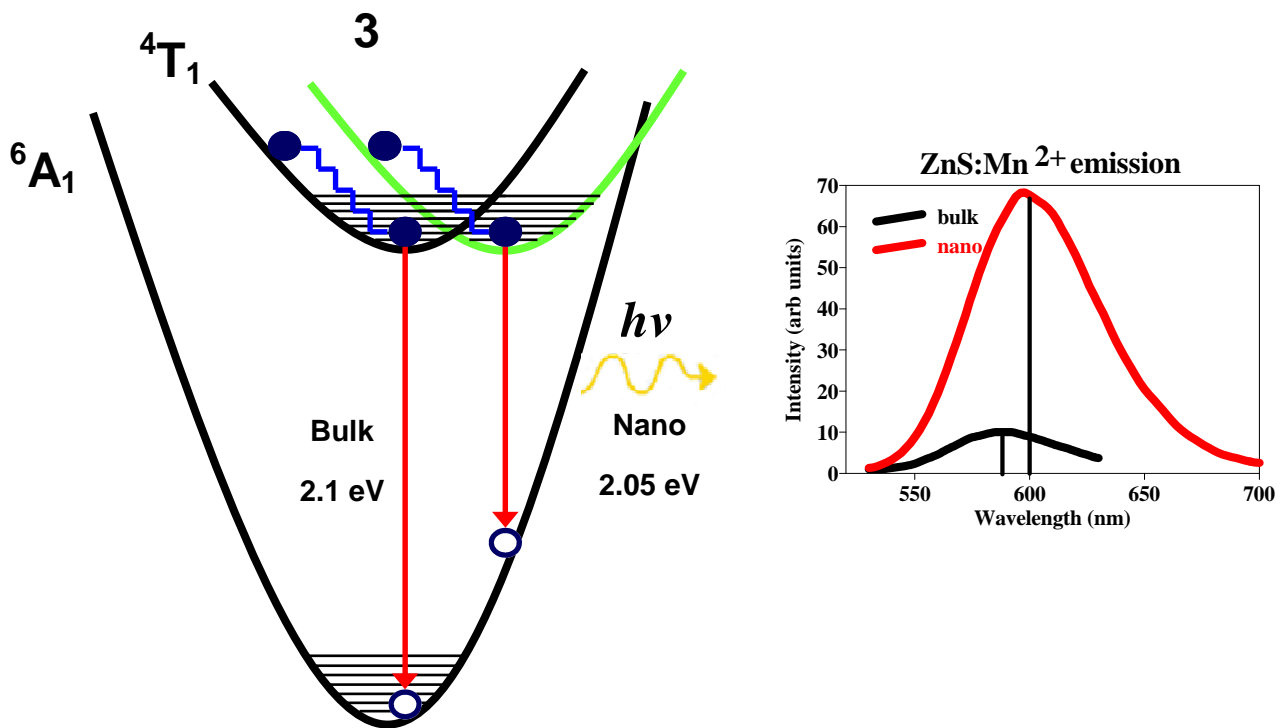


Figure 1: Schematic diagram of the proposed luminescent mechanism of ZnS and ZnS:Mn²⁺. The diagram consists of three parts. Part 1 shows the energy dispersion for a bulk semiconductor and a nanoparticle. This is the classical model and it is in k-space. Part 2 shows the band structure. The configurational coordinate model for Mn²⁺ is shown in part 3. This again is in k-space. The diagram is not drawn to scale.

Figure 1 shows possible transitions that could lead to the orange emission from the Mn²⁺ ions. These transitions were explained in terms of Tanabe-Sugano diagrams for the d⁵ level and the Ligand field theory by different researchers [1-5]. It is known that Mn²⁺ has a d⁵ electron structure with a tetrahedral symmetry. When doped into ZnS, it occupies the sites of Zn²⁺. The ground state of Mn²⁺ is ⁶A₁(⁶S) and the first excited state is ⁴G. Under tetrahedral symmetry, the excited state can be split into ⁴T₁, ⁴T₂, ⁴A₁ and ⁴E multiplets whose energies are listed in a report by McClure [4]. The d electron states of the Mn²⁺ ion acts as efficient luminescent centers while interacting strongly with the host crystal's s-p electronic states at which the external electronic states is normally directed [5].

Figure 1 is divided into 3 parts. Part 1 describes the excitation mechanism of bulk and nano ZnS (Figure 2). Part 2 describes the emission mechanism of ZnS and ZnS:Mn²⁺ (Figure 3). In part 3 the configurational coordinate model is used to describe the emission mechanism of ZnS:Mn²⁺ (Figure 6).

1.1 Part 1

Part 1 gives the excitation mechanism for bulk and nano ZnS semiconductors.

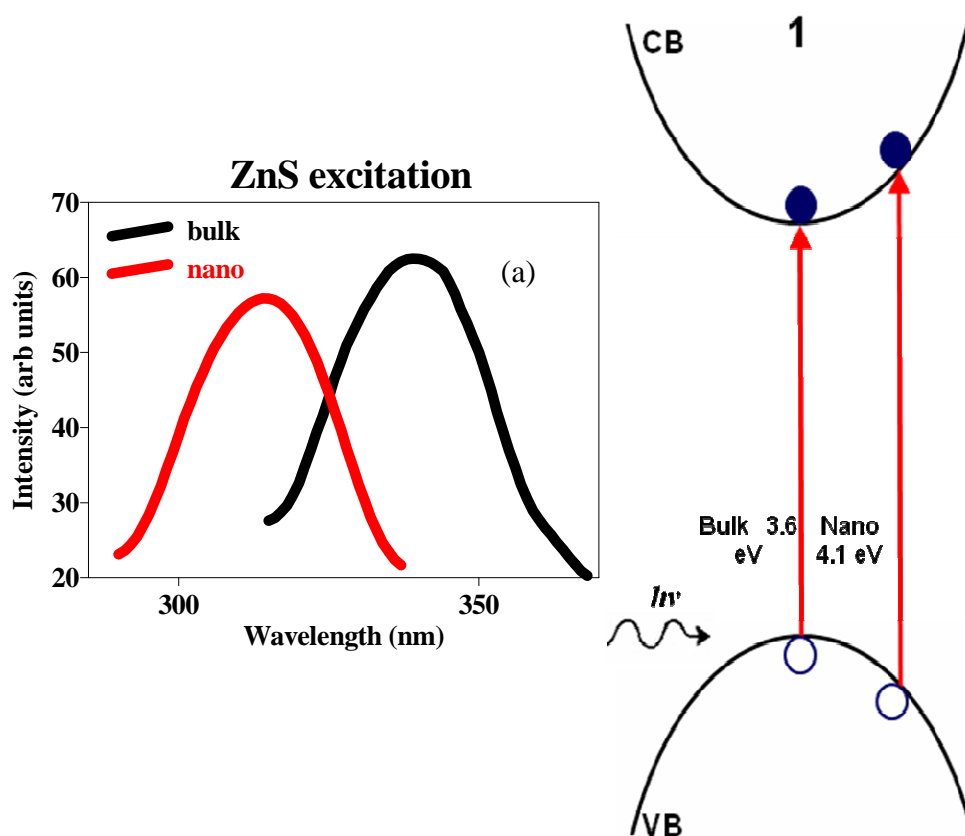


Figure 2: Excitation mechanism of bulk and nano ZnS.

The energy dispersion for a bulk semiconductor and a nanoparticle is described in ref [6]. In the case of a nanoparticle the band gap (E_g) is blue shifted. The band gap for bulk ZnS is 3.6 eV (340 nm) [7] and from the UV-vis spectra in chapter 5 the band gap for ZnS nanoparticles in this case is determined as 4.1 eV (303 nm). The insert (a) in Figure 2 shows the excitation spectra of bulk and nanoparticles of ZnS. This corresponds to excitation over the band gap. A hole is created in the valence band by the incident photon and the electron is excited over the band gap to the

conduction band. In the case of a bulk particle the energy of this excitation is 3.6 eV and for a nanoparticle it is 4.1 eV. The excitation energy of a nanoparticle is therefore blue shifted.

1.2 Part 2

Part 2 gives the emission mechanism of ZnS and ZnS:Mn²⁺.

2

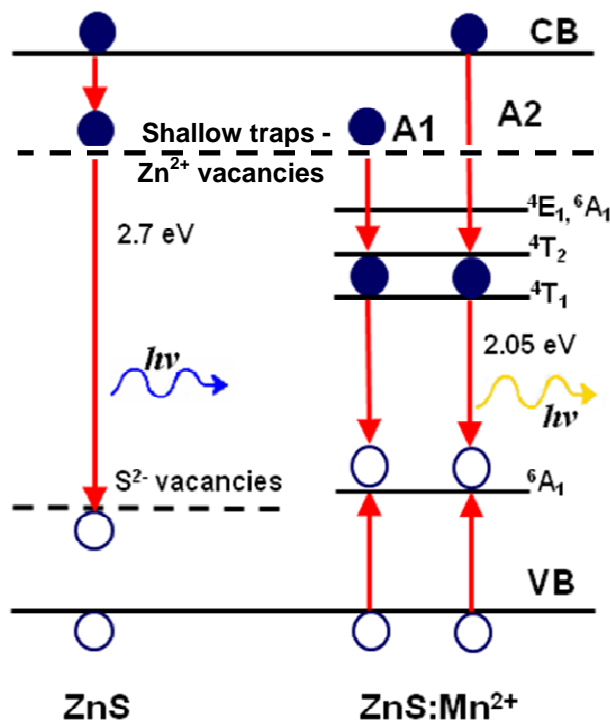


Figure 3: Emission mechanism of ZnS and ZnS:Mn²⁺.

The excited electron immediately transfers to the shallow traps (dashed line in Figure 3). This shallow trap-state is delocalized over the entire nanocrystals, because of the quite small effective mass of the electron. Because the hole has a much higher effective mass it will initially remain in the valence band and will be trapped on a longer time scale [8]. Emission spectra of ZnS:Mn²⁺ (chapter 6) show that the interaction between ZnS and Mn²⁺ resulted in two emissions peaks at 450 (minor) and 600 nm (major). The minor peak at 450 nm (blue emission) can be attributed to the hole trapping and recombination with electrons by defect states (zinc or sulphur vacancies) in ZnS. The orange emission at 600 nm for nanoparticles can be attributed to ⁴T₁ → ⁶A₁ transitions

of Mn^{2+} ions. For the process denoted by A, two possible routes for this emission are possible. For A1, an excited electron in the conduction band can relax to the vacancy level and then to the ${}^4\text{T}_1$ level of Mn^{2+} non-radiatively, followed by radiative transition to the ground state (${}^6\text{A}_1$) via recombination with a hole trapped in the ground state. The radiative transition is accompanied by orange emission of photons at 600 nm. Since the orange emission at 600 nm is more intense than the blue (violet) emission at 450 nm, this suggests that non-radiative relaxation to the ${}^4\text{T}_1$ level of Mn^{2+} was faster than hole capture and recombination with electrons by defects states of ZnS. For A2, an excited electron in the conduction band can first relaxes non-radiatively to the ${}^4\text{T}_1$ level of Mn^{2+} and finally to the ${}^6\text{A}_1$ level emitting photons in the orange range of the spectrum in the process.

1.3 Part 3

The emission peak of nano-sized $\text{ZnS}:\text{Mn}^{2+}$ was observed to be red shifted by 10 nm from that of the bulk spectrum. So far, there have been many reports about the origin of this red shift in the emission. Cruz et al. [9] reported that the red shift might be caused by a large density of surface states in the nanoparticles, or by strong electron-phonon coupling in the nanoparticles. They also report that it might be possible that the size-dependent crystal field effect is responsible for this red shift. Li et al. [10] reported that the red shift may come from the quantum confinement effect in nanoparticles which leads to a change of the crystal field surrounding the Mn^{2+} ions. The Phosphor Handbook [11] reports for Mn^{2+} phosphors that “...When a metal ion occupies a certain position in a crystal, the crystal field strength that affects the ion increases as the space containing the ion becomes smaller, ... For increases in the field, the transition energy between the ${}^4\text{T}_1$ and ${}^6\text{A}_1$ levels is predicted to decrease (shift to longer wavelengths)...”

From these reports it can be seen that a change in the crystal field will most likely cause a red shift in the emission of nanoparticles. The quantum confinement effect (that arises from the very small particle sizes), will change the crystal field. From XRD data it can also be seen that the bulk sample is much more crystalline than the nano samples.

It can therefore be concluded that a change in the crystal field would cause a change in the parabola offset in the configurational coordinate diagram. The offset is given by

$$\Delta Q = Q'_0 - Q_0 \quad (1)$$

where Q_0 is the equilibrium distance of the excited state, Q'_0 is the equilibrium distance of the ground state and ΔQ is the parabola offset (Figure 4). The configurational coordinate diagram also describes the Stokes' shift (difference in absorption and emission energy) [11]. From Figure 5 it can be seen that when there is a displacement between the potential wells of the ground and excited states, there will be a difference in the Stokes' shift. The parabola offset will therefore also increase.

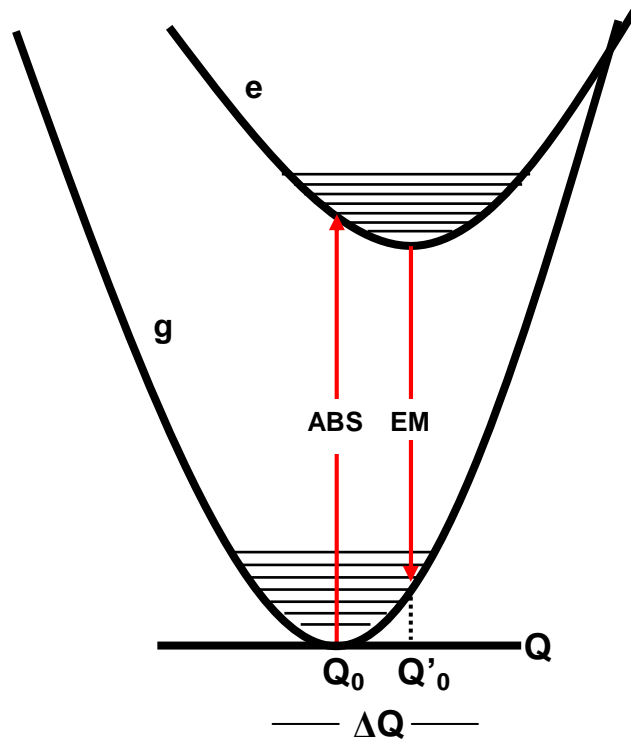


Figure 4: Configurational coordinate model showing the parabola offset (ΔQ) [12].

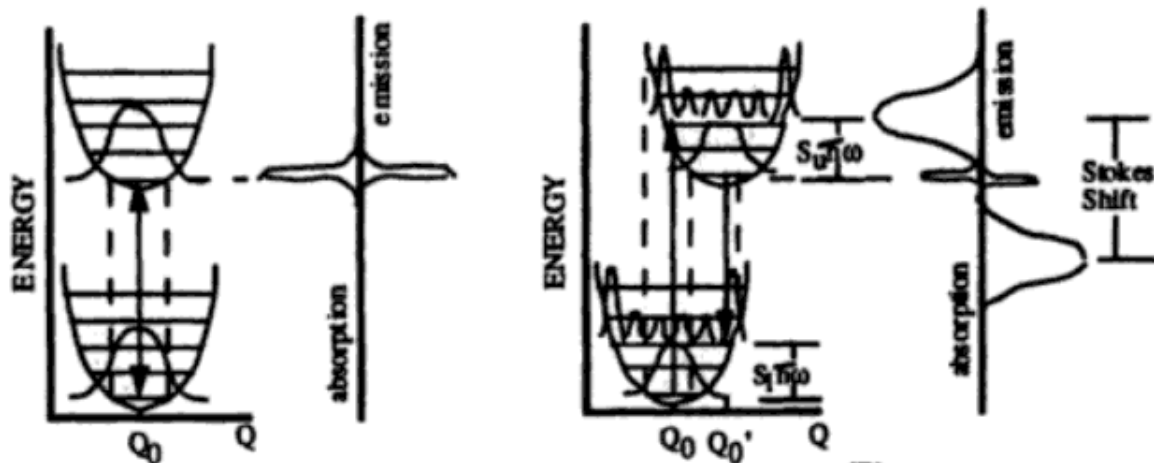


Figure 5: Displacement of potential wells [13].

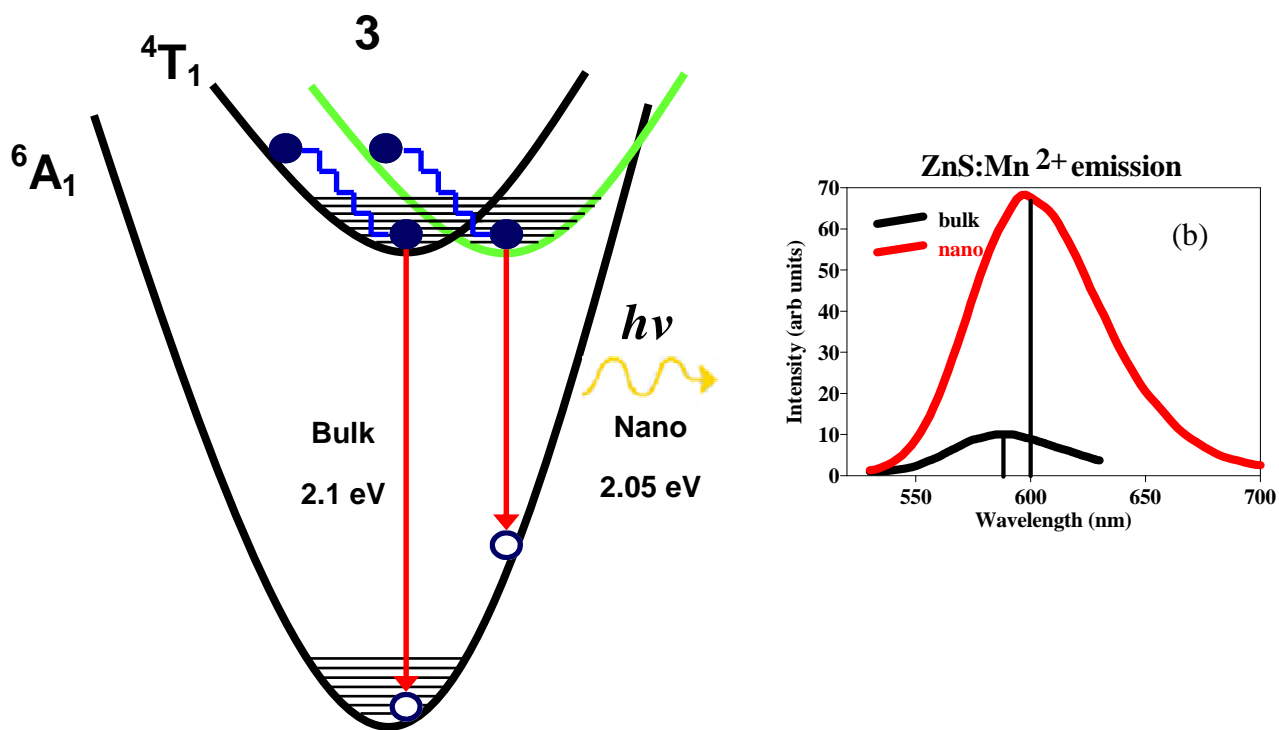


Figure 6: Emission mechanism of bulk and nano ZnS:Mn^{2+} according to the configurational coordinate model.

For part 3 the configurational coordinate model for Mn^{2+} [14, 15] is used. The same process occurs as in A, but the difference between the emission of the bulk and nanoparticles is shown. The insert (b) in Figure 6 shows the emission spectra for bulk and nanoparticles of $\text{ZnS}:\text{Mn}^{2+}$. For bulk particles there is only a slight offset in the parabola of the excited state. An electron relaxes non-radiatively from the conduction band to the $^4\text{T}_1$ state. This electron then relaxes non-radiatively to the bottom of the $^4\text{T}_1$ state. The excess energy will be released in the form of heat to the lattice. The electron will then recombine with a trapped hole in the ground state ($^6\text{A}_1$) and orange emission of photons at 590 nm takes place. In the case of nanoparticles the parabola offset is greater than that of bulk particles. The same process of electron relaxation and recombination will occur, but in this case emission at 600 nm takes place.

2. Luminescent mechanism of ZnO

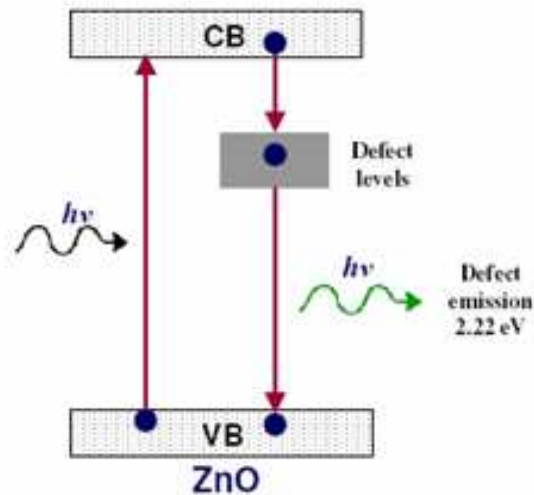


Figure 7: Luminescent mechanism of ZnO [11]

As shown in Figure 7, green emission at 550 nm from ZnO is due to hole capture and recombination with electrons by defect states as explained extensively elsewhere [16, 17]

3. Conclusion

The term symbols of the ${}^4T_1 \rightarrow {}^6A_1$ transitions of Mn^{2+} can be explained by the Tanabe-Sugano diagrams for a d^5 configuration. The terms on the left hand side of the Tanabe-Sugano diagrams can be explained by the Russell-Saunders coupling scheme and the terms on the right hand side with Ligand field theory. The proposed mechanism of ZnS and ZnS: Mn^{2+} is described according to the band theory and the configurational coordinate model. The origin of the blue emission of ZnS and the orange emission of ZnS: Mn^{2+} is described according to the proposed luminescent mechanism.

References

1. M. Tanaka, *J. Lumin.* **100**, (2002) 166.
2. M. Jain, J.L. Roberts, in: M. Jain (Ed.), *Diluted Magnetic Semiconductors*, World Scientific, Singapore, 1991, 31.
3. Y. Tanabe and S. Sugano, *J. Phys. Soc. Japan* **9**, (1954) 753 - 767.
4. D.S. McClure, *J. Chem. Phys.* **39**, (1963) 2850.
5. H. Yang, J. Zhao, L. Song, L. Shen, Z. Wang, L. Wang and D. Zhang, *Mater. Lett.* **57**, (2003) 2290.
6. B. Bhattacharjee, D. Ganguli, K. Iakoubovskii, A. Stesmans and S. Chaudhuri, *Bull. Mater. Sci.* **25**, (2002) 179.
7. C. Kittel, *Introduction to Solid State Physics*, 6th Ed., John Wiley, New York, (1986) p185.
8. S.C. Ghosh, C. Thanachayanont and J. Dutta, *ECTI-CON*, Pattaya, Thailand, 146 (2004).
9. A.B. Cruz, Q. Shen and T. Toyoda, *Thin Solid Films*, **499** (2006) 106.
10. G.H. Li, F.H. Su, B.S. Ma, K. Ding, S.J. Xu and W. Chen, *Phys. Stat. Sol.* **241** (2004) 3252.
11. S. Shionoya and W.M. Yen, *Phosphor Handbook*, CRC Press LLC, Boca Raton, (1999) p 36, 169-170.
12. A.G. Sykes, *Advances in inorganic chemistry*, Volume 35, Academic Press Inc., San Diego, (1990) p323.
13. R.C. Powell, *Physics of solid-state laser materials*, Springer-Verlag, New York, (1998) p 157.
14. T.A. Prokof'ev, B.A. Polezhaev and A.V. Kovalenko, *J. Appl. Spectro.* **72**, (2005) 869.
15. H. Hanzawa, M. Kobayashi, O. Matsuda, K. Murase and W. Giritat, *Phys. Stat. Sol. (a)* **175**, (1999) 721.
16. OM Ntwaeaborwa, HC Swart, RE Kroon, JR Botha, JM Ngaruiya, PH Holloway, in *Photoluminescence Research Progress*, editors: H.K. Wright and G.V. Edwards (Nova Publishers, New York) (2008) pp 287-306.
17. Y. Yu, Y. Wang, D. Chen, P. Haung, E. Ma and F. Bao, *Nanotechnology* **19**, (2008) 4.

Chapter 8

Conclusion and future work

This chapter contains the overall conclusion of the results obtained from ZnS, ZnS:Mn²⁺ and SiO₂-ZnS:Mn²⁺ as well as future work regarding this research study.

1. Conclusion

This thesis reports on the preparation of ZnS:Mn²⁺ via a chemical precipitation method and the incorporation of these nanoparticles into a SiO₂ matrix using the sol-gel method. It also reports on the surface morphology and chemical composition, the crystal structure and particle size, absorption properties and band gap, photoluminescence properties and cathodoluminescence and the degradation of these prepared nanoparticles. It is comparing the effect of annealing on the different properties of the samples with those of un-annealed samples. An extensive explanation of the proposed luminescent mechanism of ZnS, ZnS:Mn²⁺ and ZnO is also included.

Luminescent ZnS:Mn²⁺ and SiO₂-ZnS:Mn²⁺ particles were successfully synthesized. The un-annealed ZnS:Mn²⁺ nanoparticles sizes was in the order of 3 nm, while the annealed samples sizes was ~50 nm. X-ray diffraction and electron diffraction confirmed that both cubic ZnS and hexagonal ZnO formed during the synthesis process. Broader XRD peaks widths were observed for the ZnS:Mn²⁺ nanoparticles and this is due to size effects. Chemical composition analysis confirmed the presence of ZnS in the SiO₂ matrix.

Absorption measurements showed that the samples are absorbing in the UV ranging from 280 – 340 nm. It also confirms that there was a blue shift in the band gap of ~ 0.4 – 0.5 eV for the synthesized nanoparticles from that of bulk particles. This is due to quantum confinement effects. The particles radii were in the order of 1.5 nm corresponding to the particle size obtained from XRD. For the annealed samples the band gap compares to that of bulk ZnO indicating that ZnO had formed during the annealing process.

The PL results show two peaks for the un-annealed sample: one at 450 nm and the other at 600 nm. The 450 nm peak is associated with ZnS emission, while the 600 nm peak is associated with the ${}^4T_1-{}^6A_1$ transition of Mn^{2+} . The 7 mol% sample showed the highest intensity. For the annealed samples a broad peak is observed with its maximum at 550 nm. This peak is coming from defect emission of ZnO. The samples were capped with SiO_2 to see if there is any enhancement in their intensity. For the un-annealed samples the two peaks at 450 nm and 600 nm were again observed, but the intensity was much lower than that of the un-capped samples. The highest intensity was observed for the 10 mol% sample. It can be concluded that the SiO_2 did not enhance the luminescence intensity, but it did not influence the peak shapes and positions. The annealed SiO_2 -ZnS: Mn^{2+} samples have two main peaks at 450 nm and 550 nm. These emission peaks are associated with either structural defects or charge transfer between the Si and O atoms. ZnO defect emission can also contribute to the 550 nm peak.

AES analysis confirms that Zn, S, O and C are present on the surface of the ZnS: Mn^{2+} samples. The Zn and S peaks are from the ZnS matrix and the C peak is due to contamination. The O peak is an indication that some ZnO had formed on the surface. AES on the SiO_2 -ZnS: Mn^{2+} sample showed a big O peak, while small Si, S and Zn peaks were observed. Degradation of the commercial ZnS: Mn^{2+} sample showed a decrease in the S and C peaks, while the O peak increased. The reduction of S and C are due to desorption by formation of volatile SO_x and CO_x . The increase in O is due to the formation of ZnO or $ZnSO_4$ on the surface. There is an initial increase in the CL intensity and this is due to the removal of C from the surface. The CL intensity then decreases because a non-luminescent ZnO or $ZnSO_4$ layer is formed on the surface according to the ESSCR degradation model.

A proposed luminescent mechanism for ZnS, ZnS: Mn^{2+} and ZnO was discussed. The blue emission (450 nm) associated with ZnS can be attributed to the hole trapping and recombination with electrons by defect states (zinc or sulphur vacancies) in ZnS. The orange emission at 600 nm for nano particles can be attributed to ${}^4T_1 \rightarrow {}^6A_1$ transitions of Mn^{2+} ions. These transitions are explained in terms of the Tanabe-Sugano diagrams for the d^5 level, the Russell Saunders coupling scheme and the Ligand field theory. 6A_1 is the ground state of Mn^{2+} , while 4T_1 is one of

the excited states. In the case of ZnO emission is due to hole capture and recombination with electrons by defect states.

2. Future work:

1. Research should be done on different synthesis techniques. With the current synthesis technique ZnO is also formed in the process. This is affecting the PL intensity as well as the crystal structure. A technique should be found that is both fast, cheap and that is producing high quality, pure ZnS.
2. Only five different doping concentrations of Mn^{2+} between 2 and 20 % were studied. Research on a greater range of concentrations should be done, especially for very low concentrations between 0 and 2 %. Inductively coupled plasma atomic emission spectra (ICP-AES) should also be done on the samples to check if the dopant concentration is staying the same after the synthesis process or if it is decreasing to a lower concentration.
3. In this study only two temperatures were investigated namely room temperature (un-annealed samples) and 600°C (annealed samples). Further work can include annealing the samples from 50°C up to 1000°C. Because ZnO had formed when the samples were annealed at 600°C in air, different ambient gasses can be used to prevent the formation of ZnO. Studies can also include an investigation to see at what temperature the ZnS is converted into ZnO when annealing in air. By doing XRD on these samples annealed at different temperatures, the effect temperature has on the stress and strain can also be studied.
4. Absorption was only measured for dried samples that were dissolved in ethanol. The band gap was therefore also only calculated for dried samples. Further studies can be done on samples that are still in solution before and after washing of the samples to see if washing and drying of the samples will affect the band gap.
5. Samples can be left in solution and the PL and absorption spectra can be recorded over a period of time. This will study the effect of aging on the PL intensity, absorption spectra, band gap and particle size of the samples.

6. It is reported that the band gap of materials will increase with a decrease in particle size. This blue shift in the band gap is due to quantum confinement effects. A study can be conducted to see what the effect of reaction time and temperature is on the particle size and band gap of the prepared samples.
7. No information is currently available on the distribution of the Mn^{2+} in the ZnS matrix. For this study uniform distribution was assumed. By doing elemental mapping the distribution of the dopant in the matrix can be determined to see if it is uniformly distributed. When the ZnS:Mn^{2+} is mixed with SiO_2 it is assumed that the SiO_2 will form a protective coating around the ZnS:Mn^{2+} . By doing elemental mapping on these types of samples the assumption can be confirmed.
8. It would be ideal to prepare a phosphor that can emit from ~400 nm (blue) to ~600 nm (red). This can be achieved by using different dopants. By co-doping ZnS with Mn, Cl, Au, Ag, Al and Cu it can result in emission peaks ranging from 390 nm to 600 nm. By doing this a phosphor can be created that is emitting in the blue, green and red region resulting in a white phosphor.

Appendix A

Publications

- [1] M.M. Biggs, O.M. Ntwaeaborwa, J.J. Terblans, and H.C. Swart, Characterization and luminescent properties of $\text{SiO}_2:\text{ZnS}:\text{Mn}^{2+}$ and $\text{ZnS}:\text{Mn}^{2+}$ nanophosphors synthesized by a sol-gel method, *Physica B: Physics of Condensed Matter*, 404 (22) (2009) 4499-4503.
- [2] LF Koao, HC Swart, E Coetsee, MM Biggs and FB Dejene, The effect of Mg^{2+} ions on the Photoluminescence of Ce^{3+} doped silica, *Physica B: Physics of Condensed Matter*, 404 (22) (2009) 4470-4475.
- [3] A.G. Ali, H.C. Swart, J.R. Botha, E. Coetsee, M.M. Biggs and F.B. Dejene, Synthesis and characterization of ZnO nanoparticles by varying the sodium hydroxide to zinc acetate molar ratios by a Sol-Gel process, *Journal of Physics and Chemistry of Solids*, submitted July 2009.
- [4] Vinay Kumar, Varun Mishra, M.M. Biggs, I.M. Nagpure, O.M. Ntwaeaborwa, J.J. Terblans and H.C. Swart, Electron beam induced green luminescence and degradation study of $\text{CaS}:\text{Ce}$ nanocrystalline phosphors for FED applications. *Appl. Surf. Sci.*, 256 (6) (2010) 1720-1724.
- [5] V. Kumar, V. Mishra, S. S. Pitale, V. Mishra, I.M. Nagpure, M. M. Biggs, O.M. Ntwaeaborwa and H.C. Swart, Luminescence investigations in Ce^{3+} doped CaS nanophosphors, *Journal of Alloys and Compounds*, accepted November 2009.

Conferences

- [1] M.M. Biggs, O.M. Ntwaeaborwa, J.J. Terblans and H.C. Swart, Mechanism of luminescence of nanoparticulate and commercial ZnS:Mn²⁺ phosphors, Limpopo conference, SAIP UL, 9 - 11 July 2008.
- [2] M.M. Biggs, O.M. Ntwaeaborwa, J.J. Terblans en H.C. Swart, Luminessensie meganisme van gesintetiseerde nanodeeltjies en kommersiële ZnS:Mn²⁺ fosfor, Afrikaanse studente simposium, SAAWK, UJ, 31 Oktober 2008
- [3] M.M. Biggs, O.M. Ntwaeaborwa, J.J. Terblans, and H.C. Swart, Characterization and luminescent properties of SiO₂:ZnS:Mn²⁺ and ZnS:Mn²⁺ nanophosphors synthesized by a sol-gel method, 3rd South African Conference on Photonic Materials, 23 - 27 March 2009.
- [4] LF Koao, HC Swart, E Coetsee, MM Biggs and FB Dejene, The effect of Mg²⁺ ions on the Photoluminescence of Ce³⁺ doped silica, 3rd South African Conference on Photonic Materials, 23 - 27 March 2009.
- [5] AG Ali, HC Swart, JR Botha, E Coetsee, MM Biggs and FB Dejene. Structural and optical properties of ZnO, SiO₂:Ce³⁺ and ZnO:SiO₂:Ce³⁺ nanoparticles prepared by a Sol-Gel process. International Conference on Nanotechnology and Advanced Materials 2009. (ICNAM 2009), University of Bahrain, 4 - 7 May 2009.
- [6] M.M. Biggs, O.M. Ntwaeaborwa and H.C. Swart, Characterization and luminescent properties of ZnS:Mn²⁺ nanophosphor synthesized by a sol-gel method, Durban conference, SAIP UKZN, 7 - 10 July 2009.
- [7] LF Koao, HC Swart, E Coetsee, MM Biggs and FB Dejene. The effect of temperature on the photoluminescence characteristics of Ce;Al or Ce;Mg doped SiO₂. Durban conference, SAIP UKZN, 7 - 10 July 2009.

- [8] D.B. Bem, H.C. Swart, A.S. Luyt, M.M. Biggs, F.B. Dejene. Synthesis and Characterization of Long Persistence Strontium and Barium Aluminate Phosphors. Durban conference, SAIP UKZN, 7 - 10 July 2009.
- [9] H.C. Swart, J.J. Terblans, E. Coetsee, V. Kumar, O.M. Ntwaeaborwa and M.M. Biggs. Auger Electron Spectroscopy and X-ray Photoelectron Spectroscopy study of the electron stimulated surface chemical reaction mechanism for phosphor degradation. Ecasia09, 13th European Conference on Applications of Surface and Interface Analysis, Antalya, Turkey, 18 - 23 October, 2009.
- [10] M.M. Biggs, O.M. Ntwaeaborwa en H.C. Swart, 'n oorsig van verskillende tipes luminessensie en verskillende tipes fosfors; hulle gebruike en karakterisering, Afrikaanse studente simposium, SAAWK, UOVS, 30 Oktober 2009.